EVOLUTION OF INTERACTION AND STRUCTURE OF NANOPARTICLE-PROTEIN COMPLEXES AS STUDIED BY SCATTERING TECHNIQUES

by

INDRESH YADAV

Enrolment No. PHYS01201504017

Bhabha Atomic Research Centre, Mumbai, India

A thesis submitted to the

Board of Studies in Physical Sciences

In partial fulfillment of requirements

for the Degree of

DOCTOR OF PHILOSOPHY

of

HOMI BHABHA NATIONAL INSTITUTE

May, 2017

Homi Bhabha National Institute

Recommendations of the Viva Voce Committee

As members of the Viva Voce Committee, we certify that we have read the dissertation prepared by Indresh Yadav entitled "Evolution of Interaction and Structure of Nanoparticle-Protein Complexes as Studied by Scattering Techniques" and recommend that it may be accepted as fulfilling the thesis requirement for the award of Degree of Doctor of Philosophy.

Chairman - Prof. Saibal Basu	**Date:**
Guide - Prof. V. K. Aswal	**Date:**
Examiner - Prof. H. B. Bohidar	**Date:**
Member 1- Prof. M. Senthil Kumar	**Date:**
Member 2- Prof. P. A. Hassan	**Date:**

Final approval and acceptance of this thesis is contingent upon the candidate's submission of the final copies of the thesis to HBNI.

I hereby certify that I have read this thesis prepared under my direction and recommend that it may be accepted as fulfilling the thesis requirement.

Date: 18-08-2017

Place: Mumbai **Prof. V. K. Aswal**

(Guide)

STATEMENT BY AUTHOR

This dissertation has been submitted in partial fulfillment of requirements for an advanced degree at Homi Bhabha National Institute (HBNI) and is deposited in the Library to be made available to borrowers under rules of the HBNI.

Brief quotations from this dissertation are allowable without special permission, provided that accurate acknowledgement of source is made. Requests for permission for extended quotation from or reproduction of this manuscript in whole or in part may be granted by the Competent Authority of HBNI when in his or her judgment the proposed use of the material is in the interests of scholarship. In all other instances, however, permission must be obtained from the author.

(Indresh Yadav)

DECLARATION

I, hereby declare that the investigation presented in the thesis has been carried out by me. The work is original and has not been submitted earlier as a whole or in part for a degree / diploma at this or any other Institution / University.

(Indresh Yadav)

DECLARATION

I, hereby declare that the queries raised by the examiners of the thesis have been incorporated as suggested.

Dr. V. K. Aswal
(Guide)

List of Publications

In Refereed Journals:

1. Small-Angle Neutron Scattering Study of Differences in Phase Behavior of Silica Nanoparticles in the Presence of Lysozyme and Bovine Serum Albumin Proteins
   Indresh Yadav, Sugam Kumar, V. K. Aswal and J. Kohlbrecher
   Phys. Rev. E, **2014**, 89, 032304 (1-9).

2. Electrolyte Effect on the Phase Behavior of Silica Nanoparticles with Lysozyme and Bovine-Serum-Albumin Proteins
   Indresh Yadav, V. K. Aswal and J. Kohlbrecher
   Phys. Rev. E, **2015**, 91, 052306 (1-9).

3. Size-Dependent Interaction of Silica Nanoparticles with Lysozyme and Bovine Serum Albumin Proteins
   Indresh Yadav, V. K. Aswal and J. Kohlbrecher
   Phys. Rev. E, **2016**, 93, 052601 (1-11).

4. Structure and Interaction in pH-Dependent Phase Behavior of Nanoparticle-Protein Systems
   Indresh Yadav, Sugam Kumar, V. K. Aswal and J. Kohlbrecher
   Langmuir, **2017**, 33, 1227-1238.

5. Tuning the Phase Behavior of Nanoparticle-Protein Systems by Selective Additives
   Indresh Yadav, Sugam Kumar, V. K. Aswal and J. Kohlbrecher
   (Under Preparation).

6. Interaction of Silica Nanoparticles with Mixed Lysozyme-Bovine Serum Albumin Proteins System
   Indresh Yadav, V. K. Aswal and J. Kohlbrecher
   (Under Preparation).

In Conferences and Symposia:

1. SANS Study of Interaction of Silica Nanoparticles with BSA Protein and their Resultant Structure
   Indresh Yadav, V. K. Aswal and J. Kohlbrecher
   AIP Conf. Proc., **2014**, 1591, 216-218.

2. Understanding of Phase Behavior of Silica Nanoparticles with Lysozyme and BSA Proteins
   Indresh Yadav and V. K. Aswal
   Interdispelenery Symposium on Material Chemistry, BARC, Mumbai, India (**2014).**

3. SANS Study of Depletion Interaction in Nanoparticles-Protein System and their Resultant Structures
Indresh Yadav, V. K. Aswal and J. Kohlbrecher
MRSI Meeting, IITB, Mumbai, India (**2014**).

4. SANS Study of Evolution of Interaction and Structure in Nanoparticle-Protein Systems
Indresh Yadav, Sugam Kumar, V. K. Aswal and J. Kohlbrecher
Conference on Neutron Scattering, IISER, Pune, India (**2014**).

5. Modifications in Interaction and Structure of Silica Nanoparticle-BSA Protein System in Aqueous Electrolyte Solution
Indresh Yadav, V. K. Aswal and J. Kohlbrecher
AIP Conf. Proc. **2015,** 1665, 040008 (1-3).

6. SANS Study of Phase Behaviour of Silica Nanoparticles-Proteins System
Indresh Yadav, V. K. Aswal and J. Kohlbrecher
Conference on Neutron Scattering, HBCSE , Mumbai, India (**2015**).

7. Probing Nanoparticle-Protein Interaction using Scattering Techniques
Indresh Yadav, V. K. Aswal and J. Kohlbrecher
Winter School on Quantitative Systems Biology 2015, ICTS, Bangalore, India (**2015**).

8. Interaction of Lysozyme Protein with Different Sized Silica Nanoparticles and their Resultant Structures
Indresh Yadav, V. K. Aswal and J. Kohlbrecher
AIP Conf. Proc. **2016**, 1731, 050093 (1-3).

9. pH-Dependent Phase Behavior of Silica Nanoparticles in the Presence of Lysozyme Protein
Indresh Yadav, V. K. Aswal and J. Kohlbrecher
Conference on Neutron Scattering, BARC, Mumbai, India (**2016**).

10. pH-Dependent Depletion Induced Phase Behavior of Silica Nanoparticles
Indresh Yadav, V. K. Aswal and J. Kohlbrecher
AIP Conf. Proc. **2017**, 1832, 040015 (1-3).

11. Interplay of pH-Dependent Interactions in Nanoparticle-Protein Systems
Indresh Yadav, V. K. Aswal and J. Kohlbrecher
Mumbai-Pune Soft Matter Meeting, BARC, Mumbai, India (**2017**).

(Indresh Yadav)

Dedicated

To

My Parents

ACKNOWLEDGEMENTS

First and foremost I offer my sincere gratitude to my guide, Prof. Vinod K. Aswal, Solid State Physics Division, Bhabha Atomic Research Centre, Mumbai, who encouraged me throughout the tenure of my thesis. This Ph.D. work would not have been possible without his constant support, constructive criticism and luminous guidance. I am thankful to Prof. Saibal Basu, Head, Solid State Physics Division, Bhabha Atomic Research Centre, Mumbai, for his support and motivation. I extend my gratitude to Prof. P. A. Hassan and Prof. M. Senthil Kumar whose useful suggestions as doctoral committee members have been very helpful.

My thanks are also attributable to Dr. J. Kohlbrecher for his support in carrying out small-angle neutron scattering experiments at the SINQ, Paul Scherer Institute, Switzerland. I also wish to thank Dr. D. Sen, Dr. Debes Ray, Dr. Sugam Kumar, Dr. A. J. Chinchalikar, Dr. Sumit Mehan, Dr. S. Abbas, Dr. D. Saha and Dr. J. Bahadur for many fruitful discussions during the course of the thesis. I take the opportunity to thank all my batch mates of BARC Training School from 57^{th} batch for their encouragement and support.

Special thanks to my friends Gita, Priyanka, Neetika, Avik, Jaglal, Amandeep, Rajan, Rabeet and Suman who directly or indirectly have helped me in achieving my goals. I would like to thank Dr. R. Mittal, Dr. P. U. Sastry, Shri A. K. Patra and all other colleagues of SSPD in BARC, for being supportive during the tenure of the thesis.

Finally, I would like to express my love and gratitude to my parents and all the family members for being supportive in my endeavor and extending encouragement throughout the work.

CONTENTS

Homi Bhabha National Institute

SYNOPSIS OF Ph. D. THESIS

1. **Name of the Student:** Indresh Yadav
2. **Name of the Constituent Institution:** Bhabha Atomic Research Centre, Mumbai
3. **Enrolment No.:** PHYS01201504017
4. **Title of the Thesis:** Evolution of Interaction and Structure of Nanoparticle-Protein Complexes as Studied by Scattering Techniques
5. **Board of Studies:** Physical Sciences

SYNOPSIS

Nanoparticles possess remarkable and distinctive characteristics (e.g. high surface activity, quantum confinement, surface plasmon resonance, superparamagnetism etc.) from those of their constituent atoms/molecules and bulk materials [1]. These features are size-dependent and cover a wide range of phenomena that play an important role in the natural environment as well as in industrial and biomedical applications [2]. Many of these applications require conjugation of nanoparticles with macromolecules such as proteins, polymers and surfactants [3]. In particular, nanoparticle-protein conjugates have applications in bio-sensing, bio-imaging, drug delivery and novel functional materials [4,5]. The conjugation of nanoparticles with proteins is usually done either by direct covalent linkage or by non-covalent interactions between the nanoparticles and proteins [6]. Conjugates formed through covalent attachment are irreversible and the resultant systems are highly stable. However, this method requires good command on organic synthesis. On the other hand, non-covalent interaction provides a complementary strategy to covalent

attachment. The common way to produce non-covalent nanoparticle-protein conjugates is through electrostatic attraction between the nanoparticles and proteins. The conjugation in this case is often reversible and most importantly can be controlled by solution parameters such as ionic strength, pH, temperature and concentration [7-9]. The characteristics of nanoparticles such as shape and size, surface charge density etc. can also play important part. The conjugation may result in conformational changes of proteins as well as affect the surface properties and colloidal stability of the nanoparticles [10]. Characteristics of nanoparticle-protein conjugates depend on the interplay of nanoparticle-protein, nanoparticle-nanoparticle and protein-protein interactions. The role of these interactions has been investigated in this thesis. The studies are carried out from systems having both nanoparticle and protein charged, where their conjugation is tuned by choice of protein and varying solution conditions (ionic strength and pH) as well as size of the nanoparticles. The anionic silica nanoparticles and two globular proteins [lysozyme and bovine serum albumin (BSA)] have been used as model systems. These nanoparticle-protein systems have been characterized by protein adsorption on the nanoparticles and their resultant phase behavior. The adsorption isotherms of proteins on the nanoparticles are measured using ultraviolet-visible (UV-vis) spectroscopy and evolution of interactions and structures for understanding the phase behavior are examined using scattering techniques [dynamic light scattering (DLS) and small-angle neutron scattering (SANS)].

The thesis consists of seven chapters. Chapter 1 gives an introduction to the nanoparticles, proteins, their possible complexes and potential applications. The details of the experimental techniques and their capabilities for studying such systems are discussed in chapter 2. The results of different nanoparticle-protein complexes studied are described in chapters 3 to 6. In all the cases, measurements have been carried out for fixed concentration of silica nanoparticles (1 wt %) with varying concentration of proteins (0-5 wt %). Chapter 3 reports the study of complexes of silica nanoparticles with lysozyme and BSA proteins. The studies have been

carried out under physiological conditions (pH 7), where silica nanoparticles are anionic whereas lysozyme and BSA proteins are cationic and anionic, respectively. The effect of electrolyte on these nanoparticle-protein complexes is examined in chapter 4. The studies are done mostly in presence NaCl and its relative effect with other salts is compared. Chapter 5 presents the tuning of nanoparticle-protein complexes through pH. The pH has been varied from physiological conditions to the isoelectric point (IEP) of the respective proteins. The role of nanoparticle size on the nanoparticle-protein complexes is investigated in chapter 6. The nanoparticle size has been varied in the range so that in each case there is enough adsorption of protein on the nanoparticles. Chapter 7 gives the summary of the thesis.

A general introduction to nanoparticles, proteins and their complexes is given in **chapter 1**. The properties of nanoparticles, their methods of synthesis and applications to wide range of areas are discussed. Nanoparticles due to its small size exhibit striking physical and chemical properties. The top-down and bottom-up are commonly used methods of synthesis of nanoparticles [1]. The bottom-up method has an advantage of high control over size and also non-destructive. The different nanoparticles applications include from biomedical to electronics, energy to environment and food to textiles. In particular in biomedical applications, there is increasing recent interest to understand the interaction of nanoparticles with biomolecules such as proteins [11]. Proteins are the polymers of amino acids with a specific three-dimensional shape and do most of the work in cells required for structure, function and regulation of body tissues and organs [12]. The structures of protein, their classification and stability are discussed in this chapter. Proteins have four different levels of structure: primary, secondary, tertiary and quaternary. The linear sequence of amino acids chain is referred as the primary structure and the hydrogen bonding within the sequence leads to the secondary structure. Different interactions among secondary structures result in a specific three dimensional shape is called as tertiary structure of protein. Further, quaternary structure is formed for more than one amino acid chain.

Based on native structures, proteins can be divided in two general categories: globular and fibrous proteins. Globular proteins are generally compact, soluble in water and more or less spherical in shape. On the other hand, fibrous proteins are typically elongated and insoluble in water. The protein solutions are stabilized due to the repulsive (electrostatic and/or steric) interaction overcoming the attractive (van der Waals and/or hydrophobic interaction) interactions between protein molecules. The various solution conditions (e.g. pH, ionic strength, temperature etc.) are often used for tuning the interactions and hence the stability of protein solutions [13]. The charge nature of both nanoparticles and proteins can be utilized for their conjugation as well as comparable size of nanoparticle with protein makes this conjugate useful for biological applications where it can move in and out of the cells. The role of different interactions in the formation and stability of nanoparticle-protein complexes and potential applications are discussed. The interactions governing nanoparticle-protein complexes depend on both DLVO (van der Waals attraction along with electrostatic double-layer repulsion) and non-DLVO (e.g., solvation, steric, hydrogen bonds, depletion and hydrophobic) interactions [14]. The unique properties of nanoparticles combining with proteins lead to interesting applications. The high surface-to-volume ratio of nanoparticles is used for drug delivery, shift in surface plasmon resonance is employed for sensing of biomolecules and fluorescent properties of the nanoparticles are utilized for imaging. The nanoparticle-protein complexes are also greatly used in forming organic-inorganic hybrid multifunctional materials. A layout of the thesis is discussed in the end of this chapter.

UV-vis spectroscopy and scattering techniques [DLS and SANS] have been used to characterize the nanoparticle-protein complexes in this thesis. These experimental techniques are presented in detail in **chapter 2**. UV-vis spectroscopy is an absorption spectroscopy involving electronic transition in the typical wavelength range of 200-700 nm [15]. The presence of organic molecules such as proteins is determined by the characteristic absorption peak arising

from electron transition of highest occupied molecular orbital (HOMO) to the lowest unoccupied molecular orbital (LUMO). The quantitative information on concentration of absorbing constitute is given by the Beer-Lambert law. The amount of free protein in nanoparticle-protein complexes is calculated by measuring the absorption spectra of free protein as separated from adsorbed protein using centrifugation. The transmission of light at a particular wavelength has been used to predict the structural evolution (phase behavior) of the resultant nanoparticle-protein systems. The structure and interaction information of the system are obtained using DLS and SANS. DLS technique relies on the detection and analysis of fluctuations in the intensity of scattered light by particles in a medium undergoing Brownian motion [16]. One measures the fluctuations of scattered light intensity in terms of normalized autocorrelation function (ACF). The decay constant (Γ) of ACF is related to the translational diffusion coefficients of the particles (D) and the magnitude of scattering vector Q [$\Gamma = DQ^2$]. The structure and interaction together are contained in the average diffusion coefficient or related effective hydrodynamic size given by Stokes-Einstein relation. On the other hand, structure and interaction can be separated using SANS technique. It is a diffraction experiment measuring the scattering of monochromatic neutrons as a function of scattering vector Q [17]. The scattering intensity is given by $I(Q) \sim (\rho_p - \rho_s)^2 \times P(Q) \times S(Q)$, where ρ_p and ρ_s are scattering length densities of particles and solvent, respectively. $P(Q)$ is the orientational average of the square of the form factor [$P(Q) = \langle F(Q)^2 \rangle$] and gives information about shape and size of the particle. Analytical expressions of $P(Q)$ for standard geometries are known in the literature. $S(Q)$ is interparticle structure factor and is Fourier transform of the pair correlation function [$g(r)$]. In case of isotropic systems, $g(r)$ can be obtained using Ornstein-Zernike equation for a suitable interaction potential. The two-Yukawa (2Y) potential is commonly used taking account of both the repulsive and attractive interactions in the system. $S(Q)$ for particle aggregates are often modelled by those

of fractals. SANS is of considerable importance for multi-component hydrogenous systems due to very different contrasts for hydrogen and deuterium components. The other advantages of scattering techniques include that the systems are probed in-situ and under native conditions.

The differences in complexes of anionic silica nanoparticles with two globular proteins (lysozyme and BSA) are studied in **chapter 3** [18,19]. The measurements have been carried out at physiological pH. At this pH silica nanoparticles and BSA protein are anionic whereas lysozyme is cationic. The strong electrostatic attraction leads to adsorption of oppositely charged lysozyme on nanoparticles while electrostatic repulsion prevents any adsorption of similarly charged BSA on nanoparticle surface. The adsorption isotherm as determined by UV-vis spectroscopy shows an exponential growth behavior with increasing protein concentration for lysozyme. The absence of any kind of adsorption of BSA protein rules out the possibility of site specific adsorption. Despite having different nature of interactions, both proteins render a similar phase behavior where nanoparticle-protein systems transform from being one-phase (clear) to two-phase (turbid) above a critical protein concentration (CPC). The CPC required for phase transformation is much lower for lysozyme than for BSA. DLS measurements suggest that such phase behavior arises as a result of the attractive interaction and/or nanoparticles aggregation in the system. SANS has been used to model the evolution of interactions using 2Y potential. It is found that the interplay of electrostatic repulsion with a short-range attraction for lysozyme and long-range attraction for BSA govern the phase behavior of nanoparticle-protein complexes. The adsorption of lysozyme neutralizes the charge, and thereby causing protein-mediated bridging aggregation of the nanoparticles. On the other hand, nonadsorption of BSA results in the depletion attraction-induced aggregation of the nanoparticles [20]. In all the cases, the aggregates are characterized by diffusion limited aggregate (DLA) type of mass fractal morphology having fractal dimension about 2.4.

Chapter 4 presents the effect of electrolyte on nanoparticle-protein complexes [21,22]. The properties of complexes are decided by the combination of different interactions between components (nanoparticle-protein, nanoparticle-nanoparticle and protein-protein) undergoing in the system. All these interactions can modify in the presence of electrolyte. The measurements have been performed at pH 7 and in presence of 0.1 M NaCl. The adsorption behavior of proteins on nanoparticles in presence of electrolyte does not show any significant changes whereas the phase behavior for both the nanoparticle-protein systems is significantly modified towards lower CPC. This effect is more pronounced for BSA than for lysozyme. DLS and SANS data suggest that changes in phase behavior are related with modifications in both interaction and structure of the nanoparticle-protein systems. The suppression of the electrostatic repulsion between nanoparticles for lysozyme and enhancement of depletion interaction for BSA are found to be mainly responsible for the changes in the phase behavior of respective nanoparticle-protein systems in presence of electrolyte. The nanoparticle aggregates are characterized by fractal structures. The role of different electrolyte ions on nanoparticle-protein complexes has also been examined.

The pH-dependent behavior of nanoparticle-protein complexes is investigated in **chapter 5** [23,24]. The pH variation allows systematic changes in the electrostatic interactions of the components in the system and hence the characteristics of their complexes. The pH of the solution is varied from physiological conditions to the IEP of the respective proteins ($IEP_{Lysozyme}$ ~ 11 and IEP_{BSA} ~ 4.6). The net charge on the lysozyme decreases as pH approaches towards the IEP, which leads to increase in the lysozyme adsorption due to decrease in protein-protein repulsion. Irrespective of the pH, BSA remains non-adsorbing because of repulsive interaction between nanoparticle and protein. The CPC in phase behavior increases for lysozyme but decreases for BSA with pH approaching towards their respective IEPs. The effect is more pronounced in the case of BSA than in the case of lysozyme. Since the charge on lysozyme

decreases as pH approaches the IEP, the number of lysozyme molecules required to neutralize the charge of the nanoparticles increases. As a result, a higher CPC is required to transform a one-phase nanoparticle-protein system into a two-phase system. For BSA, the decrease in pH enhances the depletion attraction between the nanoparticles because of a decrease in the repulsion between BSA molecules and at the same time reduces the electrostatic repulsion between the nanoparticles. Lysozyme mediated attractive interaction between the nanoparticles decreases with pH approaching IEP due to decrease in charge on the protein. In the case of BSA, decrease in BSA-BSA repulsion enhances the depletion attraction between the nanoparticles as pH is shifted towards IEP. The morphology of the nanoparticle aggregates remains as mass fractal independent of the pH.

The effect of nanoparticle size on nanoparticle-protein complexes is presented in **chapter 6** [25,26]. The measurements have been done for different size nanoparticles of 10, 18 and 28 nm. The total amount of adsorbed lysozyme, as governed by the surface-to-volume ratio, increases on lowering the size of the nanoparticles for fixed volume fraction of the nanoparticles. The binding affinity of protein adsorption increases whereas the saturation value decreases with increasing the size of the nanoparticles. The increase in saturation value for smaller particles is interpreted in terms of the larger total surface area available for protein adsorption. The binding affinity depends on the curvature of the nanoparticles and hence favours the larger size of the nanoparticles. On the other hand, BSA protein does not show adsorption on any size of the nanoparticles. The phase behavior is modified towards the lower CPC for both the proteins with increasing the nanoparticle size. The decrease in CPC with increase in size for the lysozyme protein is decided by the dominance of number density effect over the surface area effect. The CPC in the case of non-adsorbing BSA protein is lowered with the increase in the size of the nanoparticles because of the enhancement of the excluded volume of an individual nanoparticle and number density effects. Size-dependent phase behavior of silica nanoparticles for lysozyme

protein arises because of the dominance of protein-mediated short-range attractive interaction over the long-range repulsion between the nanoparticles, whereas for BSA protein the excluded volume effect is enhanced with increasing nanoparticle size leading to an increase in the depletion attraction. Again, the nanoparticles aggregates are found to be mass fractal.

Finally, the **7th chapter** presents the summary of the thesis. This thesis reports the study of complexes of silica nanoparticles with lysozyme and BSA proteins under varying solution conditions (ionic strength and pH) and different sized nanoparticles. Scattering techniques (DLS and SANS) along with complementary techniques (UV-vis spectroscopy and zeta potential) have been used to probe these systems. The main results of the thesis are:

(i) Lysozyme and BSA proteins show very different adsorption on silica nanoparticles. Despite this, both proteins render a similar phase behavior where nanoparticle-protein systems transform from being one-phase to two-phase above a critical protein concentration (CPC). The bridging attraction in case of lysozyme (short-range) and depletion attraction for BSA (long-range) are responsible for aggregation of the nanoparticles in two-phase. The morphology of the aggregates is found to be mass fractal.

(ii) The phase behavior can be tuned by the presence of an electrolyte. The protein adsorption does not show any significant change in this case. The suppression of the electrostatic repulsion for lysozyme and enhancement of depletion interaction for BSA between nanoparticles are found to be responsible for the changes in the phase behavior (lower CPC) of respective nanoparticle-protein systems with an electrolyte.

(iii) Protein adsorption on nanoparticles is enhanced by varying the pH approaching its isoelectric point (IEP). For adsorbing protein (lysozyme), decrease in protein-protein repulsion results in higher adsorption. There is no pH dependent effect observed for non-adsorbing protein (BSA). The CPC increases for lysozyme but decreases for BSA with pH approaching towards their respective IEPs. The nanoparticle-nanoparticle interaction is modified through decrease in

lysozyme mediated attraction and increase BSA induced depletion attraction as pH approaches their respective IEPs.

(iv) The size of the nanoparticles has distinct effect on properties of nanoparticle-protein complexes. The amount of lysozyme adsorption on nanoparticles increases on lowering the size of the nanoparticles, whereas BSA remains non-adsorbing. The CPC decreases with increase in size of nanoparticles for both the proteins. The total (attractive + repulsive) potential leading to nanoparticles fractal aggregation in two-phase formation is found to be more attractive for larger sized nanoparticles.

To conclude, this thesis has looked into the properties of nanoparticle-protein complexes driven by the electrostatic interactions between the components. The anionic silica nanoparticles and two globular proteins (cationic lysozyme and anionic BSA) are used as model systems. The complexes are characterized by UV-vis spectroscopy and scattering techniques (DLS and SANS). The adsorption of lysozyme on silica nanoparticles follows an exponential growth behavior with increasing protein concentration, whereas no adsorption is found for BSA protein. The complexes of nanoparticles with both the proteins show unique phase transformation from one-phase to two-phase above a critical protein concentration. The presence of protein induces the short-range and long-range attraction between the nanoparticles with lysozyme and BSA, respectively. The nanoparticle aggregates in two-phase are formed in accordance with DLA fractals. The solution conditions (ionic strength and pH) as well as size of the nanoparticles are further employed to tune the properties of nanoparticle-protein complexes. The observed changes in the adsorption and phase behavior of nanoparticle-protein complexes are interpreted in terms of the modification of undergoing interactions (nanoparticle-protein, nanoparticle-nanoparticle and protein-protein) and resultant structures (nanometer to micron size) of the complexes.

The results of the present thesis can be utilized for the nanoparticle applications in biomedical such as drug delivery and bio-imaging.

REFERENCES

1. G. Cao and Y. Wang, *Nanostructures and Nanomaterials: Synthesis, Properties and Applications* (World Scientific, Singapore, 2011).
2. A. E. Nel, *et al. Nat. Mater*. **8**, 543 (2009).
3. A. C. Balazs, T. Emrick and T. P. Russell, *Science* **314**, 1107 (2006).
4. M. De, P. S. Ghosh and V. M. Rotello, *Adv. Mater*. **20**, 4225 (2008).
5. C. M. Niemeyer, *Angew. Chem. Int. Ed.* **40**, 4128 (2001).
6. S. Rana, Y. C. Yeh and V. M. Rotello, *Curr. Opin. Chem. Biol*. **14**, 828 (2010).
7. A. A. Vertegel, R. W. Siegel and J. S. Dordick, *Langmuir* **20**, 6800 (2004).
8. S. Kumar, V. K. Aswal and P. Callow, *Langmuir* **30**, 1588 (2014).
9. B. Bharti, J. Meissner, S. H. L. Klapp and G. H. Findenegg, *Soft Matter* **10**, 718 (2014).
10. J. S. Gebauer, M. Malissek, S. Simon, S. K. Knauer, M. Maskos, R. H. Stauber, W. Peukert and L. Treuel, *Langmuir* **28**, 9673 (2012).
11. I. Lynch and K. A. Dawson, *Nano Today* **3**, 40 (2008).
12. D. Whitford, *Proteins: Structure and Function* (John Wiley & Sons, England, 2005).
13. A. Shukla, E. Mylonas, E. Di Cola, S. Finet, P. Timmins, T. Narayanan and D. I. Svergun, *Proc. Natl. Acad. Sci. U.S.A.* **105**, 5075 (2008).
14. J. Israelachvili, *Intermolecular and Surface Forces* (Academic Press, London, 2011).
15. Y. Leng, *Materials Characterization: Introduction to Microscopic and Spectroscopic Methods* (John Wiley & Sons, Singapore, 2008).
16. R. Pecora, *Dynamic Light Scattering* (Plenum, New York, 1985).
17. J. S. Higgins and H. C. Benoit, *Polymers and Neutron Scattering* (Clarendon Press, 1994).

18. I. Yadav, S. Kumar, V. K. Aswal and J. Kohlbrecher, *Phys. Rev. E* **89**, 032304 (2014).
19. I. Yadav, V. K. Aswal and J. Kohlbrecher, *AIP Conf. Proc*. **1591**, 216 (2014).
20. H. N. W. Lekkerkerker and R. Tuinier, *Colloids and the Depletion Interaction* (Springer, New York, 2011).
21. I. Yadav, V. K. Aswal and J. Kohlbrecher, *Phys. Rev. E* **91**, 052306 (2015).
22. I. Yadav, V. K. Aswal and J. Kohlbrecher, *AIP Conf. Proc* **1665**, 040008 (2015).
23. I. Yadav, S. Kumar, V. K. Aswal and J. Kohlbrecher, *Langmuir* **33**, 1227 (2017).
24. I. Yadav, V. K. Aswal, and J. Kohlbrecher, *AIP Conf. Proc*. (2017).
25. I. Yadav, V. K. Aswal and J. Kohlbrecher, *Phys. Rev. E* **93**, 052601 (2016).
26. I. Yadav, V. K. Aswal and J. Kohlbrecher, *AIP Conf. Proc*. **1731**, 050093 (2016).

LIST OF FIGURES

LIST OF TABLES

Table 5.2. Fitted parameters of 5 wt % proteins (lysozyme and BSA) in D_2O at different pH. The K_1 and Z_1 are used as fitted parameters but kept constant as are expected not to change with pH.

Table 5.3. Fitted parameters of adsorption curves of lysozyme protein on 1 wt % HS40 silica nanoparticles at different pH. N_{mp} is Number of adsorbed lysozyme molecules per nanoparticle at saturation value (maximum equilibrium surface concentration).

Table 5.4. Fitted parameters of silica nanoparticles with lysozyme protein. (a) 1 wt % HS40 silica nanoparticles with varying concentration of lysozyme protein at pH9. The fitting is carried out using the 2Y potential for the systems having no aggregation or partial aggregation of nanoparticles. The parameters of repulsive interaction K_2 = 9.0 and Z_2 = 7.0 are kept fixed. (b) 1 wt % HS40 silica nanoparticles with 0.02 wt % lysozyme protein at different pH.

Table 5.5. Fitted parameters of silica nanoparticles with BSA protein. (a) 1 wt % HS40 silica nanoparticles with varying concentration of BSA protein at pH9. The parameters of repulsive interaction K_2 = 9.0 and Z_2 = 7.0 are kept fixed. (b) 1 wt % HS40 silica nanoparticles with 1 wt % of BSA protein at different pH values.

Table 6.1. Fitted parameters of 1 wt % of silica nanoparticles (SM30, HS40 and TM40) in D_2O at pH ≈ 7.

Table 6.2. Fitted parameters of adsorption curves of lysozyme protein on 1 wt % different sized silica nanoparticles at pH ≈ 7. N_p, N_s and PF are number of adsorbed lysozyme per nanoparticle, surface density of adsorbed lysozyme and packing fraction, respectively at saturation value.

Table 6.3. Fitted parameters of silica nanoparticles with lysozyme protein at pH ≈7. (a) 1 wt % TM40 with varying concentration of lysozyme protein. The parameters of repulsive interaction K_2 = 14.0, Z_2 = 11.0 are kept fixed. (b) 1 wt % different sized silica nanoparticles (SM30, HS40 and TM40) with lysozyme protein at their respective CPC values.

Table 6.4. Fitted parameters of silica nanoparticles with BSA protein at pH ≈7. (a) 1 wt % TM40 with varying concentration of BSA protein. The parameters of repulsive interaction K_2 = 14.0, Z_2 = 11.0 are kept fixed. (b) 1 wt % different sized silica nanoparticles (SM30, HS40 and TM40) with BSA protein at their respective CPC values.

Chapter 1

Introduction to Nanoparticles, Proteins and their Complexes

1.1. Introduction

Nanoparticles are particles in intermediate length scale (1-100 nm) of atoms/molecules and bulk materials. They possess remarkable and distinctive characteristics (e.g. high surface activity, quantum confinement, surface plasmon resonance, superparamagnetism etc.) from those of their constituent atoms/molecules and bulk materials [1-3]. These features are size-dependent and cover a wide range of phenomena that play an important role in the natural environment as well as in industrial and biomedical applications [4-7]. Many of these applications require the conjugation of nanoparticles with macromolecules such as proteins, polymers and surfactants [8-10]. In particular, nanoparticle-protein conjugates have applications in drug delivery, bio-sensing, bio-imaging and novel functional materials [11-14]. Figure 1.1 shows the schematic of nanoparticle-protein conjugate utilized in drug delivery, where because of their small sizes they can move in and out of the cell.

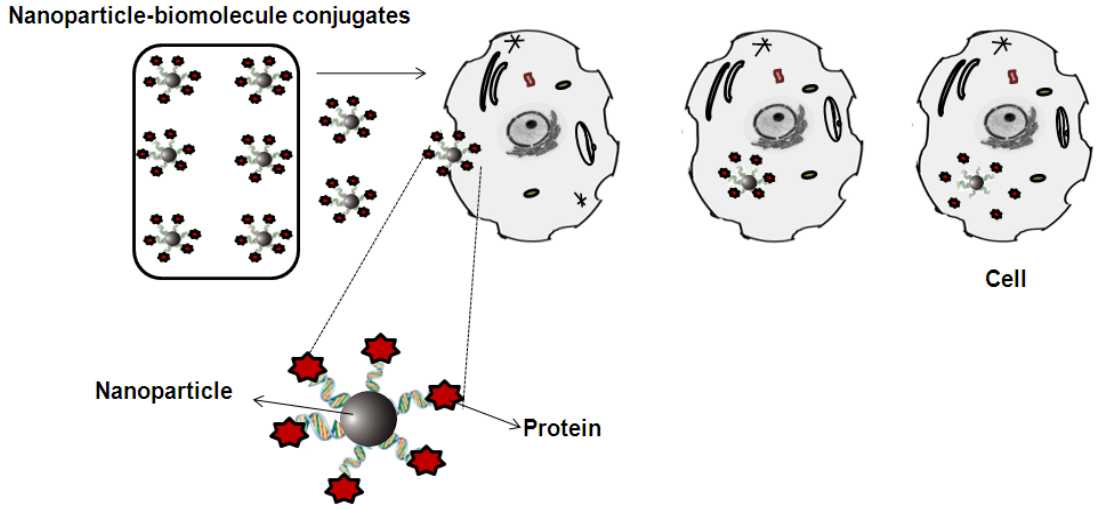

Figure 1.1. Schematic representation of a nanoparticle-protein conjugate for drug delivery application.

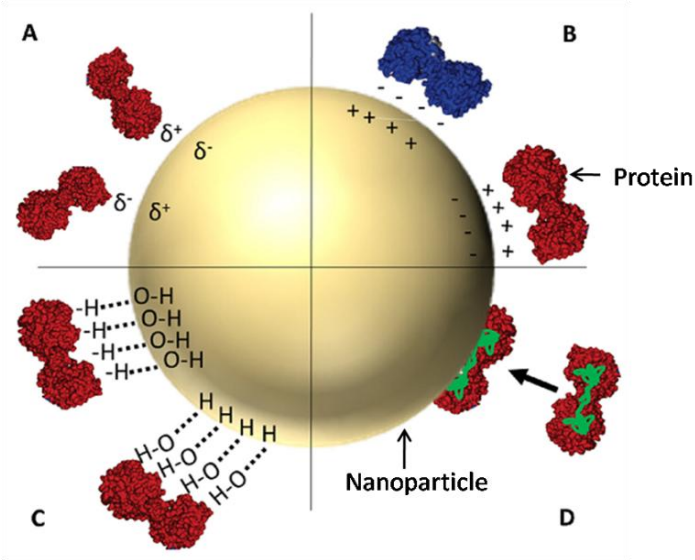

Figure 1.2. Schematic representation of nanoparticle-protein conjugation by different non-covalent interactions (A) van der Waals interaction, (B) electrostatic interaction, (C) hydrogen bonding and (D) hydrophobic interaction.

Proteins are the polymers of amino acids with a specific three-dimensional shape and charge on them and do most of the work in cells required for structure, function and regulation of body tissues and organs [15]. The conjugation of nanoparticles with proteins is usually done either by direct covalent linkage or by non-covalent interactions between the nanoparticles and proteins [16-19]. Conjugates formed through covalent attachment are irreversible and the resultant systems are highly stable. However, this method requires good command on organic synthesis. On the other hand, non-covalent interaction provides a complementary strategy to covalent attachment. There are different non-covalent interactions (e.g. van der Waals interaction, electrostatic interaction, hydrogen bonding and hydrophobic interaction) used to conjugate the nanoparticles with proteins (Figure 1.2) [20]. The most common way to produce non-covalent nanoparticle-protein conjugates is through electrostatic attraction between the nanoparticles and proteins. The conjugation in this case is often reversible and most importantly can be controlled by solution parameters such as ionic strength, pH, temperature and

concentration [21-23]. The characteristics of nanoparticles such as shape and size, surface charge density etc. also play important part [24]. The conjugation may result in conformational changes of proteins as well as affect the surface properties and colloidal stability of the nanoparticles [25, 26].

Characteristics of nanoparticle-protein conjugates depend on the interplay of nanoparticle-protein, nanoparticle-nanoparticle and protein-protein interactions [27]. These interactions in nanoparticle-protein complexes are derived from both DLVO (van der Waals attraction along with electrostatic double-layer repulsion) and non-DLVO (e.g. solvation, steric, hydrogen bonds, depletion and hydrophobic) interactions between the components [27, 28]. The role of these interactions has been investigated in this thesis. The studies are carried out from systems having both nanoparticle and protein charged, where their conjugation is tuned by choice of protein and varying solution conditions (ionic strength and pH) as well as size of the nanoparticles. A general introduction to nanoparticles and proteins, their possible interactions and applications is given in this chapter. The layout of the thesis is also provided in the end of the chapter.

1.2. Characteristics of nanoparticles

Both the natural and synthetic world contains a plenty of organic and inorganic nanoparticles. Based on the criterion of length scale, nanoparticles include small dust particles, aerosols, colloidal systems, metal and semiconductor particles, macromolecules and so on [29]. These structures can be composed of pure metal (e.g. Au, Ag, Cu, Pt etc.), semiconductor (e.g. GaAs, CdSe, CdS, ZnSe, etc.), oxides (e.g. SiO_2, TiO_2, ZnO, Al_2O_3, Fe_3O_4 etc.) and organic molecules such as polymers and amino acids [30]. Nanoparticles can be found in varieties of shapes and composition which include sphere, cube, triangle, rod, tube, needle, hollow sphere,

core-shell and alternative type. The extraordinary optical, electrical, chemical and magnetic properties of the nanoparticles emerge largely because of two effects, quantum confinement and surface atom effect [2, 30-33]. Quantum confinement can be observed in the nano size range, when the particle dimension is of the order of the de Broglie wavelength of the electron. A particle behaves as if it is confined in some potential well which otherwise feels free if the confining dimension is larger compared to its de Broglie wavelength. In confined state, electronic wave function is delocalized over the entire particle and the particle may be regarded as individual atom. On the other hand, the ratio of atoms at the surface to bulk increases sharply with decreasing the size of the particles [30-32]. Atoms at the surface are much more active because they have fewer bonding (coordination) number than bulk atoms. This effect is smoothly scalable as the number of atoms at the surface increases smoothly with decreasing size. On the contrary, quantum confinement shows discontinuous behavior due to completion of shells in systems with delocalized electrons. Some of the important properties of the nanoparticles which are the result of these two phenomena are discussed in the following.

1.2.1. Properties of nanoparticles

a. Optical properties: There are two important factors determining the optical behavior of the nanoparticles, quantum confinement and surface plasmon resonance (SPR) [5, 34]. The optical properties of the semiconductor nanoparticles are results of the discretization of energy spectrum due to quantum confinement of electron [4]. The confinement of electron induces the quantization of the electronic energy level and band gap energy level. Smaller the size of the nanoparticle bigger will be the band gap as a result the optical absorption of light can be tuned simply by change in nanoparticle size. The semiconductor particles show blue shift in the light absorption with reduction in size as the band gap is increased. The famous example of this is

quantum dots [35]. In case of the noble metals, nanoparticles optical property is mainly governed by SPR [36-38]. For these nanoparticles the conduction band electrons begin to polarize to one side of the surface by action of incident electric field of the electromagnetic wave. These electrons start to oscillate from one side of the surface of the nanoparticles to other side as the wave changes its polarity. When the frequency of the incoming wave and frequency of electron oscillation become comparable absorption of wave become very strong and this phenomenon is referred as SPR. It is highly sensitive to the free electron density, shape and size of the nanoparticles as well as dielectric constant of the surrounding medium. The brilliant colors of gold nanoparticles, the possibility of tuning these colors with varying size, shape or via adsorption of macromolecules on nanoparticle surface are due to the surface plasmon effect.

b. Electronic properties: Conducting nature of electrons of solids in bulk depends on the energy gap (δ) between valance band (which is completely filled by electrons) and conduction band (which is empty). Based on the value of δ, solids are classified as metals (δ ~ 0), semiconductors (δ ~ 1eV) and insulators (δ ~ 10 eV) [39, 40]. In nanometer size range, the band structure of bulk material can no more be observed as quasi continuous, instead has to be replaced by quantum mechanical levels (Figure 1.3) [31]. Both the density of states and band gap change with size of the particles. Single nanoparticle display an electronic structure that corresponds to an intermediate electronic structure between the band structure of the bulk and the discrete energy levels of molecules with characteristic highest occupied molecular orbital (HOMO) and lowest unoccupied molecular orbital (LUMO). As the band gap increases with reduction in nanoparticle size the electronic properties of nanoparticles are also changes. For example, the conductive properties of noble metal (gold, platinum, silver etc.) nanoparticles transits from metallic to

semiconductor to insulator with decreasing the size of the nanoparticle. However, the critical size at which transition occurs depends on the nature of the material.

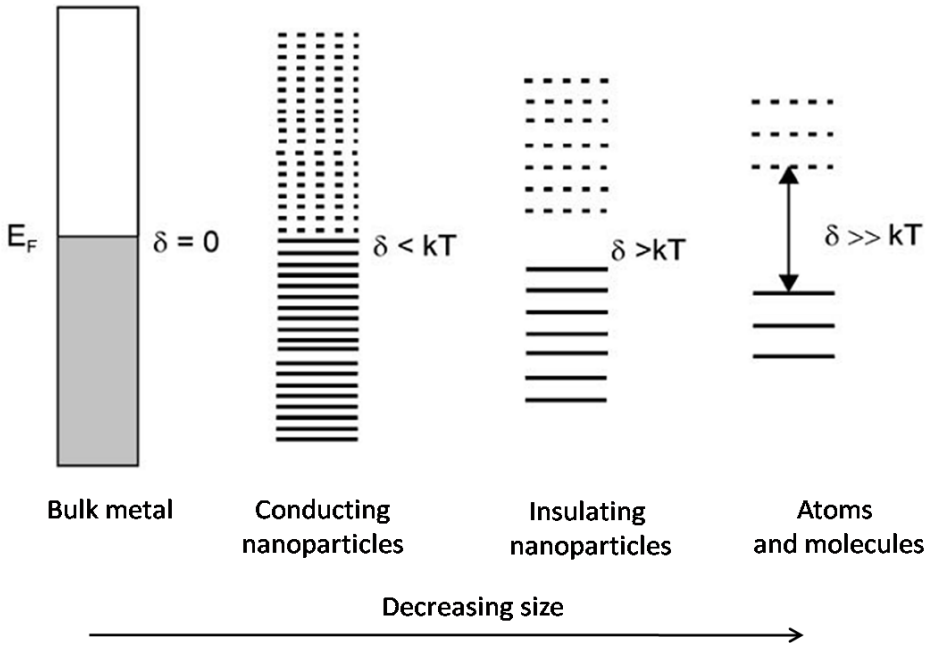

Figure 1.3. Evolution of the band gap and the density of states with decreasing particle size.

c. Magnetic properties: One of the fascinating properties of magnetic nanoparticles is the reduction from multi-domains to a single domain as the particle size reduces to some limit values depending on the material [41-43]. In such nanoparticles, magnetization can randomly flip direction due to thermal agitation. As a result, nanoparticle equivalent to single domain behave like super spins and show superparamagnetism where ferromagnetic/ferrimagnetic particles become paramagnetic. The uncompensated surface spins at nanoscale leads to high magnetic moment even for small clusters of non-magnetic materials like Pd, Au and Pt [31]. The coercively and saturation magnetization increases with decrease in particle size. A maximum coercive field is attained for the maximum size of a nanocluster that is of single magnetic domain.

d. Surface properties: The total surface area per unit mass/volume increases sharply with decreasing the size of the particles [30, 31, 44]. As a result, the fraction of atoms at the surface increases rapidly with decreasing the particles size (Figure 1.4). Atoms at the surface are highly active due to more uncompleted bonds concomitantly they provide chemically more reactive surface that might enhance the catalytic property manyfold compared to their bulk analogues. The surface on the nanoparticles is easy to functionalize due to high surface energy and provides routes for properties modulation. Versatility in the anchoring of biological ligands, organic functional groups, drugs, polymers, surfactants and proteins on the nanoparticle surface provide better spectrum for many biological applications [45-47].

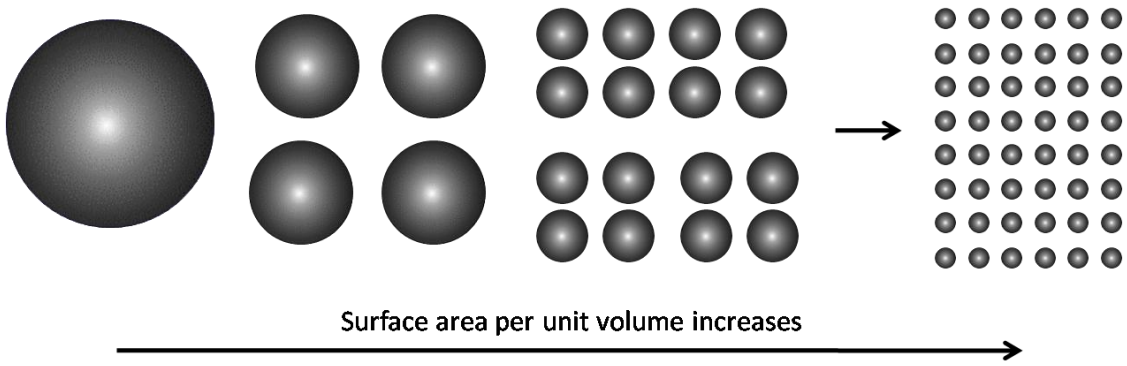

Figure 1.4. Schematic representation of surface area effect of the nanoparticles.

e. Thermodynamic properties: The boiling and melting temperatures of the nanoparticles are found to be lower than their bulk counterpart and it decreases with reducing nanoparticle size [2, 5, 31]. The lowering of boiling/melting points is in general explained by the fact that the surface energy increases with decreasing the size. The thermal conductivity of the nanoparticles is also increases with decreasing the size. Also the nanoparticles show an intrinsic thermodynamic self-purification where any heat treatment increases the diffusion of impurities towards the nanoparticle surface causing a relatively increased perfection within the volume.

Such purification has appreciable impact on other chemical and physical properties of the material.

1.2.2. Synthesis of nanoparticles

Nature exploits self-organization in many ways to produce nanostructures such as protein, DNA and viruses. Mankind is now able to design materials at the nanoscale, whether through slicing or successive cutting of a bulk material to get nano sized particles (top-down) or through self-organization (bottom-up) (Figure 1.5) [30, 48, 49]. The main focus in nanoparticles synthesis is to have a good control over shapes, sizes, and size distribution.

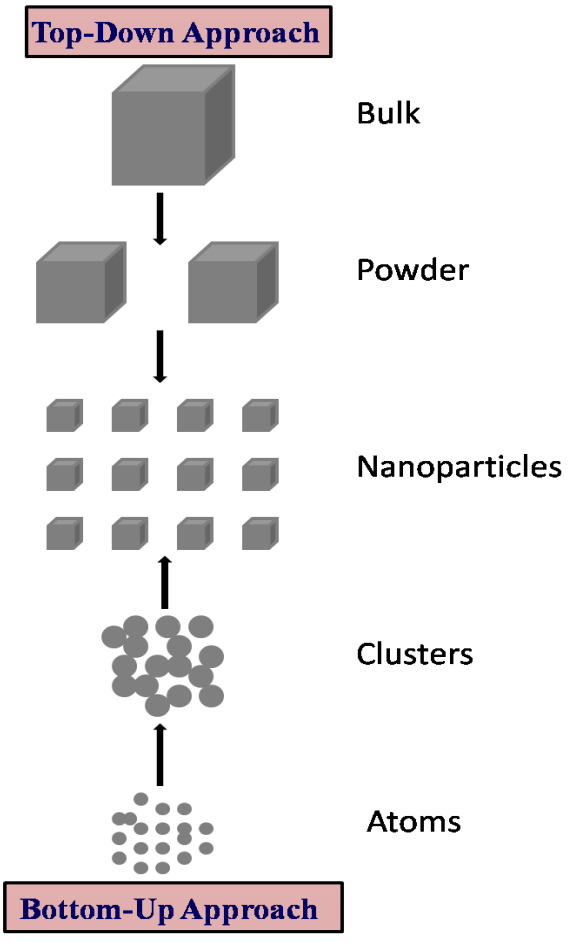

Figure 1.5. Schematic representation of the synthesis approaches of the nanoparticles.

The top-down approach relies on removal/break-up of bulk materials by applying external forces to make nanoparticles. By employing the physical, mechanical and chemical means the desired size and shape are obtained where most commonly used methods are machining, milling and lithography (e.g. optical laser and electron-beam lithography). Often these methods are destructive and can cause significant crystallographic damage to the resultant structures. Surface imperfections are more pronounced in top-down approaches and have less control over the size distribution. T**he bottom-up** approach, on the other hand, starts with individual building units that are the constituents of the nanoparticles. It is a controlled additive process, where atoms/molecules are used as the building blocks for creation of the nanoparticles. This is a highly controlled process where nanoparticles obtained by this method have less defects and more homogenous chemical compositions as well as controlled size distribution. The vapour phase deposition, sol-gel and chemical reduction methods are commonly used bottom-up approaches. Thus with lots of advantages the bottom-up approach is the most common route for production of the nanoparticles along with other nanomaterials.

In this thesis, spherical silica nanoparticles are used as model nanoparticles. Owing to high chemical and thermal stabilities, good compatibilities with other materials, low toxicity and ability to functionalize with a range of macromolecules silica nanoparticles occupy a prominent place in scientific research [50-52]. These nanoparticles have a lot of applications in catalysis, pigments, pharmacy, electronic and thin film substrates etc. Silica nanoparticles are usually electrostatically stabilized suspensions of fine amorphous, nonporous, and typically spherical particles in aqueous phase. Mostly, silica nanoparticles are synthesized in two ways: chemical vapor condensation method and sol-gel process. In former method, silica nanoparticles

are produced through high temperature flame decomposition of precursors such as silicon tetra chloride ($SiCl_4$) with hydrogen and oxygen. Though, this method has limitations like difficulties in controlling the particle size, morphology, and phase composition but is efficiently used for commercial synthesis of silica nanoparticles in powder form. The later process (sol-gel) is a multi-step process where hydrolysis and condensation of metal alkoxides [$Si(OR)_4$] such as tetraethylorthosilicate [TEOS, $Si(OC_2H_5)_4$] or inorganic salts such as sodium silicate [Na_2SiO_3] is carried out in the presence of mineral acid (e.g. HCl) or base (e.g. NH_3) as catalyst. The hydrolysis of silicon compound (TEOS) molecules forms silanol groups. The condensation/polymerization between the silanol groups creates siloxane bridges (Si-O-Si) that form entire silica structure in colloidal form. A general flow chart summarizing the silica nanoparticle synthesis by sol-gel process using silicon alkoxides [$Si(OR)_4$] is shown in Figure 1.6(a) [53]. In aqueous solution, the hydrogen ions from the surface of colloidal silica tend to dissociate, yielding an overall high negative charge [Figure 1.6(b)]. Because of the very small size, the surface charge density becomes high. The colloidal suspension is first stabilized by adjusting the pH of the solution and then concentrated, usually by evaporation. The maximum concentration obtainable depends on the particle size, such as 50 nm particles can be concentrated to greater than 50 wt % solids, while 10 nm particles can only be concentrated to approximately 30 wt % solids, before the suspension becomes unstable. The Ludox HS40, TM40 and SM30 silica nanoparticles used in this thesis have concentration of 40 wt %, 40 wt % and 30 wt %, respectively. These nanoparticles are concentrated amorphous, non-porus electrostatically stabilized solid suspensions of silica nanoparticles synthesized by sol-gel process.

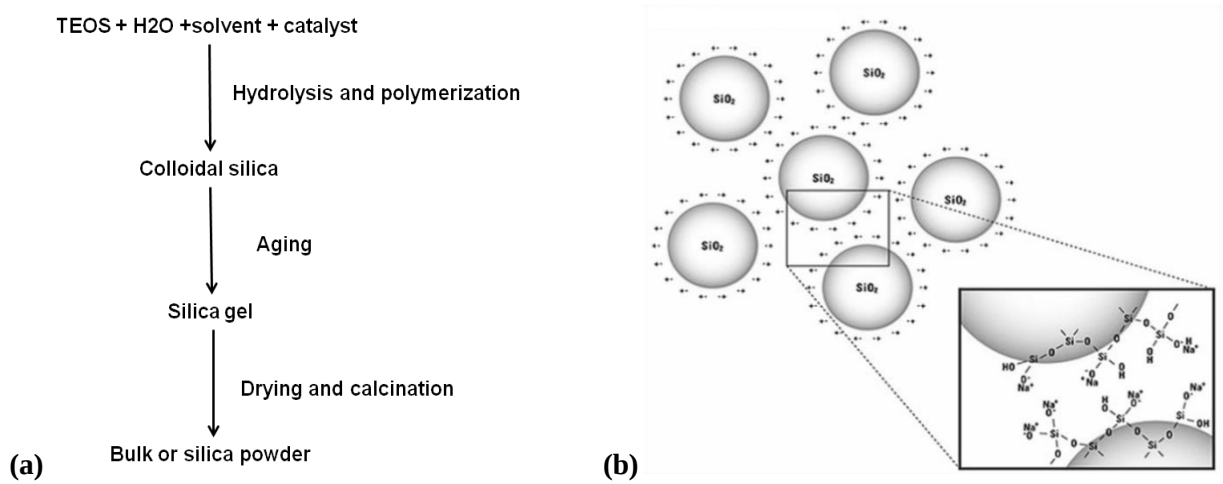

Figure 1.6. (a) A typical sol-gel process for synthesis of colloidal silica nanoparticles and (b) schematic of charged stabilized silica nanoparticles.

1.2.3. Applications of nanoparticles

Due to variety of unique properties and their easy tunability, nanoparticles have a wide range of applications. This includes the direct applications of the nanoparticles with minor modifications in surface, size and shape and applications of nanoparticles with major fabrications [2, 30, 33, 54]. Each unique property of the nanoparticles is utilized in these applications. For example, the optical properties of nanoparticles are used in photonics, solar cell and sensor applications [55-58]. The unique electronic properties of nanoparticles result in applications under the field of nanoelectronics etc [59]. The superparamagnetism property of magnetic nanoparticles has applications in memory devices, batteries, magnetic resonance imaging (MRI) etc [60, 61]. The catalytic properties of nanoparticles are utilized in improving the reaction rates for various chemical reactions [62, 63]. The enhanced mechanical properties of nanoparticles result in application in formation of high tensile materials such as scratch resistance materials, cutting tools, aircraft components that require high fatigue strength and textile fibers [64, 65]. The unique thermodynamic properties of nanoparticles are utilized in applications like

generating nanometric heat sources, probing local temperature variations and treating cancer through photo-thermal therapy [3].

In fabricated/conjugated form the nanoparticles with different macromolecules results in synergistically improved system properties as compared to individual components [66, 67]. For example, nanoparticle-polymer composites have attracted attention for engineering flexible materials with improved sustainability and multi-functionality [68]. Nanoparticle interaction with surfactant gives enhanced colloidal stability having applications in detergent industry, cosmetic industry and design of functional materials [69, 70]. Nanoparticles interaction with proteins enhances the biocompatibility of the nanoparticles, which enables them to be used in the areas of nanobiotechnology and drug delivery [71, 72].

1.3. Structure of proteins

Proteins are found in all living systems from bacteria and viruses to complex mammals such as human. Life may be defined as the ordered interaction of proteins, where proteins underpin every aspect of biological activity [15]. Diverse biological function of proteins includes transporting oxygen around the bodies of multi-cellular organisms to converting one molecule into another, forming cytoskeleton structures, DNA replication, function and regulation of body tissues and organs. Proteins come in various sizes and shapes and the function of all proteins depends on their ability to specifically interact with other biological entities. Accordingly, each kind of protein evolved to interact with a specific molecule or ligand. For example, a class of proteins combines with RNA to form the ribonucleoprotein complex known as the ribosome. Another class of proteins (e.g. hemoglobin) binds to specific ligands (in this case oxygen) and transports the ligand to a site where it is needed. Regulatory proteins interact with nucleic acids

or with other proteins to speed up or slow down some crucial biological processes. It is the shape and charge of protein which is essential for controlling and regulating the stability and biological functionality of proteins. These molecules in aqueous solution are known to undergo different interactions (electrostatic, hydrophobic, hydrogen bonding, van der Waals, etc.)[73, 74]. The interplay of these interactions controls the structure of proteins as well as their stability.

1.3.1. Different structures of proteins

Despite enormous functional diversity all proteins consist of a linear arrangement of twenty different amino acid residues assembled together into a polypeptide chain. Each amino acid consists of a central carbon atom C_α attached to an amine ($-NH_2$), a carboxyl group (-COOH), an alkyl group (R) and a hydrogen atom (-H). These twenty amino acids differ in the type of alkyl group (R) attached to the amino acids [15, 75]. The R group is responsible for the different physical properties (e.g. size, shape, charge, polarity, hydrophobicity and aromaticity) of individual amino acids. The polar amino acids have an oxygen or nitrogen atom in their side chain (R-group) that can participate in hydrogen bonding within a protein or with the solvent molecules. These amino acids tend to form hydrogen bond with the solvent molecules and thus preferentially arrange themselves on the surface of protein. The hydrophobic amino acids are mostly comprised of carbon atoms and hydrogen atoms in their side chains. These amino acids avoid the surface exposure and tend to sequester themselves in the interior of protein. There are aromatic amino acids with aromatic hydrocarbon ring in their R group. These amino acids are joined together by peptide bonds to form polypeptide chain of protein. The folding of polypeptide chain of amino acids results in three dimensional structure of protein. The three dimensional structure of protein is described by the four level of organization as primary, secondary, tertiary and quaternary structure (Figure 1.7).

Primary structure: The primary structure of a protein is the linear arrangement of the amino acid residues via peptide bonds and an average sized protein may contain 1000 peptide bonds. The peptide bond is the covalent bond associating the carboxylic acid of the previous amino acid to the amino group of the next amino acid. Thus the primary structure gives the information about the sequence of amino acids attached in the polypeptide chain of a protein. This sequence is unique to a protein and is always given starting from amino or N-terminal and ending with carboxyl or C-terminal. This N to C is the order in which amino acids are added during the synthesis of proteins within the cell on the ribosome.

Secondary structure: The local conformation of the polypeptide chain or the spatial relationship of amino acid residues leads the formation of secondary structure. The secondary structure is stabilized by the hydrogen bond formation between the atoms of the amino acid backbones of the polypeptide chain. The two most common secondary structures are α-helix and β-plated sheet. The α-helix is the structural motif in proteins and over 30 % of residues are found in helices for globular proteins. Atoms in α-helix arrange themselves in a helical pattern which has about 3.6 residues per turn and each residue offset from the proceeding residue by 0.15 nm. The hydrogen bond occurs in the peptide carboxyl oxygen of one residue and peptide amide nitrogen of a residue four places ahead in polypeptide chain. The hydrogen bonds from oxygen to nitrogen atoms are linear and parallel to the axis of α-helix. In α-helix structure the first four NH groups and last four CO groups normally lack backbone hydrogen bonds. This lack of hydrogen bonds results in distortion of α-helix structure for shorter polypeptide chain of amino acids.

The β-sheet is the second unit of secondary structure. It is an extremely elongated form of helical arrangement with two residues per turn and a translation distance of 0.34 nm between

similar atoms in neighboring residues. These β-sheets are stabilized by backbone hydrogen bonds between adjacent residues from adjacent sheets that may be widely separated in the primary sequence.

Tertiary structure: The tertiary structure can be defined as the spatial three dimensional arrangements of amino acid residues in a protein. The tertiary structure represents the folding of secondary structure elements in a compact unit arising from linking of different secondary structures. The different elements of secondary structure interact via hydrogen bonds, disulfide bridges, electrostatic interactions, van der Waals interactions, hydrophobic interactions etc. Many proteins consist of several domains, which are often connected only by a single segment of polypeptide chain. The proteins folded state is known to be marginal stable over the unfolded state and the differences in stability are governed by non-covalent interactions governing the protein folding.

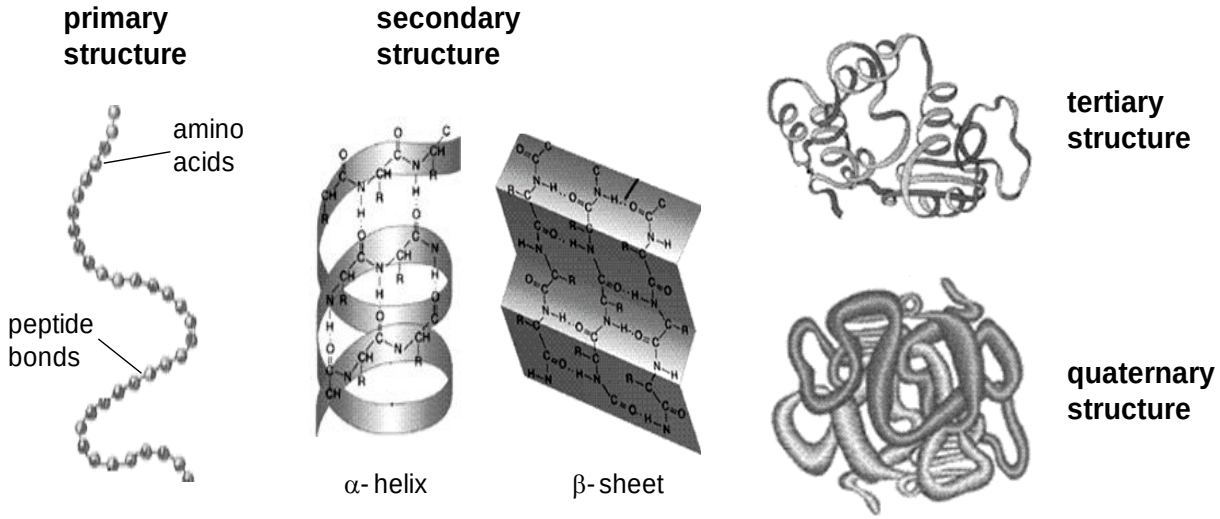

Figure 1.7. Different levels of protein structures.

Quaternary structure: Many proteins contain more than one polypeptide chain and interaction between these chains underscores quaternary structure. The condition arises for proteins with number of amino acids larger than 150 residues. The different tertiary structures of polypeptide chains are called domains. The nature of interactions (hydrogen bonds, disulfide bridges, electrostatic interactions, van der Waals interactions, hydrophobic interactions) among different domains of protein is same as those within a single domain.

1.3.2. Classification of proteins

Based on the three-dimensional structure and their physical properties, proteins have been divided into three classes globular, fibrous and membrane proteins.

a. Globular proteins: Globular proteins have an axial ratio (length/width) usually not over three or four and henceforth possess more or less spherical shape. These proteins are usually soluble in water or in aqueous media containing acids, bases, salts or alcohol owing to dipole-dipole interaction as the polar groups of atoms reside on the protein's surface [76]. The water solubility of globular proteins allows them to exist in biological fluids as individual molecules or in small clusters and to accomplish a wide range of functions, also these proteins are dynamic rather than static in their activities. Some important functions of these proteins include as enzymes, hormones, blood transportation, antibodies and nutrient storage. Some of the examples of globular proteins are lysozyme, myoglobin, hemoglobin, serum albumin, lactoglobulin and ovalbumin etc.

b. Fibrous proteins: Fibrous proteins were named so because they are the constituents of most of the fibers found in the body. These proteins generally form elongated structures and interactions are confined to local residues only. They are generally water insoluble and are found

as an aggregate due to hydrophobic groups of amino acids that stick out of the molecule. These proteins have a common role in conferring strength and rigidity to these structures as well as physically holding them together. Three major groups of fibrous proteins are the collagens, keratins and silk fibroins.

c. Membrane proteins: The membrane proteins are proteins that are attached or associated with the membrane of a cell or an organelle. These proteins are difficult to isolate from the embedded lipid bilayers and are classified in two groups based on their strength of association with the lipid bilayers. Integral membrane proteins are the proteins remain firmly embedded within the hydrophobic bilayer and removal from this environment frequently results in a loss of structure and function. On the other hand, peripheral membrane proteins are temporarily attached either to the lipid bilayer or to integral proteins by a combination of hydrophobic, electrostatic and other non-covalent interactions. Peripheral proteins dissociate on treatment with a polar reagent.

Two globular proteins-lysozyme and bovine serum albumin (BSA) have been used in this thesis. Lysozyme is an antibacterial enzyme found in tears, saliva, human milk, and mucus. Large amounts of lysozyme can be found in egg white. It has a molecular weight of 14.7 kDa and contains 129 amino acids which folds into a compact globular structure. The isoelectric point is about pH 11. Protein BSA functions biologically as a carrier for fatty acids, anions and other simple amphiphiles in the bloodstream. It has a molecular weight of 66.4 kDa and consists of 583 amino acids in a single polypeptide chain. The isoelectric point is about pH 4.7. The tertiary structure of BSA comprises three very similar domains. Figure 1.8 presents the structure of a lysozyme and BSA proteins molecule.

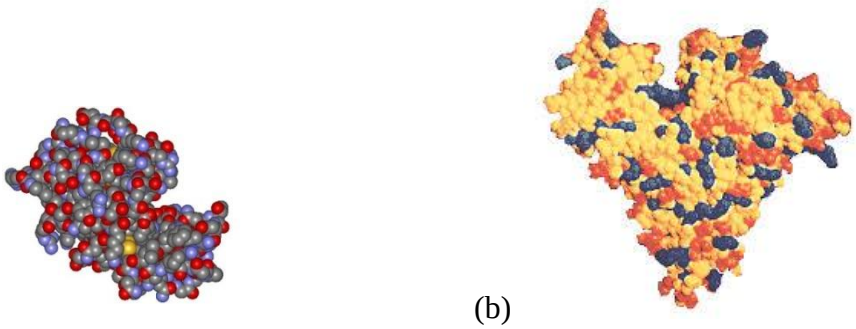

(a) (b)

Figure 1.8. Structure of a (a) lysozyme and (b) BSA proteins molecule.

1.3.3. Stability of proteins

The native conformation of a protein is controlled by the shape complementarity of the hydrophobic residues that leads close packing of the cores. Moreover, except the primary structure which is stabilized by covalent and peptide bonds, the higher levels of structures (secondary, tertiary and quaternary) are stabilized by relatively weak non-covalent interactions and disulphide bridges [75, 76]. As a result, proteins are marginally stable thus interaction with a surface can easily disrupt the native conformation and therefore the proteins function [25, 77, 78]. This has implications for the biological impact of the nanoparticles.

Although for many purposes a detailed atomistic description of protein structure is an essential part of the answer. However, many functional behaviors of proteins can be understood by coarse-grained (ignoring enough details until similarities begin to emerge) modeling [79]. In these models, protein molecules can be represented by individual particles and by their very size proteins also possess colloidal characteristics. The protein solutions are stabilized by the repulsive (electrostatic and/or steric) interactions overcoming the attractive (van der Waals and/or hydrophobic interaction) interactions between protein molecules [28, 80-82]. The various solution conditions (e.g. ionic strength, pH, temperature etc.) are often used for tuning the interactions and hence the stability of protein solutions.

1.4. Interest in nanoparticle-protein complexes

The study of the interaction of the nanoparticles with proteins has attracted considerable attention recently, evoked in part by the practical importance of their conjugates and in part to understand their complex interaction mechanism [25, 27, 83, 84]. Interactions of the nanoparticles with proteins can control protein-protein interactions, enzymatic activity, and protein delivery and can be applied to diagnostics and sensors [11, 45, 85, 86]. For their part, proteins may induce the phase transformations of the nanoparticles, for instance, glass transition, gelation, crystallization, and flocculation, which could be used to prepare multifunctional materials [14, 87-89]. There is a strong propensity of proteins to adsorb on the nanoparticles due to the high surface-to-volume ratio of the nanoparticles concomitantly form a corona which determines the biological response of the nanoparticles [25, 71]. Therefore, much research has been devoted to understand the fundamentals of protein adsorption [90-95]. A key aspect of the adsorption of proteins onto nanoparticles is that it can affect the biophysical properties of the nanoparticles often differ significantly from those of the bare nanoparticles [25, 96]. Studies show that the interaction of the nanoparticles can disrupt the native conformation of protein and therefore functional impact [18, 21, 25, 97-99]. The conformational changes in proteins are highly related to the size of the nanoparticles where larger particles with a smaller curvature gave a stronger impact [98]. Perturbation in protein structure also depends on the pH of the solution where pH approaching towards the IEP of proteins provides better stability [21]. This has been correlated to the intensity of protein interaction with the nanoparticles which increases as the surface contact area and/or surface charge increases [21, 98]. However, this may not be the universal phenomena as depends on the surface coating and protein identity as well [100].

On the other hand, it is also possible that the interaction of proteins can affect the surface properties and colloidal stability of the nanoparticles [26].

1.4.1. Role of different interactions

The interactions between the nanoparticles and proteins follow those are known between colloidal particles [28]. The important interactions governing the phase behavior of the colloidal systems are van der Waals attraction, electrostatic attraction or repulsion, steric repulsion, hydrogen bonding, depletion and hydrophobic interactions [101].

a. van der Waals interaction: The van der Waals interaction is a weak short-range interaction between atoms or molecules caused by their dipole moments, arising from transient shift of orbital electrons to one side of atom or molecule [101]. They differ from covalent and ionic bonding in that they are caused by correlations in the fluctuating polarizations of nearby particles and play a vital role in range of phenomena such as physical adsorption, wetting, adhesion, surface tension, the flocculation of particles in liquids and the structures of condensed macromolecules such as proteins and polymers. The van der Waals interaction between two colloidal particles is summation of all atomic contributions. The nature of interaction between similar particles is always attractive, while that between dissimilar particles can be attractive or repulsive. The later occurs whenever the dielectric constant of the intervening medium is intermediate between those of the two interacting particles. The strength of interaction is determined by the dielectric properties of the colloidal particles and the solvent. For two identical colloidal spheres with diameter σ, the dispersion-van der Waals interaction potential is given by [101, 102].

$$\frac{V_{VDW}(x)}{k_B T} = -\frac{A}{12}\left[\frac{1}{x^2-1} + \frac{1}{x^2} + 2\ln\left(1-\frac{1}{x^2}\right)\right] \qquad (1.1)$$

where A is the Hamaker constant (in units of k_BT, k_B is the Boltzmann constant and T is the absolute temperature) that depends on the material properties and x (>1) is the ratio of center-to-center distance of spheres (r) to the diameter (σ) of the sphere.

b. Electrostatic interaction: One of the common ways to stabilize the colloids against van der Waals attraction is through the charge on the particles [101-104]. Irrespective of the charging mechanism, the final surface charge is balanced by an equal but oppositely charged region of counter ions. Some of the counterions are strongly bound to the surface while others form an atmosphere of ions in rapid thermal motion close to the surface, known as the diffuse electric double-layer. When the double layer of two particles overlap a repulsive pair potential develops and hence particles repel each other upon approach due to screen coulomb repulsion. For two spheres of diameter σ each having a charge q (expressed in units of the elementary charge) separated by a center-to-center distance r in a fluid of dielectric constant ε containing a concentration n of monovalent ions, the electrostatic interaction is expressed as

$$\frac{V_{SC}(x)}{k_BT} = \frac{q^2\lambda_B}{\sigma\left[1+\frac{\kappa\sigma}{2}\right]^2}\frac{\exp\left[-\kappa\left(x-1\right)\right]}{x} \tag{1.2}$$

where λ_B is the Bjerrum length and is given by $\lambda_B = \frac{e^2}{4\pi\varepsilon\varepsilon_0 k_BT}$ denoting the distance between two elementary charges at which the electrostatic interaction is equal to the magnitude of thermal energy k_BT. κ^{-1} is the Debye-Hückel screening length, which is expressed by $\kappa^2 = 4\pi\lambda_B n$. The strength of the force increases with the magnitude of the surface charge density or the electrical surface potential whereas range of the interaction is decided by the ionic strength of the solution.

A combination of van der Waals attraction and electrostatic repulsion can explain the stability and the phase behavior of charged colloidal systems. This combination is known as the Derjaguin-Landau-Verwey-Overbeek (DLVO) theory [104, 105]. Thus the total potential for charged colloidal system according to DLVO theory is given as

$$V_{DLVO}(x) = V_{VDW}(x) + V_{SC}(x) \tag{1.3}$$

Figure 1.9 shows the typical variation of the total interaction energy with particle separation according to DLVO theory. If the height of the barrier in DLVO potential is more that the thermal energy the colloidal system will remain stable due to electrostatic repulsion between the particles. The height of the barrier is highly sensitive to ionic strength and decreases with increasing the ionic strength [102].

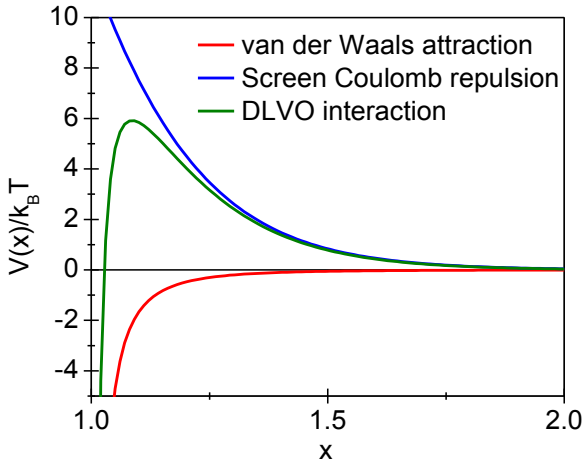

Figure 1.9. The schematic variation of van der Waals attractive and electrostatic repulsive interactions along with total (DLVO) interaction potential in a charged colloidal solution.

c. Steric repulsion: The stabilization of colloids by electrostatic repulsion does not work in high electrolyte concentration or in non-aqueous media. In that situation the stability of colloids can also be achieved by decorating the particles surface with macromolecules and it is called steric stabilization [101, 107, 108]. The adhesion of macromolecules such as polymer, surfactant etc. on particle surface prevents the approach of the particle cores to a separation where their mutual

van der Waals attraction would cause flocculation. The origin of steric repulsion lie in both volume restriction and interpenetration effects, although it is unlikely that either effect would occur in isolation to provide a repulsive force. The two polymer covered surfaces when approach (separation distance is less than R_g) each other feels a repulsive interaction due to the overlap of the outer segments formed by polymer shells. This repulsion results from the unfavorable entropy associated to the confinement of the polymer chains. The magnitude of the repulsion resulting from steric forces depends on the surface area of the particle occupied by the polymer and whether the polymer is reversibly or irreversibly attached to the particle's surface.

d. Bridging and depletion interactions: The adsorption of macromolecules on colloidal particles either can stabilize the colloids by steric repulsion or can leads to bridging attraction between particles as it can simultaneously attach to two neighboring colloidal particles [22, 23, 109-114]. There are two types of bridging forces, specific and nonspecific or chemisorbed and physisorbed. Specific bridging force involves end-functionalized binding groups or ligands attached to the ends of a macromolecule. Physisorbed (nonspecific) bridging may involve all segments of macromolecules where one side of a macromolecule may stick to a colloidal particle and the other side may stick to another one to bridge the particles. This is depicted in Figure 1.9 (a). On the other hand, the nonadsorption of macromolecules usually induces depletion interaction between particles.

The depletion interaction is known to arise between large colloidal particles that are suspended in a solution of smaller entities such as polymers, when the latter experience an excluded volume interaction with the former [103]. The first successful model to describe the depletion interaction between two hard spheres as induced by dilute non-adsorbing polymer was developed by Asakura and Oosawa [115]. According to their theory, the mechanism that is responsible for the attraction originates from the non-adsorbing nature of the smaller particles

(depletants) giving rise to a depletion layer around colloidal particles. This depletion layer can be understood as a layer around the bigger particle where smaller particle cannot be found [Figure 1.9 (b)]. The available volume for the smaller particles increases when the depletion layers overlap. It implies that the free energy of the smaller particles is minimized in the states for which the colloidal spheres are close together. The effect of this is just as if there were an attractive force between the spheres even while the direct colloid-colloid and colloid-polymer interactions may both be repulsive. The depletion interaction is purely entropic in nature and manifestation of the second law of thermodynamics. The gain in translational entropy of the smaller particles, owing to the increased available volume, is much greater than the loss of entropy from flocculation of the colloids results into the overall positive change in entropy. Depletion interaction leads to a variety of phase transitions in multi-component systems. For example, interesting phase transitions like vesicle-to-micelle transition of block copolymers, colloidal aggregation through macromolecules, and re-entrant solidification in colloid-polymer systems are driven by depletion interaction [116, 117].

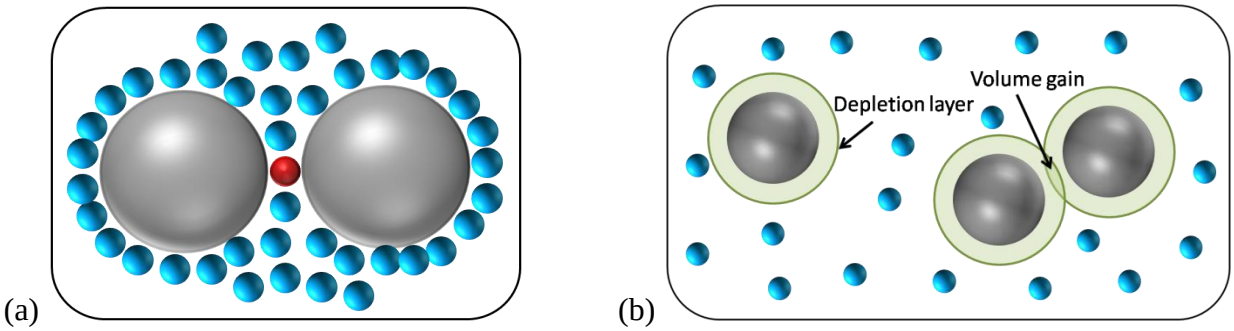

Figure 1.10. Schematic representation of (a) bridging and (b) depletion attraction. For bridging attraction, one side of a small particle may stick to a big particle and the other side may stick to another one to bridge the big particles. The bridging particle is shown in red. For depletion attraction, the big particles become closer to each other because of the excluded volume effect of the small particles.

e. Hydrogen bonding: The hydrogen bonding is a weak type of dipole-dipole attraction which occurs when a hydrogen atom bonded to a strongly electronegative atom such as nitrogen, oxygen, fluorine etc. exists in the vicinity of another electronegative atom with a lone pair of electrons [101, 118]. The electronegative atom (bonded with hydrogen) attracts the electron cloud from around the hydrogen nucleus and by decentralizing the cloud, leaves a partial positive charge on hydrogen atom while creates a small negative charge on itself. The resulting charge on hydrogen atom, however only partial, represents a large charge density because of the small size of hydrogen relative to other atoms. A hydrogen bond arises when this strong positive charge attracts a lone pair of electrons on another electronegative atom. These hydrogen-bond attractions can occur between different molecules (intermolecular) or within different parts of a single molecule (intramolecular). The strength of the hydrogen bond is relatively stronger than a van der Waals interaction, but weaker than covalent or ionic bonds. The unique and novel characteristics of water arise because of its hydrogen bonded structure. Hydrogen bonding determines the secondary and tertiary structures of proteins and functions of many biological molecules like DNA, lipids and proteins.

f. Hydrophobic interaction: Hydrophobic interactions describe the relations between water and non-polar molecules (hydrophobes) [101, 119]. The water molecules have high inclination to form hydrogen bonds with each other and this tendency influences their interactions with non-polar molecules which are incapable of forming the hydrogen bonds. The presence of such a non-polar surface into water causes interruption in the hydrogen bonding network between water molecules. The hydrogen bonds thus reorients tangentially to such surface to minimize disruption of three dimensional networks of water molecules leading to a structured water cage around the non-polar surface. As a result, the non-polar molecules experience an effective

attraction leading to their aggregation in order to reduce the surface area exposed to water to minimize their disruptive effect. Hydrophobic interaction plays vital role in understanding surface phenomena which depend on the properties of the non-polar solute as well as solution conditions. Hydrophobic interaction governs many processes occurring in macromolecules such as micelle formation, protein conformation and biological membrane structure. The amphiphilic molecules form self-assembled structures because of hydrophobic interaction. Along with hydrogen bonding, the hydrophobic forces also contribute in the formation of folded protein structure. The protein molecules while interacting with nanoparticles are reported to show the conformational changes possibly due to alteration in hydrophobic interactions.

All or some of the above interactions may act in nanoparticle-protein systems in a cumulative manner. The dominance of a particular interaction depends on the intrinsic characteristics (e.g. size, shape, charge, hydrophobicity or hydrophilicity) of the nanoparticles and proteins [27, 113]. Furthermore, the strength and range of these interactions ascertain the macroscopic properties of the resultant systems and can be easily tuned by varying the solution parameters such as ionic strength, pH, temperature and concentration [21, 28, 120-122]. The well-known DLVO theory combining attractive van der Waals and repulsive electrostatic double-layer interactions has been widely used to describe the equilibrium phase behavior of the charged colloidal systems [106]. However, in the case of nanoparticle-protein complexes, non-DLVO interactions such as depletion, steric, and solvation forces need to be taken into account [27, 123]. For example, selective adsorption of proteins can enhance colloidal stability by steric repulsion, whereas depletion-induced aggregation of the nanoparticles occurs for non-adsorbing proteins [26, 120]. In addition to this, the asymmetric distribution of charges and the presence of hydrophobic patches on protein molecules are also known to influence their interactions with the

nanoparticles [124]. In many cases, the interaction of proteins with hydrophilic surfaces has been attributed to the electrostatic interaction, where proteins strongly adsorb on the oppositely charged surfaces [22, 23, 125]. On the other hand, even under electrostatically unfavorable conditions, proteins adsorb onto hydrophobic surfaces, where the entropy-driven hydrophobic attraction dominates the electrostatic repulsion [126]. An understanding of these interactions plays an important role in controlling the nanoparticle-protein interactions and the ensuing phase behavior.

1.4.2. Potential applications

The conjugation of nanoparticles with proteins yields novel hybrid nanobiomaterials of synergetic properties and functions. These new characteristics of the conjugates can be utilized in a variety of industrial and technical fields covering from biotechnology to material science. The important applications of nanoparticle-protein conjugates include drug delivery, bio-sensing, bio-imaging and functional materials [11-14]. These applications are discussed in brief in the following:

a. Drug delivery: Versatility in the anchoring of biological ligands, organic functional groups, drugs and proteins on the nanoparticle surface can be utilized in drug delivery [11, 127]. Conjugation of nanoparticles can improve several crucial properties of free drugs such as solubility, in vivo stability, pharmacokinetics, biodistribution and enhancing their efficacy. Nanoparticles can provide effective carriers for proteins as well as for other biomolecules such as DNA and RNA, protecting these materials from degradation and transporting them across the cell-membrane barrier. Safe delivery of these biomolecules provides access to gene therapy as well as protein-based therapeutic approaches. For example, protein drug can be conjugated to

magnetic nanoparticles and the movement of conjugation can be guided by applying external magnetic field. pH-responsive nanoparticle-protein conjugates provide an alternate mechanism for protein drug release, relying on the acidic condition inside tumor and inflamed tissues [128].

b. Bio-sensing: The sensing of toxic materials, diseases and biological molecules is an important goal for diagnosis, forensic analysis and environmental monitoring [11, 13, 18]. A sensor generally consists of two components: a recognition element for target binding and a transduction element for signaling the binding event. The unique optical and electrical properties of metallic nanoparticles make them promising candidates for sensing applications. As an example, gold nanoparticles show an intense absorption peak from 500 to 550 nm of electromagnetic waves arising from surface plasmon resonance (SPR). The SPR band is sensitive to the surrounding environment and usually show the red-shift after protein binding [36]. The broadening of the plasmon band also possible due to the interparticle plasmon coupling caused by protein mediated aggregation of the nanoparticles. The conductivity and catalytic properties of metallic and semiconductor nanoparticles have been applied to electro analytical sensing [129]. The attachment of nanoparticles onto electrodes drastically enhances the conductivity and electron transfer from the redox analytes. An analogous electron transfer from protein to nanoparticles was used for monitoring hydrogen evolution from zinc-substituted cytochrome c immobilized TiO_2 nanoparticles [130].

c. Bio-imaging: The luminescent and magnetic properties of the nanoparticles have advances bio-imaging technologies. The luminescent property of the nanoparticle is being used for optical imaging and magnetic nanoparticle for magnetic resonance imaging (MRI). Nanoparticles being used in optical imaging can be subdivided into two categories: quantum dots (QDs) and dye-doped nanoparticles QDs [131]. However, issues of toxicity, photo-oxidation, water

solubility and rapid photo-bleaching of organic dyes are associated with these materials. The optical transparent property of silica nanoparticles are used to solve these problems, polymer and protein coating are also being used to resolve these issues [132]. The coating of silica on QDs makes it biocompatible and water soluble and prevents the photo-bleaching of organic dyes. In one example, aptamer-conjugated magnetic and dye-doped silica nanoparticles have been used for selective collection and detection of cancer cells [133]. In MRI, contrast agents are generally introduced to enhance the tissue contrast. The monodisperse, cross-linked iron oxide nanoparticles provide non-toxic MRI contrast agents. Protein molecules can be used to cross-link the nanoparticles [134].

d. Functional materials: The highly selective catalytic and recognition properties of biomaterials, such as proteins and DNA with the unique electronic, photonic and catalytic features of nanoparticles can be used to develop new functional materials [10-14, 87-89, 135-137]. In particular, immobilization of proteins onto nanoparticles, cross-linking of proteins with nanoparticles and self assembly of proteins with nanoparticles represent commonly used methods to prepare protein-incorporated functional materials. Self-assembly, in absence of templates, of nanoparticle-protein conjugates is governed by the balance of attractive and repulsive forces which can be tuned by solution condition and/or by applying external electric/magnetic fields. Proteins can also be used as templates for nanoparticles organization where strong interactions between proteins and nanoparticles lead to the arrangement of nanoparticles in structures that are predefined by the shape of the template. These soft templates, provide multiple well-defined binding sites for the attachment of nanoparticles and can allow nanoparticles to be organized in hierarchical structures by exploiting strategies found in natural systems.

1.5. Layout of the thesis

Nanoparticles due to their small size and large surface-to-volume ratio possess unique and distinct properties which are useful for their numerous applications. Many of these applications require interaction of nanoparticles with macromolecules such as proteins. In particular, in the field of nanobiotechnology, nanoparticle-protein complexes have great interest because they can access to and operate within the cell due to their size comparable to that of cell. This conjugation of nanoparticles with biomolecules is governed by various interactions such as covalent bonding, hydrogen bonding, electrostatic forces etc. depending on the system properties. The degree of these interactions depends on the characteristics of both nanoparticles and proteins which can easily be tuned through solution conditions. In this thesis, the interaction and complexes of charged nanoparticles with charged proteins under varying conditions (ionic strength and pH) as well as size of the nanoparticles have been investigated. The anionic silica nanoparticles and two globular proteins [lysozyme and bovine serum albumin (BSA)] have been used as model systems. The adsorption isotherms of proteins on the nanoparticles and the resultant phase behavior are measured using ultraviolet-visible spectroscopy and evolution of interactions and structures in the complexes are examined using dynamic light scattering and small-angle neutron scattering. The thesis consists of seven chapters. Chapter 1 gives an introduction to the nanoparticles, proteins, their possible complexes and potential applications. The details of the experimental techniques and their capabilities for studying such systems are discussed in chapter 2. The results of different nanoparticle-protein complexes studied are described in chapters 3 to 6. Chapter 3 reports the study of complexes of silica nanoparticles with lysozyme and BSA proteins. The studies have been carried out under physiological conditions (pH 7), where silica nanoparticles are anionic whereas lysozyme and BSA proteins are cationic

and anionic, respectively. The effect of electrolyte on these nanoparticle-protein complexes is examined in chapter 4. The studies are done mostly in presence NaCl and its relative effect with other salts is compared. Chapter 5 presents the tuning of nanoparticle-protein complexes through pH. The pH has been varied from physiological conditions to the isoelectric point (IEP) of the respective proteins. The role of nanoparticle size on the nanoparticle-protein complexes is investigated in chapter 6. The nanoparticle size has been varied in the range so that in each case there is enough adsorption of protein on the nanoparticles. Finally, the results of the thesis are summarized in Chapter 7.

Chapter 2

Characterization Techniques

2.1. Introduction

The nanoparticles and biomolecules such as proteins have common characteristic that they possess structures at nano (mesoscopic) length scale, which govern the macroscopic behavior of individuals as well as their complex systems [2, 5]. In general, there are number of techniques for the characterization of such materials, for the understanding of their structure, properties and interactions [138, 139]. For example, macroscopic techniques (e.g. zeta-potential, rheology and conductivity) explore the bulk properties of the system and hence are useful for predicting overall behavior of the systems [126, 140]. Spectroscopic techniques (e.g. ultraviolet-visible, Raman, infrared and nuclear magnetic resonance) are employed for the confirmation of the presence of molecular species and electronic transitions, monitoring phase transitions and band gap calculations, studying luminescence, fluorescence and chemical species etc [138, 139]. Any conformation changes in protein on their interaction with the nanoparticles are mostly probed by circular dichroism spectroscopy [21, 141]. Microscopic techniques (e.g. transmission electron microscopy, scanning electron microscopy, atomic force microscopy) give the direct visualization of the morphology, particle size, phases, defects etc [141, 142]. Scattering techniques (e.g. X-ray diffraction, small-angle neutron scattering, dynamic light scattering) are extremely reliable for finding the particle size, shape, number density, interactions and crystal structure [22, 23, 80, 143]. Each technique has its own advantages and disadvantages

to get the required information under the required conditions. Therefore, many times a combination of different techniques is used for obtaining complementary results.

Ultraviolet-visible (UV-visible) spectroscopy is routinely used for the quantitative determination of different analytes, including nanomaterials and biological macromolecules [144]. Spectroscopic analysis is commonly carried out in solutions but solids and gases may also be studied. UV-visible spectroscopy is based on the absorption of photons by the samples to produce electronic transitions from the ground state to an excited state. As a result the absorption spectra are generated reflecting the identity and concentration of molecules in the solution. For example, UV-vis spectroscopy provides information on protein adsorption on the nanoparticles by the red shift of the spectra for metal nanoparticles [96, 143]. On the other hand, the adsorbed and non-adsorbed proteins can be separated using centrifugation and the subsequently measured absorbance spectra of proteins are used to quantify the adsorbed protein for both metallic and nonmetallic nanoparticles [22, 23].

The scattering techniques that are popular to the studies of nanostructured materials are light scattering [includes both static light scattering (SLS) and dynamic light scattering (DLS)], small-angle neutron scattering (SANS) and small-angle X-ray scattering (SAXS) [138, 146, 147]. In each of these techniques the radiation (light, neutron or X-ray) is elastically scattered by a sample and the resulting scattering pattern is analyzed to provide information about the structure (shape and size), interaction and the order of the components of the samples. In SANS and SAXS, the nanometer length scales are probed using the X-rays and neutrons with wavelength of a few angstroms. On the other hand, DLS works on different principle which measures the time dependent fluctuations of scattered light intensity [148]. It probes the diffusion coefficient of particles by measuring the intensity autocorrelation function which is related to the

effective size of the particles. The DLS can probe the length scales down to a few nanometers to as high as in micron range. The nature of incident radiation determines the type of samples that can be studied by the scattering techniques, the length scale that can be probed and the information that can be obtained. For example, SLS and DLS cannot be use to study opaque samples whereas SAXS and SANS with high penetration depth can easily be applied to opaque samples. Moreover, SANS is more suitable over SAXS for samples containing low atomic number elements due to high sensitivity of neutron compared to X-ray. Further, isotope specific scattering and strong interaction with magnetic materials make SANS unique for condensed matter research [149].

The UV-vis spectroscopy and scattering techniques (DLS and SANS) are used in this thesis for the characterization of nanoparticles, protein and their complexes. These techniques are described in detail in this chapter.

2.2. UV-visible spectroscopy

UV-vis spectroscopy is an absorption spectroscopy involving measurement of the wavelength and intensity of absorption of near ultraviolet and visible light by a sample [144]. In this technique light of varying wavelengths (~ 200-700 nm) are incident on a sample and absorbance is measured at each wavelength. As a result the absorption spectra are generated which can be used to identify the absorbing molecules/compounds in the sample. In particular, the presence of organic molecules such as proteins is determined by the characteristic absorption peak arising due to electron transition from highest occupied molecular orbital (HOMO) to the lowest unoccupied molecular orbital (LUMO). The quantitative information on concentration of absorbing constitute is given by the Beer-Lambert law.

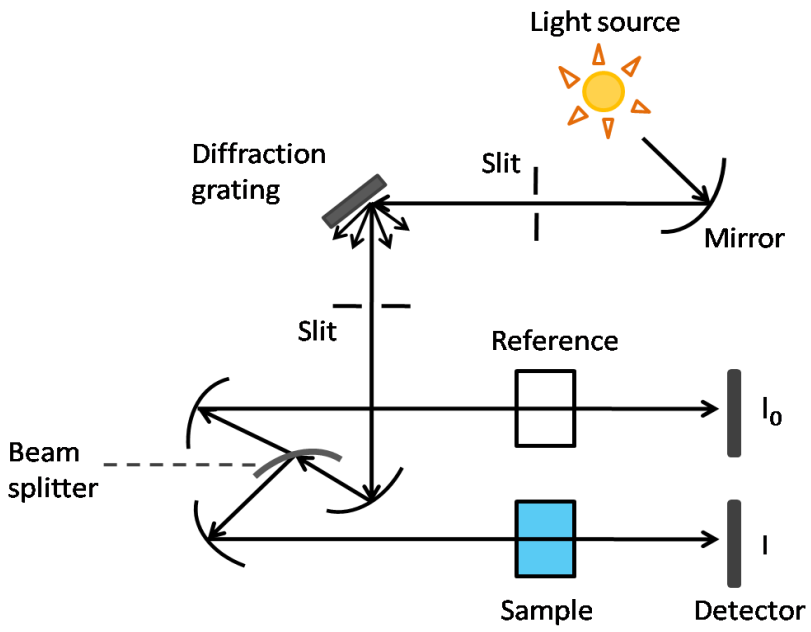

Figure 2.1. Schematic diagram for a typical UV-visible spectrophotometer.

The schematic diagram for a UV-visible spectrophotometer is shown in Figure 2.1. Radiation containing wide wavelength range from the source passes through monochromator which select and transmits the light of a particular wavelength. The transmitted light is splitted into two beams by beam splitter and each splitted beam passes through sample and reference to the photo detector. The signals are amplified and spectrum is displayed in a computer. Intensity of incident light (I_0) at a given wavelength passes through a sample solution that absorbs light of certain wavelength. Intensity of transmitted light (I) from the sample is detected by the detector [160]. The amount of radiation absorbed can be measured either by transmittance or absorbance, where transmittance $T = I/I_0$ and absorbance $A = \log_{10} (I_0/I) = -\log_{10} T$. Further, the absorbance (A), concentration of the absorbing species c (in mol/lt or M) and path length of the sample cuvette b (in cm) are related through Beer-Lambert law as $A = \varepsilon cb$, where ε is the molar absorptivity or molar extinction coefficient ($M^{-1}cm^{-1}$). This process is executed for a range of wavelength and a spectrum is recorded. Thus for a known path length of a given sample,

UV-vis spectroscopy can be used to determine the concentration of the absorbing molecules/compounds in a solution [143].

2.3. Dynamic light scattering

The scattered light intensity from a colloidal suspension depends on the scattering angle (2θ) and the observation time (t). Thus there are two classes of light scattering techniques: (i) static (elastic) light scattering (SLS) in which one measure the time averaged scattering intensity at various angles and (ii) dynamic (quasielastic) light scattering (DLS) in which the time dependence of the intensity is measured at a particular angle [148, 150]. SLS yields information on the static properties of the sample such as size and shape of the scatterers at a length scale of the order of wavelength of the light. However, DLS can measure size of particles that are much smaller than the wavelength of light. DLS is a routine tool for characterizing particle size and size distribution for the colloidal suspension [143]. It provides ensemble averaged estimate of particle size in suspensions, wide accessible range of particle sizes in the submicron range and fast data acquisition. Working principle of DLS is based on two phenomena-Tyndall effect (scattering) and Brownian motion. During the scattering process of a coherent monochromatic light each particle acts as a secondary source as a result scattered waves generate an interference pattern. At ambient conditions, colloidal particles are no longer stationary in the suspension medium rather they move by the Brownian motion process which leads to the time dependence of intensity of scattered light. This produces random speckles in space, which appear as randomly fluctuating dark or bright spots at the detector. Figure 2.2 shows the typical intensity fluctuation observed at detector. Smaller particles diffuse with faster speeds and generate rapid fluctuations in scattered light intensities, whereas diffusion of larger particles is more sluggish and result in slowly fluctuating light intensities. The information about the fluctuations in

scattered light intensity with time is related to the diffusion coefficient of particles undergoing Brownian motion.

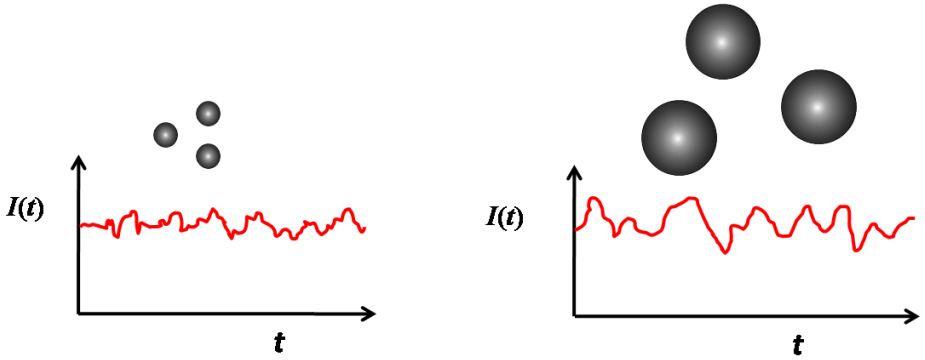

Figure 2.2. Schematic illustration of the intensity fluctuation in dynamic light scattering experiment.

2.3.1. Theory of dynamic light scattering

In DLS, the characteristic time of fluctuations in the intensity of scattered light is measured and it depends on the diffusion coefficient of the particles undergoing Brownian motion [148, 150]. The origin of light scattering is the inhomogeneities in polarizability within the sample. The excess polarizability of the volume element of the sample at position *r* is related as $\delta\alpha(\mathbf{r}) = \alpha(\mathbf{r}) - \langle\alpha\rangle$, where $\langle\alpha\rangle$ is the average polarizability of the sample.

For small particles (maximum dimension < Q^{-1}) [$Q = 2k\sin\theta$ is magnitude of the scattering vector, where 2θ is scattering angle] in dilute solution the excess polarizability $\delta\alpha(\mathbf{r})$ can be approximated by the fluctuation in solute concentration (δc). In that case, $\boldsymbol{E}_s(t) \propto \delta c(\boldsymbol{Q}, t)$, where $\boldsymbol{E}_s(t)$ is the electric field associated with scattered light at time *t*. The time dependence of the scattered field is thus related to the Brownian motion of the particles, which is responsible for the concentration fluctuations. For a monodisperse solution, the temporal evolution of concentration fluctuation can be calculated from the diffusion equation.

$$\frac{\partial \delta c(\mathbf{r},t)}{\partial t} = D\nabla^2 \delta c(\mathbf{r},t) \tag{2.1}$$

where D is the diffusion coefficient, expressing $c(\boldsymbol{r}, t)$ through a Fourier transform

$$c(\mathbf{r},t) = \int d^3\boldsymbol{Q} e^{i\boldsymbol{Q}.\mathbf{r}} c(\boldsymbol{Q},t) \tag{2.2}$$

putting this in Equation 2.1, one obtain

$$\frac{d}{dt}\int d^3\boldsymbol{Q} e^{i\boldsymbol{Q}.\mathbf{r}} \delta c(\boldsymbol{Q},t) = D\nabla^2 \int d^3\boldsymbol{Q} e^{i\boldsymbol{Q}.\mathbf{r}} \delta c(\boldsymbol{Q},t) \tag{2.3}$$

this can be written as

$$\frac{\partial \delta c(\boldsymbol{Q},t)}{\partial t} = -D\boldsymbol{Q}^2 \delta c(\boldsymbol{Q},t) \tag{2.4}$$

which has the solution

$$\delta c(\boldsymbol{Q}, t+\tau) = \delta c(\boldsymbol{Q},t) e^{-DQ^2\tau} \tag{2.5}$$

For a system fluctuating around its equilibrium state, one does not know the initial condition of $c(\boldsymbol{Q},t)$. However it can be calculated using suitable statistical averages. Multiplying both sides of Equation 2.5 with $\delta c(\boldsymbol{Q},t)$ and averaging yields

$$\left\langle \delta c(\boldsymbol{Q}, t+\tau)\delta c(\boldsymbol{Q},t)\right\rangle_t = \left\langle \delta c(\boldsymbol{Q},t)^2 \right\rangle_t e^{-DQ^2\tau} \tag{2.6}$$

where $< >_t$ indicates the time average. Since the scattered field amplitude is proportional to the concentration fluctuation, in terms of electric field Equation 2.6 can be written as

$$\frac{\left\langle \boldsymbol{E}_s(\boldsymbol{Q}, t+\tau)\boldsymbol{E}_s(\boldsymbol{Q},t)\right\rangle_t}{\left\langle \boldsymbol{E}_s(\boldsymbol{Q},t)^2 \right\rangle_t} = e^{-DQ^2\tau} = g^{(1)}(\tau) \tag{2.7}$$

where $g^{(1)}(\tau)$ is the normalized autocorrelation function of the electric field of scattered light. Thus the electric field autocorrelation function decays exponentially with time. Experimentally one measures the fluctuations in intensity and then calculates the autocorrelation function.

The normalized intensity autocorrelation function of scattered light intensity at a particular scattering vector (***Q***) is given as

$$g^{(2)}(\tau) = \frac{\langle I(t) I(t+\tau) \rangle}{\langle I(t) \rangle^2} \tag{2.8}$$

where $I(t)$ is the scattered light intensity at time t and $I(t + \tau)$ is the scattered light intensity at time t plus a lag time τ. For an ergodic system $g^{(2)}(\tau)$ is related to $g^{(1)}(\tau)$ by the Siegert relation as

$$g^{(2)}(\tau) = \beta[g^{(1)}(\tau)]^2 + 1 \tag{2.9}$$

combining Equations 2.7 and 2.9 one gets

$$g^{(2)}(\tau) - 1 = \beta e^{-2DQ^2\tau} \tag{2.10}$$

where β ($0 < \beta < 1$) is an experimental constant called spatial coherence factor and defines the resolution of the measurement. β is defined as the ratio of aperture area of photo detector (A_d) to the coherence area (A_c) ($\beta = A_d/A_c$). The area of a single speckle is known as coherence area (A_c) given by relation $A_c = \lambda^2 r^2 / \pi x^2$, where λ is wavelength of the incident beam, r is particle to detector distance and x is the radius of the scattering volume. Thus to achieve a high coherence factor and hence better resolution, the optimum aperture area and appropriate pin holes in front of the detector is required.

2.3.2. Determination of hydrodynamic size

Equation 2.7 depict that for a monodisperse system of particles, $g^{(1)}(\tau)$ decay exponentially i.e.

$$g^{(1)}(\tau) = e^{-\Gamma\tau} \tag{2.11}$$

where the decay constant ($\Gamma = DQ^2$) is proportional to the translational diffusion coefficient (D) of the particle at fixed scattering vector ***Q***. From the decay constant of the autocorrelation

function, the apparent diffusion coefficient (D) is obtained. The effective hydrodynamic size d_h (diameter) of the particles is calculated from D using Stokes-Einstein relation as

$$d_h = \frac{k_B T}{3\pi\eta D} \tag{2.12}$$

where k_B is the Boltzmann's constant, T is the absolute temperature and η is the viscosity of the solvent.

Figure 2.3 shows the calculated intensity autocorrelation function for collections of monodisperse particles having different diffusion coefficients (10×10^{-8} cm^2/s and 50×10^{-8} cm^2/s). The autocorrelation function of the particles having higher diffusion coefficients (smaller sizes) decay faster whereas for relatively small diffusion coefficients (larger sizes) intensity auto correlation function decay slowly.

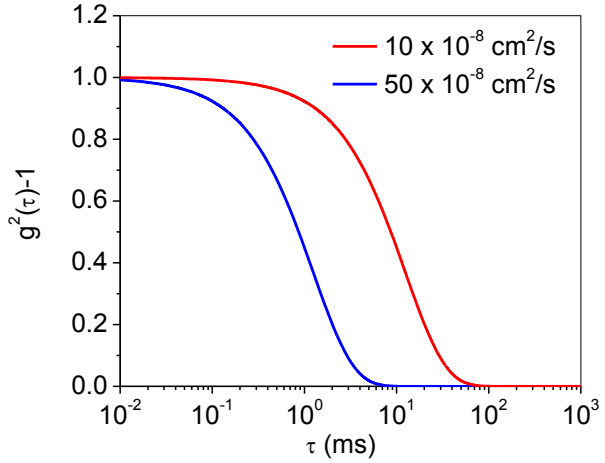

Figure 2.3. Intensity autocorrelation function for particles with different diffusion coefficients.

In case of polydisperse system Equation 2.11 can be written in terms of the Laplace transform of the distribution of decay constants $G(\Gamma)$

$$g^{(1)}(\tau) = \int_0^\infty G(\Gamma)\, \mathrm{e}^{-\Gamma\tau}\, d\Gamma \tag{2.13}$$

The distribution $G(\Gamma)$ represents the relative intensity of scattered light and depends on the size and volume fraction of the particles. In principle $G(\Gamma)$ can be obtained by doing inverse Laplace transformation on the measured autocorrelation function. However, it is difficult because the correlation function is measured discretely only over finite range of τ and there is always noise associated with the data. All these together make the Laplace inversion of Equation 2.13 an ill-conditioned problem in that there exists a large number of possible solutions all of which fit the data within experimental error. There are several ways to characterize G(Γ) from DLS data. One of the simplest and mostly used is method of cumulants [151, 152]. In this method, Equation 2.13 can be written as

$$g^{(1)}(\tau) = \exp[-\overline{\Gamma}\tau + \frac{\mu_2 \tau^2}{2}] \tag{2.14}$$

where $\overline{\Gamma}$ is the average decay constant and μ_2 is the variance. The ratio of variance to the square of the average decay constant is called the polydispersity index (PI) [$PI = \mu_2 / \overline{\Gamma}^2$]. From average diffusion coefficient, the effective hydrodynamic size can be calculated using Stokes-Einstein relation. However, the application of the method of cumulants is limited to monomodal distribution with small polydispersity where the criterion $\mu_2\tau^2 << 1$ is satisfied. For broad monomodal distribution or multimodal distributions, the most widely used method is CONTIN which is a Laplace integral transform algorithm that uses a regularized non-negatively constrained least-squares (NNLS) technique [153, 154]. In NNLS method a set of discrete numbers of decay constants Γ_i that sample the continuous distribution $G(\Gamma)$ is selected. The weighting factors (w_i) of Γ are calculated from the best fit of the data by putting constraint that size distribution is non-negative. The coefficients w_i are obtained by minimizing the following expression

$$\chi^2 = \sum_{j=1}^{N}\left[g^1(\tau_j) - \sum_{i=1}^{M} w_i e^{-\Gamma_i \tau_j} \right]^2 \quad (2.15)$$

In CONTIN algorithm to avoid the oscillation in the distribution instead of minimizing Equation 2.15 the regularized residual is minimized and the minimization equation becomes

$$\chi^2 = \sum_{j=1}^{N}\left(1/\sigma_i^2\right)\left[g^1(\tau_j) - \int G(\Gamma) e^{-\Gamma\tau} d\Gamma \right]^2 + \alpha^2 \left| LG(\Gamma) \right|^2 \quad (2.16)$$

where σ_i is the least square weight matrix, μ is the regularization parameter and L is the operator of the regularizer. Regularization will tend to smooth out spurious oscillations in the distributions. In addition to the above two criteria (non-negativity constraint and regularization) it also uses parsimony principle that prefer the distribution which has maximum smoothness.

2.3.3. Experimental aspects of dynamic light scattering

The schematic of the DLS experiment is shown in Figure 2.4. Major parts of the instrument consists a laser source, sample holder, photon detector and correlator. DLS experiments in this thesis have been carried out using SZ-100 particle size analyzer by Horiba, Japan. This instrument consists of 10 mW diode pumped solid state laser used to obtain a monochromatic beam of light of wavelength of 532 nm. The laser beam is converged at the sample using a lens. An ND filter is used in the path of the beam to control the incident intensity at sample and correspondingly optimizing the scattered intensity at the detector. The transmission of the sample is measured using a transmission detector after the sample and in line with the laser beam. The transmission of ND filter is controlled to obtain optimum value of transmission for a particular sample. The optimum transmission ensures the scattering intensity from the sample at the detector will be under the saturation of the detector. The incident laser beam is scattered from the sample at all the scattering angles. The present instrument provides

the choice of scattering intensity detection at two scattering angles, perpendicular scattering (90^o) and backscattering (173^o) detection. The scattered light is focused on the detector using lens. The detector comprises a photo-multiplier tube (PMT) to amplify the photon signal. The intensity fluctuations are converted into electrical pulses and fed into a digital correlator which generates the autocorrelation function. This instrument also has provision to measure the zeta potential by measuring the electrophoretic mobility of particles. Zeta potential (ζ) of particle with radius R is related to the electrophoretic mobility (μ_e) through Henry equation as [155]

$$\zeta = \frac{3\eta\mu_e}{2\varepsilon f(\kappa R)} \tag{2.17}$$

where η is the viscosity and ε is dielectric constant of the solvent and $f(\kappa R)$ is called the Henry's function. The Henry's function depends on the Debye length ($1/\kappa$) and size of the particle. $f(\kappa R)$ takes the value = 1.5 in the limit $\kappa R \gg 1$ (i.e. large particles and high ionic strength) (Smoluchowski approximation), whereas $f(\kappa R) = 1$ in the limit $\kappa R \ll 1$ (i.e. small particles and low ionic strength) (Hückel approximation).

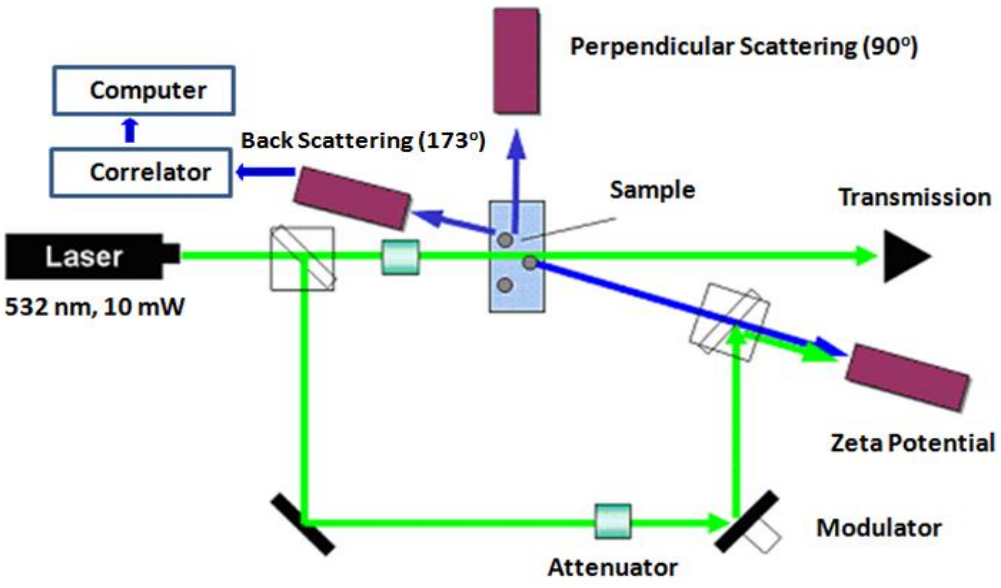

Figure 2.4. Schematic of dynamic light scattering set up.

2.4. Small-angle neutron scattering

A typical schematic of the basic scattering experiment is shown in Figure 2.5. A monochromatic radiation falls on the sample interact with sample constituents and scattered at a particular angle (2θ). The incoming (incident) and outgoing (scattered) radiation are characterized by the wave vectors $\boldsymbol{k_i}$ and $\boldsymbol{k_0}$, respectively. Change in the properties (momentum and energy) of radiation during the process of scattering contains information (structure and dynamics) about the scatterer within the sample [146, 156-158]. In case of elastic scattering (only change in momentum) the magnitude of wave vectors are given by $k_i = k_0 = (2\pi n/\lambda)$, where n in the refractive index of the solvent and λ is the wavelength of the radiation. The scattered radiation is detected at distance far from the sample (Fraunhofer criterion) and is assumed in the single scattering limit. From Figure 2.2 the phase difference between the two scattered wave can be given as $\Delta\phi = (\boldsymbol{k_0} - \boldsymbol{k_i}).\Delta\boldsymbol{r} = \boldsymbol{Q}.\Delta\boldsymbol{r}$, where $\boldsymbol{Q}$ $(= \boldsymbol{k_0} - \boldsymbol{k_i})$ is a measurement of momentum transfer and called scattering vector. From scattering geometry given in Figure 2.2 the magnitude of $\boldsymbol{Q}$ is given as $Q = 2k\sin\theta$. Thus the values of Q varies from a minimum value $Q_{min} = 0$ for $2\theta = 0^o$ to maximum value $Q_{max} = 2k = 4\pi n/\lambda$ for $2\theta = 180^o$, where n is the refractive index of the medium for a given radiation. Practically both these extreme can never be achieved because of interference from direct beam. Depending on the value of Q access by instrument it is called small-angle ($\sim < 15^o$) or wide angle ($\sim > 15^o$) scattering instrument. There is an inverse relationship between the scattering vector and length scale which restrict the structure that can be probed by a particular technique. In SANS, the nanometer length scales can easily be probed using neutrons with wavelength of a few angstroms. The wavelength of neutrons used for these experiments usually in the range 4 to 10 Å. The value of Q in SANS experiments is typically in range of 0.001 $Å^{-1}$ to 1 $Å^{-1}$. As the small Q values occur at small scattering angles, the technique

is called as small-angle neutron scattering. Thus SANS is a low resolution technique used to study the structures of materials (inhomogeneities) at larger length scales, unlike conventional diffraction experiments, where the structures of materials are examined at atomic resolution.

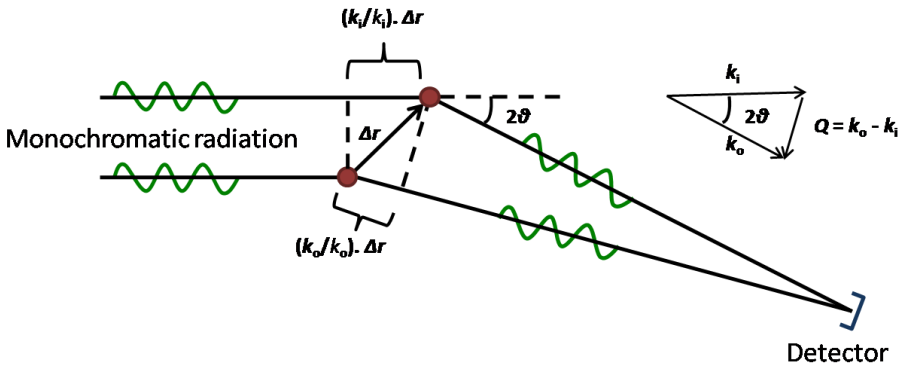

Figure 2.5. A typical scattering diagram.

2.4.1. Scattering cross section

Neutrons being quantum particles, show wave particle duality. In scattering experiments neutron can be treated as a plane wave exp($i\boldsymbol{k}_i$.r) travelling in the direction of $\boldsymbol{k}_i$. The scattered wave may be represented by a spherical wave as [$f(\theta)/r$]exp($i\boldsymbol{k}_0$.r), where $\mathbf{k}_i$ and $\boldsymbol{k}_0$ are incident and scattered wave-vectors, respectively (Figure 2.5). The parameter $f(\theta)$ gives the scattering amplitude where ff^* describes the probability that an initial plane wave with amplitude unity will be scattered in a given direction. To calculate this probability, the following Schrodinger equation is solved:

$$\left(\frac{-\hbar^2}{2m}\nabla^2 + V(\mathbf{r})\right)\psi(\mathbf{r}) = E\psi(\mathbf{r}) \tag{2.18}$$

where $V(\boldsymbol{r})$ is Fermi pseudo-potential representing the interaction between neutron and nucleus and is expressed by [157]

$$V(\mathbf{r}) = -\frac{2\pi\hbar^2}{m} b\delta(\mathbf{r}) \tag{2.19}$$

where $\hbar$ is reduced Planck's constant (Planck's constant divided by 2π), m is mass of neutron and b is scattering length representing the strength of neutron-nucleus interaction and can be positive or negative. The neutron-nucleus interaction is isotropic in nature due to the small range of nuclear potential compared to the wavelength of the neutron and varies somewhat randomly throughout the periodic table.

Using the first Born approximation, the following solution is obtained [157]

$$\psi(\mathbf{r}) = exp(i\mathbf{k}_i.\mathbf{r}) + \frac{exp(i\mathbf{k}_0.\mathbf{r})}{r}\frac{m}{2\pi\hbar^2}\int exp(-i\mathbf{k}_0.\mathbf{r}_1)V(\mathbf{r}_1)exp(i\mathbf{k}_i.\mathbf{r}_1)d\mathbf{r}_1 \qquad (2.20)$$

where first and second terms correspond to the incident and scattered neutron beams, respectively. The comparison with the outgoing spherical wave gives

$$f = \frac{m}{2\pi\hbar^2}\int exp(-i\mathbf{Q}.\mathbf{r}_1)V(\mathbf{r}_1)d\mathbf{r}_1 \qquad (2.21)$$

where $\boldsymbol{Q} = \boldsymbol{k}_0 - \boldsymbol{k}_i$. The scattering amplitude using Fermi pseudo potential in equation 2.21 is given by

$$f = -b \qquad (2.22)$$

The differential scattering cross section or the probability of the neutron being scattered in the solid angle dΩ can be defined as [124]

$$\frac{d\sigma}{d\Omega} = \frac{No.\ of\ neutrons\ scattered\ per\ unit\ time\ per\ unit\ solid\ angle}{Incident\ flux} \qquad (2.23)$$
$$= b^2$$

The integral scattering cross-section for a nucleus is thus given by $\sigma = 4\pi b^2$ and it can be looked as an effective area presented by the nucleus (scatterer) to the incident neutron.

For a single scatterer (nucleus) in a sample differential scattering cross-section is given by

$$\frac{d\sigma}{d\Omega}(\mathbf{Q}) = \left| b \exp(-i\mathbf{Q}.\mathbf{r}) \right|^2 \tag{2.24}$$

However, for an assembly of scatterers in a macroscopic sample, microscopic differential scattering cross section can be obtained by summing over all the scattering centers

$$\frac{d\sigma}{d\Omega}(Q) = \left\langle \left| \sum b_j \exp(-i\mathbf{Q}.\mathbf{r}_j) \right|^2 \right\rangle \tag{2.25}$$

where $\boldsymbol{r_j}$ is the position vector of the j^{th} scatterer in the sample and the bracket < > represents an average over all the possible orientations. In SANS, one studies large scale inhomogeneities rather than locating the individual scattering centers, the individual scattering length b_j therefore can be replaced by locally averaged scattering length density $\rho(r)$ and Equation 2.25 becomes

$$\frac{d\sigma}{d\Omega}(Q) = \left\langle \left| \int \rho(\mathbf{r}) \exp(-i\mathbf{Q}.\mathbf{r})\ d\mathbf{r} \right|^2 \right\rangle \tag{2.26}$$

where $\rho(\boldsymbol{r})$ is defined as $\rho(\mathbf{r}) = \frac{1}{V(\mathbf{r})} \sum_j b_j$ and the summation is carried over all the scatterers in volume element $V(\mathbf{r})$ around $\boldsymbol{r}$.

The macroscopic differential scattering cross section ($d\Sigma/d\Omega$) can be obtained by normalizing to differential scattering cross-section with the irradiated sample volume (V_S) and hence [156-158]

$$\frac{d\Sigma}{d\Omega}(Q) = \frac{1}{V_S} \left\langle \left| \int \rho(\mathbf{r}) \exp(-i\boldsymbol{Q}.\mathbf{r}) d\mathbf{r} \right|^2 \right\rangle \tag{2.27}$$

If the inhomogeneities and the matrix are considered to have homogeneous composition with scattering length densities denoted by ρ_p and ρ_m, respectively, Equation 2.27 can be written as

$$\frac{d\Sigma}{d\Omega}(Q) = \frac{1}{V_S} \left\langle \left| \rho_p \int_{Vptot} \exp(-i\boldsymbol{Q}.\mathbf{r}) d\mathbf{r} + \rho_m \int_{V_{mat}} \exp(-i\boldsymbol{Q}.\mathbf{r}) d\mathbf{r} \right|^2 \right\rangle \tag{2.28}$$

here the first term in the integration is over the volume V_{ptot} occupied by all inhomogeneities and the second term is over the volume V_{mat} occupied by the matrix. Above equation can be rewritten as

$$\frac{d\Sigma}{d\Omega}(Q) = \frac{1}{V_S}\left\langle \left| (\rho_p - \rho_m) \int_{V_{ptot}} \exp(-i\boldsymbol{Q}.\mathbf{r}) d\mathbf{r} + \rho_m \left\{ \int_{V_{mat}} \exp(-i\boldsymbol{Q}.\mathbf{r}) d\mathbf{r} + \int_{V_{ptot}} \exp(-i\boldsymbol{Q}.\mathbf{r}) d\mathbf{r} \right\} \right|^2 \right\rangle \quad (2.29)$$

The uniform integration in the second term of the above equation behaves like a delta function as the size of matrix is quite large and corresponding scattering contribution would be at Q value close to zero (sample dimensions)$^{-1}$. This contribution may be neglected for all practical purposes with $Q \neq 0$. After neglecting the second term, the above equation becomes

$$\frac{d\Sigma}{d\Omega}(Q) = \frac{(\rho_p - \rho_m)^2}{V_S}\left\langle \left| \int_{V_{ptot}} \exp(-i\boldsymbol{Q}.\mathbf{r}) d\mathbf{r} \right|^2 \right\rangle \quad (2.30)$$

If N_p is the number of inhomogeneities and V_p is the volume of a single inhomogeneities then $V_{ptot} = N_p V_p$ provided all the inhomogeneities are identical. Here $(\rho_p - \rho_m)^2$ is called the scattering length density contrast or simply contrast factor and it is one of the most important sample parameters in SANS studies. It is evident that with a good contrast value, the inhomogeneities are perceived clearly by the probing radiation while at low value of this factor the inhomogeneities appear to be smeared. The equation 2.30 can be rewritten as

$$\frac{d\Sigma}{d\Omega}(Q) = \frac{(\rho_p - \rho_m)^2}{V_S} V_p^{\,2} \left\langle \left| \sum_k F_k(\mathbf{Q}) \exp(-i\mathbf{Q}.\mathbf{r}_k) \right|^2 \right\rangle \quad (2.31)$$

where, $\boldsymbol{r}_\mathbf{j}$ is the position vector of the center of the k^{th} inhomogeneities and $F_k(\boldsymbol{Q})$ is the form factor amplitude associated with that inhomogeneity. From the above equation $F(\boldsymbol{Q})$ can be expressed as

$$F(\mathbf{Q}) = \frac{1}{V_p}\int_{V_p} \exp(-i\mathbf{Q}.\mathbf{r})d\mathbf{r} \tag{2.32}$$

and is normalized so that $|F(0)|^2 = 1$

For a mono-dispersed system, i.e. when all the inhomogeneities posses identical shape as well as size, Equation 2.31 can be expressed as

$$\frac{d\Sigma}{d\Omega}(Q) = \frac{N_p(\rho_p - \rho_m)^2 {V_p}^2}{V_S}\left\langle |F(\mathbf{Q})|^2 \right\rangle . \frac{1}{N_p}\left\langle \left| \sum_k \exp(-i\mathbf{Q}.\mathbf{r}_k) \right|^2 \right\rangle \tag{2.33}$$

$$\frac{d\Sigma}{d\Omega}(Q) = \frac{N_p(\rho_p - \rho_m)^2 {V_p}^2}{V_S} P(Q)\, S(Q) \tag{2.34}$$

where

$$P(Q) = \left\langle |F(\boldsymbol{Q})|^2 \right\rangle \tag{2.35}$$

and

$$S(Q) = \frac{1}{N_p}\left\langle \left| \sum_k \exp(-i\boldsymbol{Q}.\mathbf{r}_{\boldsymbol{k}}) \right|^2 \right\rangle = 1 + \frac{1}{N_p}\left\langle \sum_k \sum_{k'} \exp(i\boldsymbol{Q}.(\mathbf{r}_{\boldsymbol{k}} - \mathbf{r}_{\boldsymbol{k}'})) \right\rangle \tag{2.36}$$

The summation in Equation 2.36 extends over all the inhomogeneities in the sample. It can be seen from Equation 2.34 that the scattering cross section for a collection of inhomogeneities consists of two terms, the first term depends on the intra inhomogeneities scattering and the second on inter inhomogeneities scattering. The intra inhomogeneities scattering is the orientational average of the square of the form factor amplitude and is denoted by $P(Q)$. This term depends on the shape and size of the inhomogeneities and in principle can be calculated for any geometry. The inter inhomogeneities interference term $S(Q)$ can be evaluated in a closed form only if certain assumptions are made about the correlation between the spacing

of the inhomogeneities and their sizes and orientations. In terms of the volume fraction ($\varphi = N_p V_p / V_S$) of the inhomogeneities Equation 2.34 becomes [156-158]

$$\frac{d\Sigma}{d\Omega}(Q) = \varphi V_p (\rho_p - \rho_s)^2 P(Q) S(Q) \tag{2.37}$$

It may be mentioned that the un normalized scattering intensity is generally represented by $I(Q)$ in arbitrary unit. The typical functionality of $P(Q)$, $S(Q)$ and $d\Sigma/d\Omega$ (Q) as a function of Q are plotted in Figure 2.6.

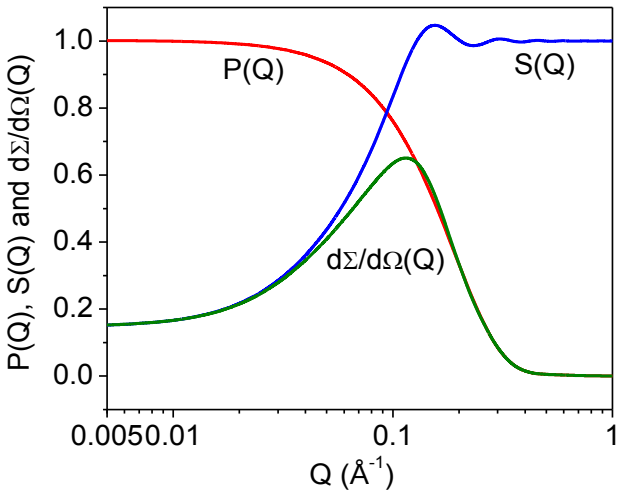

Figure 2.6. Typical curves of P(Q), S(Q) and dΣ/dΩ (Q).

So far, the inhomogeneities (particles) have been assumed to be monodispersed i.e. the shape as well as size of the particles in the system under consideration is identical. However, in reality, the particles in most cases are not strictly monodispersed in size and/or shape but polydispersed in nature. Size polydispersity can be expressed in terms of a distribution function $f(R)$. In case of a polydispersed system, the $d\Sigma/d\Omega$ (Q) can be expressed as [159, 160]

$$\frac{d\Sigma}{d\Omega}(Q) = \int \frac{d\Sigma}{d\Omega}(Q,R)\ f(R)\, dR \tag{2.38}$$

The size distributions commonly used are Gaussian distribution, Schultz distribution and log-normal distribution [161, 162].

In case of log-normal size distribution, *f*(R) is given by [162]

$$f(R) = \frac{1}{R\sigma\sqrt{2\pi}} \exp\left[-\frac{\left(\ln(R/R_{med}) \right)^2}{2\sigma^2} \right] \tag{2.39}$$

where R_{med} and σ are the median radius and standard deviation respectively. The mean and median values are related as $R_m = R_{med} \exp(\sigma^2/2)$.

2.4.2. Determination of intraparticle structure factor

For some of the regular shapes, having an axis of symmetry, the analytical expressions for $P(Q)$ are well documented in the literature [157-159, 163, 164]. It is assumed that the particles are randomly oriented in the sample so that the theoretical form factors for anisotropic particles have to be averaged over orientation. $P(Q)$ expressions for some standard shapes are given below:

a. Spherical particle: For spherical particle of radius R with uniform scattering length density the intraparticle structure factor is given as

$$P_s(Q) = 9\left[\frac{j_1(QR)}{QR} \right]^2 \tag{2.40}$$

where $j_1(x) = \frac{(\sin x - x\cos x)}{x^2}$ is first order spherical Bessel function. Figure 2.7 shows the functional form of $P(Q)$ for spherical particles of radii 25, 50 and 100 Å. It is observed that the width of distribution gets narrowed as the size of the particle increases. The oscillations in the high-Q region (observed when plotted on log-log scale) are the form factor oscillations whose maxima are analogous to the bright fringes in interference pattern.

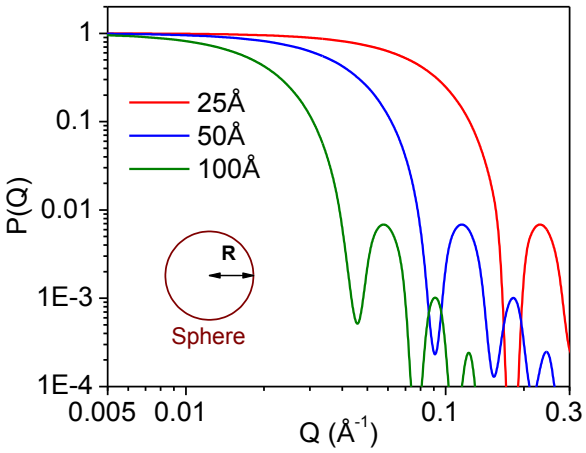

Figure 2.7. P(Q) plots for a sphere with varying radius.

b. Ellipsoidal particle: The expression for intraparticle structure factor of ellipsoidal particles with its semi axes *a* and *b* (=*εa*), $P_e(Q)$ can be written as

$$P_e(Q) = \int_0^{\pi/2} P_s(Q,r)\sin\beta d\beta \qquad (2.41)$$

where $r = a\sqrt{\sin^2\beta + \varepsilon^2\cos^2\beta}$ and β is the angle between semi-major axis and scattering vector. Here ε > 1 for prolate ellipsoidal and ε < 1 for oblate ellipsoidal shape of particles. Figure 2.8 shows the functional form of *P*(*Q*) for spherical, prolate ellipsoidal and oblate ellipsoidal shape of particles with same volume but different axial ratios. The differences in the plots suggest that the different shapes in samples can be determined.

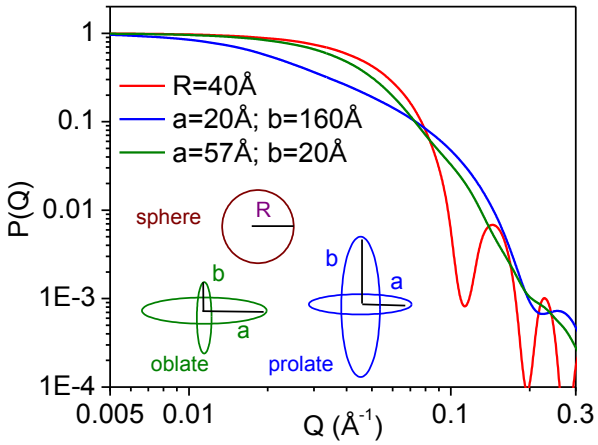

Figure 2.8. *P*(*Q*) plots for spherical, prolate ellipsoidal and oblate ellipsoidal shapes of particles having same volume.

c. Spherical shell (core-shell particle): The intraparticle structure factor for spherical shell with inner radius R and outer radius $R+t$, where t is thickness, can be obtained by subtracting the empty core of radius R from sphere of radius $R+t$ with proper weighting by the volumes. Therefore, $P_{SCS}(Q)$ for spherical shell is written as

$$P_{SCS}(Q) = \left[(\rho_c - \rho_{shell}) V_1 \frac{3 j_1(QR)}{QR} + (\rho_{shell} - \rho_m) V_2 \frac{3 j_1[Q(R+t)]}{Q(R+t)} \right]^2 \tag{2.42}$$

where ρ_c, ρ_{shell} and ρ_m are the scattering length densities of core, shell and solvent, respectively. V_1 and V_2 are the volume of the sphere with radius R and $R+t$, respectively. Figure 2.9 shows the functional form of $P(Q)$ for spherical shell with inner radius 50 Å and thickness 10 Å with contrast of shell greater than the contrast of core. The distribution for shell is compared with those with spherical particles of radii 50 and 60 Å. The particle with shell is found to have the lowest width and also show the oscillations of higher magnitude than those for spherical particles.

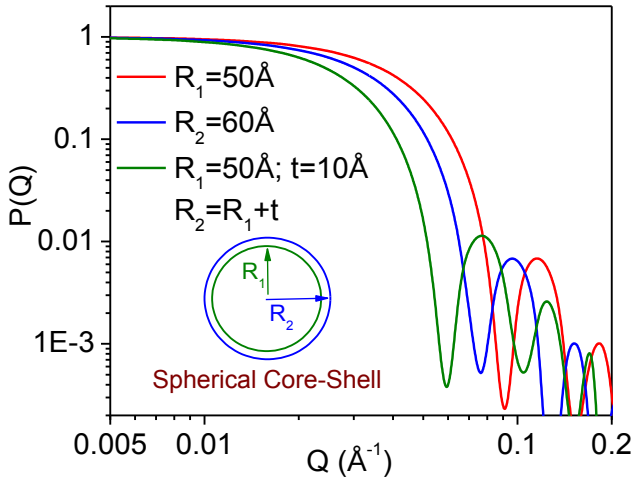

Figure 2.9. P(Q) plot for a spherical shell as compared with the spherical particles.

d. Rod-like particle: The intraparticle structure factor of randomly oriented rod-like particles with the radius R and length L (=2l) is given by

$$P(Q) = \int_0^{\pi/2} \frac{4 j_1^2(QR\sin\theta)}{Q^2R^2\sin^2\theta} \frac{\sin^2[(Ql)\cos\theta]}{(Ql)^2\cos^2\theta} \sin\theta d\theta \qquad (2.43)$$

where θ is the angle subtended by the principal axis of the rod with $\boldsymbol{Q}$. Figure 2.10 shows the functional form of $P(Q)$ for rod-like particles of different lengths and a fixed radius 50 Å. As the length of the particle increases $P(Q)$ on log-log scale shows a linear region in the intermediate Q range ($1/l < Q < 1/R$) with slope -1 of the linear region.

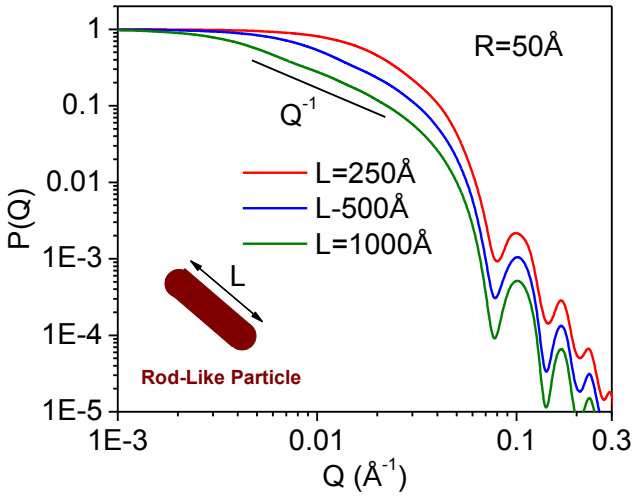

Figure 2.10. P(Q) for rod-like particles having different lengths and fixed radius.

e. Disc-like particle: The small-angle scattering technique can differentiate between rod-like particles and disc-like particles. The intraparticle structure factor for a disc is given by the same equation as that for a rod (Equation 2.43) with the diameter having much larger than the thickness. Figure 2.11 shows the functional form of $P(Q)$ for disc-like particles with same thickness and different radius. Unlike for a rod-like particle, $P(Q)$ for a disc-like particle has a slope of -2 in the intermediate Q range.

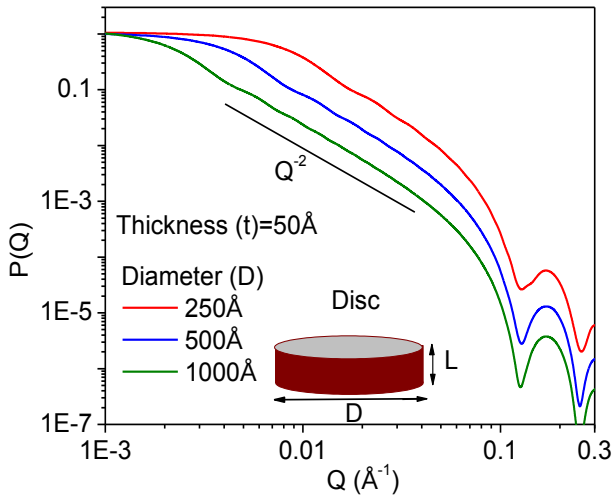

Figure 2.11. *P*(*Q*) plots for disc-like particles having same thickness and varying radius.

Guinier approximation: For a system of randomly oriented particles of any arbitrary shape, *P*(*Q*) can be approximated for small enough *Q* ($QR_g < 1$) as a form of Gaussian function such *P*(*Q*) decreases exponentially with Q^2 [159]. This is known as Guinier approximation

$$P(Q) = \exp(-\frac{Q^2 R_g^{\ 2}}{3}) \tag{2.44}$$

where R_g is the radius of gyration of the particle and gives an intuitive measure for the spatial extension of the particle. For dilute systems $S(Q) = 1$ and hence for $QR_g < 1$, Equation 2.37 can be written as [165]

$$\frac{d\Sigma}{d\Omega}(Q) = \varphi V_p(\rho_p - \rho_m)^2 \exp(-\frac{Q^2 R_g^{\ 2}}{3}) \tag{2.45}$$

from the slope of the log [$d\Sigma/d\Omega(Q)$] versus Q^2 plot R_g can be found out.

Figure 2.12 shows a Guinier plot for a dilute system having spherical particles of radius 25 Å. The plot of logarithm of the scattering intensity versus Q^2 shows a straight line in low-*Q* region and the slope gives the radius of gyration of the particle. The Guinier approximation offers the simplest, most straightforward and fairly reliable approximation to SANS for small enough *Q* values.

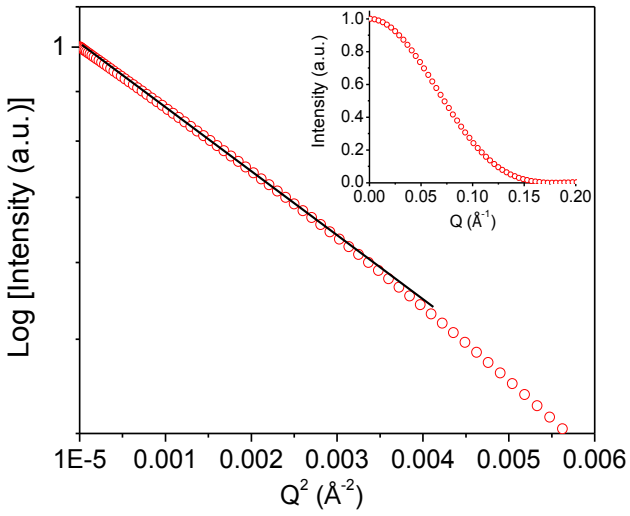

Figure 2.12. Guinier plot for a dilute system of spherical particle. Inset shows $P(Q)$ of the spherical particle.

Porod law: Porod law states that for inhomogeneity with sharp boundary and uniform scattering length density at large value of Q, $P(Q)$ can be approximated as [166]

$$P(Q) \sim \frac{2\pi S}{V}\frac{1}{Q^4} \tag{2.46}$$

where S is the surface area of the inhomogeneity. The differential cross section becomes

$$\frac{d\Sigma}{d\Omega}(Q) = \frac{2\pi N_p}{V_s}(\rho_p - \rho_m)^2 S\frac{1}{Q^4} \tag{2.47}$$

Hence the total surface area of the inhomogeneities irradiated by the incident beam can be extracted from the slope (Figure 2.13). However this is possible only when the scattering intensity $I(Q)$ is expressed in absolute scale.

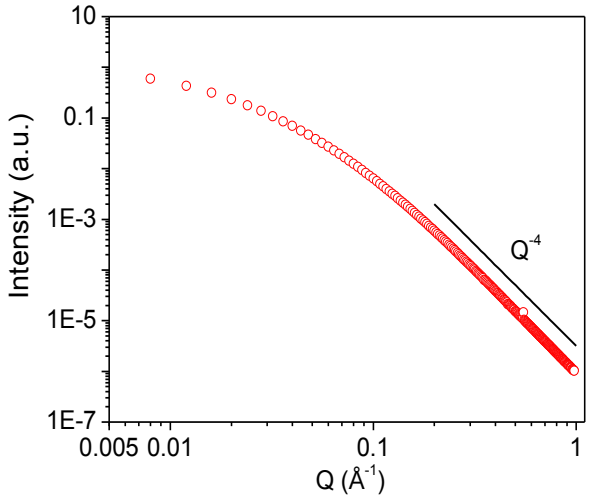

Figure 2.13. Scattering intensity at large Q values ($QR > 5$) for particles obeying Porod law.

2.4.3. Determination of interparticle structure factor

The interparticle structure factor $S(Q)$ contributes to the scattering intensity pattern above a particular concentration where the particles start interacting with each other. For these systems $S(Q) \neq 1$ and is governed by correlation between the particles. The correlation depends on interaction between the particles and hence determines the properties of the concentrated system. For an isotropic system, $S(Q)$ can be written as [157, 163, 167]

$$S(Q) = 1 + 4\pi n \int (g(r) - 1) \frac{\sin Qr}{Qr} r^2 dr \qquad (2.48)$$

where $g(r)$ is the radial distribution function and n is the number density of the particles. The radial distribution function is the probability of finding another particle at a distance r from the reference particle centered at the origin. The details of $g(r)$ depend on the interaction potential $U(r)$ between the particles [168, 169]. Thus, one has to have the knowledge of $U(r)$ for calculating $S(Q)$. This in turn implies that the measured $S(Q)$ can be used to obtain information about the interaction potential $U(r)$.

The statistical description of colloidal solutions treats the solutions in terms of a single component model. The major accountable of the model are the particles and the effect of solvent (with or without ions) introduced via an effective interaction potential $U(r)$.

$U(r)$ could consist of several terms such as (i) hard sphere term $U_{hs}(r)$, (ii) van der Waals term $U_{vw}(r)$, (iii) solvent mediated term $U_s(r)$ and (iv) Coulomb repulsion term $U_c(r)$. It is thus possible to calculate $g(r)$ or $S(Q)$ for these solutions using methods which have been developed for liquids. The $g(r)$ is related to the total correlation $h(r)$ between the two particles separated by distance r as

$$g(r) = 1 + h(r) \tag{2.49}$$

The radial distribution function for a pair of scattering particles with no internal structure separated by a distance r is called $g(r)$. The $g(r)$ is related to the interparticle interaction potential $U(r)$ as follows:

$$g(r) = \exp(-U(r)/k_B T) \tag{2.50}$$

where k_B is the Boltzmann constant and T is the absolute temperature.

Since the potential of mean-force $U(r)$ contains contributions from many-body interactions, it is expanded in terms of binary (w_{ij}), ternary (w_{ijk}), and higher order interactions as

$$U(r) = \sum_{i,j} w_{ij}(r) + \sum_{i,j,k} w_{ijk}(r) + ... \tag{2.51}$$

Note that $g(r)$ is zero for very short distances since two particles cannot occupy the same space and is equal to one for large distances since at far enough distance a particle can be located with certainty. Direct interactions between the pair of interacting particles are represented by the direct correlation function $c(r)$ whereas interactions through other particles are represented by the total correlation function $h(r) = g(r) - 1$.

The Ornstein-Zernike integral equation denotes a relation between the direct correlation function $c(r)$ and the total correlation function $h(r)$ [170]:

$$h(\boldsymbol{r}) = c(\boldsymbol{r}) + n\int c\left(\boldsymbol{r}'\right) h\left(\left|\boldsymbol{r} - \boldsymbol{r}'\right|\right) d^3\boldsymbol{r}' \tag{2.52}$$

where n (N/V) is particle number density.

The Ornstein-Zernike equation contains two unknowns [$h(r)$ and $c(r)$]. It can be solved only if another (so called closure) relation is added. Many of these closure relations have been introduced (Percus-Yevick approximation, mean spherical approximation and hypernetted chains approximation etc). Using one such closure relation, numerical solutions of the Ornstein-Zernike equation yield realistic interparticle structure factors. Some frequently used closure relations are as follows:

a. The Percus-Yevick approximation: The Percus-Yevick approximation (PYA) uses the following closure relation in order to solve the Ornstein-Zernike integral equation [171]

$$c(r) = g(r)\left[1 - \exp\left(-\frac{U(r)}{k_B T}\right)\right] \tag{2.53}$$

b. The mean spherical approximation: The mean spherical approximation (MSA) closure relation to the Ornstein-Zernike equation is given by [172]

$$\begin{aligned} c(r) &= -\frac{U(r)}{k_B T} \qquad r > \sigma \\ h(r) &= -1 \qquad\qquad r \le \sigma \end{aligned} \tag{2.54}$$

c. The hypernetted chain approximation: The hypernetted chain approximation (HNCA) closure relation to the Ornstein-Zernike equation is given by [173]

$$c(r) = -\frac{U(r)}{k_B T} + g(r) - 1 - \ln g(r) \tag{2.55}$$

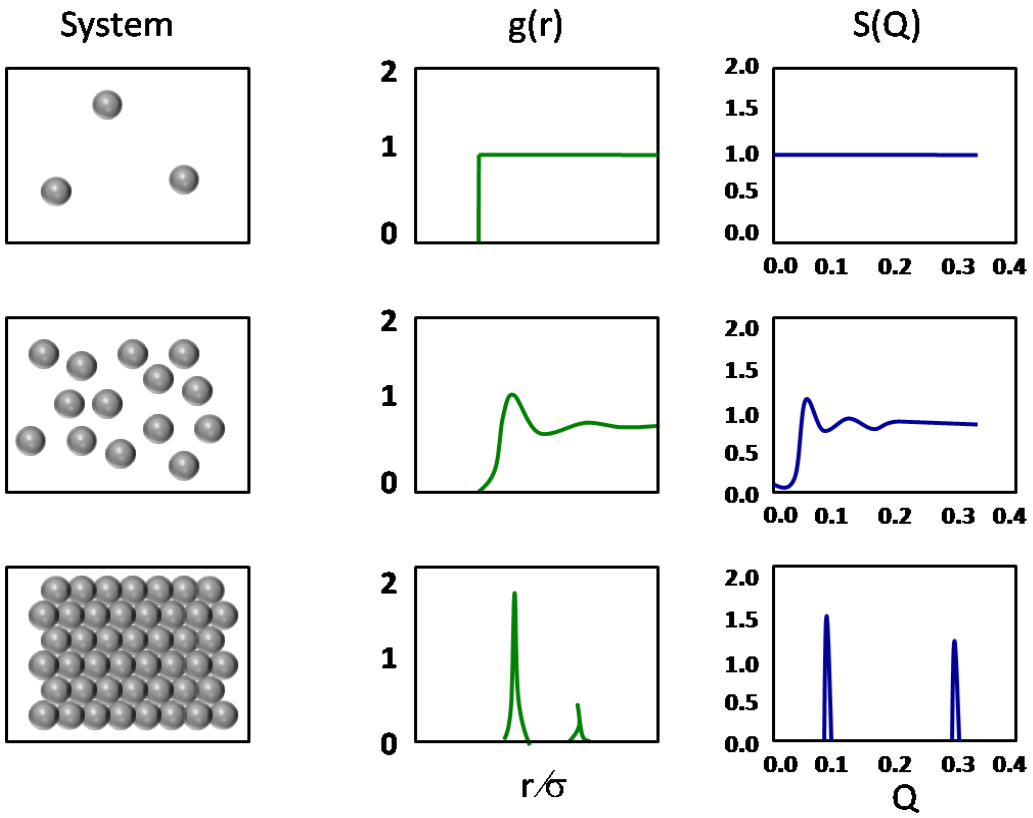

Figure 2.14. Radial distribution function $g(r)$ and corresponding interparticle structure factor S(Q) for dilute, semi-dilute and concentrated systems.

Figure 2.14 shows the radial distribution function $g(r)$ and corresponding interparticle structure factor $S(Q)$ for dilute, semi-dilute and concentrated systems. The $S(Q)$ for colloidal particles in solution as for semi dilute system shows several maxima and minima of decreasing amplitude. The first peak in $S(Q)$ occurs at $Q_{max} \approx 2\pi/d$, where d is the average distance between the particles.

The interparticle structure factors $S(Q)$ for some of the most commonly used potentials are described below:

***S*(*Q*) for hard sphere potential:** In the case of uncharged particles at higher concentrations, hard sphere potential is used which may be defined as

$$\begin{aligned} U(r) &= \infty \quad r \le 2R_{HS} \\ &= 0 \quad r > 2R_{HS} \end{aligned} \tag{2.56}$$

where R_{HS} is the hard sphere radius. The analytic solution for the structure factor is obtained using Percus-Yevick approximation as given by [174]

$$S(Q) = \frac{1}{1 + 24\varphi f(R_{HS}Q)/(R_{HS}Q)} \tag{2.57}$$

in this equation, $f(x)$ is defined as follows:

$$\begin{aligned} f(x) = {} & \alpha(\sin x - x\cos x)/x^2 \\ & + \beta[2x\sin x + (2-x^2)\cos x - 2]/x^3 \\ & + \gamma[-x^4\cos x + 4\{(3x^2-6)\cos x + (x^3-6x)\sin x + 6)\}]/x^5 \end{aligned} \tag{2.58}$$

and

$$\begin{aligned} \alpha &= (1+2\varphi)^2/(1-\varphi)^4 \\ \beta &= -6\varphi(1+\varphi/2)^2/(1-\varphi)^2 \\ \gamma &= \varphi\alpha/2 \end{aligned} \tag{2.59}$$

where $x = R_{HS}Q$ and φ is particle volume fraction.

***S*(*Q*) for screened Coulomb potential:** In case of charged particles $S(Q)$ is calculated under rescaled mean spherical approximation. This interaction takes account of a screened Coulomb potential in addition to hard sphere potential between the particles. In this approximation the particle is assumed to be equivalent sphere of diameter σ through a screened Coulomb potential, which is given by [101, 103, 167]

$$U(r) = U_0 \frac{\exp[-\kappa(r-\sigma)]}{r/\sigma}, \quad r > \sigma \tag{2.60}$$

The contact potential U_0 is given by

$$U_0 = \frac{q^2 e^2}{\pi \varepsilon \varepsilon_0 \sigma (2 + \kappa \sigma)^2} \tag{2.61}$$

where q is charge on the particles, e is the electronic charge, ε is the dielectric constant of the solvent medium and ε_0 is the permittivity of free space. The Debye-Hückel inverse screening length (κ) is calculated by

$$\kappa = \left[\frac{2 N_A e^2 I}{\varepsilon \varepsilon_0 k_B T} \right]^{1/2} \tag{2.62}$$

where I is the ionic strength (mole/m^3) of the solution.

***S*(*Q*) for Baxter's sticky hard sphere potential:** The presence of a short-range attractive interaction between the particles is taken care of using Baxter's sticky hard sphere potential [175]. This potential assumes hard sphere repulsion along with the short-range attraction (represented by a thin attractive well). The sticky hard sphere interaction of particles of diameter σ interacting via a thin attractive potential of width Δ is given by

$$\begin{aligned} \frac{U(r)}{kT} &= \infty && (0 < r < \sigma) \\ &= \ln \frac{12\ \tau\ \Delta}{\Delta + \sigma} && (\sigma \le r \le \Delta + \sigma) \\ &= 0 && (r > \Delta + \sigma) \end{aligned} \tag{2.63}$$

The parameter stickiness ($1/\tau$) provides information about the strength of adhesion.

Figure 2.15 represents the comparison of $S(Q)$ for different interaction potentials of hard sphere, sticky hard sphere and screened coulomb potential for same effective size of particles.

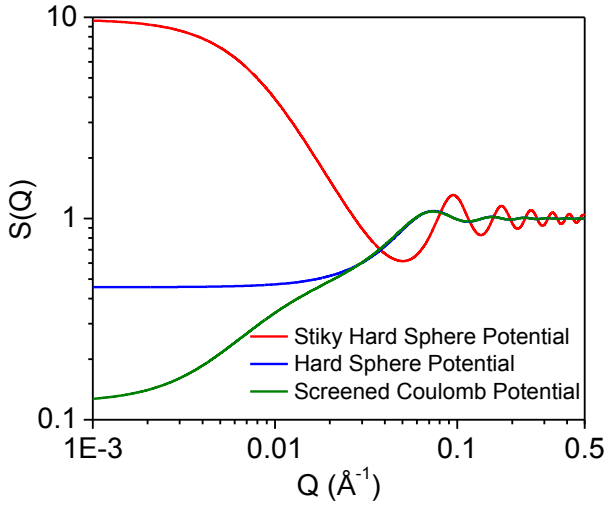

Figure 2.15. Typical S(*Q*) plots for sticky hard sphere, hard sphere and screened coulomb potentials.

***S*(*Q*) for two-Yukawa potential:** The two-Yukawa (2Y) potential having four dimensionless parameters (K_1, K_2, Z_1 and Z_2) is expressed by [81, 82, 176]

$$\frac{U(r)}{kT} = \infty \qquad (0 < r < \sigma) \tag{2.64}$$

$$= -K_1 \frac{\exp[-Z_1(r/\sigma - 1)]}{r/\sigma} + K_2 \frac{\exp[-Z_2(r/\sigma - 1)]}{r/\sigma} \qquad (\sigma < r)$$

where K_1 and K_2 (in units of k_BT) are strength of the attractive and repulsive part of the interaction, respectively. Z_1 and Z_2 are inversely proportional to the range of the interactions. Interparticle distance is represented by r and σ is hard sphere diameter of the particle. $S(Q)$ for 2Y potential is calculated numerically, the details about the calculation may be found elsewhere [176]. The 2Y potentials provide the strength and the range of the individual parts (attractive and repulsive) of the total potential without any predefined assumption. Figure 2.16 shows the calculated $S(Q)$, under mean spherical approximation (MSA), for different values of strength and

range of attractive and repulsive interactions for spherical particle of diameter 100 Å with volume fraction 0.1.

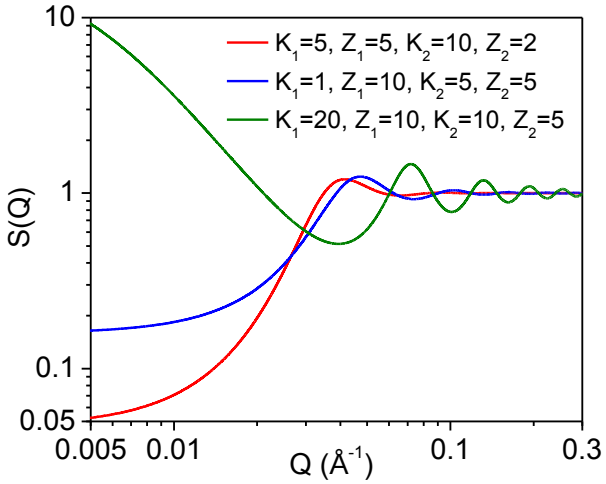

Figure 2.16. Typical S(*Q*) plots for two-Yukawa potential for different values of strength and range of attractive and repulsive interactions.

***S*(*Q*) for fractal structure:** The origin of the term fractal is due to the fact that some objects or some processes exhibit a self-similarity/self-affinity over a wide length scale and possess a characteristic fractional dimension [177-180]. These objects appear same when examined on different scales of magnification. The properties of the fractal systems can be described by quantities, which are proportional to a power of another quantity. This relation is frequently called a power law. These structures may be mass fractals where mass distribution shows self similar behavior throughout the volume, or can be surface fractals where self similarity exists only on the surfaces. For mass fractals, the mass $M(r)$ inside a spherical surface with radius r inscribing the structure is given by $M(r) \alpha r^d$, $d \leq 3$ and $S(Q)$ for such fractal structure can be expressed as [178]

$$S_{mf}(Q) = 1 + \frac{1}{(QR_b)^{D_m}} \frac{D_m \Gamma(D_m - 1)}{[1 + (Q\xi)^{-2}]^{[(D_m-1)/2]}} \times \sin[(D_m - 1)\tan^{-1}(Q\xi)] \qquad (2.65)$$

where $\Gamma(x)$ is the mathematical gamma function of argument x. R_b is the building-block size forming the fractal structure. D_m and ξ are the fractal dimension and the correlation length of the fractal network, respectively.

The expression of $S(Q)$ for surface fractal structure is given by [179, 180]

$$S_{sf}(Q) = Q^{-1}\Gamma(5-D_s)\xi^{5-D_s}\left[1+(Q\xi)^2\right]^{(D_s-5)/2} \sin\left[(D_s-1)\tan^{-1}(Q\xi)\right] \qquad (2.66)$$

It may be mentioned that the scattering intensity from both kind of fractal structures is governed by power law behavior in a definite Q range.

$$\frac{d\Sigma}{d\Omega}(Q) \sim Q^{-D_m} \qquad \frac{1}{\xi} < Q < \frac{1}{R_b} \qquad \text{for mass fractals} \qquad (2.67)$$

$$\frac{d\Sigma}{d\Omega}(Q) \sim Q^{-(6-D_s)} \qquad \frac{1}{\xi} < Q \qquad \text{for surface fractals} \qquad (2.68)$$

Figure 2.17 shows the scattering intensity of mass fractals for various fractal dimensions and fixed building block size (R = 50 Å) and correlation length (ξ = 500 Å). The slope of curve increases with increasing fractal dimension. The higher and lower Q cut off of linearity is decided by the building block size and overall size of fractal in the range given by $1/\xi < Q < 1/R$.

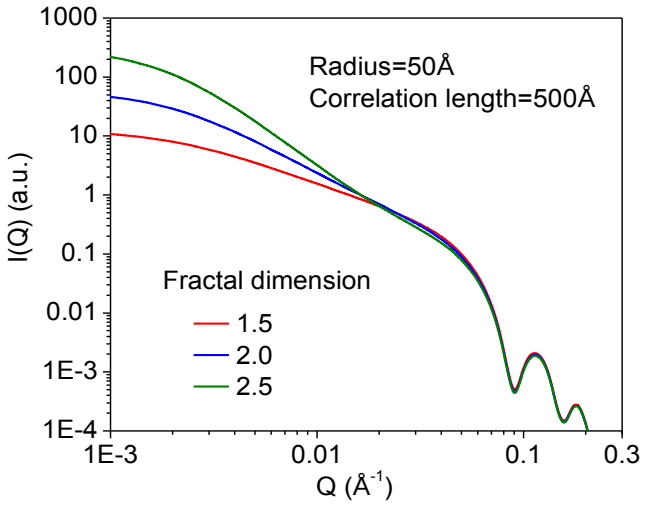

Figure 2.17. Scattering intensity plots for mass fractal structures with varying fractal dimension.

Concept of contrast in SANS: The fundamental difference between neutrons and electromagnetic radiation is the mechanism by which they interact with matter. The x-rays are scattered by electrons surrounding atomic nuclei, but neutrons are scattered by the nuclei [157-159]. As one moves across the periodic table, the x-ray scattering length increases with the atomic number of the atom whereas the neutron scattering length vary in a random fashion (Figure 2.18). For neutrons, isotopes of the same element can have significantly different scattering length. For example the scattering length of hydrogen is negative (- 0.3741 × 10^{-12}cm) and that of deuterium is positive (0.6674 × 10^{-12}cm). This difference of scattering length between *H* and *D* is utilized to have a good contrast between the hydrogenous particle and the solvent by deuterating either the particle or the solvent. Further the scattering length density of solvent can be varied over a long-range by using mixed hydrogenated and deuterated solvents. The variation of scattering length density of solvent can be used to contrast match the scattering length density of solvent to the particle. Thus for ($\rho_p = \rho_m$), the null scattering from that particle is obtained [181-183]. This fact is used to study the multi-component system in a solution, where the scattering contribution from the each component can be studied by contrast matching the other component.

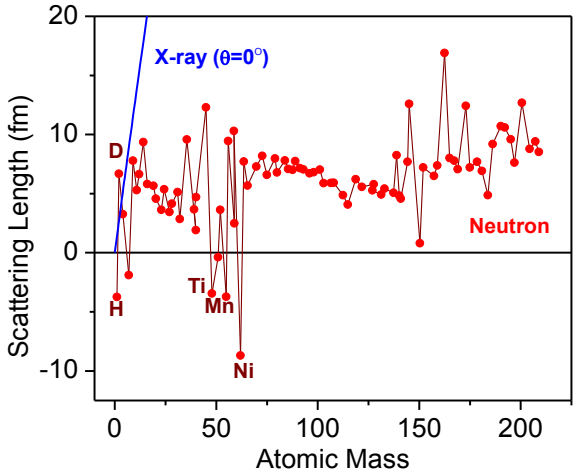

Figure 2.18. Scattering length variation for X-rays and neutrons as a function of atomic mass.

2.4.4. Experimental aspects of small-angle neutron scattering

Schematic of a typical state-of-art SANS facility is shown in Figure 2.19. In a SANS experiment, the incident neutron beam from the source passes through four different regions (i) monochromator, (ii) collimator, (iii) sample and (iv) detector [157]. A particular wavelength of neutron from neutron beam coming from source is selected using a monochromator (e.g. velocity selector) and is then collimated with a slit arrangement. This monochromatic beam of neutrons is scattered by the sample and the angular distribution of scattered radiation is recorded using a position sensitive detector (He^3 gas detector). Large distances between the monochromator to the sample and the sample to the detector are kept to ensure fine beam collimation (low $\Delta\theta/\theta$). It is desirable to use circular apertures for defining the incident beam. However, rectangular apertures (slit geometry) can be used to gain in intensity. Resolution corrections are more important for slit-geometry as compared to those for pinhole geometry. In a typical SANS instrument, $\Delta\theta/\theta$ ~0.1 and thus it is not necessary to have a high wavelength resolution ($\Delta\lambda/\lambda$ ~ 10%).

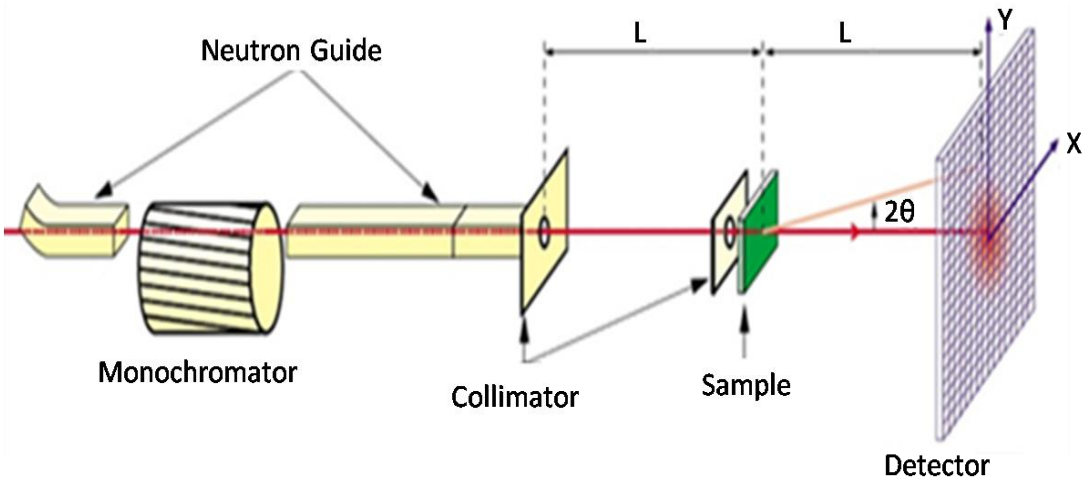

Figure 2.19. Schematic of a typical state-of-art SANS facility.

The small-angle neutron scattering experiments presented in this thesis are performed at SANS diffractometer, Dhruva reactor, BARC [184] and Swiss Spallation Neutron Source, SINQ, Paul Scherrer Institute, Switzerland [185]. Figure 2.20 shows the schematic of SANS diffractometer installed at the guide tube laboratory of Dhruva reactor. The neutron beam from the guide is monochromatized using a velocity selector. The velocity selector selects the particular velocity neutrons using multi-slotted multi-discs rotating at high speed (rpm = 4000-7000). The mean wavelength (λ) and wavelength spread ($\Delta\lambda/\lambda$) of the monochromated beam can be varied in the range 4 to 10 Å and 8 to 20%, respectively. This beam passes through two slits S_1 (2 cm × 3 cm) and S_2 (1 cm × 1.5 cm) before it reaches the sample. Distance between S_1 and S_2 is 2 m and gives an angular divergence of ± 0.5º. The angular distribution of neutrons scattered by the sample is recorded using a one-dimensional position sensitive detector. The sample to detector distance is 1.85 m. The *Q* range of the diffractometer is 0.015-0.35 $Å^{-1}$.

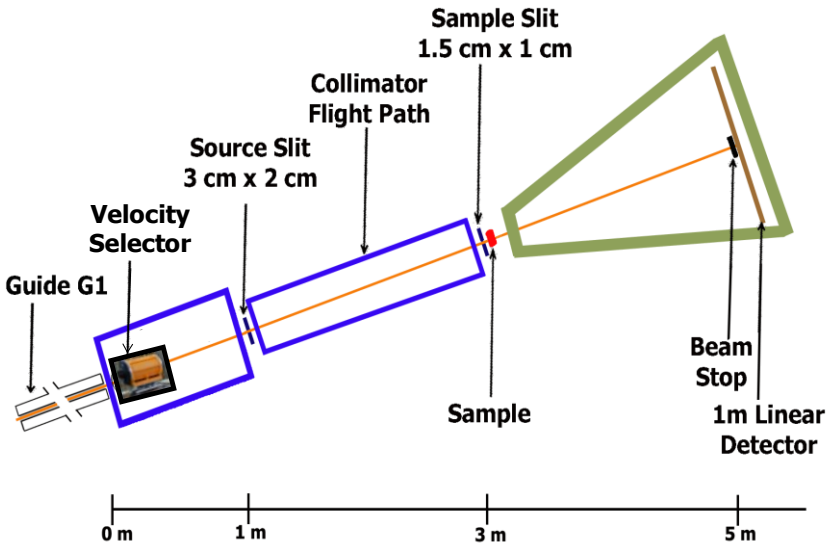

Figure 2.20. Schematic the SANS facility at DHRUVA, BARC, Mumbai, India.

The SANS facilities at SINQ, PSI, Switzerland is 40 m long state-of-art instruments (Figure 2.21). This instrument makes use of a cold neutron source to get sufficient flux at higher

wavelengths. The two-dimensional (96 × 96 cm^2) detector and variable sample to detector distance (1 to 20 m) are used to obtain low-Q values and high signal to background ratio. This instrument can collect the data in the Q range of 0.001 to 1 $Å^{-1}$.

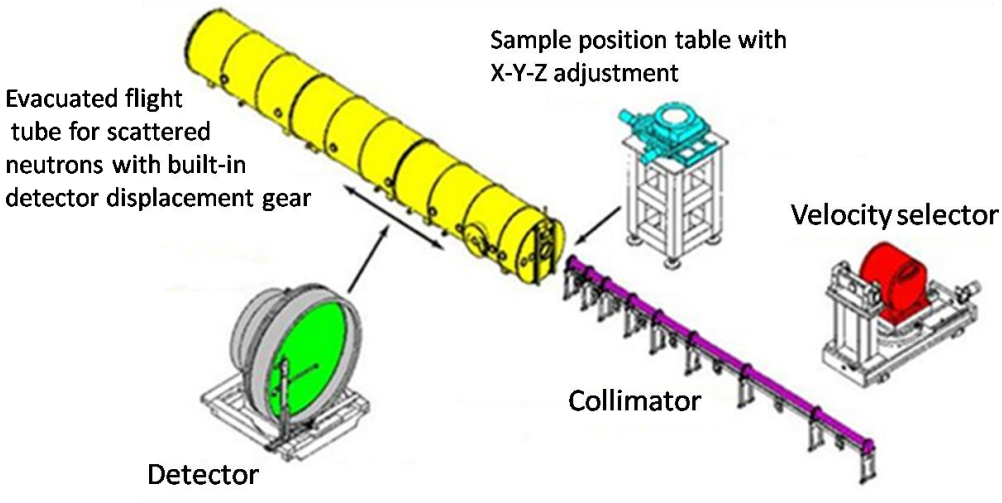

Figure 2.21. Schematic of the SANS-I facility at PSI, Switzerland.

2.4.5. Data reduction and analysis

In a SANS measurement from a sample in solution requires also evaluation of the scattered intensity contributions from the solvent I_{so} and the ambient background I_B. The transmissions of the sample and the solvent should also be determined to correct for the attenuation of neutrons in traversing them. The transmission of the sample T_s should be kept high to minimize multiple scattering effects. The sample cells are usually flat quartz cells with path lengths of 1 to 10 mm. The measured intensity from the sample I_S is corrected for the above various contributions [157, 184, 186]

The background is determined by blocking the beam using a cadmium sheet. The measured intensity $I_B(Q)$ consists of the two contributions, namely the room background [$BKG(Q)$] and the fast neutrons [$I_F(Q)$] because cadmium does not block the fast neutrons.

$$I_B(Q) = BKG(Q) + I_F(Q) \tag{2.69}$$

The measured intensity with solvent I_{SO} consists of three terms: first from the fast neutrons [$I_F(Q)$], second from the room background [$BKG(Q)$] and the third is un-scattered transmitted intensity from the solvent $I_O T_{SO}$, where T_{SO} is the transmission of the solvent and I_O is the incident intensity of thermal neutrons in the beam.

$$I_{SO}(Q) = I_O T_{SO} + BKG(Q) + I_F(Q) \tag{2.70}$$

When the scattered intensity (I_S) with the sample is measured, we get

$$I_S(Q) = I_O T_S + BKG(Q) + I_F(Q) + I_c(Q) \tag{2.71}$$

where T_S is the transmission of the sample, $I_O T_S$ is the un-scattered transmission intensity from the sample and $I_c(Q)$ is the scattered intensity of interest from the sample. The counting time for the experiment is controlled using the monitor detector, which is installed in the incident beam. Solving equations 2.69-2.71 for $I_c(Q)$ gives

$$I_c(Q) = \left[\frac{I_S(Q) - I_B(Q)}{T_S} - \frac{I_{SO}(Q) - I_B(Q)}{T_{SO}} \right] T_S \tag{2.72}$$

In a SANS experiments, the sample is usually taken in a cell, so that it has uniform thickness over the beam area. If $d\Sigma/d\Omega(Q)$ is the differential scattering cross section per unit volume of the sample, the measured scattered neutron intensity is given by

$$I_c(Q) = K T_S t \frac{d\Sigma}{d\Omega}(Q) \tag{2.73}$$

where t is the sample thickness, K is a constant, which depends on instrumental parameters such as incident neutron flux, detector efficiency and solid angle subtended by detector element at sample position etc.

The following expression for the scattering cross section of the sample can be obtained by combining equations 2.72 and 2.73

$$\frac{d\Sigma}{d\Omega}(Q) = \frac{1}{Kt}\left[\frac{I_S(Q) - I_B(Q)}{T_S} - \frac{I_{SO}(Q) - I_B(Q)}{T_{SO}}\right] \tag{2.74}$$

The instrumental constant K is determined by recording the data from a standard sample (e.g. H_2O or Vanadium), the measurement thus provides $d\Sigma/d\Omega\,(Q)$ in absolute units (cm^{-1}).

In SANS experiments, the measured SANS distribution is a convolution of the theoretical $(d\Sigma/d\Omega)(Q)$ and the resolution function of the instrument. Thus one needs to take account of these resolution effects while comparing the calculated and the measured distributions. There are three components to the resolution function for the diffractometer. These contributions arise from the finite collimation, the wavelength distribution and the spatial resolution of the detector. The Q resolution from the first two factors (uncertainties in θ and λ) is given by

$$\frac{\Delta Q}{Q} = \left[\left(\frac{\Delta\theta}{\theta}\right)^2 + \left(\frac{\Delta\lambda}{\lambda}\right)^2\right]^{1/2} \tag{2.75}$$

When a diffractometer is set to detect neutrons with wave vector transfer Q, neutrons with wave vector transfers Q' in the neighbourhood of Q also contribute to the scattering due to the finite instrument resolution. If we describe the resolution function of the diffractometer by $R(Q, Q')$ at the scattering vector Q, the measured intensity $I(Q)$ is related to the scattering cross-section $(d\Sigma/d\Omega)\,(Q)$ by the integral

$$I(Q) = \int R(Q,Q')\frac{d\Sigma}{d\Omega}(Q')dQ' \tag{2.76}$$

The resolution function from the collimation and the detector are independent of *Q* but to wavelength it depends linearly on *Q*. Thus the resolution function is decided by the beam collimation at low-*Q* values whereas by wavelength resolution at high-*Q* values.

2.5. Usefulness of scattering techniques

Scattering techniques are widely used due to several reasons [146, 147]. First, scattering techniques measure the samples in situ and under native conditions. Second, scattering techniques are able to provide fully three-dimensional information and highly sensitive to interactions in the system. Third and most important, scattering techniques can measure average over many particles than can direct method and thus most often provide better quantitative measurements of the average structural and dynamical properties. In this thesis, scattering techniques DLS and SANS has been used to characterize the nanoparticles, proteins and their complexes. Some of the important advantages of these two techniques are:

(i) DLS is a nondestructive technique for particle size characterization of colloidal suspensions, mainly in the submicron range. Most of the colloidal systems such as micelles, nanoparticles and proteins fall in this range. DLS is very fast and provide ensemble average information.

(ii) DLS measures the autocorrelation function of scattered light intensity from which the diffusion coefficient of the particles and hence the apparent particle size and size distribution can be calculated. Thus any changes in interaction between particles and/or structural evolution within the system can be monitor by DLS. Appropriate corrections to the diffusion coefficient can be applied to account for interparticle interactions. Since DLS provides intensity weighted particle size distribution which can be used as a guide to assess the presence of agglomerates or different sizes of particles.

(iii) SANS is an excellent technique that provides information about both the structure (size and shape) and interaction through form factor and structure factor of the scattering intensity, respectively. SANS measures the scattering intensity in the absolute scale and this fact can be used to obtain different levels of information such as particle concentration, internal structure of particle, formation of aggregates etc.

(iv) The unique advantage of SANS to study multi-components system is due to easy possibility of contrast-variation in this technique. The scattering due to internal variation of scattering length density could be separately determined if the solvent scattering density is changed isomorphously. Due to large difference between neutron scattering amplitudes of hydrogen and deuterium, SANS is of considerable importance for mulit-component systems unlike the complementary SAXS and light scattering techniques.

In this theis, UV-vis spectroscopy and scattering techniques [DLS and SANS] have been used to characterize the nanoparticle-protein complexes. The adsorption isotherms of proteins on nanoparticles and their resultant phase behaviour are determined by UV-vis spectroscopy. On the other hand, the structure and interaction information of the complexes are obtained using DLS and SANS. The studies are carried out from the complexes of silica nanoparticles with two proteins lysozyme and BSA under varying solution conditions (ionic strength and pH) as well as size of the nanoparticles.

Chapter 3

Study of Complexes of Silica Nanoparticles with Lysozyme and BSA Proteins

3.1. Introduction

The properties of nanoparticle-protein complexes depend on the characteristics of both the nanoparticles and proteins. These complexes have been mostly studied for the interaction of inorganic nanoparticles with globular proteins [187, 188]. Use of inorganic nanoparticles in such complexes is particularly of interest because they are easy to functionalize and can be prepared readily in large amount by relatively simpler methods with good control over size and size distribution. Different nanoparticles used are those of metals (e.g. Au, Ag, Cu), oxides (e.g. Fe_3O_4, SiO_2, TiO_2) and semiconductor materials (e.g. Ag_2S, CdS, CdSe) [10, 25, 189, 190]. Amongst these silica (SiO_2) nanoparticles are one of the most commonly used model nanoparticles, which are nontoxic and biocompatible as well as less expensive and commercially available [50]. The globular proteins (e.g. lysozyme, BSA) are known to be highly stable, available with high purity and easily soluble in water [15, 76]. For charged stabilized nanoparticles, the electrostatic interaction between nanoparticles and proteins governs their phase behavior [21-23, 126]. For example, the adsorption of the cationic lysozyme on the surface of anionic silica nanoparticles has been found to leading the protein-mediated bridging aggregation of the nanoparticles [191, 192]. On the other hand, despite BSA and silica nanoparticles having similar charges at physiological condition, site-specific adsorption of BSA on silica nanoparticles has been reported [193]. Site-specific adsorption of proteins can enhance

the colloidal stability by steric and/or electrosteric effects. Thus, the formation of the core-shell structure as a consequence of adsorption of BSA on a silica surface is believed unlikely to favor any kind of nanoparticle aggregates [141].

In this chapter, the interaction of anionic silica nanoparticles with two globular proteins lysozyme and BSA over a wide range of proteins concentration at physiological condition (pH 7) has been studied [194, 195]. At pH 7, the electrostatic nature of lysozyme is cationic whereas of BSA is anionic. The adsorption behavior of proteins on the nanoparticles and resultant effect on the phase behavior of the nanoparticle-protein complexes have been measured by a combination of spectroscopy and scattering techniques. UV-vis spectroscopy provides the adsorption of protein on the nanoparticles and phase behavior of the complexes. The lysozyme is found to be adsorbing whereas BSA remains non-adsorbing in all these systems. Interestingly, both the proteins show similar phase behavior with the nanoparticles. The evolution of structure and interaction is examined by the scattering techniques-dynamic light scattering (DLS) and small-angle neutron scattering (SANS). The interactions governing the phase behavior have been modeled using the two-Yukawa (2Y) potential accounting for the competitive electrostatic repulsion and protein induced attraction between the nanoparticles. The 2Y potential provides the strength and the range of the individual parts (repulsive and attractive) of the total potential without any predefined assumption [176].

3.2. Experimental details

Spherical silica nanoparticles (Ludox HS40 catalog no. 420816), hen egg lysozyme (catalog no. 62970) and BSA (catalog no. A2153) proteins were purchased from Sigma-Aldrich. Electrostatically stabilized Ludox silica nanoparticles was received as dispersed colloidal particles having 40 wt % concentration in water and proteins were in lyophilized powder form.

Samples were prepared by dissolving the weighted amount of nanoparticles and proteins in a 20 mM phosphate buffer at pH 7 prepared in H_2O or D_2O. Samples for neutron scattering experiments were prepared in D_2O instead of H_2O because of the high contrast for the hydrogenous sample in D_2O. All the measurements were carried out for a fixed concentration (1 wt %) of silica nanoparticles and varying the concentration (0-5 wt %) of proteins. The adsorption isotherms of proteins on the nanoparticles were obtained using a nanodrop spectrophotometer ND 1000. This instrument has a pulsed Xenon flash lamp as a source (2200-7500 Å) and the sample absorbance spectra were measured using CCD arrays. The DLS measurements were performed on nanoparticle size analyzer SZ-100 (HORIBA, Japan). This instrument is equipped with a green (5320 Å) laser and photomultiplier tube detectors. A detection angle of 173° was chosen for the DLS measurements. The SANS experiments were performed using SANS instrument at the Dhruva Reactor, Bhabha Atomic Research Centre (BARC), Mumbai, India [184] and SANS-I at the Swiss spallation neutron source, SINQ, Paul Scherrer Institut (PSI), Switzerland [185], to probe different length scales of the system. The SANS facility at BARC has limited *Q*-range, whereas the facility at PSI can allow access of much lower-*Q* values. The freshly prepared samples were held in Hellma quartz cells having thickness 2 mm and temperature kept constant at 30°C during the measurements. The data were corrected and normalized to absolute scale following the standard procedure.

3.3. Data analysis

a. Dynamic light scattering. DLS has been used to measure the collective diffusion of the nanoparticles, proteins and their complexes. The intensity autocorrelation function (ACF) of the respective monodisperse system is related to the translational diffusion coefficients of the particle through the relation as discussed in section 2.3.2 and given by [148, 150]

$$g^2(\tau) = 1 + \beta \left| \exp(-DQ^2\tau) \right|^2 \tag{3.1}$$

where D is the diffusion coefficient of particle and β is the spatial coherence factor which depends on the instrument optics. As expected, the pure components (nanoparticles and proteins) exhibit a single relaxation mode due to their diffusion in the aqueous medium and the data can be analyzed by cumulant method. Subject to proteins adsorption on the nanoparticles surface, the corresponding changes in the diffusion of complex can be detected by DLS. In the case of high polydispersity and/or bimodal distributions, CONTIN method has been used to calculate the effective value of diffusion coefficient and size distribution [153, 154].

b. Small-angle neutron scattering. SANS has been employed to determine the structure (size and shape) of the individual components (nanoparticles and proteins), the evolution of interaction and morphology of the resultant nanoparticle-protein complexes. For a collection of monodisperse interacting particles, the coherent differential scattering cross-section per unit volume [$d\Sigma/d\Omega(Q)$] as described in section 2.4.1 and can be expressed by [156-158]

$$\frac{d\Sigma}{d\Omega}(Q) = \varphi V \left(\rho_p - \rho_s\right)^2 P(Q) S(Q) + B \tag{3.2}$$

where φ is the volume fraction and V is the volume of particle. ρ_p and ρ_s are scattering length densities of particles and solvent, respectively. $P(Q)$ is the orientational average of the square of the form factor amplitude [$P(Q) = \langle F(Q)^2 \rangle$] and gives information about shape and size of the particle. Form factor of standard geometry (e.g. spherical, ellipsoidal) for nanoparticles and proteins are used to model the scattering. The evolution of interaction between nanoparticles in presence of proteins has been modeled by the two-Yukawa potential (Equation 2.64) [176]. The structure factor $S(Q)$ for this potential is obtained numerically by solving the Ornstein-Zernike equation under mean spherical approximation (Equation 2.54). $S(Q)$ for the aggregates structure

has been modeled by mass fractal morphology (Equation 2.65) [178]. The details of $S(Q)$ used are give in chapter 2.

Throughout the data analysis corrections were made for instrumental smearing where calculated scattering profiles are smeared by the appropriate resolution function to compare with the measured data. The parameters in the analysis were optimized by means of nonlinear least-squares fitting program [163].

3.4. Results and discussion

3.4.1. Characterization of nanoparticles and proteins

The structural parameters of the individual nanoparticles and proteins (lysozyme and BSA) are obtained by SANS and DLS. The measurements have been performed at 1 wt % for each component in aqueous solution at pH 7. The data are shown in Figure 3.1. In the case of SANS [Figure 3.1(a)], all the data show a monotonically decreasing profile as a function of scattering vector Q. At low concentration (1 wt %) [φ = 0.00454] and in absence of any correlation peak these systems can be treated as noninteracting dilute system i.e. $S(Q) \sim 1$. This has also been confirmed by scaling of the SANS data of lower concentration (say 0.5 wt %) to 1 wt %. Thereby, the scattering is only modeled by the form factor of the scatterers [192]. The variation in SANS profiles of the nanoparticles and proteins can be attributed to differences in size and shape as well as contrast of the constituent with respect to the solvent. The magnitude of scattering from such dilute systems increases with the volume of individual particles and the width of the scattering profile is reciprocal to the size of the particles (Equation 2.37 and 2.40). This suggests that qualitatively the size of the nanoparticles is larger than the proteins used and BSA is larger than the lysozyme protein. Fitted parameters of silica nanoparticles and proteins are given in Table 3.1. A polydisperse spherical model, combining Equations 2.37, 2.38 and

2.39, is used to fit the scattering profile of the silica nanoparticles. The mean radius of the silica nanoparticles is found to be 8.80 nm with a polydispersity of 0.16. Both lysozyme and BSA proteins are known to have globular structures and hence have been modeled with ellipsoidal shapes. Lysozyme data are best fitted with prolate ellipsoidal having semimajor and semiminor axes of 2.40 and 1.35 nm, respectively. On the other hand, BSA has an oblate ellipsoidal shape with semimajor and semiminor axes of 4.20 and 1.50 nm, respectively. These structural parameters of both the nanoparticles and proteins are found to be in agreement with earlier reported values [22, 23, 196]. The visibility of form factor oscillations at higher-Q region depends on the polydispersity of the particles and their smearing increases with the polydispersity. The relatively poor resolution in the case of SANS also smears these oscillations as reflected in the protein data. The main reason for poor Q resolution (ΔQ) arises from the contribution of wavelength spread ($\Delta\lambda/\lambda$), where ΔQ increases linearly with Q [184, 197]. There is the possibility of the existence of some permanent aggregates in proteins solution which could be responsible for scattering buildup at low Q as seen in the case of lysozyme [28]. The calculated values of the surface area per particle, and number density of the nanoparticles and protein systems, as well as the specific surface area of the nanoparticles are also given in Table 3.1. Figure 3.1(b) shows the autocorrelation function of DLS data of nanoparticles and proteins. The data show only one relaxation mode and hence cumulant method has been used for analysis. The corresponding size distributions are shown in inset of Figure 3.1(b). The mean hydrodynamic sizes (diameters) of the nanoparticles, lysozyme and BSA are found to be 21 nm, 4.4 nm and 8.3 nm, respectively. The sizes obtained by DLS for all three components are little higher than those obtained by SANS. The contribution of the hydration layer in diffusion of particles is mainly responsible for the higher size in case of DLS. The significantly larger size of

the nanoparticles than those of the proteins has been chosen from the point of view that there is enough adsorption of proteins on the nanoparticles, if any.

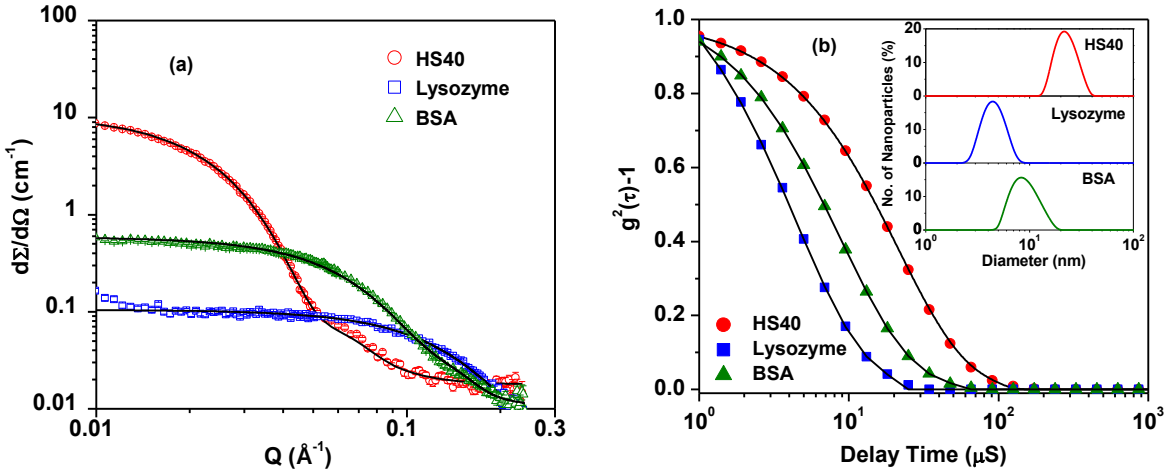

Figure 3.1. (a) SANS data and (b) DLS data of 1 wt % of HS40 silica nanoparticles, lysozyme and BSA proteins in aqueous solution. Inset in (b) shows the corresponding size distributions.

Table 3.1. Fitted parameters of 1 wt % of HS40 silica nanoparticles, lysozyme and BSA proteins in aqueous solution. The mass density of the silica nanoparticles used is 2.2 g/cc.

(a) HS40 silica nanoparticles

Nanoparticle	Mean radius R (nm)	Polydispersity σ	Surface area per particle (nm^2)	Number density n_{NP} (m^{-3})	Specific surface area (m^2/g)
HS40	8.80	0.16	9.7×10^{2}	1.57×10^{21}	155

(b) Proteins

Protein system	Shape	Semimajor axis a (nm)	Semiminor axis b (nm)	Equivalent radius R_e (nm)	Surface area per molecule (nm^2)	Number density n_P(m^{-3})
Lysozyme	Prolate ellipsoidal	2.40	1.35	1.63	35	4.09×10^{23}
BSA	Oblate ellipsoidal	4.20	1.50	2.98	130	9.07×10^{22}

3.4.2. Adsorption of proteins on nanoparticles

The interaction of the nanoparticles with individual protein in terms of adsorption is studied using UV-vis spectroscopy. The samples for these measurements were prepared by mixing a fixed concentration (1 wt %) of silica nanoparticles with varying concentration of lysozyme and BSA proteins in aqueous solution. These samples are filled in cuvettes and centrifuged at 18000g for 30 minutes to separate free protein if any from that of the protein adsorbed on the nanoparticles. The absorbance spectra for both the proteins show a peak at about 280 nm and are used to determine the protein concentration in the supernatant [141, 191, 192]. The difference between initial (total) and supernatant concentration gives the amounts of adsorbed proteins. Figure 3.2 shows the amount of adsorbed protein on silica nanoparticles versus total protein in the system. The adsorption of cationic lysozyme and anionic BSA on anionic silica nanoparticles is found to be very different. The adsorption of lysozyme increases with concentration and follows typical exponential growth behavior [Figure 3.2(a)]. On the other hand, BSA protein does not show any adsorption [Figure 3.2(b)]. The dominance of electrostatic repulsion between similarly charged nanoparticles and BSA molecule over their site-specific attraction seems to prevent the adsorption of BSA on the nanoparticles. The data of lysozyme protein is fitted with equation $A = A_0\,[1\text{-}\exp^{-KC}]$, where A is the adsorbed protein, A_0 is the saturation value, K is the adsorption coefficient and C is the total lysozyme concentration. The saturation value is found to be 0.50 wt % and adsorption coefficient is 2.50 wt $\%^{-1}$. The adsorption is decided by the interplay of nanoparticle-protein attraction and protein-protein repulsion. At higher concentration protein-protein repulsion leads the saturation of protein adsorption on the nanoparticles. At saturation value, the number of adsorbed lysozyme molecules per nanoparticles is found to be about 130.

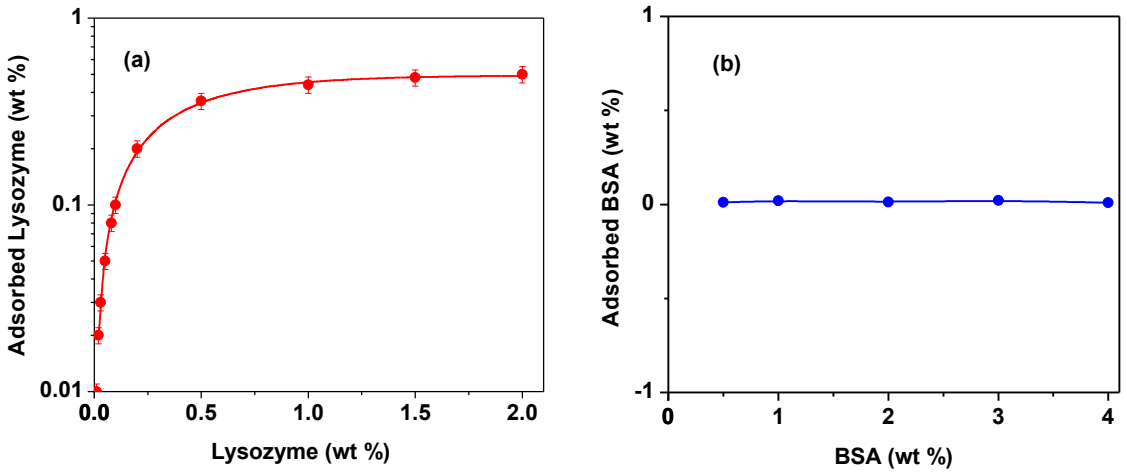

Figure 3.2. Adsorption isotherms of (a) lysozyme and (b) BSA proteins on 1 wt % HS40 silica nanoparticles at pH 7. Lysozyme adsorbs strongly on the nanoparticles, whereas BSA does not adsorb on the nanoparticles. Data were calculated from the absorbance spectra for both the proteins at 280 nm.

3.4.3. Phase behavior of nanoparticle-protein complexes

Figure 3.3 shows the phase behavior of 1 wt % of HS40 silica nanoparticles with varying concentration of lysozyme and BSA. The figure depicts the variation in the transmission of light (600 nm) of a silica nanoparticle system as a function of protein concentration. The transmission of light depends on the evolution of the structure in the system where the formation of larger structures will scatter more light and hence the decrease in the transmission. It is interesting to note that despite having a different nature of interactions of lysozyme and BSA with the nanoparticles [Figure 3.2], both proteins render the similar phase behavior where nanoparticle-protein system transform from one-phase (clear) to two-phase (turbid) above a critical protein concentration (CPC). As a result the transmission of light decreases dramatically above a critical concentration for both the proteins. The CPC is very different for lysozyme and BSA, almost two orders higher in the case of BSA. The comparison of phase behavior for the two proteins can be divided in three concentration-dependent regions. The first region corresponds to the very low

protein concentrations (<0.01 wt %) where silica nanoparticles with both lysozyme and BSA have high transmissions corresponding to the systems having similar structures of the nanoparticles without and with proteins. All the systems form a clear solution in this region. In the second region of intermediate protein concentration (0.01-1 wt %), the transmission for lysozyme decreases and becomes very low whereas transmission with BSA remains unchanged. The decrease in the transmission with lysozyme is expected if the nanoparticles aggregate in the presence of lysozyme. This system is also observed to be turbid in this region. In the last (third) region (> 1wt %), BSA also shows low transmission (becomes turbid) similar to that observed with lysozyme. This suggests both proteins show a similar phase behavior of structural evolution despite the difference in the electrostatic interaction (attraction versus repulsion) of the two proteins with the nanoparticles. However, the concentration range over which the structural evolution is observed and more importantly the mechanism leading to the similar phase behavior is very different. The evolutions of structure and interplay of interactions governing the phase behavior of nanoparticle-protein complexes have been investigated using DLS and SANS.

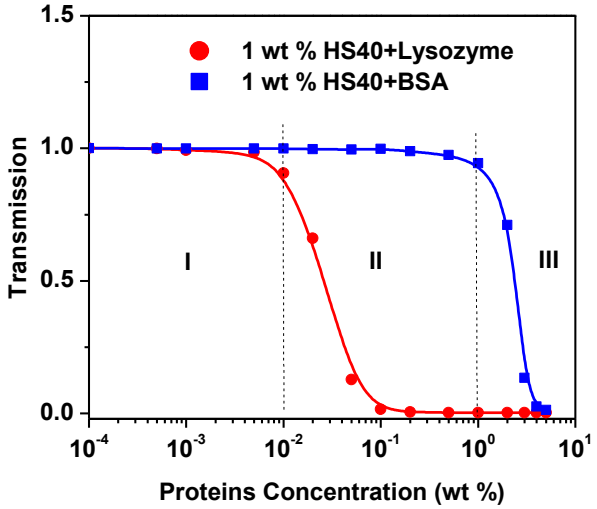

Figure 3.3. Transmission of light (600 nm) in 1 wt % HS40 silica nanoparticles with varying concentration of lysozyme and BSA proteins.

3.4.4. Structure and interaction of nanoparticle-protein complexes

The DLS autocorrelation functions of the nanoparticle with varying the concentration of lysozyme corresponding to the phase behavior (Figure 3.3) are shown in Figure 3.4(a). The addition of proteins into the nanoparticles leads to a shift of the diffusive relaxation to longer relaxation time and most prominently to the appearance of additional, slower relaxation modes. This can arise due to the evolution of attractive interaction between the nanoparticles and/or the formation of the nanoparticle aggregates mediated by the lysozyme. The calculated intensity-average size distributions of the nanoparticles with varying lysozyme concentration using Equation 2.13 employing CONTIN analysis are given in Figure 3.4(b). Addition of lysozyme shifts the mean size of the distribution to larger values, which may be attributed to the formation of nanoparticle-protein complexes. Furthermore, increase in the lysozyme concentration leads to the aggregation of the nanoparticles resulting in significantly large sizes of the distribution. Moreover, there exists a range of lysozyme concentrations where the size distribution is bimodal, indicating the coexistence of nanoparticles undergoing an attractive interaction along with nanoparticle aggregates. The distribution in the size of the nanoparticles and their thermal energy is believed to be mostly responsible for the bimodal distribution. At sufficiently high protein concentrations, the system again converts into a monomodal distribution having a higher mean size corresponding to nanoparticle aggregates in two-phase region of the nanoparticle-protein phase behavior.

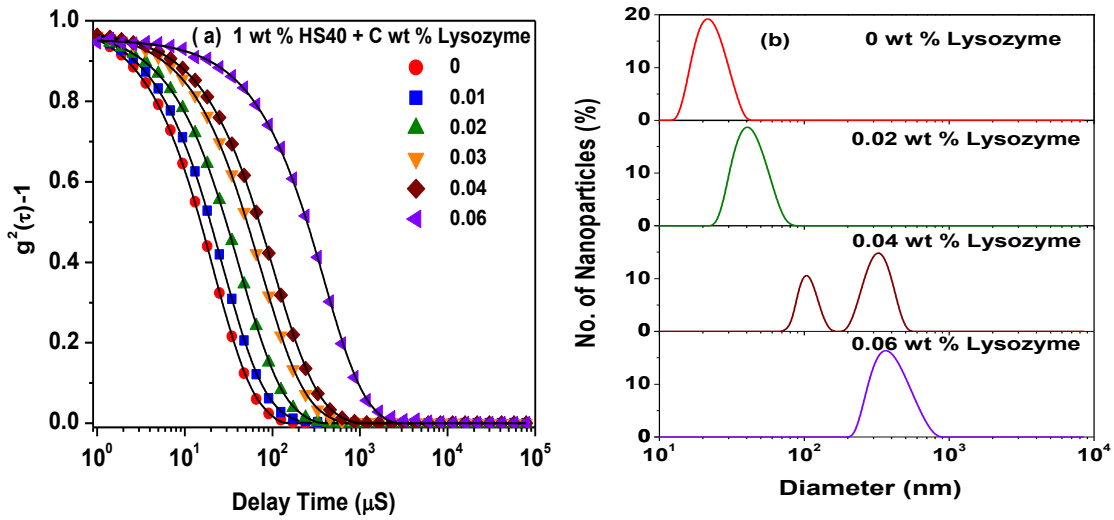

Figure 3.4. DLS data of 1 wt % HS40 silica nanoparticles with varying concentration of lysozyme (a) autocorrelation function and (b) particles size distribution.

Figure 3.5 presents the DLS data of the nanoparticle-BSA system. The overall features are similar to those of the nanoparticle-lysozyme system at higher BSA concentration. The auto correlation functions of the nanoparticles as a function of BSA concentration are shown in Figure 3.5(a). The inset of Figure 3.5(a) shows the autocorrelation function in the low concentration region of BSA. Unlike the case of the nanoparticle-lysozyme system, there are no significant changes in autocorrelation function of the nanoparticle-BSA system observed up to 0.2 wt % of BSA protein. This supports the fact that BSA protein is nonadsorbing to the nanoparticles. The nonadsorption of BSA induces the depletion attraction between the nanoparticles [103]. The changes in autocorrelation function at higher BSA concentrations are due to evolution of the depletion interaction and resultant structures. The corresponding intensity-weighted size distributions are provided in Figure 3.5(b). The strength of the depletion interaction is known to increases with the depletant (BSA) concentration [103, 115, 198]. The depletion-induced attractive interaction slows down the diffusion of the individual nanoparticles and hence

increases the apparent size of the nanoparticles. The further increase in depletion interaction with BSA concentration leads to aggregation of the nanoparticles in two-phase region.

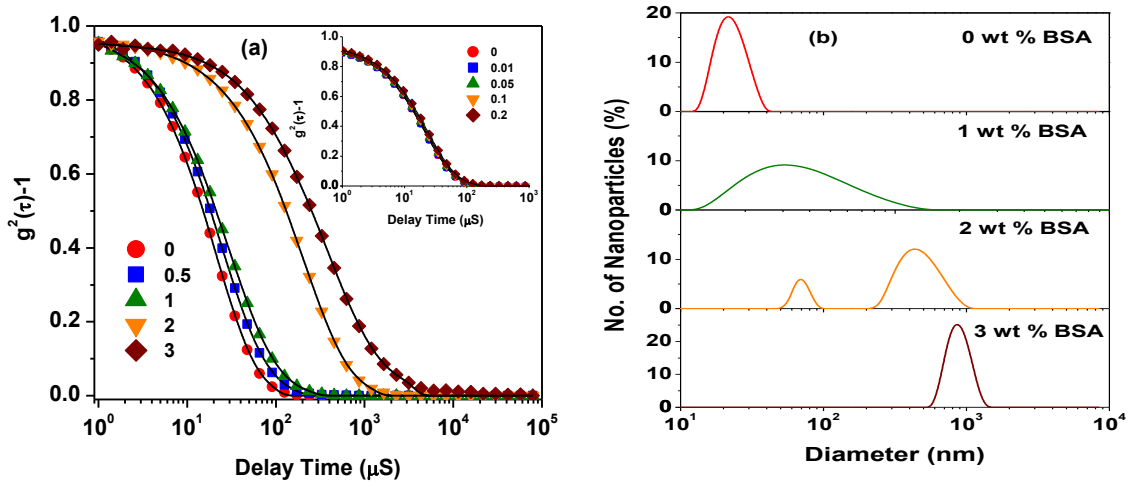

Figure 3.5. DLS data of 1 wt % HS40 silica nanoparticles with varying concentration of BSA (a) autocorrelation function and (b) particles size distribution. Inset in Figure (a) shows the autocorrelation function at low BSA concentrations.

It has been observed in DLS data that the phase behavior of nanoparticle-protein systems can be interpreted in terms of the evolution of attractive interaction and/or aggregation. However, DLS has limitations in separating contributions of interaction and structure, both of which can influence the data in the same way. SANS can measure structure and interaction separately through the form factor and structure factor of the scattering intensity, respectively. The SANS data from 1 wt % of HS40 silica nanoparticles with lysozyme and BSA proteins in the different regions of their phase behavior (Figure 3.3) are compared in Figure 3.6. In region I of the phase behavior, at very low protein concentrations, the SANS data in the presence of both protein systems overlap that of the pure silica nanoparticles system [Figure 3.6(a)]. This region represents where the number density of proteins is very low and therefore their interaction (lysozyme and BSA) if any with the nanoparticles seems negligible. For region II, silica nanoparticles with lysozyme and BSA behave very differently which is also reflected in the

SANS data [Figure 3.6(b) and 3.6(c)]. The data of BSA in region II are similar to that in region I, which is an indication of no significant interaction of BSA with nanoparticles observed even up to 0.5 wt % concentration of BSA. In the low-*Q*, the scattering is dominated by the individual nanoparticles, whereas, at high-*Q*, the scattering from the noninteracting protein becomes visible with the increase in protein concentration [Figure 3.6(c)]. Unlike the case of BSA, the lysozyme data show a strong scattering buildup in the low-*Q* which is usually seen for aggregated particles [82,198]. These aggregates are believed to be responsible for the decrease in the transmission of the nanoparticle-lysozyme system in region II. In region III, the presence of both BSA and lysozyme make the nanoparticles system turbid. The SANS data of BSA in this region (region III) are found to be similar to that as observed for lysozyme in region II [Figure 3.6(d)]. The low-*Q* data for both proteins suggest similar aggregation in these systems, whereas the difference at high-*Q* arises due to the difference in the sizes of the two proteins. The fact that lysozyme and BSA are oppositely charged, their expected different interactions with the nanoparticles are responsible for the similar behavior of the nanoparticles in region III.

To understand the evolution of interaction and structure of silica nanoparticles in the presence of lysozyme, the scattering profiles of 1 wt % of silica nanoparticles with varying concentration (0-5 wt %) of the lysozyme protein are shown in Figure 3.7. Based on the features of scattering data, these have been divided into three concentration-dependent groups: a low protein concentration (0.0-0.02 wt %) group [Figure 3.7(a)] where the system goes from region I to region II of the phase behavior and the remaining two groups corresponding to region II for the intermediate protein concentration (0.05-0.2 wt %) group [Figure 3.7(b)] and the higher protein concentration (0.5-5 wt %) group [Figure 3.7(c)]. Figure 3.7(a) shows that adding small amounts of lysozyme with silica nanoparticles gives a scattering buildup in the low-*Q* and the system moves from region I to region II. It is also seen that there is no significant change in the

scattering profiles except in the low-*Q*. The scattering buildup in the low-*Q* arises due to a change in interaction between nanoparticles and/or by the evolution of a structure to larger sizes [81, 191, 192]. At the physiological condition (pH 7), silica nanoparticles and lysozyme are oppositely charged, as a result lysozyme adsorbs on the surface of the silica nanoparticles neutralizes the charge and induces the attractive attraction between the nanoparticles. At low protein concentrations (≤0.02 wt % lysozyme), the system is characterized by the nanoparticles undergoing attractive interactions [Figure 3.7(a)] and the corresponding *S*(*Q*) has been modeled by the 2Y potential giving a signature for the existence of short-range attractive interaction in the system [22, 23]. The fitted parameters are given in Table 3.2 (a). With further increase in the protein concentration the data belong to the region of phase behavior where the bimodal distribution has been observed in DLS [Figure 3.4(b)]. The data are therefore fitted considering nanoparticles undergoing attractive interaction and coexisting with the aggregates of the nanoparticles. It has been found that the linearity of scattering increases at the low-*Q* range without affecting the high-*Q* range with increasing the concentration of lysozyme [Figure 3.7(b)]. The linearity at low-*Q* on the log-log scale suggests that the structure of aggregates could be fractal [178, 199]. The mass fractal aggregates along with some particles interacting with the 2Y potential (Equation 2.64) have been used to fit the scattering profile for lysozyme concentration (0.05-0.2 wt %) giving a signature for the existence of short-range attractive interaction in the system. As the lysozyme concentration is not enough to bind every particle in the fractal structure, the remaining particles form flocculates interacting via oppositely charged protein-mediated short-range attractive interaction between nanoparticles. On increasing the protein concentration, the fraction of aggregates increases. For protein concentration (0.5-5 wt %), as shown in Figure 3.7(c), all the nanoparticles have undergone fractal aggregation. The scattering hump at higher-*Q* values suggests the excess protein coexisting with the nanoparticle

aggregates [192]. Thus, the strong electrostatic attractive interaction in the case of silica nanoparticles with lysozyme proteins leads to the protein-mediated bridging aggregation of nanoparticles irrespective of the protein concentration used. The fractal dimension is found to be about 2.4 in all these systems [Table 3.2 (b) and (c)]. The observations of phase behavior in Figure 3.3 are found to be consistent with that of the SANS results in Figure 3.7. The decrease in light transmission for lysozyme in moving from region I to region II in Figure 3.3 follows the increase in the calculated volume fraction of the aggregated nanoparticles [Table 3.2 (b)].

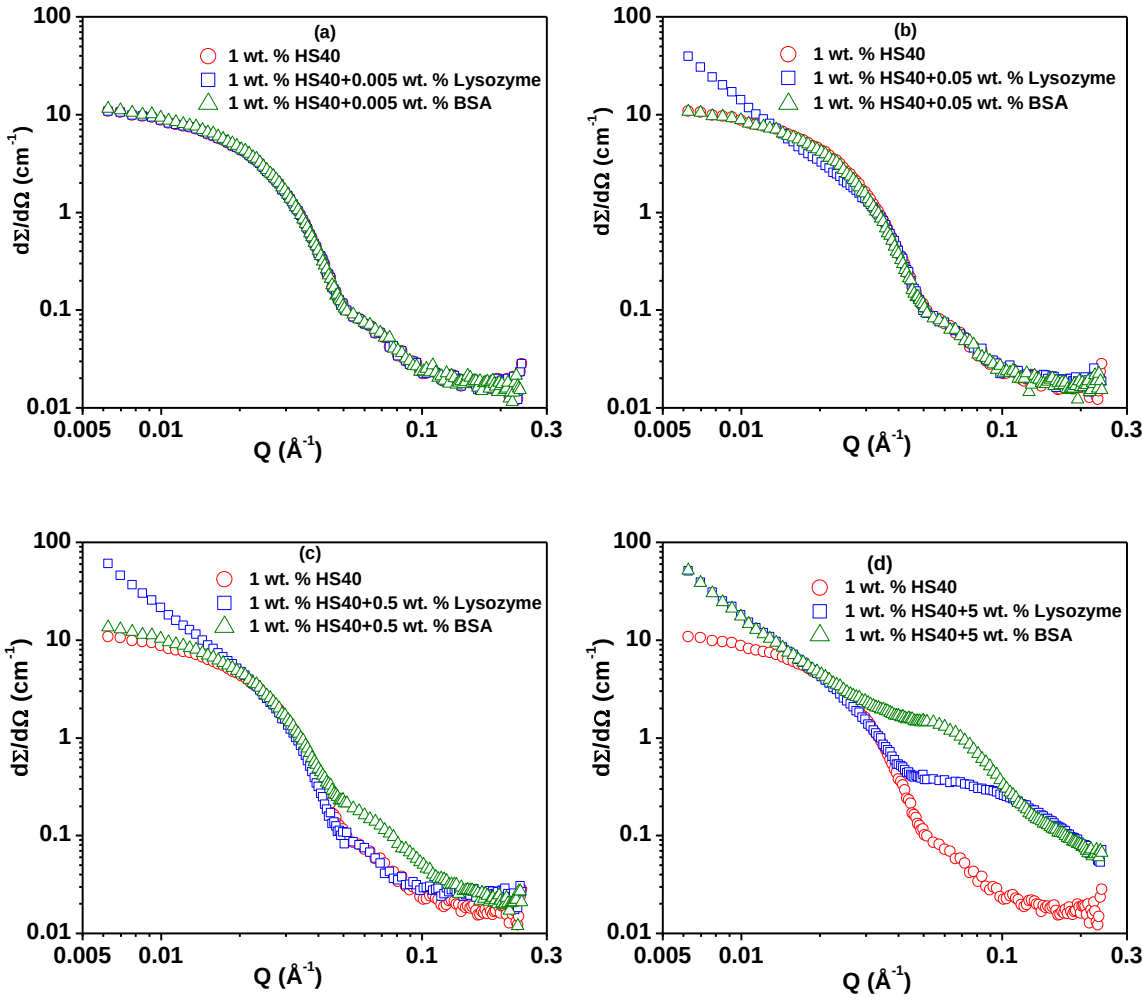

Fgure 3.6. SANS data of 1 wt. % HS40 silica nanoparticles with (a) 0.005 wt. %, (b) 0.05 wt. %, (c) 0.5 wt. % and (d) 5 wt. % of lysozyme and BSA concentrations.

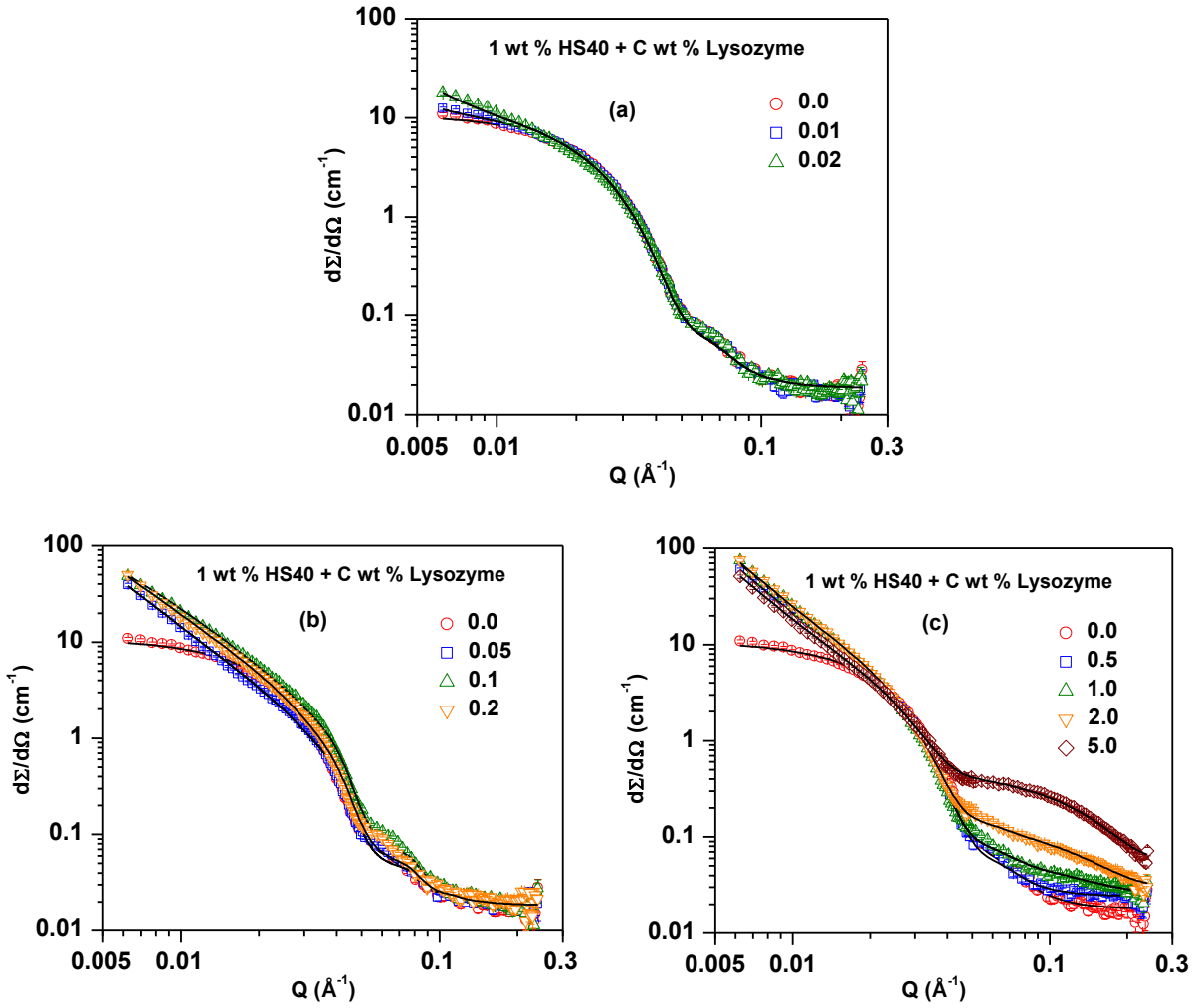

Figure 3.7. SANS data of 1 wt % of HS40 silica nanoparticles with lysozyme protein (a) low concentration (0.0-0.02 wt %), (b) intermediate concentration (0.05-0.2 wt %) and (c) high concentration (0.5-5 wt %).

The protein-mediated interaction between nanoparticles is fitted using the 2Y potential comprising four fitting parameters (K_1, K_2, Z_1, Z_2). Here, K_1 and Z_1 are the fitting parameters of the attractive potential to give the strength (proportional to K_1) and range (proportional to $1/Z_1$), respectively [176, 200]. On the other hand, K_2 and Z_2 are the fitting parameters of the repulsive potential, which provides the strength (related to effective charge) and range (related to ionic strength), respectively [82]. The parameters of the repulsive potential have been determined from the pure concentrated solution of the nanoparticles as it is difficult to see the $S(Q)$ contribution

from the repulsive interaction in 1 wt % or lower concentration of the nanoparticle system. The SANS data for pure nanoparticles are taken at different concentrations as shown in Figure 3.8. The parameters (K_1 and Z_1) for attractive interaction were taken for van der Waals interaction and are found to be 5.5 and 30, respectively, and kept fixed for all concentration of the nanoparticles. However, parameters (K_2 and Z_2) for repulsive interaction were treated as fitting parameters. Repulsive parameters for 1 wt % nanoparticles are obtained by the extrapolation of the fitted parameters of higher concentrations (inset of Figure 3.8). These parameters of repulsive interactions are kept fixed in the analysis of the SANS data in presence of protein and the parameters of the attractive interaction are obtained as only fitted parameters to account the protein induce attraction between the nanoparticles. The strength of the attractive interaction (K_1) increases with the protein concentration, whereas the range (σ/Z_1) remains almost unchanged. The range of attractive interaction is found to be short compared to the screened Coulomb repulsion and has a value of the order of the size of the lysozyme molecule. It seems to be governed by the distance over which the protein is effectively mediating the attractive interaction between two nanoparticles. The short-range arises as a result of non-uniform charge distribution on the protein, which makes it highly site specific to mediate between oppositely charged nanoparticles.

Table 3.2. Fitted parameters of 1 wt % HS40 + C wt % Lysozyme.
(a) Low protein concentration regime where the nanoparticles undergoing protein induced attractive interaction. The parameters of repulsive interaction K_2 =9.0, Z_2=7.0 are kept fixed.

Concentration C (wt %)	K_1	Z_1
0.01	18.0	9.0
0.02	20.0	9.0

(b) Intermediate protein concentration regime where the nanoparticle aggregates coexist with interacting unaggregated nanoparticles. The fractal dimension of nanoparticle aggregates D=2.4 and parameters of repulsive interaction K_2 = 9.0, Z_2 = 7.0 were kept fixed.

Concentration C (wt %)	Building block radius R_b (Å)	K_1	Z_1	Fraction of unaggregated nanoparticles ϕ_{unp} (%)
0.05	90.0	26.5	10.0	40
0.1	94.5	29.5	13.0	30
0.2	93.2	40.0	14.5	10

(c) High protein concentration regime where nanoparticle aggregates coexist with excess free proteins.

Concentration C (wt %)	Fractal dimension D	Building block radius R_b (Å)	Fraction of free protein ϕ_{fp} (%)
0.5	2.4	94.2	-
1.0	2.5	95.2	35
2.0	2.4	93.1	70
5.0	2.4	94.0	85

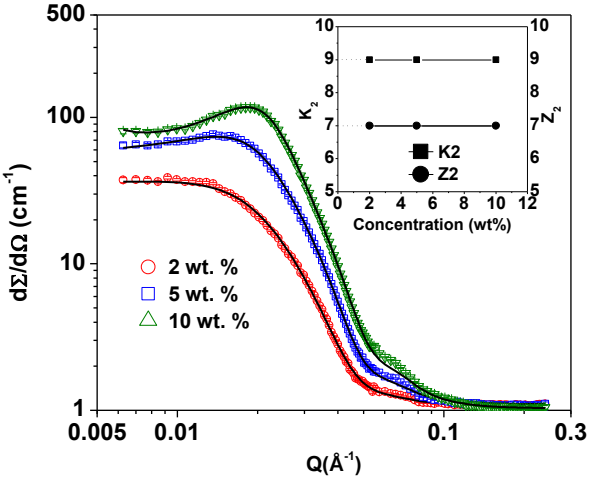

Figure 3.8. SANS data of HS40 silica nanoparticles with varying concentration. Inset shows the values of K_2 and Z_2 obtained by fitting the SANS data.

SANS profiles of the silica nanoparticle-BSA system are shown in Figure 3.9. Data similar to those of the silica nanoparticle-lysozyme are divided in three groups of protein concentrations. First, the low concentration group (0.0-0.2 wt %) [Figure 3.9(a)] is corresponding to regions I and II of the phase behavior (Figure 3.3) where the system remains transparent. The data of second group [Figure 3.9(b)] presents the intermediate concentration range (0.5-1 wt %) corresponding to transition regions II to III of the phase behavior. The third (2-5 wt %) group [Figure 3.9(c)] for high protein concentrations corresponds to region III of the phase behavior where the system becomes turbid. It is observed that the silica nanoparticle-BSA data have very different features than the silica nanoparticle lysozyme. Figure 3.9(a) shows no significant change in SANS data of 1 wt % of silica nanoparticles on the addition of the BSA protein up to 0.2 wt % concentration. Data of the silica nanoparticle-BSA system are similar to that of pure silica nanoparticles. There is no indication of any formation of large structure in the system by SANS and the system is seen to be transparent. The scattering is dominated by that of the silica nanoparticles and data were fitted by considering the scattering contributions from the individual nanoparticles and the free proteins. This is unlike the silica nanoparticle-lysozyme system, both the nanoparticles and protein in the silica nanoparticle-BSA system remain as individual entities in the solvent. There is the possibility that the site-specific adsorption of BSA on the silica surface can take place to form a protein corona (core-shell structure) [30, 201], but is not supported by the SANS analysis and endorse the adsorption isotherms [Figure 3.3(b)]. Thus, it is clear that electrostatic repulsion prevents any kind of protein adsorption on the nanoparticles since both components are similarly charged. There could be another kind of force in the system, for example entropic force (depletion, etc.) whose effect is not visible in the SANS data as the concentration of BSA may not be enough. As the concentration of BSA protein

increases (≥ 0.5 wt %), buildup in scattering intensity starts at low-*Q* as well as at high-*Q* regions [Figure 3.9(b)]. In this case, the scattering buildup at low-*Q* unlike the silica nanoparticle-lysozyme system cannot be attributed to some structural evolution (aggregates). This is because the phase behavior is not consistent with the formation of the aggregates as the transmission of the silica nanoparticle-BSA system does not decrease in the concentration range of the protein. There are some interactional changes expected in the system responsible for scattering buildup at lower-*Q*. Scattering data in Figure 3.9(b) have been modeled by the 2Y potential (Equation 2.64). Fitted parameters are given in Table 3.3. In this case, the attractive potential is found to be relatively long-range [198]. The silica nanoparticle-BSA system becomes turbid at higher BSA concentrations (2-5 wt %) as shown in region III of the phase behavior. SANS data shows linearity on the log-log scale at low-*Q* as seen with the silica nanoparticle-lysozyme system [Figure 3.7(c)]. It is believed that nonadsorption of BSA leads to depletion induced aggregation of the nanoparticles. The aggregate size in such a case is known to depend on the depletant (BSA protein) concentration and increases with increase in concentration [198], which could give the difference in the light transmission as observed for 2 and 5 wt % of BSA in Figure 3.3(b). The aggregates sizes are expected to be much larger (as reflected in DLS measurement) than that can be determined in the present *Q* range ($2\pi/Q_{min}$ ~ 100 nm) of the SANS measurements. This may be the reason that SANS data are almost similar for 2 and 5 wt % of BSA. It would require the data in the much lower-*Q* region to measure the sizes of the aggregates. SANS data of silica nanoparticle-BSA were fitted by the fractal structure of the nanoparticle aggregates coexisting with the free proteins. The fractal dimension is found to be about 2.4 in all the aggregated nanoparticle systems.

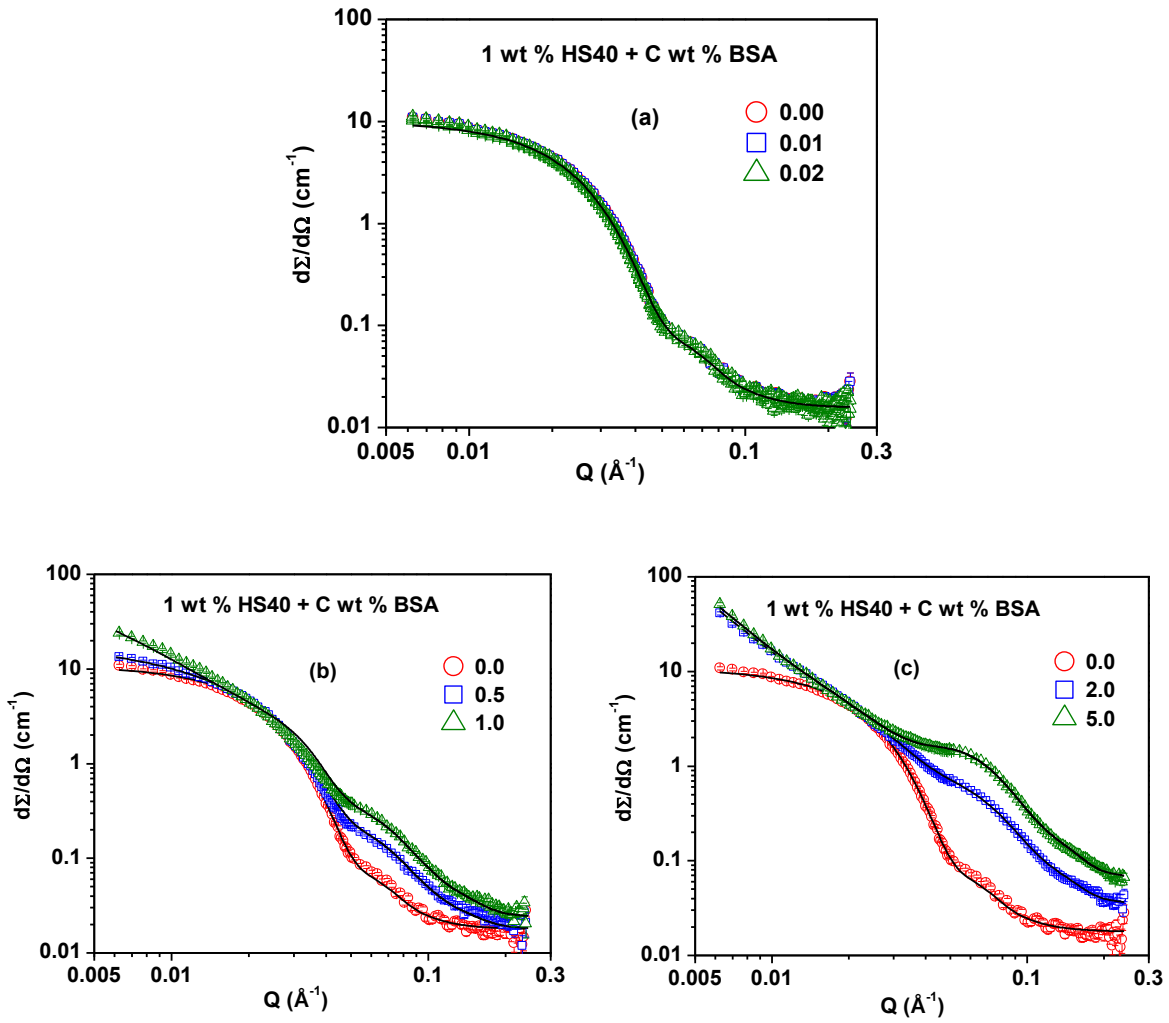

Figure 3.9. SANS data of 1 wt % HS40 silica nanoparticles on addition with BSA protein having (a) low concentration (0.01-0.2 wt %) (b) Intermediate concentration (0.5-1 wt %) and (c) high concentration (2-5wt %).

Table 3.3. Fitted parameters of 1 wt % HS40 + C wt % BSA in the intermediate protein concentration regime where the nanoparticles undergo depletion interaction prior to their aggregation. The parameters of repulsive interaction K_2 = 9.0, Z_2 = 7.0 were kept fixed.

Concentration C (wt %)	K_1	Z_1
0.5	10.5	4.0
1.0	26.5	3.0

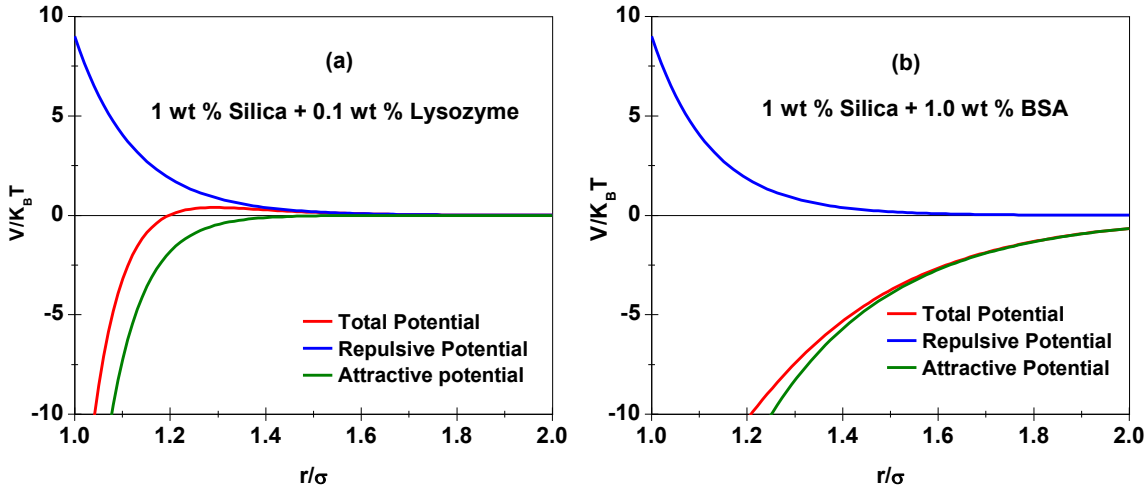

Figure 3.10. The calculated interaction potentials responsible for the aggregation of silica nanoparticles in the presence of (a) lysozyme and (b) BSA proteins.

Thus, it has been shown that BSA similar to lysozyme protein induces the aggregation of silica nanoparticles through the different interaction mechanism. The dominance of the attractive interaction over the repulsive interaction responsible for the aggregation of the nanoparticles for lysozyme and BSA is compared in Figure 3.10. In the case of oppositely charged lysozyme, the aggregation arises as a result of charge neutralization on the nanoparticles and their bridging by the protein. The attractive interaction responsible for aggregation is found to be the short-range interaction. On the other hand, the aggregation of the silica nanoparticles in the presence of similarly charged BSA is entropy driven. It arises because of nonadsorption of the BSA protein on the nanoparticles. This entropy driven attraction (depletion) is determined to be the long-range attraction.

3.5. Conclusions

The differences in the complexes of anionic silica nanoparticles with cationic lysozyme and anionic BSA proteins have been studied. It has been found that the adsorption isotherms of proteins on the nanoparticles and phase behavior of the nanoparticle-protein complexes are highly affected by the type of protein and its concentration. The electrostatic interaction plays a

crucial role in tuning the nanoparticle-protein interaction. In the case of silica nanoparticle-lysozyme system, the protein adsorbs strongly on the surface of the nanoparticles due to the electrostatic attractive interaction and follows an exponential growth behavior. On the other hand, BSA does not show any adsorption on similarly charged nanoparticles. Despite having different nature of interactions, both proteins render the similar kind of phase behavior where nanoparticle-protein systems transform from one-phase to two-phase above a critical protein concentration (CPC). The CPC value is found to be much higher for BSA than lysozyme. DLS measurements suggest that the phase behavior arises as a result of the nanoparticles aggregation on the addition of protein. The adsorption of lysozyme neutralizes the charge on the nanoparticles and leads to their protein-mediated bridging aggregation. However, the nonadsorption of BSA induces the depletion attraction between the nanoparticles. At higher BSA concentrations, the domination of depletion interaction over the electrostatic repulsion between the nanoparticles results in the aggregation of the nanoparticles similar to that for lysozyme. The evolution of interactions responsible for the phase behavior is determined by SANS. The results suggest that the phase behavior of the nanoparticle-protein complexes is governed by the interplay of electrostatic repulsion with a short-range attraction for lysozyme and long-range attraction for BSA. The morphology of the aggregates in two-phase region irrespective of protein type and concentration shows mass fractal having a fractal dimension about 2.4.

Chapter 4

Electrolyte Effect on Silica Nanoparticle-Protein Complexes

4.1. Introduction

There is a strong propensity of protein to adsorb on the nanoparticles due to the high surface-to-volume ratio of the nanoparticles [25-27]. The formation of a corona around each nanoparticle is determined by the different interactions (e.g. electrostatic force, hydrogen bonding etc.) between nanoparticle and protein [18, 20, 27, 202]. However, the resultant structure (phase behavior) depends on the nanoparticle-protein, nanoparticle-nanoparticle and protein-protein interactions. The phase behavior for a given nanoparticle-protein system can be modulated by changing the solution conditions such as the concentration of components, pH, ionic strength etc [22, 23, 203, 204]. The Derjaguin-Landau-Verwey-Overbeek (DLVO) theory has been successfully used to explain the phase behavior of a number of charged colloidal systems [205, 206]. However, this theory has limitations in the case of nanoparticle-protein systems because of the presence of non-DLVO interactions (e.g. solvation, steric and depletion) [207, 208]. Many studies have been carried out on the phase behavior of charged stabilized silica nanoparticles with both similarly and oppositely charged proteins [22, 23, 120, 209]. In the case of oppositely charged protein, nanoparticle-protein system has strong tendency to form two-phase (nanoparticle aggregation) due to the protein-mediated aggregation of nanoparticles [191, 192]. On the other hand, the possibility of site-specific adsorption of similarly charged protein on individual nanoparticles enhances the stability of the system [141, 193]. In the absence of site-specific adsorption, the nonadsorption of protein can induce the depletion force and modify the

phase behavior of the nanoparticle-protein system [198]. Chapter 3 presented the results of similar phase behavior of anionic silica nanoparticles with cationic lysozyme and anionic bovine serum albumin (BSA), where both the proteins induce nanoparticle aggregation [194, 195]. The aggregation of nanoparticles is interpreted as a result of domination of short-range attraction (protein-mediated) for lysozyme and long-range attraction (protein-depleted) for BSA over the long-range electrostatic repulsion between the nanoparticles. The resultant interaction is decided by the combination of different interactions between components (nanoparticle-protein, nanoparticle-nanoparticle and protein-protein) present in the system [23]. In this chapter, the investigation of the effect of an electrolyte modifying the phase behavior of nanoparticle-protein systems in terms of these interactions has been reported [210, 211]. The phase behavior of anionic Ludox silica nanoparticles (HS40) with cationic lysozyme and anionic BSA at pH 7 and in the presence of an electrolyte (NaCl) has been studied. The results with the electrolyte effect are compared with those of without electrolyte.

4.2. Experimental details

Electrostatically stabilized colloidal suspension of 40 wt % of spherical silica nanoparticles (Ludox HS40) and proteins (hen egg lysozyme and BSA) were used and required samples prepared as discussed in chapter 3 (section 3.2). All the measurements were carried out for fixed concentration of silica nanoparticles (1 wt %) with varying the concentration of proteins in the range 0-5 wt % and in the presence of 0.1M NaCl. UV-vis spectroscopy has been used for measuring adsorption isotherms of proteins on the nanoparticles and their resultant phase behavior. The structure and interaction of nanoparticle-protein complexes are determined by scattering techniques DLS and SANS. The instruments and their parameters used for characterizing the samples were same as discussed in chapter 3.

4.3. Data analysis

a. Dynamic light scattering. The evolution of structure and interaction of nanoparticle-protein systems in presence of an electrolyte has been determined through the autocorrelation function in DLS in terms of change in the effective diffusion coefficient (Equation 3.1) [150]. CONTIN method is used to obtain the effective value of diffusion coefficient and corresponding size distribution of the nanoparticle-protein complexes form the measured autocorrelation function [154].

b. Small-angle neutron scattering. The structure and interaction in SANS are calculated from the form factor $P(Q)$ and structure factor $S(Q)$, respectively [163]. The individual nanoparticles and proteins are fitted with the form factor of standard geometries and their aggregation by the fractal structure. The modification in interactions of nanoparticle-protein complexes in presence of electrolyte is modeled using the 2Y potential taking account of changes in both repulsive and attractive interactions [176]. Comparing Equations 2.60 and repulsive part of 2Y potential (Equation 2.64), K_2 and Z_2 are related to the charge (q) on the particles and Debye length (κ^{-1}) as follows [102]

$$\frac{q^2 e^2}{\pi\varepsilon\varepsilon_0\sigma(2+\kappa\sigma)^2} = K_2 k_B T \tag{4.1}$$

$$\kappa^{-1} = \frac{\sigma}{Z_2} \tag{4.2}$$

The data were fitted by comparing model scattering with the experimental data using the nonlinear least-squares method [212]. The required corrections were also made for the instrumental smearing of the experimental data.

4.4. Results and discussion

4.4.1. Modification in phase behavior of nanoparticle-protein complexes in presence of an electrolyte

The SANS data of 1 wt % of silica nanoparticles and 1 wt % of proteins (lysozyme and BSA) without and with 0.1 M NaCl are presented in Figure 4.1. The data without and with electrolyte are found almost overlapping over the entire measured *Q* range. All these data have been fitted by *P*(*Q*) for respective system. The fitted parameters of individual components with electrolyte do not show any observable changes from those without electrolyte [Table 3.1]. This behavior is attributed to the fact that at 1 wt % all the studied systems can be treated as dilute [194]. As a result, change in interaction reflected in *S*(*Q*) in presence of 0.1 M NaCl is not visible. The interaction within the system can be observed from the SANS data at higher concentrations.

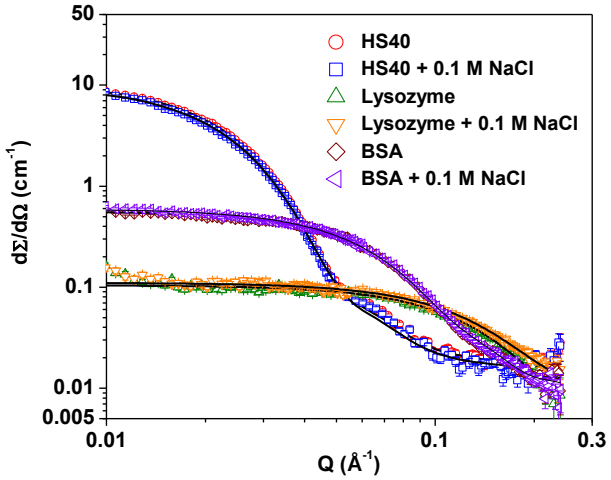

Figure 4.1. SANS data of 1 wt % of silica nanoparticles, lysozyme and BSA proteins with and without 0.1 M NaCl.

Figure 4.2 presents the measured SANS data at 10 wt % of nanoparticles and proteins (lysozyme and BSA) without any electrolyte. All the system shows a correlation peak arising

from corresponding peak in $S(Q)$. This peak arises at $Q_p \sim 2\pi/d$, where d is the average distance between the particles [80]. The value of d varies with number density (n) of particles as $1/n^{1/3}$ and n is related to the volume fraction (φ) of particles having radius (R) by $n = 3\varphi/(4\pi R^3)$. The positions of correlation peaks in Figure 4.2 are at different Q_p values because of different sizes of the nanoparticles and two proteins. The data have been fitted with $P(Q)$ from that of dilute system (Figure 4.1) and $S(Q)$ for 2Y potential [28, 176,]. The fitted parameters of 2Y potential are given in Table 4.1. The parameters of attractive interaction (K_1 and Z_1) for silica nanoparticles are fitted corresponding to van der Waals attraction. The range of attraction (σ/Z_1) is found to be very small as expected for van der Waals attraction. On the other hand, proteins data are fitted with a short-range attraction (cannot be accounted only by van der Waals attraction) and is believed to be arising due to non-uniform charge distribution of proteins (coexistence of positive and negative patches). The repulsive parameters (K_2 and Z_2) represent the screened Coulomb interaction between the constituents (nanoparticles or proteins), where range (σ/Z_2) is determined by the ionic strength of the solution. Insets in Figure 3.2 show the changes in the calculated SANS data in presence of an electrolyte (0.1 M NaCl) with respect to no electrolyte using DLVO theory [210]. In this case, the repulsive interaction is modified in presence of an electrolyte through the change in Debye length. There is also possibility of non-DLVO interactions getting modified in presence of electrolyte in these systems.

Though the interactions between different components (nanoparticle-protein, nanoparticle-nanoparticle and protein-protein) within the system are modified in presence of an electrolyte, the adsorption behavior of both proteins on the nanoparticles in presence of 0.1 M NaCl is found to be quite similar to that without any electrolyte (Figure 3.2). In this particular

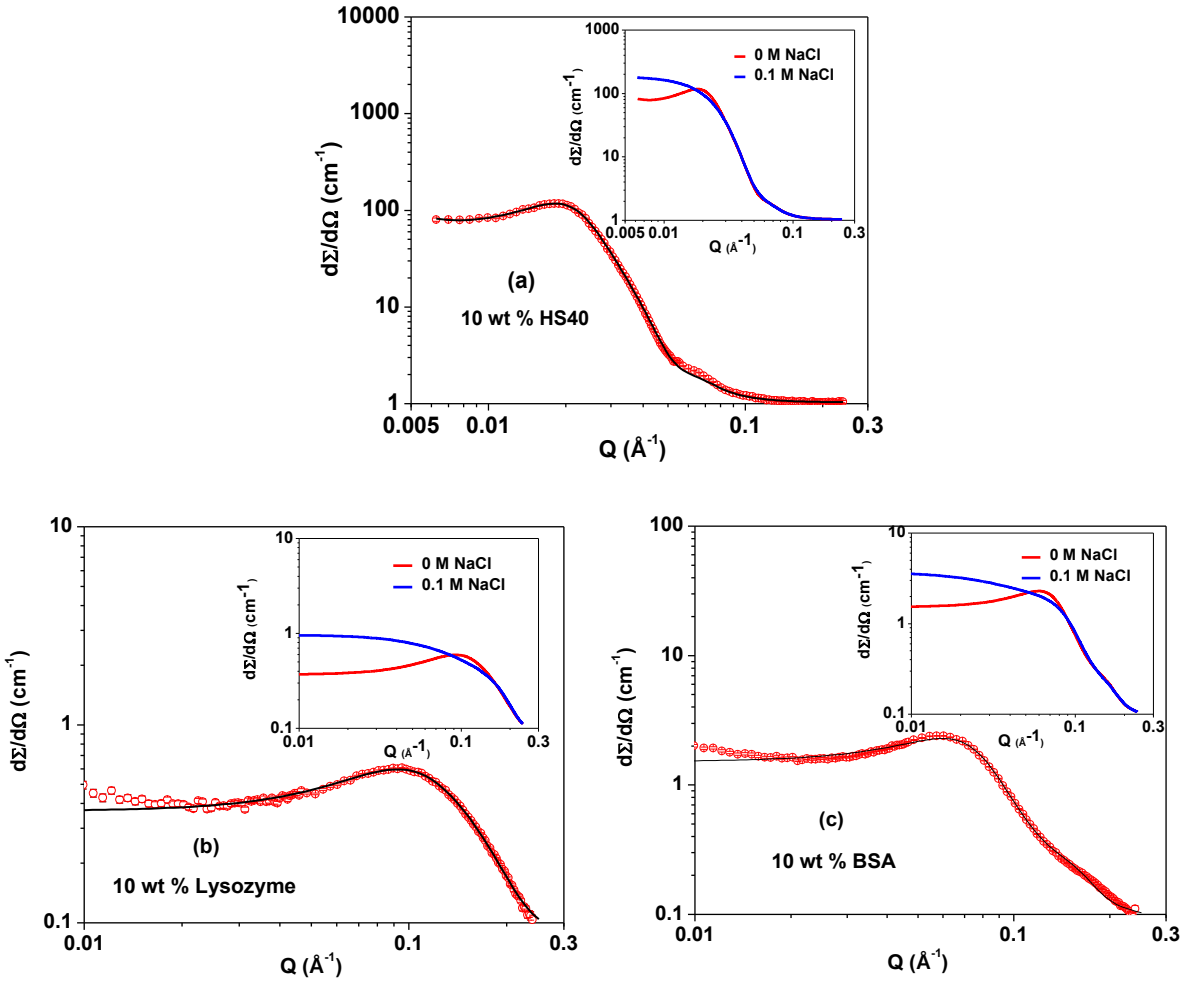

Figure 4.2. SANS data of 10 wt % of (a) silica nanoparticles, (b) lysozyme and (c) BSA proteins without electrolyte. Insets compare the fitted data without electrolyte with the calculated data in presence of 0.1 M NaCl.

Table 4.1. Fitted parameters of 10 wt % of silica nanoparticles (HS40), lysozyme and BSA proteins in aqueous solution at pH 7.

System	NaCl	K_1	Z_1	K_2	Z_2
HS40	0 M	5.5	30.0	9.0	7
	0.1 M	5.5	30.0	1.5	19.5
Lysozyme	0 M	4.0	11.0	2.0	3.0
	0.1 M	4.0	11.0	0.6	7.3
BSA	0 M	7.0	14.0	4.0	4.7
	0.1 M	7.0	14.0	1.0	11.5

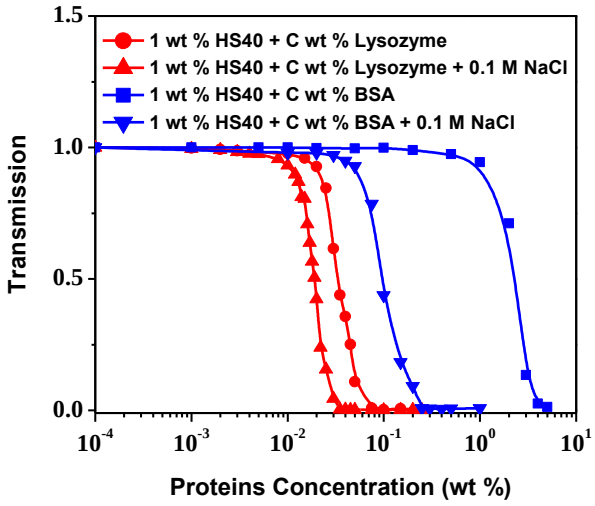

Figure 4.3. Transmission of light (600 nm) in 1 wt % HS40 silica nanoparticles with varying concentrations of lysozyme and BSA proteins in presence of 0.1 M NaCl.

case for lysozyme, it seems that competing interactions (nanoparticle-protein attraction and protein-protein repulsion) somehow balance and as a result no change in the adsorption of protein is observed [21]. On the other hand, BSA remains non-adsorbing because of dominance of nanopartricle-protein repulsion even in the presence of electrolyte. Figure 4.3 shows the phase behavior of 1 wt % HS40 silica nanoparticles with lysozyme and BSA proteins in the presence of 0.1M NaCl. The comparison is also made with the phase behavior of nanoparticle-protein systems without any electrolyte [194, 210]. The figure depicts the variation of transmission of light (6000 Å) through silica nanoparticles as a function of protein concentration. The transformation from one-phase to two-phase is characterized by sudden decrease in transmission beyond a critical protein concentration (CPC). It is noticed from Figure 4.3 that the value of CPC strongly depends on the type of protein and the presence of an electrolyte. The CPC values are very different for the two proteins, which are expected because of their different nature of interactions with the nanoparticles. It is observed that the phase behavior of

silica nanoparticles with both the proteins is significantly modified in the presence of an electrolyte. The CPC values are suppressed on addition of an electrolyte. The effect is more pronounced for BSA than lysozyme. The evolution of interaction and structure responsible for the electrolyte effect in phase behavior of nanoparticle-protein systems have been further studied by scattering techniques.

4.4.2. Electrolyte effect on structure and interaction of nanoparticle-protein complexes

The DLS data of the silica nanoparticle-lysozyme system in presence of 0.1 M NaCl are shown in Figure 4.4. The autocorrelation function is found to broaden with increasing lysozyme concentration as approaching from one-phase to two-phase system [Figure 4.4(a)]. The features of the autocorrelation functions are very similar to that without an electrolyte except that the corresponding changes are observed at lower protein concentration. The calculated size distribution of the nanoparticles at different lysozyme concentrations are plotted in Figure 4.4(b). The mono-modal size distribution of the nanoparticles for one-phase region changes to bi-modal for two-phase region in the phase behavior. In bi-modal size distribution, the nanoparticle aggregates coexist with the individual nanoparticles undergoing attractive interaction. The comparison of size distributions of the nanoparticle-lysozyme system at a fixed concentration of lysozyme with and without electrolyte is shown in Figure 4.4(c). The electrolyte effect clearly shows that the attractive interaction is enhanced (shifting of individual nanoparticles size distribution) leading to aggregation of the nanoparticles (occurrence of second size distribution).

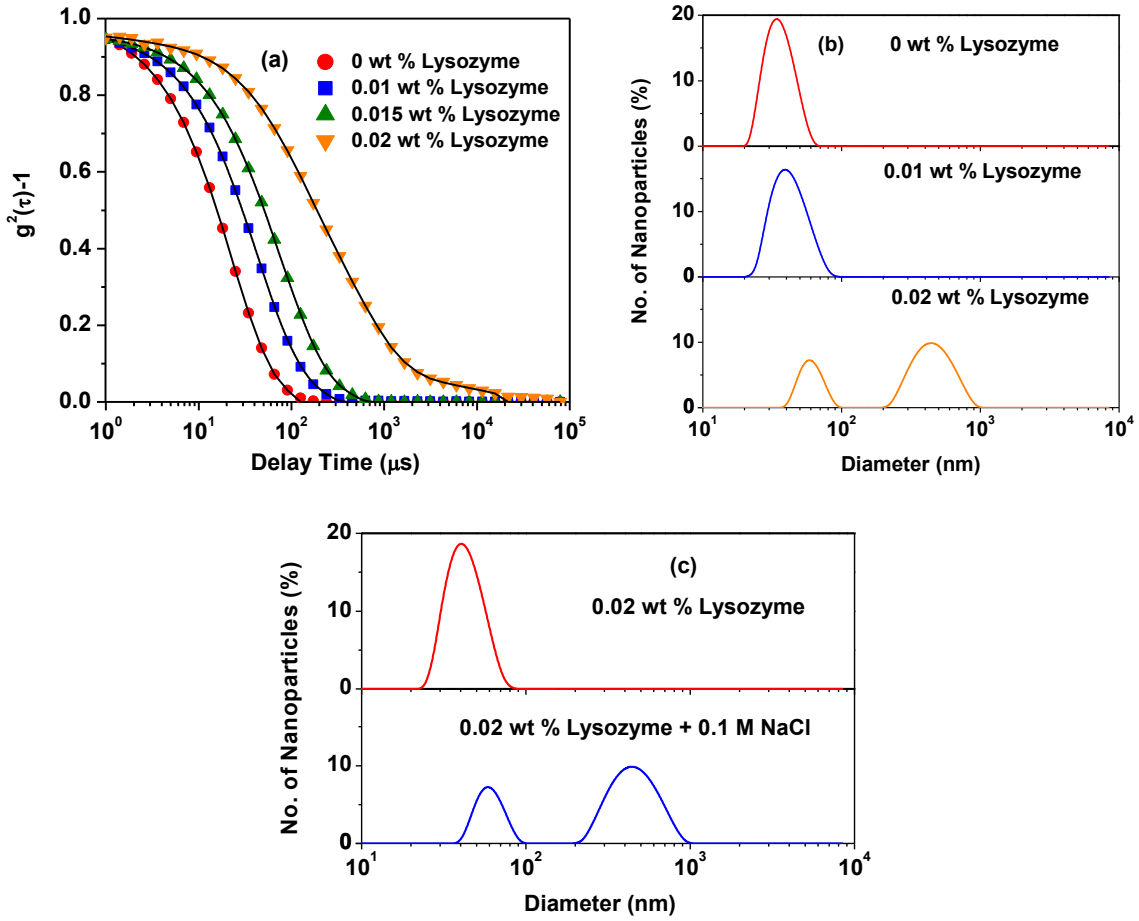

Figure 4.4. DLS data of 1 wt % HS40 silica nanoparticles with varying concentration of lysozyme protein in the presence of 0.1MNaCl (a) autocorrelation function, (b) calculated size distributions and (c) comparison of size distribution at 0.02 wt % lysozyme without and with 0.1 M NaCl.

It has been observed that silica nanoparticles and BSA protein despite having a similar charge (both are anionic) show phase behavior similar to that of nanoparticles with lysozyme. The electrolyte effect on the phase behavior is found to be more pronounced for BSA than lysozyme. Figure 4.5 presents DLS data of a silica nanoparticle-BSA system with varying protein concentration in presence of 0.1 M NaCl. The features are similar to that in Figure 4.4, where the broadening of autocorrelation function corresponding to transformation of one-phase to two-phase is shifted towards lower protein concentration with respect to without electrolyte. In silica nanoparticle-BSA system, it is expected that electrolyte effect is mostly governed by the

enhancement in depletion interaction due to suppression in protein-protein repulsion. This is because individual silica nanoparticles and BSA systems are stable up to very high concentration of NaCl [102, 196].

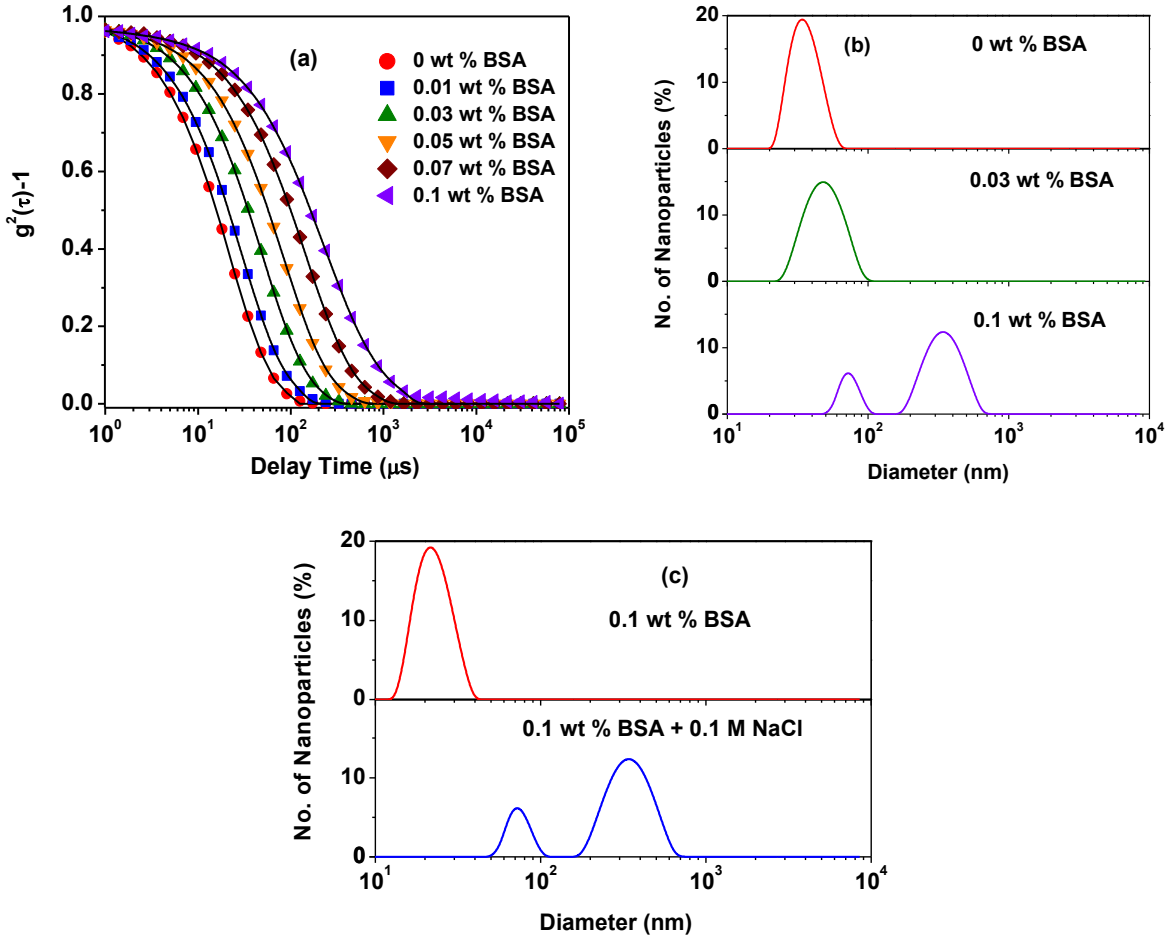

Figure 4.5. DLS data of 1 wt % HS40 silica nanoparticles with varying concentration of BSA protein in the presence of 0.1MNaCl (a) autocorrelation function, (b) calculated size distributions and (c) comparison of size distribution at 0.0.1 wt % lysozyme without and with 0.1 M NaCl.

Figure 4.6 presents the SANS data of 1 wt % HS40 silica nanoparticles with varying concentration of lysozyme protein in the presence of 0.1 M NaCl. The data are taken over a wide concentration range (0-1 wt %) to cover different regions of the phase behavior in Figure 4.3. It is found that there is systematic scattering buildup in the low-*Q* regime with the increase in protein concentration. These data basically correspond to a region of phase behavior where

nanoparticle-protein systems transform from one-phase to two-phase system. The data in the low-*Q* regime do not show any change after some amount of protein concentration in the two-phase region, whereas there is an increase in the scattering in the higher-*Q* regime as expected from the protein contribution. Based on the overall features of the SANS data, the analysis has been divided into two sets of data where nanoparticle-protein systems (i) transform from a one-phase to a two-phase system [Figure 4.6(b)] and (ii) they have been fully transformed into a two-phase system [Figure 4.6(c)].

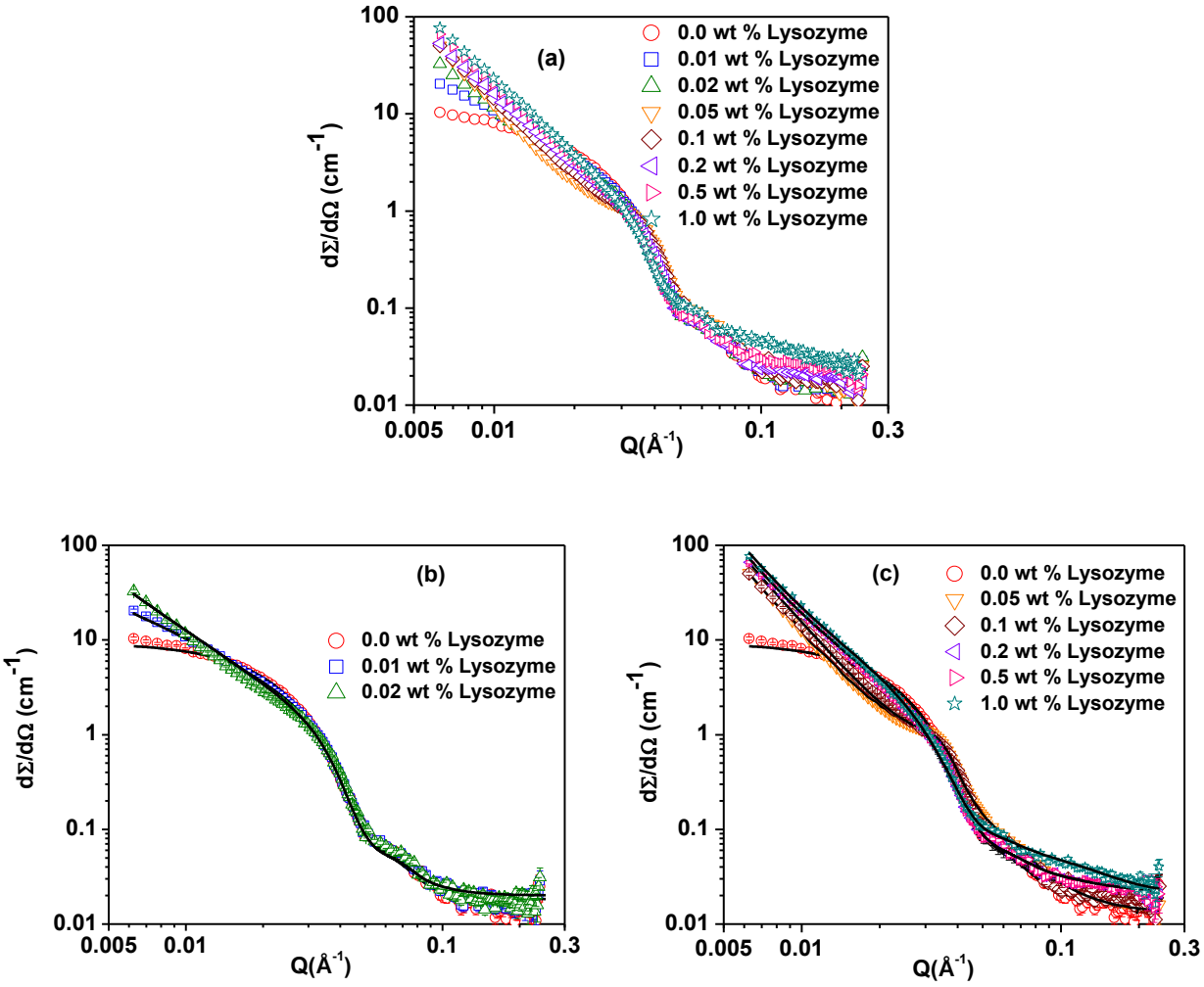

Figure 4.6. (a) SANS data of 1 wt % HS40 silica nanoparticles in presence of 0.1 M NaCl with varying concentration of lysozyme protein. Further the data are divided into two sets of low (b) and high (c) lysozyme concentrations.

The buildup of scattering with the increase in lysozyme concentration in the low-Q regime of SANS data are fitted with two populations (nonaggregated and aggregated) of nanoparticles [Figure 4.6(b)]. The oppositely charged lysozyme adsorbs on the nanoparticles and results in protein-mediated aggregation of the nanoparticles; the amount of aggregation depends on the protein concentration [191, 192]. The aggregation phenomenon is modeled through the structure factor of 2Y potential between nonaggregated nanoparticles. The form factor for these nanoparticles used is that of polydispersed spherical. The aggregated nanoparticles are fitted with the fractal structures. The fitted parameters are given in Table 4.2. The nanoparticle aggregates at low protein concentration are characterized by a surface fractal whose number fraction increases with the protein concentration. The 2Y potential comprises four fitting parameters K_1, K_2, Z_1, and Z_2. The parameters K_1 and Z_1 represent the attractive part of the total potential to decide the strength (proportional to K_1) and range (proportional to $1/Z_1$), respectively. On the other hand, K_2 and Z_2 provide the strength (related to effective charge) and range (related to ionic strength) of repulsive electrostatic interaction, respectively. The values of K_2 and Z_2 have been determined from the concentration-dependent SANS data of pure silica nanoparticles [194]. The effect of the electrolyte on these parameters is incorporated by Debye-Huckel theory as governed by the ionic strength of the system [213]. To minimize the number of fitting parameters during the data analysis, the values of K_2 and Z_2 were kept fixed whereas the parameters of the attractive interaction (K_1 and Z_1) were used as fitted parameters. It is found that the strength of attractive interaction is prominently high compared to the repulsive interaction. The range is of the order of the size of the lysozyme protein as protein mediating the attractive interaction between nanoparticles. The contribution of aggregated nanoparticles is considered as a surface fractal.

The SANS data corresponding to a two-phase system (nanoparticle aggregation) at higher lysozyme concentrations are shown in Figure 4.6(c). All the scattering profiles show the linearity in the low-Q regime indicating the fractal nature of nanoparticle aggregates [178, 179]. It is observed that there are two groups of data with different slopes in the low Q region. The first group of data has a slope of about 3.2 describing the surface fractal behavior of the nanoparticle aggregates. The Bragg peak kind of feature around Q_p=0.035 Å in these data indicates the ordered packing of nanoparticles within the aggregates. The sum of power law behavior for a surface fractal and contribution from ordered particles within the aggregate is used to fit the data [214]. The surface fractal dimension and the volume fraction of particles within the aggregates decrease with increasing lysozyme concentration. This is perhaps because of the competition of nanoparticle-protein (attractive) and protein-protein (repulsive) interactions resulting in change of the morphology of the nanoparticle aggregates. In the second group of data at higher lysozyme concentrations, the slope of the scattering curve decreases to a value about 2.5, suggesting morphology of nanoparticle aggregates changing from surface to mass fractal. This can be understood in terms of lysozyme molecules in a corona around the nanoparticle controlling the binding of the nanoparticles.

Table 4.2. Fitted parameters of 1 wt % HS40 silica nanoparticles with varying concentration of lysozyme protein in presence of 0.1 M NaCl.

(a) Low lysozyme concentration where the interacting nanoparticles coexist with nanoparticle aggregates. The data are fitted with 2Y potential. The parameters of repulsive interaction K_2 = 1.5, Z_2 = 19.5 are fixed.

Lysozyme concentration C (wt %)	K_1	Z_1	Fraction of aggregated nanoparticles ϕ_a (%)
0.01	12.5	9.0	17
0.02	15.0	9.0	40

(b) Intermediate lysozyme concentration where the nanoparticle aggregates are characterized by surface fractal.

Lysozyme concentration C (wt %)	Surface fractal dimension D_s	Volume fraction of nanoparticles within the aggregates ϕ
0.05	2.9	0.29
0.1	2.8	0.23
0.2	2.6	0.07

(c) High lysozyme concentration where the nanoparticle aggregates are characterized by mass fractal.

Lysozyme concentration C (wt %)	Mass fractal dimension D_m	Building block radius R_b (Å)
0.5	2.5	94.5
1	2.5	95.0

SANS data of 1 wt % HS40 silica nanoparticles with varying concentration of BSA protein in the presence of 0.1M NaCl are shown in Figure 4.7. The features are quite similar to that of the silica nanoparticles with lysozyme protein [Figure 4.6]. The data are again divided into two sets corresponding to the regions of one-phase to two-phase system and only two-phase system exists. In the first set at low protein concentrations [Figure 4.7(b)], the data are fitted with the interaction between nanoparticles via the 2Y potential accounting for electrostatic repulsion and depletion attraction as induced by the nonadsorption of BSA. The fitted parameters are given in Table 4.3. The parameters of electrostatic repulsion are kept fixed as used in the case of the nanoparticle-lysozyme system. Unlike the case of the nanoparticle-lysozyme system, the attractive depletion interaction for the nanoparticle-BSA system is found to be long-range.

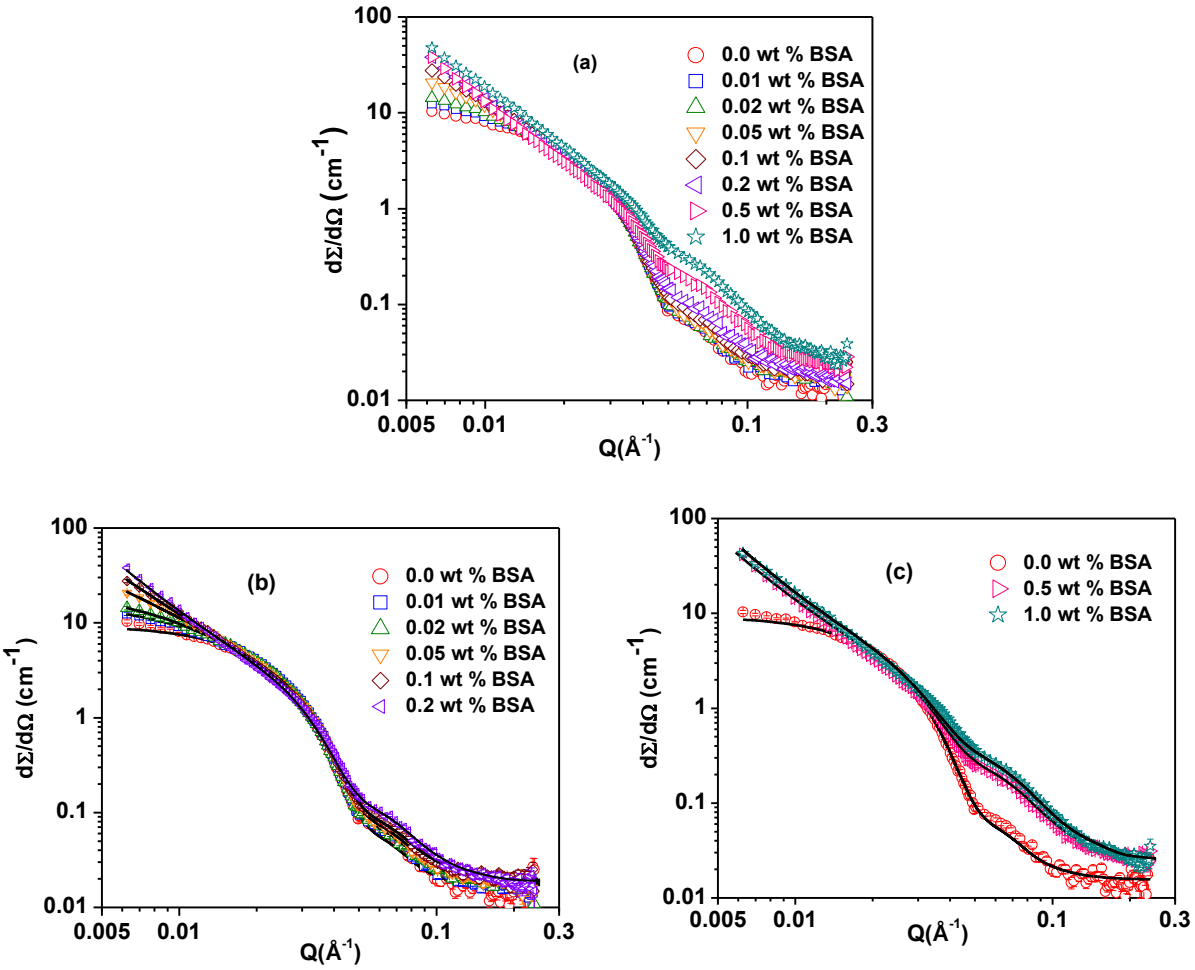

Figure 4.7. (a) SANS data of 1 wt % HS40 silica nanoparticles in presence of 0.1 M NaCl with varying concentration of BSA protein. Further the data are divided into two sets of low (b) and high (c) BSA concentrations.

Both the magnitude and range of this attractive interaction increase with the BSA concentration. The similar long-range attractive potential has also been reported in other systems [214, 215]. The long-range attraction is justified from the fact that this interaction can induce aggregation in long-range repulsive charged stabilized systems. A fraction of aggregated nanoparticles also coexists in these systems. The fraction of aggregated nanoparticles increases with the BSA concentration. The contribution of aggregated nanoparticles is fitted as a mass fractal. In the second set of SANS data at high protein concentrations [Figure 4.7(c)], the nanoparticle-BSA

protein has mostly nanoparticle aggregates as characterized by a mass fractal. The differences in evolution of fractal structures of nanoparticle-BSA (mass fractal only) and nanoparticle-lysozyme (surface to mass fractal) systems perhaps arise because of the different mechanisms of the aggregation for two systems.

Table 4.3. Fitted parameters of 1 wt % HS40 silica nanoparticles with varying concentration of BSA protein in presence of 0.1 M NaCl.

(a) Low BSA concentration where the interacting nanoparticles coexist with nanoparticle aggregates. The data are fitted with 2Y potential. The parameters of repulsive interaction $K_2 = 1.5$, $Z_2 = 19.5$ are fixed.

BSA concentration C (wt %)	K_1	Z_1	Fraction of aggregated nanoparticles ϕ_a (%)
0.01	18.0	5.5	0
0.02	21.5	5.0	0
0.05	24.0	4.8	15
0.1	27.5	4.5	30
0.2	32.0	4.2	60

(b) High BSA concentration where the nanoparticle aggregates are characterized by mass fractal.

BSA concentration C (wt %)	Mass fractal dimension D_m	Building block radius R_b (Å)
0.5	2.5	90.5
1	2.5	91.0

The electrolyte effect with respect to the case without any electrolyte for nanoparticle-protein systems is compared in Figure 4.8. In the case of the nanoparticle-lysozyme system, the comparison of SANS data with and without an electrolyte for 1 wt % HS40 with 0.02 wt % lysozyme is shown in Figure 4.8(a). The differences in the data, in particular in the low-Q regime

with and without electrolyte, arise as a result of the modifications in the interaction and structure of the system. Table 4.4(a) gives the comparison of the fitted parameters in these systems. The parameters of repulsive interaction (K_2 and Z_2) are kept constant and modified with electrolyte as decided by the change in the ionic strength of the system. Both the strength (proportional to K_2) and range (proportional to $1/Z_2$) of the repulsive interaction as expected decrease in presence of an electrolyte. The parameters of the lysozyme-mediated attractive interaction (K_1 and Z_1) vary as K_1 deceases whereas Z_1 remains almost the same. Because this interaction is derived from the electrostatic nature, K_1 decreases in the presence of the electrolyte. The range of the interaction ($1/Z_1$) depends on the protein conformation, which is usually known to be unchanged at the moderate amount of electrolyte as is the present case. The total potential between nanoparticles and its individual components are plotted in Figure 4.9(a). These observations suggest that the electrolyte effect in enhancing the nanoparticle aggregation of a silica nanoparticle-lysozyme system is primarily dictated by the decrease in the strength and range of the electrostatic repulsive interaction between nanoparticles.

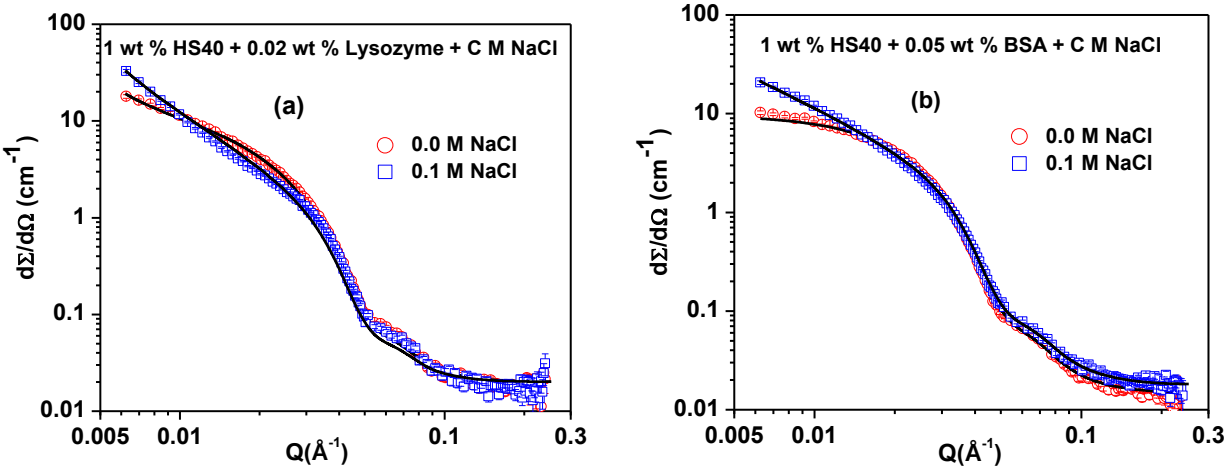

Figure 4.8. Comparison of SANS data without and with 0.1 M NaCl (a) 1 wt % HS40 silica nanoparticles with 0.02 wt % lysozyme protein and (b) 1 wt % HS40 silica nanoparticles with 0.05 wt % BSA protein.

Table 4.4. Comparison of fitted parameters of 2Y interaction potential without and with 0.1 M NaCl

(a) 1 wt % HS40 silica nanoparticles with 0.02 wt % lysozyme protein

[NaCl]	K_1	Z_1	K_2	Z_2
0 M	20.0	9.0	9.0	7.0
0.1 M	15.0	9.0	1.5	19.5

(b) 1 wt % HS40 silica nanoparticles with 0.05 wt % BSA protein.

[NaCl]	K_1	Z_1	K_2	Z_2
0 M	7.5	4.8	9.0	7.0
0.1 M	24.0	4.8	1.5	19.5

Figure 4.8(b) compares the nanoparticle-BSA system with and without electrolyte for 1 wt % HS40 with 0.05 wt % BSA. The changes in features of the data of a nanoparticle-BSA system are observed to be different than that of a nanoparticle-lysozyme system. The comparison of the fitted parameters in a nanoparticle-BSA system without and with electrolyte is given in Table 4.3(b). The electrostatic repulsive interaction has the same variation as in the case of lysozyme [Table 4.4(a)]. The parameters of the BSA-induced depletion interaction (K_1 and Z_1) show a trend where K_1 increases (unlike the nanoparticle-lysozyme system) whereas Z_1 does not change. The increase in the strength of the depletion interaction (proportional to K_1) can be understood in terms of decrease in protein-protein repulsion in the presence of an electrolyte. The suppression of repulsion significantly increases the excluded volume available for proteins and hence higher magnitude of depletion interaction [198]. The total potential between nanoparticles and its electrostatic and depletion components are plotted in Figure 4.9(b). The results show that the presence of an electrolyte leads in significant modifications in both the electrostatic and depletion interactions in a nanoparticle-BSA system. These modifications in interactions are responsible for the change in phase behavior of the nanoparticle-BSA system.

The changes are found different for lysozyme and BSA proteins and hence differences in their phase behavior.

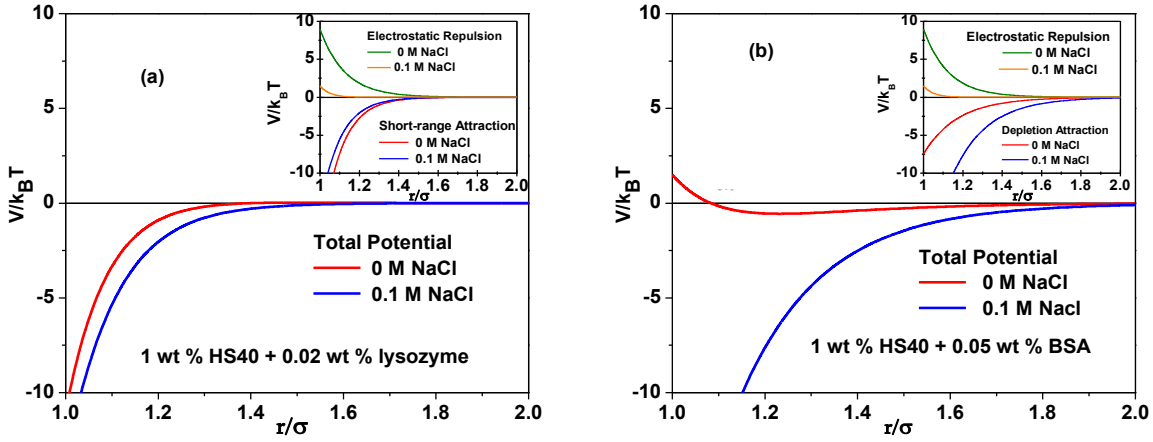

Figure 4.9. The calculated total interaction potential between nanoparticles without and with 0.1M NaCl: (a) 1 wt % HS40 silica nanoparticles with 0.02 wt % lysozyme protein and (b) 1 wt % HS40 silica nanoparticles with 0.05 wt % BSA protein. Insets show the repulsive and attractive components of the total potential.

4.4.3. Role of varying electrolyte ions on nanoparticle-protein complexes

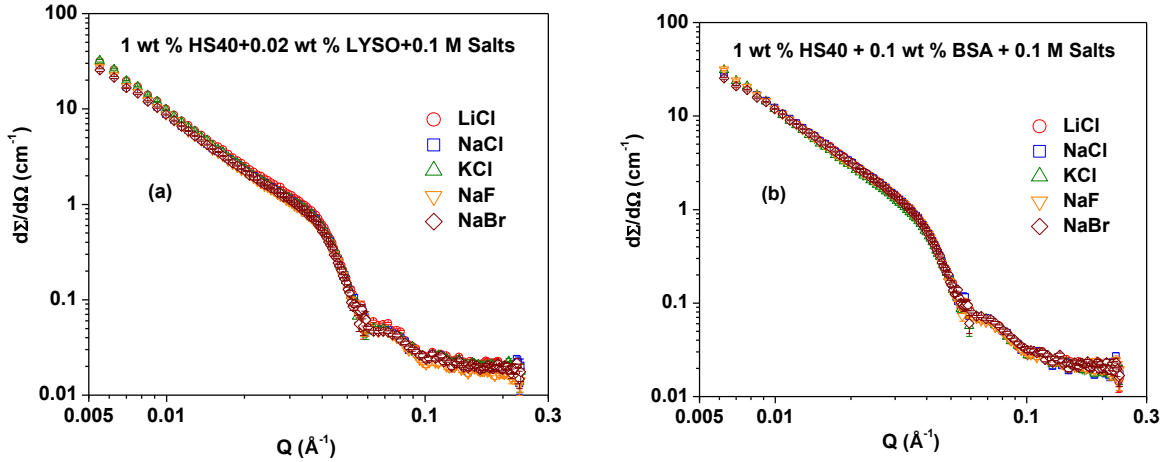

Figure 4.10. SANS data of 1 wt % HS40 silica nanoparticles in presence of 0.1 M different salts at fixed concentration of (a) lysozyme and (b) BSA proteins.

The ions of electrolyte play an important role and their effect in charged colloids could be very different for different ions. Usually the effect of counterions on the aggregation of charged particles follows well known Hofmeister series. On the other hand, co-ions have negligible effect

on charged colloids. Figure 4.10 shows SANS data of 1 wt % HS40 + 0.02 wt % lysozyme and 1 wt % HS40 + 0.1 wt % BSA in presence of 0.1 M of different single-valence electrolytes. Interestingly, the data do not show any significant changes with varying ions. It could be because that the electrolyte effect on protein mediated interactions of the nanoparticles at the electrolyte concentration of interest (0.1 M) is dominated by the electrolyte concentration than the ion specificity of electrolyte. However, the dramatic effects can be observed in presence of multi-valence ions.

4.5. Conclusions

The influence of electrolyte on the adsorption of proteins on the nanoparticles and the resultant phase behavior of their complexes has been investigated. The strong adsorption of lysozyme and non-adsorbing nature of BSA proteins on the silica nanoparticles remain unaltered in presence of electrolyte. Both the proteins show a similar kind of phase behavior where the respective nanoparticle-protein system transforms from one-phase to two-phase system. The phase behavior for both the proteins is significantly modified in the presence of an electrolyte. The protein concentration required for phase transformation is suppressed on addition of the electrolyte and the effect is more pronounced for BSA than lysozyme. DLS and SANS data suggest that changes in phase behavior are related with modifications in both interaction and structure of the nanoparticle-protein systems. The combination of short-range attraction and electrostatic repulsion for lysozyme protein leads to protein-mediated aggregation of the nanoparticles, whereas nonadsorption of BSA protein with nanoparticles induces long-range depletion interaction to overcome electrostatic repulsion to aggregate the nanoparticles. The suppression of the electrostatic repulsion for lysozyme protein and enhancement of depletion interaction for BSA are found to be mainly responsible for the changes in the phase behavior of respective nanoparticle protein systems in the presence of an electrolyte.

Chapter 5

Effect of pH on Silica Nanoparticle-Protein Complexes

5.1. Introduction

Nanoparticle-protein interactions have been studied mostly for charged nanoparticles with globular proteins [126, 141, 143]. The important issues that have been looked into are adsorption isotherms of proteins on nanoparticles, conformational changes of adsorbed proteins, and structures and the resultant phase behavior of the complexes. Interaction of anionic silica nanoparticles with two globular proteins-lysozyme and bovine serum albumin (BSA) without and in presence of electrolyte has been studied in chapters 3 and 4. In these systems, electrostatic interactions dictate the nanoparticle-protein interactions and their resultant phases [194, 195, 210, 211]. Interactions between the nanoparticles in the presence of proteins are successfully modeled by combining electrostatic repulsion with short-range attraction for lysozyme and long-range attraction for BSA protein. Systems dominated by attractive interaction exhibits nanoparticle aggregation, which is characterized as fractal. Differences in the phase behavior of the nanoparticles with lysozyme and BSA proteins are interpreted in terms of different adsorption isotherms of these proteins on the nanoparticles. When the ionic strength is varied, the modifications in the nanoparticle-nanoparticle, nanoparticle-protein and protein-protein interactions result in significant changes in the phases of the nanoparticle-protein systems [210]. pH of the solution is another important parameter that can be used to tune the nanoparticle-protein interactions and the resultant phase behavior [21, 22, 191]. In this chapter, the effect of pH on the nanoparticle-protein interactions has been studied as the pH of the

solution is varied from physiological conditions to the isoelectric point (IEP) of the proteins [216, 217]. Proteins with a defined conformation carry a net positive or negative surface charge depending on the pH of the surrounding medium [126, 209]. Thus, the adsorption of proteins from aqueous media onto hydrophilic nanoparticles surfaces can be controlled by pH and in this way allows controlled binding and release of the protein molecules [21-23]. Moreover, the pH variation also allows for systematic changes in the electrostatic interactions of the components in the system. The pH-dependent interaction of anionic silica nanoparticles with lysozyme and BSA proteins has been examined using zeta potential, UV-vis spectroscopy, DLS, and SANS. The effect of pH on protein adsorption, phase behavior (one-phase to two-phase transformation), structures, and interactions in these systems are reported.

5.2. Experimental details

Samples were prepared from electrostatically stabilized colloidal suspension of 40 wt % of spherical silica nanoparticles (Ludox HS40) and proteins (hen egg lysozyme and BSA) as described in chapter 3 (section 3.2). The concentration of silica nanoparticles was fixed (1 wt %) and of proteins was varied (0-5 wt %) in 20 mM phosphate buffer at pH 7. The pH was raised or lowered by adding a small amount of 1 M NaOH or 1 M HCl, respectively. The pH-dependent charge behavior of nanoparticles and proteins was examined by zeta potential. The corresponding adsorption isotherms of proteins on the nanoparticles and their resultant phase behavior with varying pH were measured by UV-vis spectroscopy. The modifications of structure and interaction of nanoparticle-protein complexes were determined by scattering techniques DLS and SANS. The instruments and their parameters used for characterizing the samples were same as discussed in chapter 3.

5.3. Data analysis

a. Dynamic light scattering. The autocorrelation function in DLS provides effective diffusion coefficient of the system (Equation 3.1) [150]. Any change in the value of effective diffusion coefficient relates to the evolution of structure and/or interaction and has been used to monitor pH effect on nanoparticle-protein systems. The effective value of diffusion coefficient and corresponding size distribution of the nanoparticle-protein complexes from the measured autocorrelation function are obtained using CONTIN method [154].

b. Small-angle neutron scattering. The structure and interaction in SANS are calculated separately from the form factor $P(Q)$ and structure factor $S(Q)$, respectively [165]. The individual nanoparticles and proteins are fitted with the form factor of standard geometries and their aggregation by the fractal structure. The pH-dependent modification in interactions of nanoparticle-protein complexes is modeled using the 2Y potential taking account of changes in both repulsive and attractive interactions [176].

The experimental data are fitted with model scattering using the nonlinear least-squares method [163]. The resolution corrections for the instrumental smearing of the experimental data are also made during the analysis.

5.4. Results and discussion

5.4.1 pH-dependent adsorption of proteins on nanoparticles

The zeta potential is an important parameter for the characterization of charged colloids to predict their stability. The higher the magnitude of the zeta potential, the higher the stability. The zeta potentials of the silica nanoparticles (HS40), lysozyme and BSA proteins as a function of pH are shown in Figure 5.1. Under physiological conditions (pH 7), the zeta potentials of the

silica nanoparticles and BSA protein have negative values of -30 and -14 mV, respectively. On the other hand, the zeta potential is positive (+6 mV) for lysozyme. The higher magnitude of the zeta potential of the nanoparticles is responsible for the commonly observed high stability of these nanoparticles. The lower magnitude of the zeta potential of the proteins limits their stability, which may lead to aggregation. That is perhaps why most of the protein solutions are studied at a low concentration and with freshly prepared samples. The pH-dependent zeta potential of the silica nanoparticles shows interesting features and can be divided into three regions. The zeta potential remains almost constant in the pH range 7-10, whereas below pH 7 and above pH 10 it decreases with varying pH. A similar behavior has also been observed in other silica nanoparticle systems [52, 218]. The ionization of the surface silanol group decreases with decreasing pH as the hydroxyl ion reduces. As a result, the surface charge density of the nanoparticles decreases, and hence the zeta potential also decreases. Above pH ≈ 10, the silica nanoparticles form sodium silicate, which also reduces the surface charge density [52]. The zeta potentials of lysozyme and BSA are typical of proteins, where their values change from positive to negative at the IEP with increasing pH. The IEPs of lysozyme and BSA are found to be 10.7 and 4.6, respectively, which are in good agreement with the reported values [126, 191]. The surface charge density and the effective charge on the colloids using zeta potential can be calculated under certain approximations [219]. Based on this, Table 5.1 provides the surface charge density and the effective charge per nanoparticle. The size obtained from SANS has been used to perform the charge calculation. These results are consistent with those from SANS, as discussed later. The values of the surface charge density and the effective charge on proteins calculated in this way are found to be very small compared with those known from the literature.

The difference arises because of the non spherical shape and the relatively small size of proteins, for which the approximations used may not be valid.

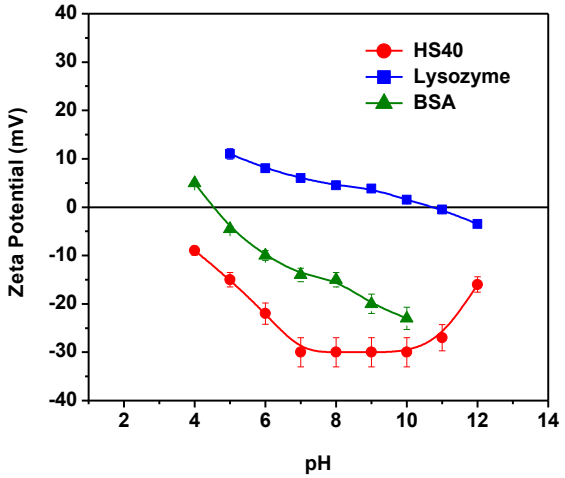

Figure 5.1. The zeta potential of HS40 silica nanoparticles, lysozyme and BSA proteins as a function of pH.

Table 5.1. Measured zeta potential of HS40 silica nanoparticles along with calculated surface charge density and the charge per nanoparticle.

pH	Zeta potential (mV)	Surface charge density (C/m^2)	Effective charge |q| (e.u.)
4	-9	-3.6×10^{-3}	22
5	-15	-6.1×10^{-3}	37
6	-22	-9.1×10^{-3}	55
7	-30	-1.3×10^{-2}	77
11	-27	-1.1×10^{-2}	68
12	-16	-6.5×10^{-3}	40

The pH-dependent structure and interaction of individual components (nanoparticles and proteins) have been examined using SANS. Figure 5.2 presents the SANS data of HS40 silica nanoparticles and proteins (lysozyme and BSA) prepared in D_2O at different pH values [216]. The data for 1 wt % silica nanoparticles [Figure 5.2(a)] are typical of those of a dilute system

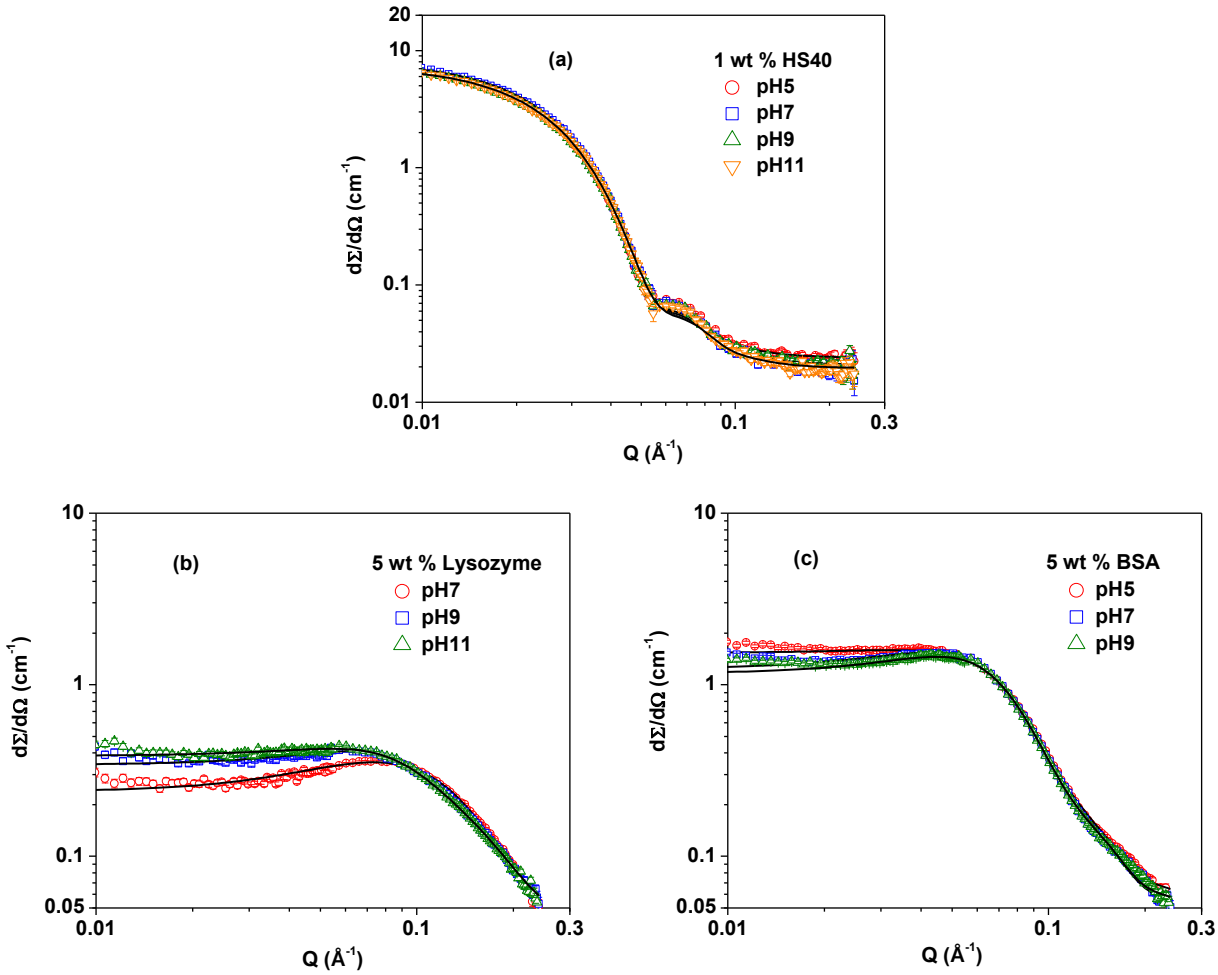

Fgure 5.2. SANS data of (a) 1 wt % HS40 silica nanoparticles, (b) 5 wt % lysozyme and (c) 5 wt % BSA proteins at different pH.

[$S(Q) \approx 1$]. The fact that 1 wt % silica nanoparticles represent a dilute system means that there is no pH-dependence corresponding to the change in interaction (Table 5.1) of the nanoparticle observed in Figure 5.2(a). The interaction within the nanoparticles can be observed from the SANS data at higher concentrations (Figure 3.8). The SANS data of 1 wt % proteins (lysozyme and BSA) also reveal that the systems can be treated as dilute. Data have been modeled by a prolate ellipsoid for lysozyme and by an oblate ellipsoid for BSA [Table 3.1]. The interaction parameters of proteins are obtained from 5 wt % SANS data [Figure 5.2 (b) and (c)]. The data show a correlation peak usually appearing at $Q_p = 2\pi/d$, where d signifies the average

interparticle distance. The corresponding $S(Q)$ has been modeled using the 2Y potential, and the fitted parameters are given in Table 5.2. The parameters for the attractive part of the potential (K_1 and Z_1) are mainly due to van der Waals attraction and are kept fixed [200]. The parameters for the repulsive interaction (K_2 and Z_2) are used as the fitting parameters, which are related to the effective charge and the ionic strength, respectively (Equation 4.1 and 4.2). As expected, the effective charge on both protein molecules increases with pH variation away from the IEP. The values of the effective charge are consistent with the reported values [200, 126].

Table 5.2. Fitted parameters of 5 wt % proteins (lysozyme and BSA) in D_2O at different pH. The K_1 and Z_1 are used as fitted parameters but kept constant as are expected not to change with pH.

System	pH	K_1	Z_1	K_2	Z_2	Effective charge |q| (e.u.)
Lysozyme	7	4.0	11.0	1.9	2.2	6.3
	9	4.0	11.0	0.7	1.7	3.4
	11	4.0	11.0	0.5	1.6	2.7
BSA	5	7.3	15.0	1.8	3.6	11.0
	7	7.3	15.0	3.4	4.5	17.5
	9	7.3	15.0	3.9	5.0	20.3

The interaction of the nanoparticles with individual proteins in terms of adsorption is studied using UV-vis spectroscopy. Samples for these measurements were prepared by mixing a fixed concentration (1 wt %) of silica nanoparticles with a varying concentration of lysozyme and BSA proteins in aqueous solution. Figure 5.3 shows the pH-dependent adsorption isotherms of proteins on the nanoparticles. The adsorption of the cationic lysozyme and the anionic BSA on the anionic silica nanoparticles is found to be very different because it is mostly governed by the electrostatic interaction. Lysozyme adsorbs strongly on the nanoparticles and the resultant adsorption depends on the pH [Figure 5.3(a)]. The adsorption for lysozyme protein as a function

of its concentration (C) is modeled by $A=A_0\,(1\text{-}\exp^{-KC})$, where A_0 is the saturation value and K is the adsorption coefficient. The saturation value increases with increasing pH, whereas the adsorption coefficient follows an opposite trend (Table 5.3). The adsorption is decided by the interplay of nanoparticle-protein attraction and protein-protein repulsion. The net charge on the lysozyme decreases as pH approaches the IEP (Table 5.2), which leads to an increase in the lysozyme adsorption because of a decrease in the protein-protein repulsion. The adsorption coefficient is a measure of the affinity between the nanoparticle and the protein, a higher value indicating a stronger attraction. The value of the adsorption coefficient decreases as pH approaches the IEP, which suggests a decrease in the attraction between the nanoparticles and the protein and results in the reduction in the charge on the lysozyme molecule. Unlike the behavior of lysozyme, BSA does not show any adsorption on the nanoparticles. Figure 5.3(b) shows a measured nonadsorption behavior of proteins on nanoparticles at pH 9 and is found to be unchanged with varying pH (e.g. 5 and 7). The electrostatic repulsion due to a similar charge seems to prevent the adsorption of BSA on the nanoparticles [125,194].

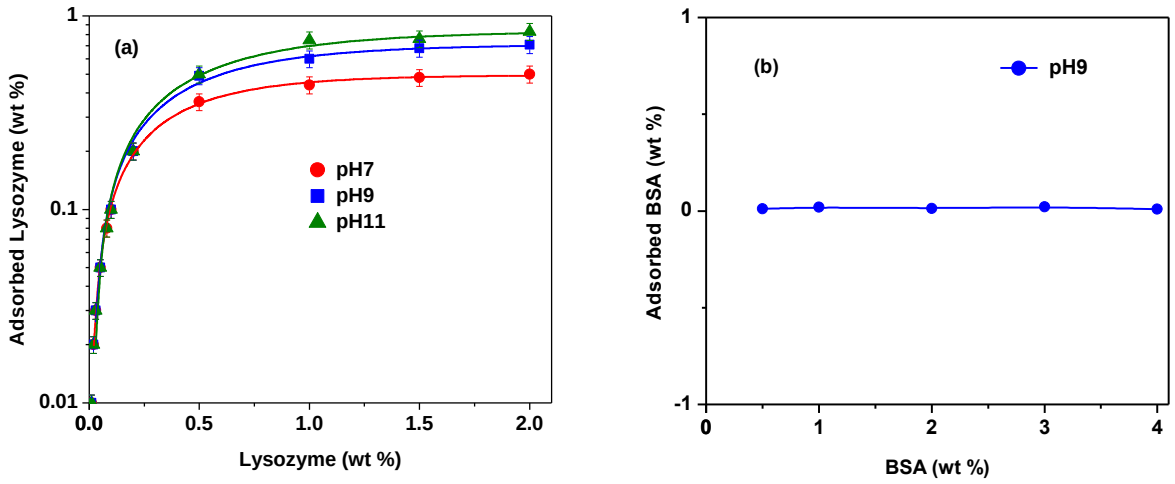

Figure 5.3. Adsorption isotherms of (a) lysozyme and (b) BSA proteins on 1 wt % HS40 silica nanoparticles at different pH. Lysozyme adsorption shows pH-dependent an exponential growth behavior, whereas BSA does not adsorb on the nanoparticles irrespective of the pH.

Table 5.3. Fitted parameters of adsorption curves of lysozyme protein on 1 wt % HS40 silica nanoparticles at different pH. N_{mp} is Number of adsorbed lysozyme molecules per nanoparticle at saturation value (maximum equilibrium surface concentration).

pH	Saturation value A_0 (wt %)	Adsorption coefficient K (1/wt %)	N_{mp}
7	0.5	2.5	130
9	0.7	2.1	185
11	0.8	1.8	216

5.4.2 Tuning the phase behavior of nanoparticle-protein complexes by varying pH

Both the adsorption of lysozyme and the nonadsorption of BSA may modify the interaction between the nanoparticles and lead to the phase change in the nanoparticle-protein systems. The phase behavior of these systems is determined by measuring the transmission of light (532 nm) through the samples as a function of protein concentration (Figure 5.4). Irrespective of pH and the protein type, the nanoparticle-protein phase behavior shows similar features where the transmission of light drops drastically beyond a particular protein concentration, referred to as the critical protein concentration (CPC) [210]. It is explained in terms of the transformation of the nanoparticle-protein system from one-phase (clear) to two-phase (turbid) from the CPC onwards. The two-phase is characterized by the formation of larger aggregates, which scatter more light and hence cause a reduction in the transmitted light intensity. The value of CPC is found to be strongly dependent on the type of protein and the pH of the system. The CPC increases for lysozyme, whereas it decreases for BSA as pH approaches their respective IEPs. The effect is more pronounced in the case of BSA than in the case of lysozyme. The observed differences in the phase behavior arise because of the interplay among the various interactions (nanoparticle-nanoparticle, nanoparticle-protein, and protein-protein)

present in the system. The strong electrostatic attraction between the nanoparticle and the lysozyme protein leads to the protein adsorption on the nanoparticles, neutralizing the charge and thereby causing protein-mediated bridging aggregation of the nanoparticles. It may be mentioned that the charge neutralization on the nanoparticle with lysozyme dominates at low protein concentrations, whereas bridging takes over at higher lysozyme concentrations when the charge neutralization is enough to bring the nanoparticles close to each other. On nanoparticles aggregation, the lysozyme protein also aggregates via the adsorbed shell on the nanoparticles. Because the charge on lysozyme decreases as pH approaches the IEP, the number of lysozyme molecules required to neutralize the charge of the nanoparticles increases. As a result, a higher CPC is required to transform a one-phase nanoparticle-protein system into a two-phase system for lysozyme at a higher pH [Figure 5.4(a)]. On the other hand, the nonadsorption of BSA results in the depletion attraction-induced aggregation of the nanoparticles and hence the phase transformation [194, 220, 221]. In this case, the decrease in pH enhances the depletion attraction between the nanoparticles because of a decrease in the repulsion between BSA molecules and at the same time reduces the electrostatic repulsion between the nanoparticles. Both of these effects are responsible for the decrease in the CPC for BSA as the pH approaches the IEP [Figure 5.4(b)]. It may be mentioned here that despite having a similar charge, the weak adsorption of BSA protein on silica nanoparticles due to site-specific interactions has been reported in some studies [141, 222]. In this case, the formation of a core-cell structure due to BSA adsorption is believed to stabilize the nanoparticles against aggregation by steric and/or electrosteric effects [26, 222, 223]. This is unlike the observed phase behavior of the nanoparticle-protein systems where the nanoparticle dispersion turns into aggregates at high BSA concentrations [120, 194, 210]. The nonadsorption of BSA results in the depletion attraction-induced aggregation of the

nanoparticles as supported by our measurements [Figure 5.2(b)]. In such a case, the BSA protein remains in the individual native condition irrespective of the nanoparticles aggregation. The interplay among the interactions and the resultant structures governing the phase behavior have been investigated using DLS and SANS.

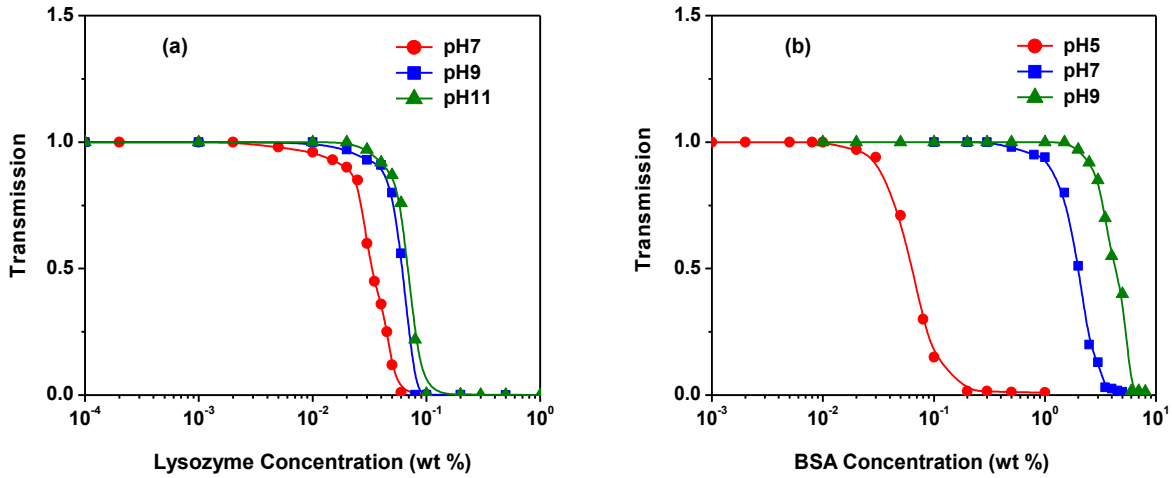

Figure 5.4. Transmission of light (532 nm) in 1 wt % of HS40 silica nanoparticles with varying concentrations of (a) lysozyme and (b) BSA proteins at different pH.

5.4.3 Effect of pH on structure and interaction of nanoparticle-protein complexes

The evolution of structure and interaction in DLS are reflected in the measured diffusion coefficient. It is usually difficult to separate these two contributions and are combined in the calculated effective size from the diffusion coefficient using Stokes-Einstein relation. Figure 5.5(a) shows the DLS data of the nanoparticle-lysozyme system with varying lysozyme concentration at a fixed pH value of 9. The decay constant of the auto correlation function decreases systematically with increasing concentration of lysozyme, suggesting the evolution of structure/interaction in the system. The intensity-average distributions of effective size of the selective nanoparticle-protein conjugates obtained employing CONTIN analysis are depicted in Figure 5.5(b). The results are very similar to that discussed earlier [Figures 3.4 and 4.4].

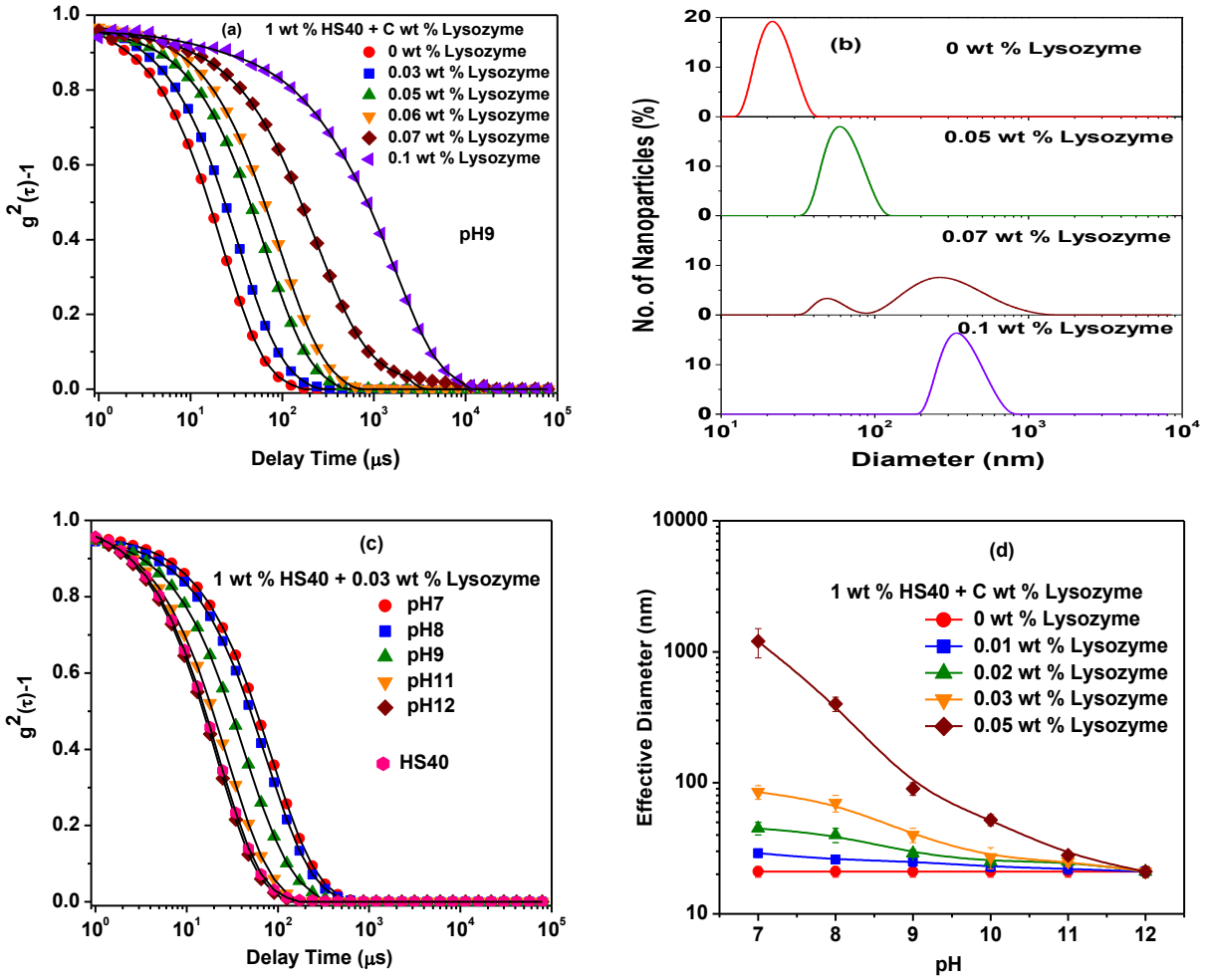

Figure 5.5. DLS data of 1 wt % HS40 silica nanoparticles in presence of lysozyme protein (a) auto correlation function with varying concentration of lysozyme at fixed pH 9, (b) particle size distribution of some of the data in (a), (c) auto correlation function at fixed lysozyme concentration (0.03 wt %) with varying pH and (d) effective hydrodynamic size of the nanoparticles and aggregates of nanoparticles with varying pH at different lysozyme concentrations.

The pH effect for a given silica nanoparticles-lysozyme system (1 wt % HS40 nanoparticles + 0.03 wt % lysozyme) is examined in Figure 5.5(c). The autocorrelation function systematically becomes narrow (high decay rate or high diffusion coefficient) with increasing pH and almost matches that of the pure nanoparticles at pH 11. This means that as the charge on the lysozyme decreases on approaching its IEP, the formation of the nanoparticle-protein complex and nanoparticle aggregation is suppressed. In comparison, the DLS data of the pure

nanoparticles system are found to be the same irrespective of the pH. Figure 5.5(d) presents the variation in the effective mean size of the system from DLS data at different concentrations of lysozyme as a function of pH. It is found that at a given lysozyme concentration, the mean size of the nanoparticle-lysozyme system decreases with increasing pH. The degree of nanoparticle aggregation at a low pH (e.g. pH 7) depends on the ratio of protein to nanoparticles (bridging of nanoparticles by protein), whereas above the IEP (e.g. pH 12), the system is characterized by individual nanoparticles as the protein becomes non-adsorbing.

Figure 5.6 presents the pH-dependent DLS data of the nanoparticle-BSA system. The overall features are similar to those of the nanoparticle-lysozyme system when the pH approaches the IEP. The autocorrelation functions of the nanoparticle-BSA system with varying protein concentrations at a fixed pH value of 9 are shown in Figure 5.6(a). Unlike the case of the nanoparticle-lysozyme system, there is no significant change in the autocorrelation function of the nanoparticle-BSA system as the BSA concentration is increased up to 3 wt %. Only at higher BSA concentrations is the behavior of the nanoparticle-BSA system similar to that of the nanoparticle-lysozyme system. The corresponding intensity-weighted size distributions are provided in Figure 5.6(b). The size distribution in this case is bimodal where the larger peak represents the effective size of the nanoparticles and the smaller peak corresponds to the size of the BSA molecule [Figure 5.6(b-II, III)]. The presence of bimodal distribution endorses the fact that BSA does not adsorb on the nanoparticles as seen in the adsorption isotherm of the nanoparticle-BSA system [Figure 5.2(b)]. Instead, the nonadsorption of BSA induces a depletion attraction between the nanoparticles resulting in a slow diffusion. Subsequently, the mean value of the larger peak shifts toward the higher magnitude with increasing concentration of BSA. At BSA concentrations above the CPC, sufficient depletion attraction gives rise to nanoparticle aggregation, as reflected by the large sizes in the size distribution [Figure 5.6(b-IV)].

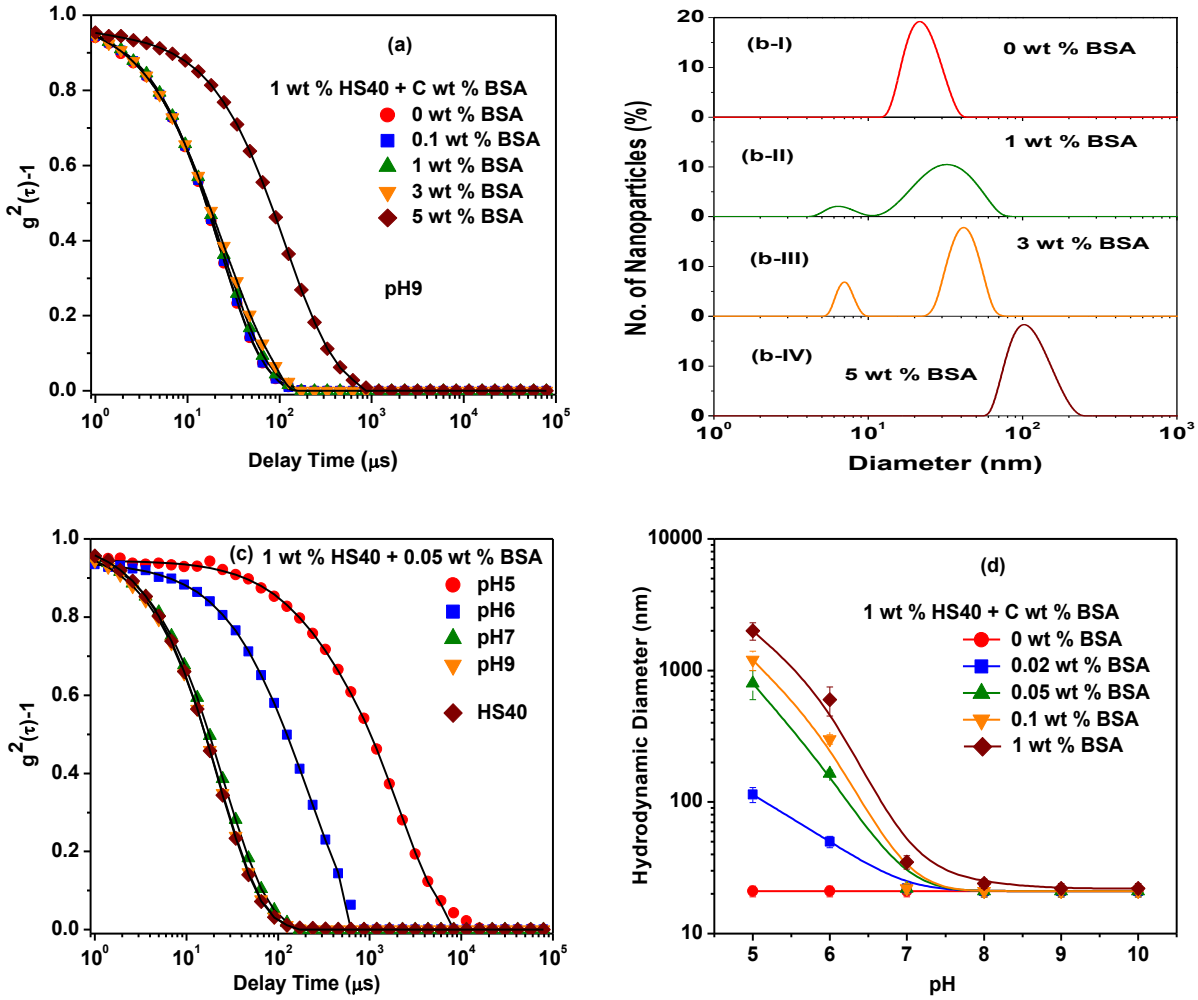

Figure 5.6. DLS data of 1 wt % HS40 silica nanoparticles in presence of BSA protein (a) auto correlation function with varying concentration of BSA at fixed pH 9, (b) particle size distribution of some of the data in (a), (c) auto correlation function at fixed BSA concentration (0.05 wt %) with varying pH and (d) effective hydrodynamic size of the nanoparticles and aggregates of nanoparticles with varying pH at different BSA concentrations.

It may be noted that the mean value of the smaller peak remains unchanged irrespective of the BSA concentration, suggesting no modifications in the BSA structure. The BSA peak, however, disappears at higher concentrations (5 wt % BSA) because of the scattering dominance by large nanoparticle aggregates. The effect of pH on the nanoparticle-BSA interaction is examined in Figure 5.6(c), where the DLS data of a typical data set of 1 wt % HS40 with 0.05 wt % BSA are plotted at different pH values. The variation in the calculated effective hydrodynamic size of the

nanoparticles with varying pH at different BSA concentrations is shown in Figure 5.6(d). It is found that the effective size of the nanoparticles decreases with increasing pH of the solution at a particular BSA concentration. This is because the charge on the nanoparticles and BSA decreases with decreasing pH [Figure 5.1], which eventually suppresses the electrostatic repulsion (nanoparticle-nanoparticle and protein-protein) and enhances the depletion attraction between the nanoparticles [210]. The effective size of the system increases with decrease in pH and increase in the protein concentration.

Finally, SANS is used to determine the interactions in order to understand the pH-dependent phase behavior of the nanoparticle-protein systems. SANS data of 1 wt % silica nanoparticles with varying concentrations of lysozyme protein at pH 9 are shown in Figure 5.7. The data show a systematic scattering buildup in the low and high-Q regions with increasing protein concentration. The scattering buildup at high-Q values is found to be governed by the additive form factor of the nanoparticle and protein, whereas that at low-Q values cannot be simply accounted for by such addition of the individual components. The observed change in the low-Q data may arise because of the evolution of attractive interaction and/or aggregation of the nanoparticles in the presence of protein [164]. At low protein concentrations ($\leq$0.05 wt % lysozyme), the data represent the one-phase system characterized by the nanoparticles undergoing attractive interactions [Figure 5.4(a)], and the corresponding $S(Q)$ has been modeled by the 2Y potential. The fitted parameters are given in Table 5.4. The parameters for the repulsive interaction (K_2 and Z_2) have been determined from the pure concentrated solution of the nanoparticles and kept fixed during the analysis (Figure 3.8) [194]. The strength of the attractive interaction increases with the protein concentration, whereas the range remains almost unchanged. The range of attractive interaction is found to be short compared to the screened Coulomb repulsion and has a value of the order of the size of the lysozyme molecule, over which

it mediates the attraction between the nanoparticles. On further increase in the protein concentration (~0.05 wt %), the data belong to the region of phase behavior where the bimodal distribution has been observed in DLS [Figure 5.5(b)]. In this case, the SANS data have been fitted by combining the scattering contributions from the aggregates of the nanoparticles along with a fraction of individual nanoparticles undergoing an attractive interaction. For protein concentrations higher than 0.1 wt %, the SANS data correspond to the region of phase behavior [Figure 5.4(a)] where the transmission of light is almost negligible and are fitted by considering the scattering only from the nanoparticle aggregates. The linearity of the scattering profile on the log-log scale indicates the fractal nature of the aggregates, where the low-Q cutoff and high-Q cutoff are determined by the reciprocals of the overall size of the aggregates and the building block size, respectively [178]. The low-Q cut off is not seen as the aggregate size and could be much larger than the corresponding size of the measured lowest-Q value ($2\pi/Q_{min} \approx 100$ nm). The buildup of scattering at the higher-Q region is due to the increasing contribution from the protein. The aggregates are found to be mass fractal having a fractal dimension of approximately 2.4.

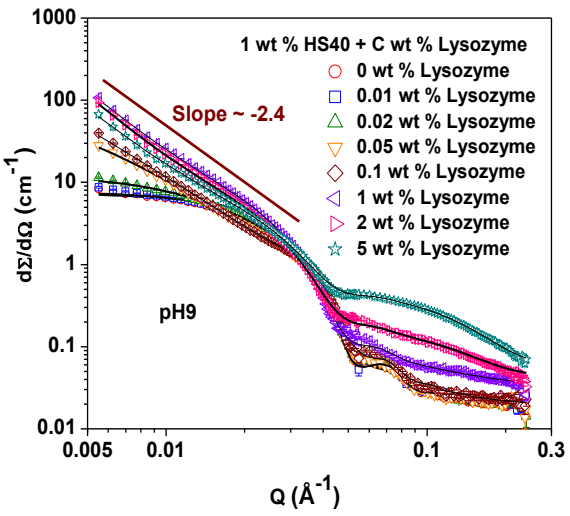

Figure 5.7. SANS data of 1 wt % HS40 silica nanoparticles with varying concentration of lysozyme protein at pH9.

Table 5.4. Fitted parameters of silica nanoparticles with lysozyme protein.

(a) 1 wt % HS40 silica nanoparticles with varying concentration of lysozyme protein at pH9. The fitting is carried out using the 2Y potential for the systems having no aggregation or partial aggregation of nanoparticles. The parameters of repulsive interaction K_2 = 9.0 and Z_2 = 7.0 are kept fixed.

Lysozyme concentration C (wt %)	Fractal dimension (D_m)	Building block radius R_b (Å)	K_1	Z_1	Fraction of unaggregated nanoparticles ϕ_{unp} (%)
0.01	-	-	5.5	30	100
0.02	-	-	15.0	9.0	100
0.05	-	-	25.0	9.0	100
0.1	2.4	92.0	28.0	10.0	40
1.0	2.4	90.0	-	-	0
2.0	2.5	91.0	-	-	0
5.0	2.4	90.0	-	-	0

(b) 1 wt % HS40 silica nanoparticles with 0.02 wt % lysozyme protein at different pH.

pH	K_1	Z_1	K_2	Z_2
7	20.0	9.0	9.0	7.0
9	15.0	9.0	9.0	7.0
11	9.0	9.0	8.0	7.0

SANS data of the nanoparticle-lysozyme system at different pH values for a particular lysozyme concentration (0.02 wt %) are used to examine the influence of pH on the phase behavior in terms of the interaction potential, as shown in Figure 5.8(a) [216]. The data in each case correspond to the one-phase region of the phase behavior where there exist individual nanoparticles undergoing attractive interaction due to protein adsorption. The buildup of scattering intensity in the low-Q region is observed with decreasing pH, indicating the pH-dependent enhancement in the attractive interaction. The data have been analyzed using the 2Y

potential [Table 5.4(b)], and the fitted total interaction potentials are shown in Figure 5.8(b). The total interaction potential becomes progressively attractive with decreasing pH. This can be understood as the charge on the lysozyme protein is high at lower pH, which in turn makes protein adsorption on nanoparticles more effective in mediating the attraction between nanoparticles. The repulsive and attractive components of the total potentials are also depicted in the inset of Figure 5.8(b). The magnitude of the repulsive part of the potential remains the same for pH 7 and 9 but decreases slightly at pH 11. This is consistent with the zeta potential (surface charge) on the nanoparticles, which is the same for pH 7 and 9, but comparatively less for pH 11 (Table 5.1). The ionic strength of the system is the same at all pH values, and hence the range (σ/Z_2) of repulsion remains unchanged. On the other hand, the strength of the attractive interaction (K_1) depends on the charge of the protein and increases with decreasing pH, whereas the range (σ/Z_1) remains almost the same, as decided by the size of the protein molecule. The combination of attractive and repulsive parts leads to an overall increase in the attraction between the protein-adsorbed nanoparticles with decreasing pH and moving away from the IEP.

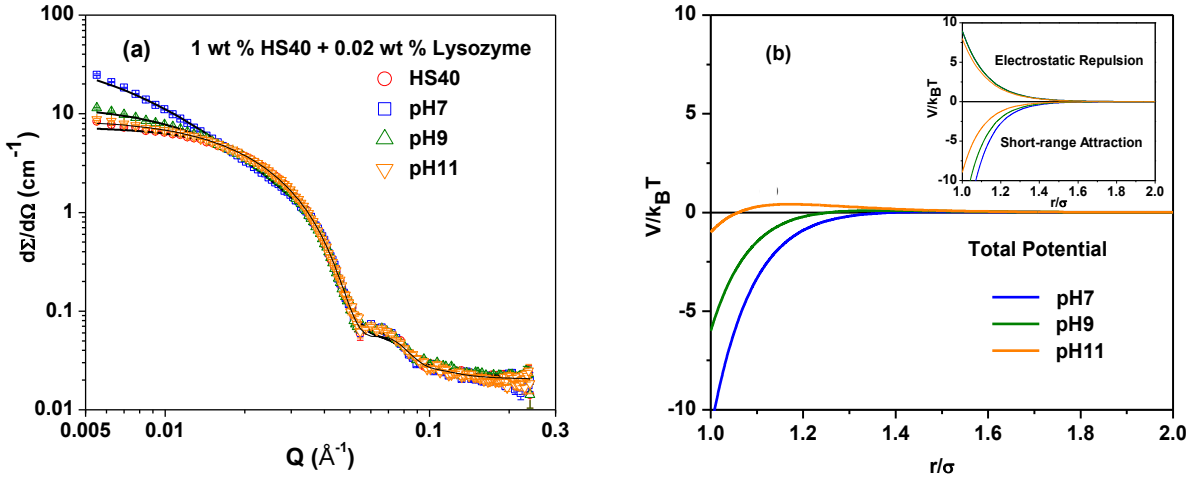

Figure 5.8. (a) SANS data of 1 wt % HS40 silica nanoparticles with 0.02 wt % lysozyme at different pH and (b) corresponding calculated total interaction potentials along with repulsive and attractive components (inset) between nanoparticles.

Figure 5.9 presents the SANS data of HS40 silica nanoparticles with varying BSA concentrations at pH 9. The data are interpreted with respect to the three protein concentration regions of the phase behavior [Figure 5.4(b)]. At low protein concentrations (<1 wt %), the scattering data are from the additive scattering contributions of the silica nanoparticles and BSA protein over the entire *Q* range. This is consistent with the nonadsorption of BSA on nanoparticles, as observed in the adsorption isotherm [Figure 5.3(b)] and DLS measurements [Figure 5.6(b)]. The nonadsorption of protein induces a depletion attraction between nanoparticles at sufficiently high BSA concentrations (1-5 wt %). The evolution of depletion attraction in SANS data is seen as a systematic buildup of the scattering in the low-*Q* region with increasing BSA concentration. The data are fitted using the 2Y potential, and the fitted parameters are given in Table 5.5. Unlike the case of lysozyme, the BSA-induced attractive interaction between the charged nanoparticles is found to be long-range. At a higher BSA concentration (5 wt %), the dominance of the depletion interaction over the electrostatic repulsion leads to the aggregation of the nanoparticles. The data have been fitted by mass fractal structure of the nanoparticle aggregates and the fractal dimension is found to be 2.4. It is an interesting result that in spite of very different mechanisms of nanoparticle aggregation by lysozyme and BSA protein, the fractal dimension of the nanoparticle aggregates is the same in both cases.

The pH-dependent modifications in the interaction of silica nanoparticles-BSA protein have been examined using SANS at a particular BSA concentration (1 wt %) in Figure 5.10(a). As observed in the case of lysozyme, the scattering data here also show an increase in low-*Q* with decreasing pH but moving toward IEP. The total interaction potentials along with their

individual components are plotted in Figure 5.10(b). The magnitude of the attractive interaction depends on the charge of both the protein and the nanoparticles. Though the charges on the nanoparticles are the same at pH 7 and 9, the charge of BSA is higher at pH 9 than at pH 7. As a result, the BSA-BSA repulsion suppresses with decreasing pH. The reduced BSA-BSA repulsion enhances the excluded volume gain for BSA molecules and hence enhances the magnitude of the depletion attraction (K_1) on approaching the IEP of protein. Also, the nanoparticle-nanoparticle repulsion is less at pH 5 because of a decrease in the charge on the nanoparticles [Table 5.1]. Thus, the decrease in the nanoparticle-nanoparticle repulsion and increase in the BSA-induced depletion attraction is responsible for the decrease in the CPC value with decrease in pH. The range of attraction ($1/Z_1$) is found to be independent of pH. The present study has thus shown that the difference in the adsorption behaviors of lysozyme and BSA proteins on silica nanoparticles leads to different interactions in silica nanoparticles-lysozyme and silica nanoparticles-BSA systems, which are further tuned by varying the pH.

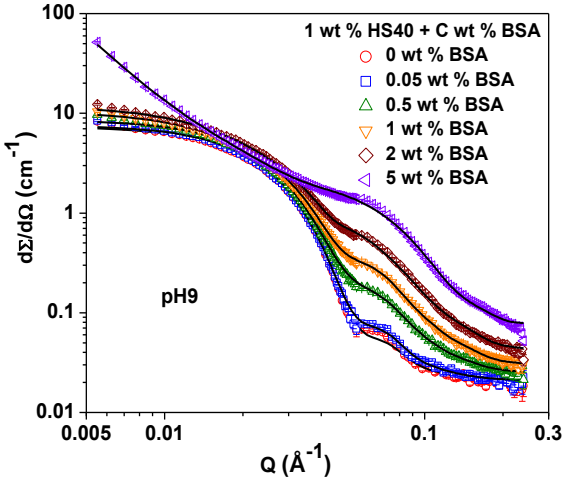

Figure 5.9. SANS data of 1 wt % HS40 silica nanoparticles with varying concentration of BSA protein at pH9.

Table 5.5. Fitted parameters of silica nanoparticles with BSA protein.

(a) 1 wt % HS40 silica nanoparticles with varying concentration of BSA protein at pH9. The parameters of repulsive interaction K_2 = 9.0 and Z_2 = 7.0 are kept fixed.

BSA concentration C (wt. %)	Fractal dimension (D_m)	Building block radius R_b (Å)	K_1	Z_1	Fraction of unaggregated nanoparticles ϕ_{unp} (%)
0.05	-	-	5.5	30	100
0.5	-	-	5.5	30	100
1	-	-	7.0	4.0	100
2	-	-	10.0	3.0	100
5	2.4	88.5	-	-	0

(b) 1 wt % HS40 silica nanoparticles with 1 wt % of BSA protein at different pH values.

pH	K_1	Z_1	K_2	Z_2
pH5	28.0	3.0	2.5	7.0
pH7	26.5	3.0	9.0	7.0
pH9	7.0	4.0	9.0	7.0

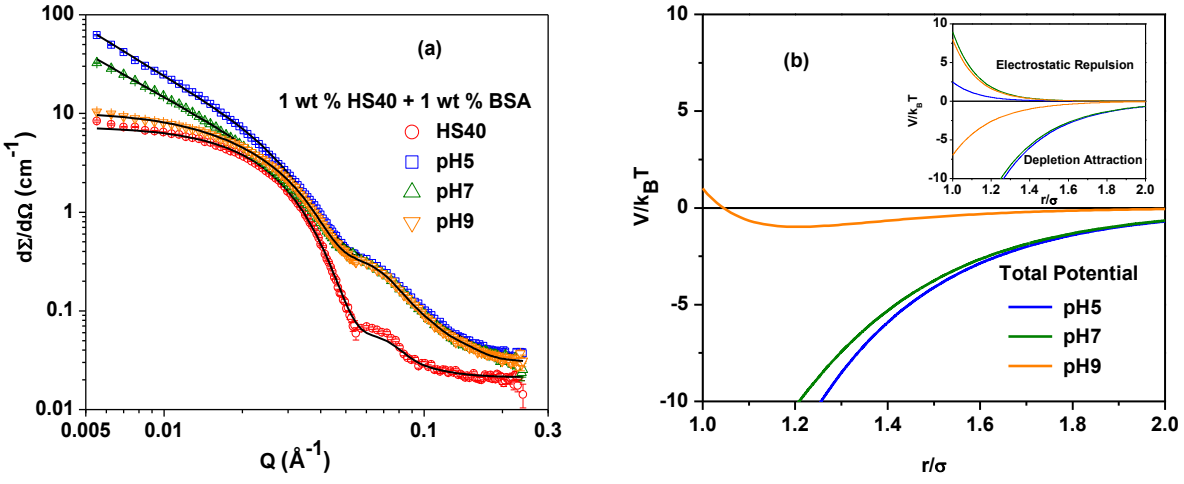

Figure 5.10. (a) SANS data of 1 wt % HS40 silica nanoparticles with 1 wt % BSA at different pH and (b) corresponding calculated total interaction potentials along with repulsive and attractive components (inset) between nanoparticles.

5.5. Conclusions

The pH-dependent adsorption isotherm, phase behavior, structure and interaction of two globular proteins (lysozyme and BSA) with silica nanoparticles have been studied by varying the pH with respect to the respective IEPs of the proteins. Because of the different charge nature of proteins, electrostatic attractive interaction leads to a strong adsorption of lysozyme whereas electrostatic repulsion prevents the adsorption of BSA on the nanoparticles. The lysozyme adsorption shows exponential growth behavior with protein concentration and the saturation value increases with pH approaching the IEP of the protein. In spite of different adsorption characteristics, both proteins exhibit a similar phase behavior where the nanoparticle-protein systems transform from one-phase (clear) to two-phase (turbid) above the CPC. The CPC is found to be much higher for BSA than lysozyme and increases for lysozyme but decreases for BSA with pH approaching their respective IEPs. The modifications in the phase behavior with pH have been explained in terms of the interplay of the nanoparticle-nanoparticle, nanoparticle-protein and protein-protein interactions present in the system. The lysozyme-mediated attractive interaction between the nanoparticles reduces with pH approaching the IEP because of the reduction in the charge on the protein. In the case of BSA, the enhancement of depletion attraction due to a decrease in the protein-protein repulsion and the diminution in the nanoparticle-nanoparticle repulsion are responsible for a shift in the CPC as pH is varied toward the IEP. The morphology of the nanoparticle aggregates is found to be mass fractal having a fractal dimension of 2.4, even though the underlying mechanisms are completely different.

Chapter 6

Size-Dependent Interaction of Silica Nanoparticles with Proteins

6.1. Introduction

In earlier chapters the differences in phase behavior of anionic silica nanoparticles with two model proteins (lysozyme and BSA) under varying solution conditions (concentration, ionic strength and pH) have been studied [194, 195, 210, 211, 216, 217]. Both proteins can render the same kind of phase behavior where nanoparticle-protein systems transform from one-phase (monodisperse) to two-phase (nanoparticle aggregation) as a function of protein concentration [194]. The differences in the interactions of the nanoparticles with two proteins are reflected in the much higher value of protein concentration required for BSA than for lysozyme in inducing aggregation in the respective nanoparticle-protein system. The aggregation of the nanoparticles irrespective of the charge nature of proteins indicates the nanoparticle-protein systems undergoing from repulsive to attractive behavior. The interactions between the nanoparticles have successively been modeled by combining electrostatic repulsion with short-range attraction for lysozyme protein adsorption and long-range depletion attraction in the case of nonadsorption of BSA protein. The understanding of these interactions eventually decides the phase behavior and resultant structures [27]. The characteristics of the nanoparticles and proteins (size, shape, charge, etc.) as well as solution conditions (ionic strength, pH, temperature) play an important role in these systems [18, 25, 27,100, 143, 187, 224]. For example, both the repulsive and attractive components of the interactions have been found to be significantly modified in the

presence of an electrolyte [23, 210, 213]. As a consequence of this, the concentration of protein at which nanoparticle-protein systems transform from one-phase to two-phase has been dramatically suppressed [210]. The decrease in the electrostatic repulsion for lysozyme and increase in depletion attraction for BSA are found to be mainly responsible for the differences in the phase behavior. The size of the nanoparticles is another parameter which plays a vital role in the nanoparticle-protein interactions [78, 126, 141, 225, 226]. Tuning the size of the nanoparticles not only changes the curvature but also the surface area of the nanoparticles for protein interaction. In the case of protein adsorbing on the nanoparticles, the competition of decreasing curvature (favoring adsorption) and decreasing overall surface area (disfavoring adsorption) with increasing the nanoparticle size controls the adsorption behavior of protein on the nanoparticles [227]. On the other hand, for non-adsorbing proteins, the excluded volume increases and the number density of the nanoparticles decreases with increasing the size of the nanoparticles. Both of these effects lead to the enhancement of depletion interaction [228-230]. In this chapter the interactions and resultant structures of nanoparticle-protein systems for both the adsorbing and non-absorbing proteins for different sized nanoparticles have been studied [231, 232]. The adsorption isotherm and phase behavior as well as interaction and resultant structure in these systems have been examined by a combination of spectroscopy and scattering techniques.

6.2. Experimental details

The electrostatically stabilized colloidal suspensions of different sized spherical silica nanoparticles (Ludox SM30, HS40 and TM40) and lyophilized powder proteins (hen egg lysozyme and BSA) were purchased from Sigma-Aldrich. Samples for different nanoparticles with proteins were prepared in 20 mM phosphate buffer at pH 7 in D_2O as discussed in chapter 3

(section 3.2). The adsorption isotherms of proteins on different sized nanoparticles and their resultant phase behavior were measured by UV-vis spectroscopy. The modifications of structure and interaction of nanoparticle-protein complexes were determined by scattering techniques SANS and DLS. The instruments and their parameters used for measurements were same as discussed in chapter 3.

6.3. Data analysis

a. Dynamic light scattering. The structure and/or interaction in DLS are determined through the effective diffusion coefficient in measured autocorrelation function [150]. The autocorrelation function broadens as the diffusion coefficient decreases either by increase in size of the constituents (nanoparticles/proteins) or enhancement of attractive interaction between them. In the case when the size distribution is not narrow, CONTIN method is widely used for high polydispersed as well as multimodal systems [154].

b. Small-angle neutron scattering. The form factor $P(Q)$ and structure factor $S(Q)$ provide the structure and interaction in SANS, respectively [164]. The individual nanoparticles and proteins are fitted with the form factor of standard geometries and their aggregation by the fractal structure. The modifications in interactions of nanoparticle-protein complexes with varying the size of the nanoparticles is modeled using the 2Y potential taking account of changes in both repulsive and attractive interactions [176].

The experimental data were fitted with model scattering using the nonlinear least-squares method [163]. The resolution corrections for the instrumental smearing of the experimental data were also made during the analysis.

6.4. Results and discussion

6.4.1. Adsorption of proteins on different sized nanoparticles

Figure 6.1 shows the SANS data of 1 wt % of three different sized silica nanoparticles (SM30, HS40 and TM40) prepared in D_2O at pH 7. This variation in SANS profiles can be attributed to differences in size and polydispersity of the nanoparticles [147]. At low concentration (1 wt %) and in the absence of any correlation peak, these systems can be treated as noninteracting dilute systems, i.e. $S(Q) \sim 1$. This has been, in fact, confirmed by scaling of the SANS data of lower concentration (say, 0.5 wt %) to 1 wt %. Thereby, the scattering is mainly governed by the form factor of the scatterers. The magnitude of scattering from such dilute systems increases with the volume of individual particles and the width of the scattering profile is reciprocal to the size of the particles (Equation 2.37). This suggests that qualitatively the size of the TM40 nanoparticles is the largest among the three nanoparticles. The SANS data have been fitted for the form factor of polydisperse spheres for the nanoparticles. The values of fitted parameters are given in Table 6.1. The mean radii of SM30, HS40, and TM40 are found to be 5.0, 8.8, and 13.8 nm with polydispersity 0.25, 0.16, and 0.13, respectively. These parameters are found to be in agreement with earlier reported values [194, 196]. The visibility of form factor oscillations at higher-*Q* region depends on the polydispersity of the particles and their smearing increases with the polydispersity of the nanoparticles. The calculated values of the surface area per particle and number density of the nanoparticles, as well as the specific surface area and curvature of the nanoparticles are also given in Table 6.1 [231]. There is an increase in surface area per nanoparticles, about one order, and a decrease in number density by two orders among the nanoparticles. The overall area for the nanoparticles (specific surface area) and curvature decreases with the increase in size of the nanoparticles. The significant difference in size of the

nanoparticles and proteins (Table 3.1) allows a high enough number of proteins to interact with the nanoparticles.

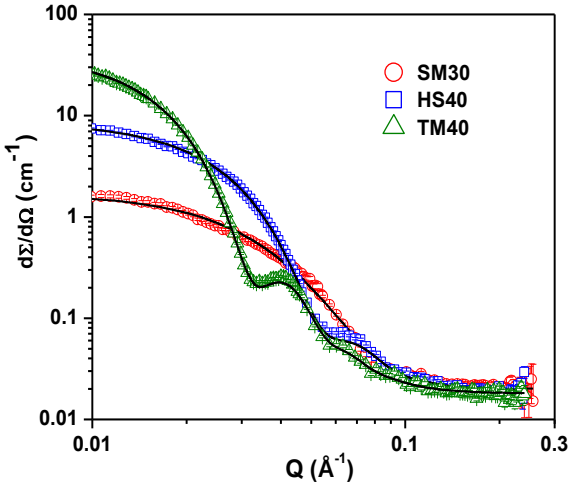

Figure 6.1. SANS data of 1 wt % silica nanoparticles (SM30, HS40 and TM40 in D_2O at pH ≈7.

Table 6.1. Fitted parameters of 1 wt % of silica nanoparticles (SM30, HS40 and TM40) in D_2O at pH ≈ 7.

Nanoparticle system	Mean radius R_m (nm)	Polydispersity σ	Surface area per particle (nm^2)	Number density n_{NP} (m^{-3})	Specific surface area (m^2/g)	Curvature (nm^{-1})
SM30	5.00	0.25	3.1×10^2	8.59×10^{21}	272	0.20
HS40	8.80	0.16	9.7×10^2	1.57×10^{21}	155	0.11
TM40	13.80	0.13	2.4×10^3	4.08×10^{20}	99	0.07

The adsorption isotherms of lysozyme and BSA proteins on three different sized silica nanoparticles as obtained by UV-vis spectroscopy are presented in Figure 6.2. The measurements were carried out for a fixed concentration (1 wt %) of silica nanoparticles with a varying concentration of lysozyme and BSA proteins. The data in Figure 6.2 show the amount of adsorbed protein on silica nanoparticles versus total protein in the system. The adsorption isotherms irrespective of the nanoparticle size show similar features. The adsorption of lysozyme

increases with concentration and follows typical exponential growth behavior [Figure 6.2(a)]. On the other hand, BSA protein does not show any adsorption [Figure 6.2(b)]. The electrostatic repulsion between similarly charged nanoparticles and BSA protein over their site-specific attraction seems to prevent the adsorption of BSA protein on the nanoparticles. The data of lysozyme protein are fitted with equation $A=A_0\,(1\text{-}\exp^{-KC})$, where A is the adsorbed protein A_0 is the saturation value and K is the adsorption coefficient and C is the total lysozyme concentration. The fitted parameters are given in Table 6.2. The adsorption coefficient increases whereas saturation value decreases with increasing the size of the nanoparticles. The higher value of saturation in the case of smaller size of the nanoparticles (SM30) can be attributed to the larger total surface area available for protein adsorption [Table 6.1]. The contact area of the protein is expected to increase with the decrease in the nanoparticle curvature (increasing nanoparticle size) and hence the adsorption coefficient increases with the nanoparticle size. From the adsorption data, the number of adsorbed lysozyme molecules per nanoparticles, surface number density, and packing fraction of adsorbed lysozyme have also been calculated [Table 6.2]. The number of adsorbed proteins per nanoparticle as expected increases with the size of the nanoparticles. The maximum adsorption of protein on nanoparticles (A_0) concomitant with the total surface area of the nanoparticles increases with the decrease in the size of the nanoparticles [Table 6.1]. This increase (about 2 times) is not scaled solely by change in the surface area (about 3 times) due to the important curvature effect, as reflected in the significant reduction in the surface number density and packing fraction of adsorbed protein on the nanoparticles with decrease in the size of the nanoparticles [141, 227].

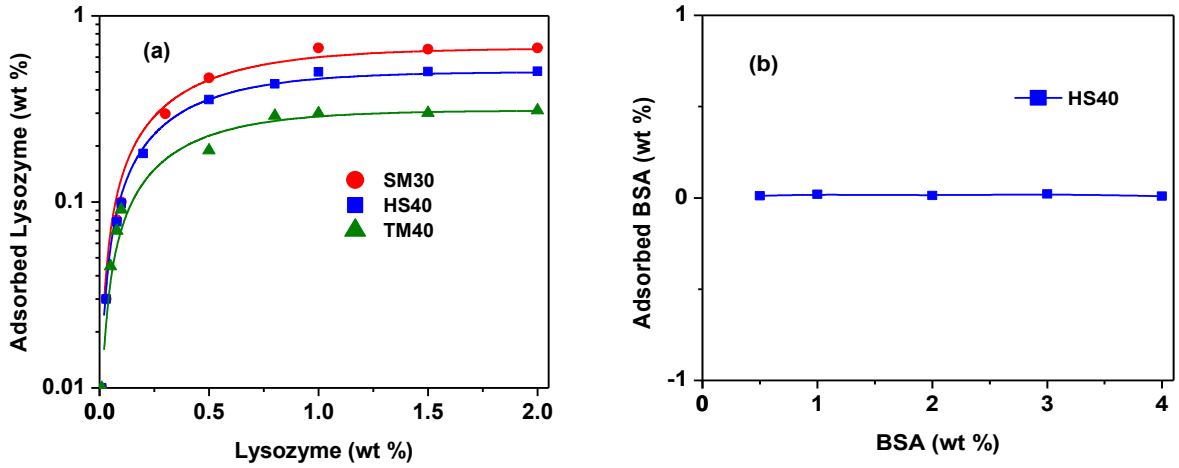

Figure 6.2. Adsorption isotherm of (a) lysozyme and (b) BSA proteins on 1 wt % silica nanoparticles at pH ≈7. Lysozyme shows an exponential growth behavior whereas BSA does not adsorb irrespective of the nanoparticle size.

Table 6.2. Fitted parameters of adsorption curves of lysozyme protein on 1 wt % different sized silica nanoparticles at pH ≈ 7. N_p, N_s and PF are number of adsorbed lysozyme per nanoparticle, surface density of adsorbed lysozyme and packing fraction, respectively at saturation value.

Nanoparticle system	Saturation value A_0 (wt %)	Adsorption coefficient K (1/wt %)	N_P	N_s (m^{-2})	PF
SM30	0.67	2.25	32	10.2×10^{16}	0.48
HS40	0.50	2.49	130	13.4×10^{16}	0.79
TM40	0.31	2.63	310	13.5×10^{16}	0.86

6.4.2. Size-dependent phase behavior of nanoparticles with proteins

The adsorption of lysozyme leads to the bridging aggregation of the nanoparticle and thereby nanoparticle-protein system transform from one phase (clear) to two phase (turbid) [22, 23, 216]. Similar behavior is also observed for the non-adsorbing BSA for much higher

concentration than lysozyme. The phase behavior is examined by measuring the transmission of light (6000 Å) through silica nanoparticles (1 wt %) as a function of protein concentration. The size-dependent phase behavior of the nanoparticles with proteins is shown in Figure 6.3. The two-phase nanoparticle-protein system is identified by a sudden decrease in the transmission of light. The phase behavior in Figure 6.3 shows similar features irrespective of protein type and size of the nanoparticles. However, the aggregation commences at lower concentration for the larger sized nanoparticles for both proteins (insets of Figure 6.3). In the case of lysozyme, they adsorb on the surface of the oppositely charged nanoparticles neutralizing the charge and thereby causing protein-mediated aggregation of the nanoparticles (formation of two-phase system) [216] The critical protein concentration (CPC) to induce phase transformation [inset of Figure 6.3(a)] is governed by the charge neutralization through the competition of surface area effect (the larger the size, the higher will be the protein required) and particle number density effect (the higher the size, the lower will be the protein required) as decided by the number ratio of protein to nanoparticle [23]. The decrease in CPC with increase in size suggests the dominance of the number density effect over the surface area effect. For similarly charged BSA, the phase transformation arises from their nonadsorption leading to the depletion-induced aggregation of the nanoparticles. The CPC [inset of Figure 6.3(b)] in this case is lowered with the increase in the size of the nanoparticles because of enhancement of the excluded volume effect of individual nanoparticles (the higher the size, the higher will be the excluded volume) as well as the number density effect (the higher the size, the higher will be the protein molecules per nanoparticle). The evolution of interaction and structure in these systems has been studied by DLS and SANS.

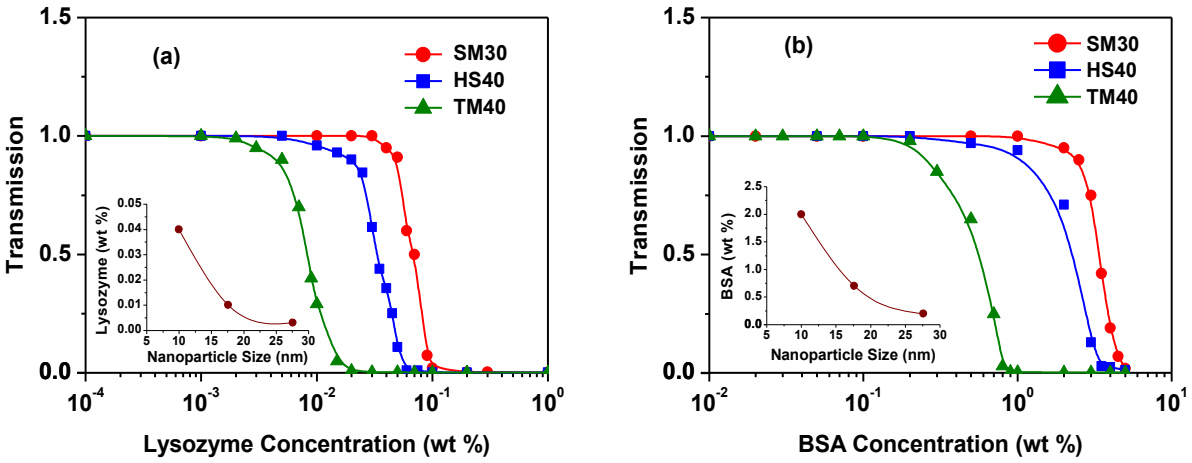

Figure 6.3. Transmission of light (600 nm) in 1 wt % of silica nanoparticles (SM30, HS40 and TM40) with varying concentrations of (a) lysozyme and (b) BSA proteins at pH ≈ 7. Insets show the size-dependent variation of critical protein concentration for two-phase system.

6.4.3. Influence of nanoparticle size on structure and interaction of nanoparticle-protein complexes

The DLS autocorrelation function and corresponding size distribution of one of the nanoparticle systems (TM40) at different concentrations of lysozyme in their respective phase behavior (Figure 6.3) are shown in Figure 6.4. The features are similar to HS40 nanoparticles as shown in Figure 3.4. The autocorrelation function is systematically broadened with the increase in the concentration of lysozyme owing to the evolution of attractive interaction between the nanoparticles and/or the formation of the nanoparticle aggregates mediated by the lysozyme. The evolution of attractive interaction followed by the nanoparticles aggregation is reflected in the corresponding size distribution [Figure 6.4(b)]. Nanoparticles, irrespective of their size, show similar features of evolution of interaction and structure in respective phase behavior. However, the concentration of protein needed to get the required changes is lowered in favor of large sized

nanoparticles because of the interplay of surface area, number density and curvature effects in the system. Figure 6.4(c) shows the size distribution of different sized nanoparticles in presence

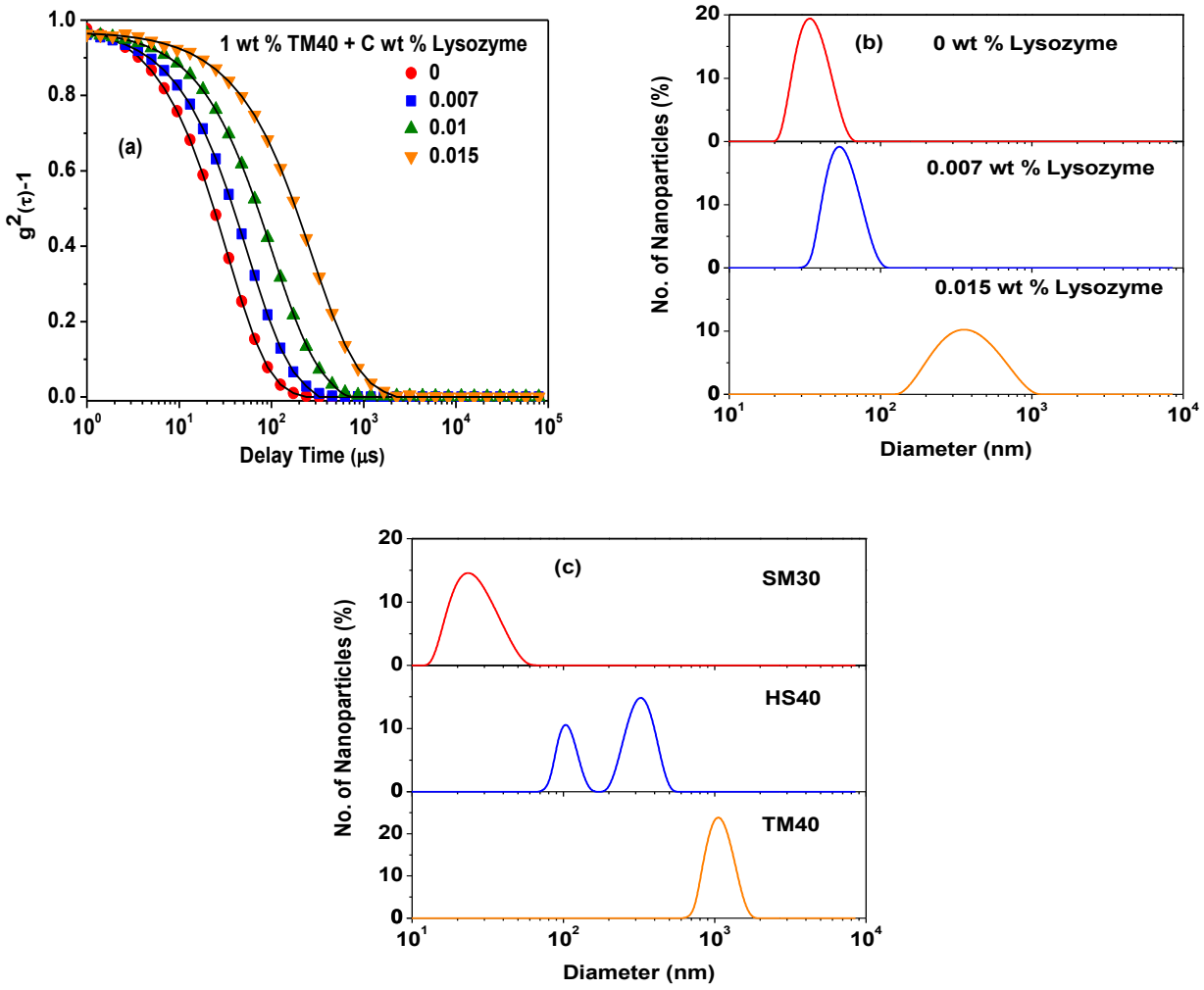

Figure 6.4. DLS data of 1 wt % TM40 silica nanoparticles with varying concentration of lysozyme (a) autocorrelation function, (b) particles size distribution and (c) size distributions of three different sized nanoparticles (SM30, HS40 and TM40) in presence of 0.04 wt % lysozyme.

of 0.04 wt % lysozyme. At this particular concentration of lysozyme SM30 remains in one-phase, HS40 shows the bimodal distribution corresponding to the transition region of phase behavior and TM40 has been found in complete aggregation region of phase behavior. With increasing the size, number density of the nanoparticles decreases as a result the number of

protein molecules per nanoparticles is more for bigger sized nanoparticles. Further in bridging aggregation, higher is the number ratios of protein to nanoparticles higher is the tendency of aggregation and hence change in effective size of for larger size nanoparticle is more.

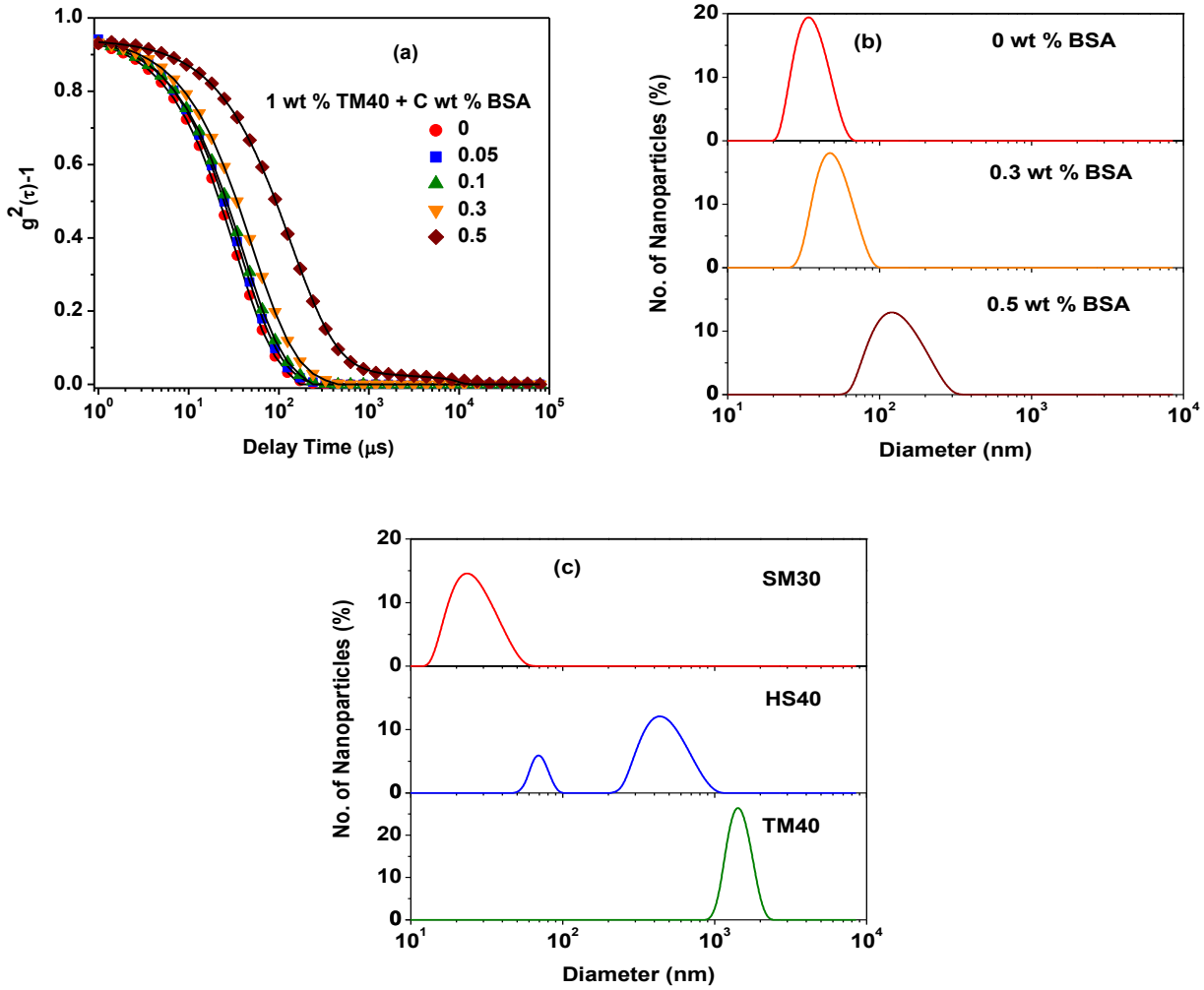

Figure 6.5. DLS data of 1 wt % TM40 silica nanoparticles with varying concentration of BSA (a) autocorrelation function, (b) particles size distribution and (c) size distributions of three different sized nanoparticles (SM30, HS40 and TM40) in presence of 2 wt % BSA.

It has been seen that in spite of different interactions (adsorption isotherms in Figure 6.2) of lysozyme and BSA proteins with silica nanoparticles, both proteins show similar phase behavior (Figure 6.3). The attractive interaction responsible for the aggregation of the

nanoparticles in the presence of BSA protein is induced by depletion from the nonadsorption of protein. The autocorrelation function and corresponding size distribution of TM40 silica nanoparticles with BSA protein are shown in Figures 6.5(a) and (b), respectively. Overall features are similar to that of HS40 silica nanoparticles with BSA protein (Figure 3.5). The strength of the depletion interaction is known to increase with the depletant (BSA) concentration [117, 233]. Thus the changes in autocorrelation function at higher BSA concentrations are due to evolution of the depletion interaction and resultant structures. Similar behavior has also been observed for the other nanoparticles (SM30) in the presence of BSA proteins and the results are consistent with the corresponding phase behavior. Figure 6.5(c) compares the size distribution of different sized nanoparticles in presence of 2 wt % BSA. At this particular concentration of BSA, SM30 remains in one-phase, HS40 shows the bimodal distribution corresponding to the transition region of phase behavior and TM40 has been found in complete aggregation region of phase behavior. With increasing the size of the nanoparticles excluded volume increases and hence strength of the depletion attraction which is responsible for the structural evolution of the nanoparticles.

The SANS data of TM40 silica nanoparticles with lysozyme in their phase behavior [Figure 6.3(a)] are shown in Figure 6.6. The structure and interaction are measured by SANS separately through the form factor and structure factor of the scattering intensity, respectively. Significant changes in scattering profiles have been found as a function of lysozyme concentration. Based on the *Q*-dependent features, data at different protein concentrations can be divided into two regions, low-*Q* (<0.02 Å) and high-*Q* (>0.02 Å). There is systematic buildup in scattering intensity in the low-*Q* region whereas no significant changes have been found in the

high-*Q* region (up to 0.1 wt %). The scattering at high-*Q* is found to be governed by the additive form factor of the nanoparticles and protein. On the other hand, the rise of scattering in low-*Q* from the nanoparticle-lysozyme system cannot be additive from the individual components since the scattering from lysozyme is about two orders less than the nanoparticles. The changes in scattering in low-*Q* are expected due to the evolution of interaction and/or structure in the nanoparticles in the presence of protein as observed in DLS data [194]. The features of the buildup in scattering intensity in low-*Q* are similar to that of attractive interaction in the system. The scattering intensity at $S(Q=0)$ is inversely related to the osmotic pressure of the system. This results in a very high value of $S(Q=0)$ for attractive interaction and $S(Q)$ diverges in the low-*Q* region. The SANS data are therefore fitted with the $S(Q)$ of attractive interaction between nanoparticles as induced by the presence of protein. Data have been fitted with the 2Y potential and the fitted parameters are given in Table 6.3(a). Data at higher concentration of lysozyme have been fitted by nanoparticle aggregates. The morphology of the nanoparticle aggregates is found to be mass fractal.

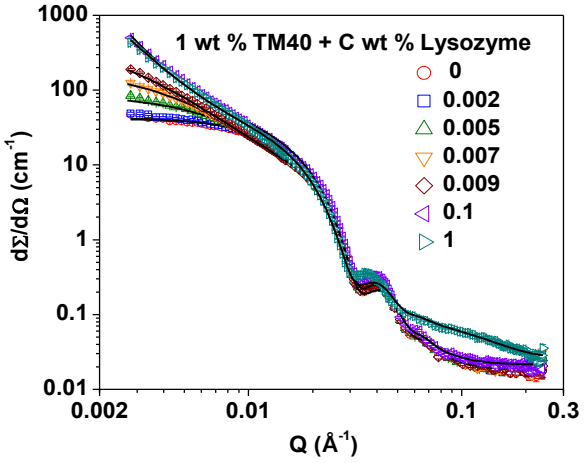

Figure 6.6. Fitted SANS data of 1 wt % TM40 silica nanoparticles with varying concentration of lysozyme protein.

Table 6.3. Fitted parameters of silica nanoparticles with lysozyme protein at pH ≈7.

(a) 1 wt % TM40 with varying concentration of lysozyme protein. The parameters of repulsive interaction K_2 = 14.0, Z_2 = 11.0 are kept fixed.

Lysozyme Concentration C (wt %)	Fractal Dimension (D_m)	Building block radius R_b (Å)	K_1	Z_1	Fraction of unaggregated nanoparticles ϕ_{unp} (%)
0.002	-	-	17	14.0	100
0.005	-	-	45	13.0	100
0.007	-	-	48	13.5	55
0.009	-	-	52	13.0	30
0.1	2.5	161.5	-	-	0
1	2.5	155.0	-	-	0

(b) 1 wt % different sized silica nanoparticles (SM30, HS40 and TM40) with lysozyme protein at their respective CPC values.

Nanoparticle system	Lysozyme concentration (wt %)	K_1	Z_1	K_2	Z_2
SM30	0.04	7	5	4.5	3.5
HS40	0.01	18	9	9	7
TM40	0.003	40	14	14	11

It has been observed that the CPC value strongly depends on the nanoparticle size as discussed earlier and it is significantly smaller for larger sized nanoparticles. The SANS data of different sized silica nanoparticles with lysozyme protein at close to their respective CPC values are shown in Figure 6.7(a).The data in each case have been fitted with the 2Y potential and the values of fitted parameters are given in Table 6.3(b). The total potential between nanoparticles and its individual components are plotted in Figure 6.7(b). It has been found that the strength of repulsion (K_2) increases with the size of the nanoparticles whereas the range (σ/Z_2) remains

almost the same. This is in accordance with the DLVO theory where the magnitude of the potential is proportional to the size of the nanoparticles when stabilized by the same zeta potential [234].The range depends on the ionic strength (20 mM buffer for all the system) of the solution and therefore has been found independent of the size of the nanoparticles [23, 210]. Interestingly, in spite of increased repulsion between nanoparticles for larger size nanoparticles, the CPC follows the reverse trend. This happens as the attractive interaction is also enhanced with the increase in the size of the nanoparticles [Table 6.3(b)]. It has also been observed that the CPC of all nanoparticle-protein systems corresponds to the values of adsorbed proteins per nanoparticle (2 for SM30, 2.6 for HS40, and 3 for TM40) which are greater than 1. This is possibly used to reduce the repulsive interaction between nanoparticles [23, 210]. The size-dependent phase behavior in Figure 6.3(a) thus arises because of the dominance of protein-mediated short-range attractive interaction over the long-range repulsion between the nanoparticles. Irrespective of the size of the nanoparticles, the morphology of the nanoparticle aggregates in the two-phase system is found to be mass fractal.

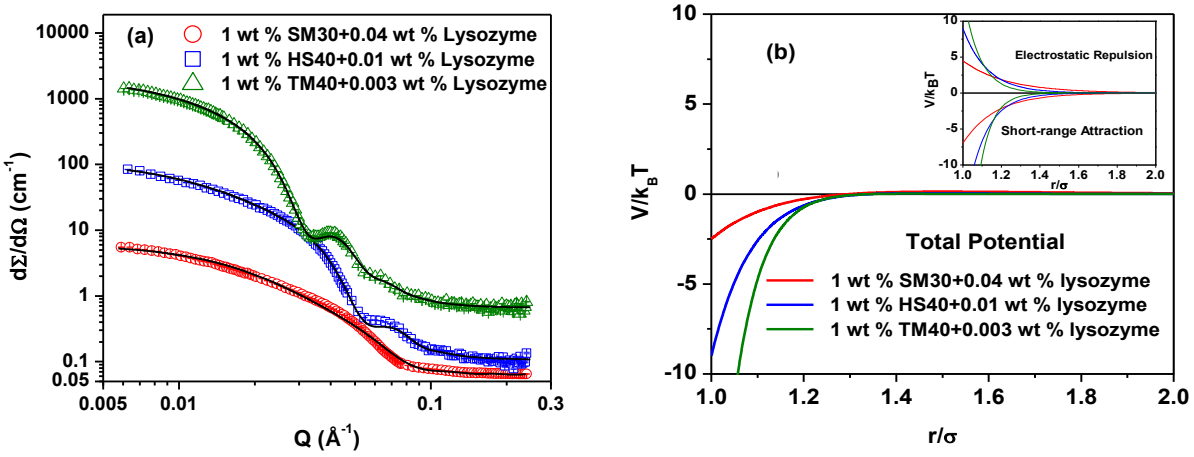

Figure 6.7. (a) SANS data of 1 wt % three different sized silica nanoparticles with lysozyme protein at their respective CPC values and (b) the calculated total interaction potentials along with components (inset) between nanoparticles from the fitting of SANS data at pH ≈7.

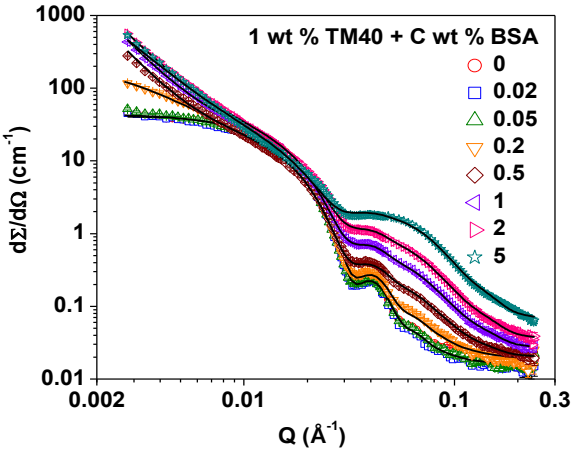

Figure 6.8. Fitted SANS data of 1 wt % TM40 silica nanoparticles with varying concentration of BSA protein.

Table 6.4. Fitted parameters of silica nanoparticles with BSA protein at pH ≈7.

(a) 1 wt % TM40 with varying concentration of BSA protein. The parameters of repulsive interaction K_2 = 14.0, Z_2 = 11.0 are kept fixed.

BSA Concentration C (wt. %)	Fractal Dimension (D_m)	Building block radius R_b (Å)	K_1	Z_1	Fraction of unaggregated nanoparticles ϕ_{unp} (%)
0.2	-	-	40	4.5	100
0.5	2.7	140.0	-	-	0
1	2.6	136.0	-	-	0
2	2.6	136.0	-	-	0
5	2.6	136.0	-	-	0

(b) 1 wt % different sized silica nanoparticles (SM30, HS40 and TM40) with BSA protein at their respective CPC values.

Nanoparticle system	BSA concentration (wt %)	K_1	Z_1	K_2	Z_2
SM30	2	9	2.5	4.5	3.5
HS40	0.7	20	3.5	9	7
TM40	0.2	40	4.5	14	11

The phase behavior of a nanoparticle-BSA system [Figure 6.3(b)] is similar to that of a nanoparticle-lysozyme system [Figure 6.3(a)], but the CPC values are much higher for BSA protein. The SANS data of TM40 silica nanoparticles with varying BSA concentration are shown in Figure 6.8. Data representing different regions of phase behavior show a trend similar to that of a nanoparticle-lysozyme system. The fitted parameters are given in Table 6.4(a). At low BSA concentration (0-0.05) data can be fitted by adding the scattering contribution due to form factor of the nanoparticles and proteins over the entire Q range. At intermediate concentration data are modeled by structure factor for 2Y potential. Unlike lysozyme-mediated short-range attraction, BSA-induced attractive depletion interaction between charged nanoparticles is found to be long-range [194, 215]. The magnitude of depletion attraction increases with the concentration of BSA protein whereas the range remains almost the same [194]. At higher BSA concentrations the dominance of the depletion interaction leads to the aggregation of the nanoparticles and the system transforms from one-phase to two-phase. Again the morphology of the aggregates is found to be mass fractal. The SANS data of different sized silica nanoparticles with BSA protein at their respective CPC values are shown in Figure 6.9(a). The data have been fitted with the 2Y potential and the values of the fitted parameters are given in Table 6.4(b). The calculated resultant interaction potentials and their individual components are plotted in Figure 6.9(b). Both the strength of attraction (K_1) and the range (σ/Z_1) of depletion interaction are found to be much larger than that of repulsion. The strength of attraction increases whereas the range remains almost the same with the increase in the size of the nanoparticles. The excluded volume effect is enhanced with increasing nanoparticle size leading to increase in the depletion interaction. It is observed that the total interaction potential of silica nanoparticles for both proteins leading to two-phase formation is more attractive for larger sized nanoparticles. This can be understood in

terms of the particles number density effect which leads to a lesser number of nanoparticles for larger size nanoparticles than smaller ones at a constant (1 wt %) concentration and therefore require a larger interaction to aggregate them [200].

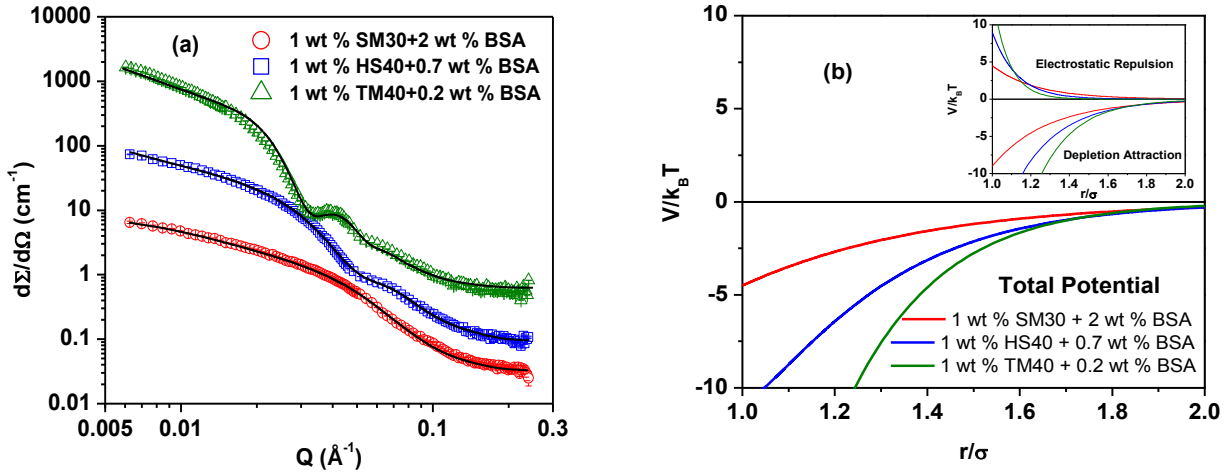

Figure 6.9. (a) SANS data of 1 wt % three different sized silica nanoparticles with BSA protein at their respective CPC values and (b) the calculated total interaction potentials between nanoparticles along with components (inset) from the fitting of SANS data at pH ≈7.

6.5. Conclusions

The size-dependent interaction of silica nanoparticles with lysozyme and BSA proteins has been studied. The adsorption of lysozyme on silica nanoparticles increases with concentration and follows an exponential growth behavior. The adsorption coefficient increases whereas the saturation value decreases with increasing the size of the nanoparticles. The increase in saturation value for smaller particles is interpreted in terms of the larger total surface area available for protein adsorption. The adsorption coefficient depends on the curvature of the nanoparticles and hence favors the larger size of the nanoparticles. On the other hand, the BSA protein does not show adsorption on any size of the nanoparticles. The adsorption of lysozyme as well as nonadsorption of BSA on silica nanoparticles leads to one-phase (clear) to two-phase

(turbid) transformation in the respective nanoparticle-protein system. The phase transformation is observed at lower concentration for the larger sized nanoparticles for both proteins. The decrease in CPC with increase in size for the lysozyme protein is decided by the dominance of number density effect over the surface area effect. The CPC in the case of nonadsorbing BSA protein is lowered with the increase in the size of the nanoparticles because of the enhancement of the excluded volume of an individual nanoparticle and number density effects. The hydrodynamic sizes as obtained by DLS in these systems are found to be consistent with size-dependent phase behavior of the nanoparticles with proteins. SANS suggests that the size-dependent phase behavior of silica nanoparticles for lysozyme protein arises because of the dominance of protein-mediated short-range attractive interaction over the long-range repulsion between the nanoparticles, whereas for BSA protein the excluded volume effect is enhanced with increasing nanoparticle size leading to an increase in the depletion interaction. The morphology of the nanoparticle aggregates for both proteins in the two-phase system irrespective of nanoparticle size is found to be mass fractal.

Chapter 7

Summary

The nanoparticle-protein complexes are of great recent interests as they show rich phase behavior which has myriad applications in biology and material science [11, 14]. The interactions of the nanoparticles with proteins can control the protein-protein interactions, enzymatic activity, protein delivery and applied to diagnostics and sensors [6, 11, 45]. For their part, proteins may induce the phase transformations of the nanoparticles for instance glass transition, gelation, crystallization and flocculation which could be used to prepare multifunctional materials [27, 235]. The important interactions those govern the phase behavior of the nanoparticle-protein systems are van der Waals, hydrogen bonding, steric repulsion, electrostatic and depletion [27]. The role of varying electrostatic interaction in controlling the phase behaviour of nanoparticle-protein complexes has been investigated in this thesis. The studies are carried out from systems having both nanoparticle and protein charged, where their conjugation is tuned by choice of protein and varying solution conditions (ionic strength and pH) as well as size of the nanoparticles. The anionic silica nanoparticles and two globular proteins [lysozyme and bovine serum albumin (BSA)] have been used as model systems.

There are wide ranges of techniques which can be employed to get complementary information on nanoparticle-protein complexes [139]. A combination of UV-vis spectroscopy and scattering techniques [DLS and SANS] has been used to characterize the nanoparticle-protein complexes in this thesis. The presence of organic molecules such as proteins is determined by the characteristic absorption peak and used to determine the adsorption isotherms

of proteins on nanoparticles. The transmission of light at a particular wavelength provides the structural evolution (phase behavior) of the resultant nanoparticle-protein systems. DLS and SANS are powerful techniques for obtaining the structure and interaction information of the system. DLS technique relies on the detection and analysis of fluctuations in the intensity of scattered light by particles in a medium undergoing Brownian motion [148]. The structure and interaction together are contained in the average diffusion coefficient or related effective hydrodynamic size given by Stokes-Einstein relation. On the other hand, structure and interaction can be separated using SANS technique through the form factor and structure factor, respectively [157]. SANS is of considerable importance for multi-component hydrogenous systems due to very different contrasts for hydrogen and deuterium components. The other advantages of scattering techniques include that the systems are probed in-situ and under native conditions.

The thesis consists of seven chapters including this chapter on summary of thesis. Chapter 1 provides an introduction to the nanoparticles, proteins and their complexes. The details of the experimental techniques used for the characterization of nanoparticle-protein complexes are discussed in chapter 2. The results of different studies on nanoparticle-protein complexes are described in chapters 3 to 6. Chapter 3 reports the study of differences in complexes of silica nanoparticles with lysozyme and BSA proteins. The effect of electrolyte on these nanoparticle-protein complexes is examined in chapter 4. Chapter 5 presents the tuning of nanoparticle-protein complexes through pH. The role of nanoparticle size on the nanoparticle-protein complexes is investigated in chapter 6.

A general introduction to nanoparticles, proteins and their complexes is given in **chapter 1**. Nanoparticles due to its small size exhibit striking physical and chemical properties [1, 2]. The

top-down and bottom-up are commonly used methods of synthesis of nanoparticles [2]. The different nanoparticles applications include from biomedical to electronics, energy to environment and food to textiles. In particular in biomedical applications, there is increasing recent interest to understand the interaction of nanoparticles with biomolecules such as proteins [25]. Proteins are the polymers of amino acids with a specific three-dimensional shape and do most of the work in cells required for structure, function and regulation of body tissues and organs [15]. Proteins have four different levels of structure: primary, secondary, tertiary and quaternary. Based on native structures, proteins can be divided in two general categories: globular and fibrous proteins. Globular proteins are generally compact, soluble in water and more or less spherical in shape. On the other hand, fibrous proteins are typically elongated and insoluble in water. The protein solutions are stabilized due to the repulsive (electrostatic and/or steric) interaction overcoming the attractive (van der Waals and/or hydrophobic interaction) interactions between protein molecules. The various solution conditions (e.g. pH, ionic strength, temperature etc.) are often used for tuning the interactions and hence the stability of protein solutions [28]. The charge nature of both nanoparticles and proteins can be utilized for their conjugation as well as comparable size of nanoparticle with protein makes this conjugate useful for biological applications where it can move in and out of the cells. The interactions governing nanoparticle-protein complexes depend on both DLVO (van der Waals attraction along with electrostatic double-layer repulsion) and non-DLVO (e.g., solvation, steric, hydrogen bonds, depletion and hydrophobic) interactions [101]. The unique properties of nanoparticles combining with proteins lead to interesting applications. The high surface-to-volume ratio of nanoparticles is used for drug delivery, shift in surface plasmon resonance is employed for sensing of biomolecules and fluorescent properties of the nanoparticles are utilized for imaging. The

nanoparticle-protein complexes are also greatly used in forming organic-inorganic hybrid multifunctional materials.

The experimental techniques used are presented in detail in **chapter 2**. UV-vis spectroscopy is an absorption spectroscopy involving electronic transition in the typical wavelength range of 200-700 nm [144]. The presence of proteins is determined by the characteristic absorption peak arising from electron transition of highest occupied molecular orbital (HOMO) to the lowest unoccupied molecular orbital (LUMO). The quantitative information on concentration of absorbing constitute is given by the Beer-Lambert law. The amount of free protein in nanoparticle-protein complexes is calculated by measuring the absorption spectra of free protein as separated from adsorbed protein using centrifugation. The transmission of light at a particular wavelength has been used to predict the structural evolution (phase behavior) of the resultant nanoparticle-protein systems. The structure and interaction information of the system are obtained using DLS and SANS. In DLS, the fluctuation of scattered light intensity is measured in terms of normalized autocorrelation function [148]. The decay constant of autocorrelation function provides the translational diffusion coefficient of the particles. The structure and interaction together are contained in the average diffusion coefficient or related effective hydrodynamic size given by Stokes-Einstein relation. On the other hand, structure and interaction can be separated using SANS technique [157]. The scattering intensity is given by $I(Q) \sim (\rho_p - \rho_s)^2 \times P(Q) \times S(Q)$, where ρ_p and ρ_s are scattering length densities of particles and solvent, respectively. $P(Q)$ is the orientational average of the square of the form factor and gives information about shape and size of the particle. $S(Q)$ is interparticle structure factor and depends on interaction potential between the particles. SANS has unique advantage for multi-component hydrogenous systems due to very different contrasts for hydrogen and

deuterium components. The other advantages of scattering techniques include that the systems are probed in-situ and under native conditions.

The main results of thesis are:

The cationic lysozyme and anionic BSA proteins show very different adsorption on anionic silica nanoparticles [194, 195]. The strong electrostatic attraction leads to adsorption of oppositely charged lysozyme on nanoparticles while electrostatic repulsion prevents any adsorption of similarly charged BSA on nanoparticle surface. The adsorption isotherm shows an exponential growth behavior with increasing protein concentration for lysozyme. The absence of any kind of adsorption of BSA protein rules out the possibility of site specific adsorption. Despite the differences in the adsorption of two proteins on nanoparticles, they render a similar phase behavior where nanoparticle-protein systems transform from being one-phase to two-phase above a critical protein concentration (CPC) and is much lower for lysozyme than for BSA. The bridging attraction in case of lysozyme (short-range) and depletion attraction for BSA (long-range) are proposed for aggregation of the nanoparticles in two-phase. The morphology of the aggregates is found to be mass fractal.

The phase behavior can be tuned by the presence of an electrolyte. The protein adsorption on nanoparticles does not show any significant change in presence of an electrolyte, whereas the phase behavior for both the nanoparticle-protein systems is significantly modified towards lower CPC [210, 211]. The suppression of the electrostatic repulsion between nanoparticles for lysozyme and enhancement of depletion interaction for BSA are found to be mainly responsible for the changes in the phase behavior of respective nanoparticle-protein systems in presence of electrolyte. The nanoparticle aggregates are characterized by fractal structures. There is no significant effect observed with the variation of counterions or co-ions in these systems.

Protein adsorption on nanoparticles is enhanced by varying the pH approaching its isoelectric point (IEP) [216, 217]. The pH variation allows systematic changes in the electrostatic interactions of the components in the system and hence the characteristics of their complexes. The pH of the solution is varied from physiological conditions to the IEP of the respective proteins ($IEP_{Lysozyme}$ ~ 11 and IEP_{BSA} ~ 4.6). For adsorbing protein (lysozyme), decrease in protein-protein repulsion results in higher adsorption. There is no pH dependent effect observed for non-adsorbing protein (BSA). The CPC increases for lysozyme but decreases for BSA with pH approaching towards their respective IEPs. Since the charge on lysozyme decreases as pH approaches the IEP, the number of lysozyme molecules required to neutralize the charge of the nanoparticles increases. As a result, a higher CPC is required to transform a one-phase nanoparticle-protein system into a two-phase system. For BSA, the decrease in pH enhances the depletion attraction between the nanoparticles because of a decrease in the repulsion between BSA molecules and at the same time reduces the electrostatic repulsion between the nanoparticles. Lysozyme mediated attractive interaction between the nanoparticles decreases with pH approaching IEP due to decrease in charge on the protein. In the case of BSA, decrease in BSA-BSA repulsion enhances the depletion attraction between the nanoparticles as pH is shifted towards IEP. The morphology of the nanoparticle aggregates remains as mass fractal independent of the pH.

The size of the nanoparticles has distinct effect on properties of nanoparticle-protein complexes. The amount of lysozyme adsorption on nanoparticles increases on lowering the size of the nanoparticles, whereas BSA remains non-adsorbing [231, 232]. The total amount of adsorbed lysozyme, as governed by the surface-to-volume ratio, increases on lowering the size of the nanoparticles for fixed volume fraction of the nanoparticles. The binding affinity of protein

adsorption increases whereas the saturation value decreases with increasing the size of the nanoparticles. The increase in saturation value for smaller particles is interpreted in terms of the larger total surface area available for protein adsorption. The binding affinity depends on the curvature of the nanoparticles and hence favours the larger size of the nanoparticles. The CPC decreases with increase in size of nanoparticles for both the proteins. The decrease in CPC with increase in size for the lysozyme protein is decided by the dominance of number density effect over the surface area effect. The CPC in the case of non-adsorbing BSA protein is lowered with the increase in the size of the nanoparticles because of the enhancement of the excluded volume of an individual nanoparticle and number density effects. The total (attractive + repulsive) potential leading to nanoparticles fractal aggregation in two-phase formation is found to be more attractive for larger sized nanoparticles.

To conclude, this thesis has investigated the properties of nanoparticle-protein complexes as tuned by the electrostatic interactions between the components. The anionic silica nanoparticles and two globular proteins (cationic lysozyme and anionic BSA) were used as model systems. The complexes were characterized by UV-vis spectroscopy and scattering techniques (DLS and SANS). The lysozyme and BSA proteins show very different adsorption on silica nanoparticles. However, the complexes of nanoparticles with both the proteins show unique phase transformation from one-phase to two-phase above a critical protein concentration. The presence of protein induces the short-range and long-range attraction between the nanoparticles with lysozyme and BSA, respectively. The nanoparticle aggregates in two-phase are characterized as fractals. The solution conditions (ionic strength and pH) as well as size of the nanoparticles were employed to tune the properties of nanoparticle-protein complexes. The observed changes in the adsorption and phase behavior of nanoparticle-protein complexes are

interpreted in terms of the modification of underlying interactions (nanoparticle-protein, nanoparticle-nanoparticle and protein-protein) and resultant structures (nanometer to micron size) of the complexes. The results of the present thesis can be utilized for the nanoparticle applications in biomedical such as drug delivery and bio-imaging. In particular, the pH-dependent results have shown that the adsorption of protein (or drug) on nanoparticles can be significantly enhanced with minimum changes in stability of resulting system near the isoelectric point of protein. The amount of adsorbed protein is also found to be significantly higher for small sized nanoparticles at a given volume fraction of nanoparticles. Further, the high bio-compatibility of silica nanoparticles in conjugation with fluroscence materials makes them useful for bio-imaging application. Future work involves to make the BSA protein adsorbing with the help of selective additives such as ionic surfactant and also to monitor the conformational changes of the adsorbed proteins.

References

1. P. Moriarty, Rep. Prog. Phys. **64**, 297 (2001).
2. G. Cao and Y. Wang, Nanostructures and Nanomaterials: Synthesis, Properties and Applications (World Scientific, Singapore, 2011).
3. M.-C. Daniel and D. Astruc, Chem. Rev. **104**, 293 (2004).
4. A. P. Alivisatos, Science **271**, 933 (1996).
5. E. Roduner, Nanoscopic Materials: Size Dependent Phenomena (RSC Publishing, Cambridge, 2006).
6. T. A. Taton, Nature **412**, 491 (2001).
7. O. V. Salata, J. Nanobiotechnol. **2**, 3 (2004).
8. E. Katz and I. Willner, Angew. Chem. Int. Ed **43**, 6042 (2004).
9. A. C. Balazs, T. Emrick and T. P. Russell, Science **314**, 1107 (2006).
10. Z. Nie, A. Petukhova and E. Kumacheva, Nat. Nanotechnol. **5**, 15 (2010).
11. M. De, P. S. Ghosh and V. M. Rotello, Adv. Mater. **20**, 4225 (2008).
12. J. Leszczynski, Nat. Nanotechnol. **5**, 633 (2010)**.**
13. N. L. Rosi and C. A. Mirkin, Chem. Rev. **105**, 1547 (2005).
14. C. M. Niemeyer, Angew. Chem. Int. Ed. **40**, 4128 (2001).
15. D. Whitford, Proteins: structure and function (John Wiley & Sons, England, 2005).
16. S. Rana, Y. -C Yeh and V. M. Rotello, Curr. Opin. Chem. Biol. **14**, 828 (2010).
17. U. Drechsler, N. O. Fischer, B. L. Frankamp and V. M. Totello, Adv. Mater. **16**, 271 (2004).
18. M-E A. Tam and K. H. Schifferli, Biomed. Mater. **3**, 034001(2008).
19. M. Sastry, M. Rao and K. N. Ganesh, Acc. Chem. Res. **35**, 847 (2002).
20. M. Mahmoud, N. Bertrand, H. Zope, O. C. Farokhzad, Nano Today **11**, 817 (2016).
21. A. A. Vertegel, R. W. Siegel and J. S. Dordick, Langmuir **20**, 6800 (2004).
22. S. Kumar, V. K. Aswal and P. Callow, Langmuir **30**, 1588 (2014).
23. B. Bharti, J. Meissner, S. H. L. Klapp and G. H. Findenegg, Soft Matter **10**, 718 (2014).

24. W. Shang, J. H. Nuffer, J. S. Dordick and R. W. Siegel, Nano Lett. **7**, 1991 (2007).
25. I. Lynch and K. A. Dawson, Nano Today **3**, 40 (2008).
26. J. S. Gebauer, M. Malissek, S. Simon, S. K. Knauer, M. Maskos, R. H. Stauber, W. Peukert and L. Treuel, Langmuir **28**, 9673 (2012).
27. A. E. Nel, L. Mädler, D. Velegol, T. Xia, E. M. V. Hoek, P. Somasundaran, F. Klaessig, V. Castranova, and M. Thompson, Nat. Mater. **8**, 543 (2009).
28. A. Shukla, E. Mylonas, E. Di Cola, S. Finet, P. Timmins, T. Narayanan and D. I. Svergun, Proc. Natl. Acad. Sci. U.S.A. **105**, 5075 (2008).
29. B. Viswanathan, Nanomaterials (Narosa Publishing House: Kolkata, 2013).
30. Y. S. Lee, Self-Assembly and Nanotechnology: A Force Balance Approach (John Wiley & Sons, New Jersey, 2008).
31. E. Roduner, Chem. Soc. Rev. **35**, 583 (2006).
32. C. N. R. Rao, G. U. Kulkarni, P. J. Thomas and P. P. Edwards, Chem. Eur. J. **8**, 29 (2002).
33. D. L. Feldhim and C. A. Foss, Metal Nanoparticles: Synthesis, Characterization, and Applications (Marcel Dekker Inc, New York, 2002).
34. J. Z. Zhang, Optical Properties and Spectroscopy of Nanomaterials (World Scientific Publishing, Singapore, 2009).
35. I. Moreels, K. Lambert, D. Smeets, D. D. Muynck, T. Nollet, J. C. Martins, F. Vanhaecke, A. Vantomme, C. Delerue, G. Allan and Z. Hens, ACS Nano **3**, 3023 (2009).
36. S. Eustis and M.A. El-Sayed, Chem. Soc. Rev. **35**, 209 (2006).
37. L.M. Liz-Marzán, Langmuir **22**, 32 (2006).
38. S.K. Ghosh and T. Pal, Chem. Rev. **107**, 4797 (2007).
39. R. Rigler and H. Vogel, Eds. Single Molecules and Nanotechnology (Springer, Berlin, 2008).
40. C. N. R. Rao, A. Müller and A. K. Cheetham, The Chemistry of Nanomaterials: Synthesis, Properties and Applications (Wiley-VCH Verlag GmbH & Co. KGaA, Weinheim, 2004).
41. N. A. Frey, S. Peng, K. Cheng and S. Sun, Chem. Soc. Rev. **38**, 2532 (2009).

42. A.-H. Lu, E. L. Salabas and F. Schüth, Angew. Chem. Int. Ed. **46**, 1222 (2007).
43. R. H. Kodama, J. Magn. Magn. Mater. **200**, 359 (1999).
44. V. H. Grassian, J. Phys. Chem. C **112**, 18303 (2008).
45. N. L. Rosi and C. A. Mirkin, Chem. Rev. **105**, 1547 (2005)
46. W. Jiang, B. Y. S. Kim, J. T. Rutka and W. C. W. Chan, Nature Nanotechnol. **3**, 145 (2008).
47. A. Verma and F. Stellacci, Small **6**, 12, (2010).
48. K. J. Klabunde and R.M. Richards, Nanoscale materials in chemistry (John Wiley & Sons: New Jersey, 2009).
49. I. W. Hamley, Angew. Chem. Int. Ed. **42**, 1692 (2003).
50. L. Wang, W. Zhao, and W. Tan, Nano Res. **1**, 99 (2008).
51. N. J. Halas, ACS Nano **2**, 179 (2008).
52. W. O. Roberts and H. E. Bergna, Colloidal Silica: Fundamentals and Applications-Surfactant Science Series, Vol. **131** (Taylor and Francis: US, 2006).
53. I. A. Rahman and V. Padavettan, J. Nanomater. **15**, 132424 (2012).
54. W. Lu and C. M. Lieber, Nat. Mater. **6**, 841 (2007).
55. W. L. Barnes, A. Dereux, and T. W. Ebbesen, Nature **424**, 824 (2003).
56. M. R. Connolly *et al.*, Nature Nanotechnol. **8**, 417 (2013).
57. S. S. Kim, S. I. Na, J. Jo, D. Y. Kim and Y. C. Nah, Appl. Phys. Lett. **93**, 07 (2008).
58. S. Mokkapati, F. J. Beck, A. Polman and K. R. Catchpole, Appl. Phys. Lett. **95**, 053115 (2009).
59. M. Homberger and U. Simon, Phil. Trans. R. Soc. A **368**, 1405 (2010).
60. P. P. Cowbum, Appl. Phys. Lett. **93**, 9310 (2003).
61. Q. A. Pankhurst, J. Connolly, S. K. Jones and J. Dobson, J. Phys. D: Appl. Phys. **36**, R167 (2003).
62. J. Tang, J. Liu, N. L. Torad, T. Kimura, and Y. Yamauchi, Nano Today **9**, 305 (2014).
63. Y. Wang *et al.*, J. Am. Chem. Soc. **138**, 3278 (2016).
64. J. N. Coleman, U. Khan, W. J. Blau, and Y. K. Gun'ko, Carbon **44**, 1624 (2006).

65. A. P. Kumar, D. Depan, N. S. Tomer, and R. P. Singh, Prog. Polym. Sci. **34**, 479 (2009).
66. C. C. Fleischer and C. K. Payne, Acc. Chem. Res. **47**, 2651 (2014).
67. I. Willner and B. Willner, Nano Lett. **10**, 3805 (2010).
68. T. Hanemann and D. V. Szabó, Materials **3** (2010).
69. B. P. Binks and J. A. Rodrigues, Langmuir **23**, 7436 (2007).
70. S. Santra, R. Tapec, N. Theodoropoulou, J. Dobson, A. Hebard, and W. Tan, Langmuir **17**, 2900 (2001).
71. D. Walczyk, F. B. Baldelli, M. P. Monopoli, I. Lynch and K. A. Dawson, J. Am. Chem. Soc. **132**, 5761 (2010).
72. P. Watson, A. T. Jones and D. J. Stephens, Adv. Drug Delivery Rev. **57**, 43 (2005).
73. K. A. Dill, Biochemistry **29**, 7133 (1990).
74. K. A. Dill and J. L. MacCallum, Science **338**, 1042 (2012).
75. C. I. Branden and J. Tooze, Introduction to Protein Structure (Tayler & Francis, New York, 2009).
76. A. V. Finkelstein and O. B. Ptitsyn, Protein Physics (Academic Press, London, 2002).
77. J. Klein, Proc. Natl. Acad. Sci. USA. **104**, 2029 (2007).
78. M. Lundqvist, J. Stigler , G. Elia, L. Iseult, T. Cedervall, and K. A. Dawson, Proc. Natl. Acad. Sci. USA **105**, 14265 (2008).
79. W. C. K. Poon and D. Andelman, Soft Condensed Matter Physics in Molecular and Cell Biology (Tayler & Francis, Boca Raton, 2006).
80. A. Stradner, H. Sedgwick, F. Cardinaux, W. C. K. poon, S. U. Egelhaaf and P. Schurtenberger, Nature **432**, 492 (2004).
81. Y. Liu, E. Fratini, P. Baglioni, W.-R. Chen, and S.-H. Chen, Phys. Rev. Lett. **95**, 118102 (2005).
82. Y. Liu, L. Porcar, J. Chen, W.-R. Chen, P. Falus, A. Faraone, E. Fratini, K. Hong, and P. Baglioni, J. Phys. Chem. B **115**, 7238 (2011).

83. D. J. Bharali, I. Klejbor, E. K. Stachowiak, P. Dutta, I. Roy, N. Kaur, E. J. Bergey, P. N. Prasad, and M. K. Stachowiak, Proc. Natl. Acad. Sci. USA **102**, 11539 (2005).
84. R. A. Mcmillan, C. D. Paavola, J. Howard, S. L. Chan, N. J. Zaluzec, and J. D. Trent, Nat. Mater. **1**, 247 (2002).
85. H. Bayraktar, P. S. Ghosh, V. M. Rotello and M. J. Knapp, Chem. Commun. **10**, 1390 (2006).
86. R. L. Phillips, O. R. Miranda, C. C. You, V. M. Rotello, U. H. F. Bunz, Angew. Chem. Int. Ed. **47**, 2590 (2008).
87. H. Xiong, D. V. D. Lelie, O. Gang, Phys. Rev. Lett. **102**, 015504 (2009).
88. R. J. Macfarlane, B. Lee, M. R. Jones, N. Harris, G. C. Schatz, C. A. Mirkin, Science **334**, 204 (2011).
89. S. Mann, W. Shenton, M. Li, S. Connolly, D. Fitzmaurice, Adv. Mater. **12**, 147 (2000).
90. C. M. Roth and A. M. Lenhoff , Langmuir **11**, 3500 (1995).
91. J. Buijs and V. Hlady, J. Colloid Interface Sci. **190**, 171 (1997).
92. M. van der Veen, W. Norde and M. C. Stuart, Colloids Surf. B **35**, 33 (2004).
93. P. M. Biesheuvel, M. van der Veen and W. Norde, J. Phys. Chem. B **109**, 4172 (2005).
94. R. A. Hartvig, M. van de Weert, J. Østergaard, L. Jorgensen and H. Jensen, Langmuir **27**, 2634 (2011).
95. F. Felsovalyi, P. Mangiagalli, C. Bureau, S. K. Kumar and S. Banta, Langmuir **27**, 11873 (2011).
96. R. Podila, R. Chen, P. C. Ke, J. M. Brown, A. M. Rao, Appl. Phys. Lett. **101**, 263701 (2012).
97. M. De, O. R. Miranda, S. Rana, V. M. Rotello, Chem. Commun. **16**, 2157 (2009).
98. M. Lundqvist, I. Sethson, B. H. Jonsson, Langmuir **20**, 10639 (2004).
99. R. Sarkar, S. S. Narayanan, L. O. Palsson, F. Dias, A. Monkman and S. K. Pal, J. Phys. Chem. B **111**, 12294 (2007).
100. P. Roach, D. Farrar, C. C. Perry, J. Am. Chem. Soc. **128**, 3939 (2006).

101. J. Israelachvili, Intermolecular and Surface Forces (Academic Press, London, 2011).

102. S. Abbas, I. Yadav, S. Kumar, V. K. Aswal and J. Kohlbrecher, Chem. Phys. Lett. **675**, 124 (2017).

103. H. N. W. Lekkerkerker and R. Tuinier, Colloids and the Depletion Interaction (Springer, New York, 2011).

104. P. Attard, Adv. Chem. Phys. **92**, 1(159) (1996).

105. B.V. Deryaguin, L. Landau, Acta Phys. Chem. **14**, 633 (1941).

106. E. J. W. Verwey, J. T. G. Overbeek, Theory of the Stability of Lyophobic Colloids (Elsevier, Amsterdam, 1948).

107. D. H. Napper, J. Colloid Interface Sci. **58**, 390 (1977).

108. K. van Gruijthuijsen, M. Obiols-Rabasa, M. Heinen, G. Nägele, and A. Stradner, Langmuir **29**, 11199 (2013).

109. O. V. Borisov and A. Halperin, Macromolecules **29**, 2612 (1996).

110. A. A. Louis, E. Allahyarov, H. Löwen, and R. Roth, Phys. Rev. E **65**, 061407 (2002)

111. M. E. Leunissen et al. Nature **437**, 235 (2005).

112. R. Podgornik and M. Licer, Curr. Opin. Colloid Interface Sci.**11**, 273 (2006).

113. R. J. Macfarlane, B. lee, m. R. Jones, N. Harris, G. C. Schatz and C. A. Mirkin, Science **334**, 204 (2011).

114. J. Chen, S. R. Kline and Y. Liu, J. Chem. Phys. **142**, 084904 (2015).

115. S. Asakura and F. Oosawa, J. Chem. Phys. **22**, 1255 (1954).

116. W. Agut, D. Taton, A. Brûlet, O. Sandre, and S. Lecommandoux, Soft Matter **7**, 9744 (2011).

117. V. J. Anderson and H. N. W. Lekkerkerker, Nature, **416**, 811 (2002).

118. E. Arunan, et al. Pure Appl. Chem., **83**, 1637 (2011).

119. C. Tanford, The Hydrophobic Effect; Wiley: New York (1980).

120. S. Mehan, A. J. Chinchalikar, S. Kumar, V. K. Aswal, and R. Schweins, Langmuir **29**, 11290 (2013).

121. S. Mehan, V. K. Aswal and J. Kohlbrecher, Phys. Rev. E **92**, 032713 (2015).

122. D. Ray, V. K. Aswal, and J. Kohlbrecher, J. App. Phys. **117**, 164310 (2015).

123. D. N. Petsev, P. G. Vekilov, Phys. Rev. Lett. **84**, 1339 (2000).

124. M. Carpineti, R. Piazza, Phys. Chem. Chem. Phys. **6**, 1506 (2004).

125. S. Patil, A. Sandberg, E. Heckert, W. Self, S. Seal, Biomaterials **28**, 4600 (2007).

126. K. Rezwan, A. R. Studart, J. Voros, L. J. Gauckler, J. Phys. Chem. B **109**, 14469 (2005).

127. T. Neuberger, B. Schopf, H. Hofmann, M. Hofmann and B. V. Rechenberg, J. Magn. Magn. Mater. **293**, 483 (2005).

128. Q. Yang, S. H. Wang, P. W. Fan, L. F. Wang, Y. Di, K. F. Lin and F. S. Xiao, Chem. Mater. **17**, 5999 (2005).

129. E. Katz, I. Willner, J. Wang, Electroanalysis **16**, 19 (2004).

130. Y. Astuti, E. Palomares, S. A. Haque and J. R. Durrant, J. Am. Chem. Soc. **127**, 15120 (2005).

131. A. M. Derfus, W. C. W. Chan and S. N. Bhatia, Nano Lett. **4**, 11 (2004).

132. H. S. Choi, W. Liu, P. Misra, E. Tanaka, J. P. Zimmer, B. I. Ipe, M. G. Bawendi and J. V. Frangioni, Nat. Biotechnol. **25**, 1165 (2007).

133. J. K. Herr, J. E. Smith, C. D. Medley, D. H. Shangguan and W. H. Tan, Anal. Chem. **78**, 2918 (2006).

134. R. Weissleder, K. Kelly, E. Y. Sun, T. Shtatland and L. Josephson, Nat. Biotechnol. **23**, 1418 (2005).

135. R. Wang, Y. Zhang, D. Lu, J. Ge, Z. Liu and R. N. Zare, Nanomed Nanobiotechnol 2013. doi: 10.1002/wnan.1210.

136. R. A. Mcmillan, C. D. Paavola, J. Howard, S. L. Chan, N. J. Zaluzec, and J. D. Trent, Nat. Mater. **1**, 247 (2002).

137. W. H. Suh, Y. H. Suh, and G. D. Stucky, Nano Today **4**, 27 (2009).

138. Soft Matter Characterization, edited by R. Borsali, and R. Pecora (Springer, Netherlands, 2008).

139.M. Mahmoudi, I. Lynch, M. R. Ejtehadi, M. P. Monopoli, F. B. Bombelli, and S. Laurent, Chem. Rev. **111**, 5610 (2011).

140.W. S. Gosal and S. B. Ross-Murphy, Curr. Opin. Colloid Interface Sci. **5**, 188 (2000).

141.J. Wang, U. B. Jensen, G. V. Jensen, S. Shipovskov, V. S. Balakrishnan, D. Otzen, J. S. Pedersen, F. Besenbacher, D. S. Sutherland, Nano Lett. **11**, 4985 (2011).

142.J. J. Bozzola and L. D. Russell, Electron Microscopy: Principles and Techniques for Biologists (Jones and Bartlett Publishers, Canada, 1999).

143.E. Casals, T. Pfaller, A. Duschl, G. J. Oostingh, and V. Puntes, ACS Nano **4**, 3623 (2010).

144.Y. Leng, Materials Characterization: Introduction to Microscopic and Spectroscopic Methods (John Wiley & Sons: Singapore, 2008).

145. R. Podila, R.; Chen, R.; Ke, P. C.; Brown, J. M.; Rao, A. M. Effects of Surface Functional Groups on the Formation of Nanoparticle-Protein Corona. Appl. Phys. Lett. **101**, 263701 (2012).

146.L. Cipelletti, V. Trappe, D. J. Pine, Fluids, Colloids and Soft Materials: An Introduction to Soft Matter Physics (John Wiley & Sons, 2016), pp 131-138.

147.T. Li, A. J. Senesi and B. lee, Chem. Rev. **116**, 11128 (2016).

148.R. Pecora, Dynamic Light Scattering (Plenum, New York, 1985).

149.S.W. Lovesey, Theory of neutron scattering from condensed matter (Oxford University Press, New York, 2003).

150.P. A. Hassan, S. Rana, and G. Verma, Langmuir, **31**, 3 (2015).

151.D. E. Koppel, J. Chem. Phys. **57**, 4814 (1972).

152. B. J. Frisken, Appl. Opt. **40**, 4087 (2001).

153.S. W. Provencher, Comput. Phys. Commun. **27**, 213 (1982).

154.S. W. Provencher, Comput. Phys. Commun. **27**, 229 (1982).

155. R. J. Hunter, Zeta potential in colloid science: principles and applications (Academic Press, UK, 1988).

156.P. Linder and T. Zemb (Eds.), Neutron, X-ray and Light Scattering (North Holland, Amsterdam, 1991).

157.J. S. Higgins and H. C. Benoit, Polymers and Neutron Scattering (Clarendon Press, Oxford, 1994).

158. L. A. Feigin and D. I. Svergun, Structure Analysis by Small-Angle X-Ray and Neutron Scattering (Plentum Press, New York, 1987).

159.A. Guinier and G. Fournet, Small angle scattering of X-rays (Wiley, New York, 1955).

160.S.-H. Chen and T.-L. Lin, Methods in Experimental Physics, edited by D. L. Price, and K. Sköld (Academic Press, New York, 1987), pp. 489.

161.E. Y. Sheu, Phys. Rev. A **45**, 2428 (1992).

162.G. Beaucage, H. K. Kammler and S. E. Pratsinis, J. Appl. Cryst.**37**, 523 (2004).

163.J. S. Pedersen, Adv. Colloid Interface Sci. **70**, 171 (1997).

164.D. I. Svergun and M. H. J. Koch, Rep. Prog. Phys. **66**, 1735 (2003).

165.C. G. Windsor, J. Appl. Crystallogr. **21**, 582 (1988).

166.G. Porod, Kolloid Z., **124**, 83 (1951).

167.J. B. Hayter and J. Penfold, Colloid Polym. Sci. **261**, 1022 (1983).

168.P. A. Egelstaff, An introduction to the liquid state (Academic Press, London, 1967).

169.R. J. Hunter, Foundations of colloid science (Oxford University Press, Oxford, 2001).

170.L. S. Ornstein and F. Zernike, Proc. Acad. Sci. Amsterdam, **17**, 793 (1914).

171.J. K. Percus and G. Yevik, J. Phys. Rev. **110**, 1 (1958).

172.J. P. Hansen and J. B. Hayter, Mol. Phys. **46,** 3 (1982).

173.A. Perera, P. G. Kausalik and G. N. Patey, J. Chem. Phys. **87**, 1295 (1987).

174. N. W. Ashcroft and J. Lekner, Phys. Rev. **145**, 83 (1966).

175.R. J. Baxter, J. Chem. Phys., **49**, 2770 (1968).

176.Y. Liu, W.-R. Chen, and S.-H. Chen, J. Chem. Phys. **122**, 044507 (2005).

177.T. A. Witten and L. M. Sander, Phys. Rev. Lett. **47**, 1400 (1981).

178.J. Teixeira, J. Appl. Cryst., **21**, 781 (1988).

179. D. F. R. Mildner and P. L. Hall, J. Phys. D: Appl. Phys. **19**, 1535 (1986).

180. A. P. Radlinski, E. Z. Radlinska, M. Agamalian, G. D. Wignall, P. Lindner and O. G. Randl, Phys. Rev. Lett., **82**, 3078 (1999).

181. S. Kumar, V. K. Aswal, and J. Kohlbrecher, Langmuir **28**, 9288 (2012).

182. D. Ray and V. K. Aswal, J. Phys.: Condens. Matt. **26**, 035102 (2014).

183. S. Mehan, V. K. Aswal, and J. Kohlbrecher, Langmuir **30**, 9941 (2014).

184. V. K. Aswal and P. Goyal, Curr. Sci. **79**, 947 (2000).

185. J. Kohlbrecher and W. Wagner, J. Appl. Cryst. **33**, 804 (2000).

186. G. D. Wignall and F. S. Bates, J. Appl. Cryst. **20**, 28 (1987).

187. I. Lynch, T. Cedervall, M. Lundqvist, C. Cabaleiro-Lago, S. Linse, K. A. Dawson, Adv. Colloid Interface Sci. **167**, 134 (2007).

188. R. Chen, P. Choudhary, R. N. Schurr, P. Bhattacharya, J. M. Brown, and P. C. Ke, Appl. Phys. Lett. **100**, 013703 (2012).

189. X. Yu, D. Y. Lei, F Amin, R. Hartmann, G. P. Acuna, A. G.-Martínez, S. A. Maier, P. Tinnefeld, S. C.-Romero, and W. J. Parak, Nano Today **8**, 480 (2013).

190. H. He, X. Xu, H. Wu, Y. Zhai, and Y. Jin, Anal. Chem., **85**, 4546 (2013).

191. B. Bharti, J. Meissner, and G.H. Findenegg, Langmuir **27**, 9823 (2011).

192. S. Kumar, V. K. Aswal, and J. Kohlbrecher, Langmuir **27**, 10167 (2011).

193. T. J. Su, J. R. Lu, R. K. Thomas, Z. F. Cui, and J. Penfold, J. Phys. Chem. B **102**, 8100 (1998).

194. I. Yadav, S. Kumar, V. K. Aswal and J. Kohlbrecher, Phys. Rev. E **89**, 032304 (2014).

195. I. Yadav, V. K. Aswal and J. Kohlbrecher, AIP Conf. Proc. **1591**, 216 (2014).

196. F. Zhang, M. W. A. Skoda, R. M. J. Jacobs, R. A. Martin, C. M. Martin, and F. Schreiber, J. Phys. Chem. B **111**, 251 (2007).

197. J. S. Pedersen, D. Posselt, and K. Mortensen, J. Appl. Cryst. **23**, 321 (1990).

198. S. Kumar, M. J Lee. V. K. Aswal,and S. M. Choi, Phys. Rev. E **87**, 042315 (2013).

199. S. Chodankar, V. K. Aswal, J. Kohlbrecher, R. Vavrin, and A. G. Wagh, Phys. Rev. E **79**, 021912 (2009).

200. A. J. Chinchalikar, V. K. Aswal, J. Kohlbrecher, and A. G. Wagh, Phys. Rev. E **87**, 062708 (2013).

201. A. M. Yake, C. E. Snyder, and D. Velegol, Langmuir **23**, 9069, (2007).

202. S. R. Saptarshi, A. Duschl, and A. L. Lopata, J. Nanobiotech. **11**, 26 (2013).

203. Y. Min, M. Akbulut, K. Kristiansen, Y. Golan, and J. Israelachvili, Nat. Mater. **7**, 527 (2008).

204. H. Yuan, J. Li, G. Bao, and S. Zhang, Phys. Rev. Lett. **105**, 138101 (2010).

205. L. Belloni, J. Phys. Condens. Matter **12**, 549 (2000).

206. T. Missana and A. Adell, J. Colloid Interface Sci. **230**, 150 (2000).

207. M. Boström, D. R. M. Williams, and B. W. Ninham, Phys. Rev. Lett. **87**, 168103(2001).

208. M. Ruths, H. Yoshizawa, L. J. Fetters, and J. N. Israelachvili, Macromolecules **29**, 7193 (1996).

209. K. Rezwan, L. P. Meier, and L. J. Gauckler, Biomaterials **26**, 4351 (2005).

210. I. Yadav, V. K. Aswal and J. Kohlbrecher, Phys. Rev. E **91**, 052306 (2015).

211. I. Yadav, V. K. Aswal and J. Kohlbrecher, AIP Conf. Proc **1665**, 040008 (2015).

212. P. R. Bevington, Data Reduction and Error Analysis for Physical Sciences (McGraw-Hill, New York, 1969).

213. Y. Zeng, S. Grandner, C. L. P. Oliveira, A. F. Thunemann, O. Paris, J. S. Pedersen, S. H. L. Klapp and R. von Klitzing, Soft Matter **7**, 10899 (2011).

214. S. Kumar, D. Ray, V. K. Aswal, and J. Kohlbrecher, Phys. Rev. E **90**, 042316 (2014).

215. J. C. Crocker, J. A. Matteo, A. D. Dinsmore, and A. G. Yodh, Phys. Rev. Lett. **82**, 4352 (1999).

216. I. Yadav, S. Kumar, V. K. Aswal and J. Kohlbrecher, Langmuir **33**, 1227 (2017).

217. I. Yadav, V. K. Aswal, and J. Kohlbrecher, AIP Conf. Proc. (2017).

218. P. Leroy, N. Devau, A. Revil, M. Bizi, J. Colloid Interface Sci. **410**, 81 (2013).

219. K. Ohsawa, M. Murata, H. Ohshima, Colloid Polym. Sci. **264**, 1005 (1986).

220. A. Fortini, M. Dijkstra, R. Tuinier, J. Phys.: Condens. Matter **17**, 7783 (2005).

221. A. R. Denton, M. Schmidt, J. Chem. Phys. **122**, 244911 (2005).

222. F. Catalano, G. Alberto, P. Ivanchenko, G. Dovbeshko, G. Martra, J. Phys. Chem. C **119**, 26493 (2015).

223. J. -T. Tai, C. -S. Lai, H. -C. Ho, U.-S. Yeh, H.-F. Wang, R.-M. Ho, D.-H. Tsai, Langmuir **30**, 12755 (2014**).**

224. P. Asuri, S. S. Karajanagi, H. C. Yang, T. J. Yim, R. S. Kane, and J. S. Dordick, Langmuir **22**, 5833 (2006).

225. A. Albanese, P. S. Tang, and W. C. W. Chan, Annu. Rev. Biomed. Eng. **14**, 1 (2012).

226. A. J. Chinchalikar, V. K. Aswal, J. Kohlbrecher, and A. G. Wagh, J. Nanofluids **2**, 194 (2013).

227. C. D. Walkey, J. B. Olsen, H. Guo, A. Emili, and W. C. W. Chan, J. Am. Chem. Soc. **134**, 2139 (2012).

228. S. M. Ilett, A. Orrock, W. C. K. Poon, and P. N. Pusey, Phys. Rev. E **51**, 1344 (1995).

229. B. Gotzelmann, R. Evans, and S. Dietrich, Phys. Rev. E **57**, 6785 (1998).

230. K. Park, H. Koerner, and R. A. Vaia, Nano Lett. **10**, 1433 (2010).

231. I. Yadav, V. K. Aswal and J. Kohlbrecher, Phys. Rev. E **93**, 052601 (2016).

232. I. Yadav, V. K. Aswal and J. Kohlbrecher, AIP Conf. Proc. **1731**, 050093 (2016).

233. H. N. W. Lekkerkerker, W. C. Poon, P. N. Pusey, A. Stroobants, and P. B. Warren, Europhys. Lett. **20**, 559 (1992).

234. J. C. Crocker and D. G. Grier, Phys. Rev. Lett. **77**, 1897 (1996).

235. T. prozorov, S. K. Mallapragada, B. Narasimhan, L. Wang, P. Palo, M. N. Hamilton, T. J. Williams, D. A. Bazylinski, R. Prozorov, P. C. Canfield, Adv. Funct. Mater. **17**, 951 (2007).